

# Analysis of Key Electronic, Optical and Structural Parameters in Mesoscopic Solid-State Solar Cells

THÈSE N° 6238 (2014)

PRÉSENTÉE LE 11 JUILLET 2014

À LA FACULTÉ DES SCIENCES DE BASE  
LABORATOIRE DE PHOTONIQUE ET INTERFACES  
PROGRAMME DOCTORAL EN PHOTONIQUE

ÉCOLE POLYTECHNIQUE FÉDÉRALE DE LAUSANNE

POUR L'OBTENTION DU GRADE DE DOCTEUR ÈS SCIENCES

PAR

**Amalie DUALEH**

acceptée sur proposition du jury:

Prof. M. Chergui, président du jury  
Prof. M. Graetzel, Dr M. K. Nazeeruddin, directeurs de thèse  
Prof. A. Fontcuberta i Morral, rapporteuse  
Prof. A. Hagfeldt, rapporteur  
Prof. N. Mathews, rapporteur



ÉCOLE POLYTECHNIQUE  
FÉDÉRALE DE LAUSANNE

Suisse  
2014



Nobody ever figures out what life is all about,  
and it does not matter.  
Explore the world.  
Nearly everything is really interesting if you go into it deeply enough.  
— Richard P. Feynman

*To my parents.*



# Abstract

In the neverending race to fulfill the world's growing energy needs, the generation of clean renewable and low-cost energy is of crucial importance. This has stimulated the development of third generation photovoltaic technologies such as the dye-sensitized solar cell (DSSC). The DSSC is inspired by the natural process of photosynthesis where a light harvesting species adopts the role of chlorophyll in the absorption of solar irradiation for the direct conversion of sunlight into electricity. In the solid-state dye-sensitized solar cell (ssDSSC) the liquid redox electrolyte utilized in the conventional liquid-based DSSC is replaced by a solid hole-transporting material (HTM).

The inherent complexity of the system and the interplay between the many different components signifies that in many ways the device operating mechanisms of this system are still poorly and/or not fully understood. In this thesis I examine the operating processes of mesoscopic solar cells employing the organic *p*-type semiconductor 2,2',7,7'-tetrakis(*N,N*-di-*para*-methoxyphenylamine)-9,9'-spirobifluorene (spiro-MeOTAD) with the aim to gain a more in-depth understanding that can be implemented in the development of high performance solid-state solar cells.

Using impedance spectroscopy (IS) I extensively examine the internal electrical processes occurring in ssDSSCs type systems without any sensitizer present. Different device configurations are used to differentiate and evaluate the individual interfaces, charge-transfer and transport processes of ssDSSCs. The charge-transport within the HTM is uncovered and found to contribute to the net series resistance of the system. This is further evaluated using the Arrhenius equation to determine an activation energy for the hole-hopping transport in undoped spiro-MeOTAD. Photodoping – exposure to light and oxygen – and chemical *p*-doping of the spiro-MeOTAD are found to improve the photovoltaic performance of the devices by increasing the conductivity of the HTM. Subtle differences in the effect of the two doping procedures are exposed using IS, revealing an improved contact between the HTM and the back contact in the presence of oxygen and light.

The photovoltaic performance of ssDSSCs using different molecular sensitizers is examined and the physical and chemical properties of the dyes are correlated with the investigated device mechanisms. The interface between the sensitized mesoporous TiO<sub>2</sub> and the HTM is examined, revealing the influence of the dye dipole moment and surface coverage on the TiO<sub>2</sub> conduction band position and thus on the open-circuit potential. Furthermore the relationship between the dye molecular structure and efficient charge separation is probed.

---

Finally optical measurements reveal the beneficial de-aggregating ability of spiro-MeOTAD.

The hybrid organic-inorganic lead-iodide based perovskite  $\text{CH}_3\text{NH}_3\text{PbI}_3$  is implemented as light harvesting material in mesoscopic solid-state solar cells and analyzed by IS. Using existing equivalent circuit models for liquid and solid-state DSSCs as a basis, a working model is developed and validated for these perovskite type cells. Separate features corresponding to the electronic and ionic conductivities of the perovskite material are identified. These features are heavily dependent on the nature, crystallinity and morphology of the perovskite material which define its transport and electrical properties. Furthermore the architecture and device configuration also play an important role.

The solution processability of these materials present one of their major advantages. Here I examine the deposition of the material from a mixture of its precursors in a common solvent. The structure and shape of the perovskite film formed can be controlled by the choice of solvent. The composition of the precursor solution determines the nature of the perovskite formed. The conversion step is achieved by annealing the as deposited precursor solution, which strongly influences the perovskite film morphology. At temperatures above  $120^\circ\text{C}$  there is a detrimental formation of  $\text{PbI}_2$ . The  $\text{PbI}_2$  acts as a sink for charges, limiting the injection to and from the  $\text{TiO}_2$  preventing the buildup of charges. This results in a deviation from the typical chemical capacitive behavior of the devices determined by IS.

Finally the thermal properties and behavior of  $\text{CH}_3\text{NH}_3\text{PbI}_3$  perovskite and its individual components are scrutinized. Mixed halide systems led to the formation of excess organic material, which undergoes sublimation. The enthalpy and temperature of sublimation of the organic  $\text{CH}_3\text{NH}_3\text{X}$  ( $\text{X}=\text{I}$  or  $\text{Cl}$ ) constituents are determined. The decomposition of the perovskite follows the initial loss of the organic component – consecutive loss of the acid and amine components – and the second degradation loss of the inorganic species. Subtle differences in the crystal structure of the  $\text{CH}_3\text{NH}_3\text{PbI}_3$  perovskite formed from different precursor solutions are exposed.

The comprehensive studies presented here examine the key parameters governing the device mechanisms of solid-state mesoscopic cells. The knowledge and insight gained on the operating processes and interfaces provide a valuable contribution to the improvement and development of high performance solar cells.

**Keywords:** photovoltaics, solid-state dye-sensitized solar cells, hole-transport material, spiro-MeOTAD, hybrid perovskite solar cell, organic-inorganic lead-iodide perovskite, organic sensitizers, impedance spectroscopy, thermal properties.

# Résumé

Dans la course pour répondre aux besoins énergétiques croissants de la planète, la production d'énergie renouvelable à bas coût est d'une importance cruciale. Le développement des technologies photovoltaïques de troisième génération telles que la cellule solaire à colorant (dye-sensitized solar cell ou DSSC en anglais) – également appelée « cellule Grätzel » en référence à son concepteur – a notamment été stimulé. Les DSSCs s'inspirent du processus naturel de la photosynthèse : le rôle de la chlorophylle dans l'absorption du rayonnement solaire est joué par un pigment photosensible pour convertir la lumière du soleil en électricité. Dans la DSSC de type solide (solid-state DSSC ou ssDSSC en anglais), l'électrolyte redox de la DSSC classique est remplacé par un conducteur de trous solide (solid hole-transporting material ou HTM en anglais).

La complexité inhérente au système et l'interaction entre les nombreux composants signifient que, dans de nombreux cas, les mécanismes de fonctionnement de ce dispositif sont encore mal et/ou pas complètement compris. Dans cette thèse, j'examine les processus de fonctionnement des cellules solaires mésoscopiques employant le semiconducteur organique de type *p* 2,2',7,7'-tetrakis(*N,N*-di-*para*-methoxyphenylamine)-9,9'-spirobifluorene (spiro-MeOTAD) dans le but d'acquérir une compréhension plus profonde d'une part et de développer des ssDSSCs à haut rendement d'autre part.

En utilisant la spectroscopie d'impédance, j'examine les processus électriques internes qui se produisent dans les systèmes du type ssDSSC sans pigment. Les interfaces individuelles ainsi que les processus de transfert et de transport des charges dans les ssDSSCs sont différenciés et évalués. Le transport de charge à l'intérieur du HTM est exposé et sa contribution à la résistance en série du système est présentée. Le rendement photovoltaïque des ssDSSCs est amélioré par photo-dopage – *via* l'action de la lumière et de l'oxygène – et par dopage chimique *p* en augmentant la conductivité du HTM. Les mesures d'impédance révèlent de subtiles différences dans les effets de ces deux méthodes de dopage. En outre, il est démontré que le contact entre la contre-électrode et le HTM est meilleur en présence d'oxygène et de lumière.

Le rendement photovoltaïque des ssDSSCs utilisant différents pigments moléculaires est examiné et les propriétés physiques et chimiques des colorants sont corrélées avec les mécanismes de fonctionnement étudiés. L'interface entre le TiO<sub>2</sub> mésoporeux couverte par le colorant et le HTM est étudiée. L'influence du moment dipolaire et également celle de la couverture de la surface par le colorant sur la position de la bande de conduction de TiO<sub>2</sub>,

---

et donc sur le potentiel à circuit ouvert, sont révélées. De plus, la relation entre la structure moléculaire du colorant et l'efficacité de séparation des charges est démontrée. Enfin, des mesures optiques révèlent la capacité de désagrégation bénéfique du spiro-MeOTAD.

La pérovskite hybride organique-inorganique à base de plomb iodure  $\text{CH}_3\text{NH}_3\text{PbI}_3$  est utilisé en tant que matériau absorbeur de lumière dans les cellules solaires mésoscopiques solides et analysé par impédance. En utilisant des modèles de circuits équivalents existants pour les DSSCs liquides et solides comme références, un modèle pour ce type de cellules à pérovskites est développé et validé. Les caractéristiques distinctes correspondant aux conductivités électronique et ionique de la pérovskite sont identifiées. Ces propriétés sont fortement dépendantes de la nature, de la cristallinité et de la morphologie du matériau et définissent le transport ainsi que les propriétés électriques de la pérovskite

La facilité de traitement de ces matériaux en solution représente un de leurs avantages principaux. Le dépôt de ce matériau à partir d'un mélange de précurseurs dans un solvant communément utilisé est examiné. Nos expériences montrent que la structure et la forme du film de la pérovskite formé peuvent être contrôlées par le choix du solvant. La composition de la solution de précurseurs détermine la nature du cristal de la pérovskite formé. L'étape de conversion est effectuée par un chauffage de la solution de précurseur à déposer, une étape qui influence fortement la morphologie de la couche de pérovskite. À des températures supérieures à  $120^\circ\text{C}$ , il y a une formation préjudiciable de  $\text{PbI}_2$ . Le  $\text{PbI}_2$  agit comme un puits pour les charges, ce qui limite l'injection dans et hors du  $\text{TiO}_2$  et empêche par conséquent l'accumulation de charges. Cela se traduit par une déviation par rapport au comportement typique de la capacité chimique.

Enfin, les propriétés thermiques et le comportement de la pérovskite  $\text{CH}_3\text{NH}_3\text{PbI}_3$  et de ses composants individuels sont analysés. Les systèmes composés d'halogénures mixtes conduisent à la formation de matière organique en excès qui subit une sublimation. Ensuite, l'enthalpie et la température de sublimation des constituants organiques  $\text{CH}_3\text{NH}_3\text{X}$  ( $\text{X}=\text{I}$  ou  $\text{Cl}$ ) sont déterminées. La décomposition de la pérovskite suit la perte initiale d'éléments organiques – la perte successive des composants acide et amine – puis la dégradation des espèces inorganiques. Des petites différences dans la structure cristalline de la pérovskite formée à partir des solutions de précurseurs différents sont exposées.

Les études de cette thèse fournissent une enquête approfondie sur les principaux paramètres régissant les mécanismes de fonctionnement des cellules solaires mésoscopiques solides. Les connaissances et informations récoltées sur les processus d'exploitation et les interfaces apportent une contribution précieuse à l'amélioration et au développement de cellules solaires de haute efficacité.

**Mots-clés :** photovoltaïque, cellule solaire à colorant de type solide, conducteur de trous, spiro-MeOTAD, cellule solaire à pérovskite hybride, pérovskite organique-inorganique à base de plomb iodure, colorant organique, spectroscopie d'impédance, propriétés thermiques.



# Zusammenfassung

Um den wachsenden Energiebedarf der Welt zu erfüllen, ist die Erzeugung von sauberer, erneuerbarer und kostengünstiger Energie von entscheidender Bedeutung. Dies hat die Entwicklung der Dritten Generation Photovoltaik Technologien wie die Farbstoffsolarzelle – auch Grätzel-Zelle nach ihrem Erfinder genannt – angeregt. Das Prinzip der Farbstoffsolarzelle wird von dem natürlichen Prozess der Photosynthese inspiriert, wobei die Rolle des Chlorophylls in der Absorption von Sonnenlicht für die direkte Umwandlung von Sonnenenergie in elektrischen Strom von einem lichtabsorbierendem Farbstoffmolekül übernommen wird. In der Feststoff-Farbstoffsolarzelle wird das flüssige Redoxelektrolyt von der konventionellen Farbstoffsolarzelle durch einen festen Lochleiter ersetzt.

Die inhärent Komplexität des Systems und das Zusammenspiel der verschiedenen Komponenten bedeutet, dass in vielerlei Hinsicht die Betriebsmechanismen dieses Systems immer noch schlecht und/oder nicht vollständig verstanden sind. In dieser Arbeit untersuche ich die Betriebsprozesse von nanostrukturierten Solarzellen die den organischen *p*-Halbleiter 2,2',7,7'-tetrakis(*N,N*-di-*para*-methoxyphenylamine)-9,9'-spirobifluorene (spiro-MeOTAD) verwenden um ein vertieftes Verständnis zu erreichen, dass umgesetzt zu der Entwicklung von Hochleistungs-Feststoff-Solarzellen führt.

Impedanzspektroskopie (IS) wird benutzt um die internen elektrischen Prozesse von Feststoff-Farbstoff-artigen-Solarzellen ausgiebig zu untersuchen. Verschiedene Vorrichtungskonfigurationen werden verwendet um die einzelnen internen Oberflächen, Ladungstransfer und Transportprozesse zu identifizieren und differenzieren. Der Ladungstransport innerhalb des festen Lochleiter wird freigelegt und der Beitrag auf den Nettoserienwiderstand des Systems festgestellt. Die Verwendung der Arrhenius-Gleichung bestimmt die Aktivierungsenergie für den Lochtransport im undotierten spiro-MeOTAD. Die Photovoltaik-Leistung von Feststoff-Solarzellen wird durch Photodotierung – die Einwirkung von Licht und Sauerstoff – und chemische *p*-Dotierung verbessert in dem die Leitfähigkeit des Lochleiters erhöht wird. IS Messungen offenbaren feine Unterschiede in der Wirkung der zwei Dotierungsmethoden. Zusätzlich ist erwiesen, dass in Gegenwart von Sauerstoff und Licht der Kontakt zwischen Lochleiter und Gegenelektrode besser ist.

Weiterhin wird die Anwendung von unterschiedlichen Farbstoffmolekülen in Feststoff-Farbstoffsolarzellen und die Wirkung ihrer physikalischen und chemischen Eigenschaften auf die photovoltaische Leistung untersucht. Dieser Teil der Arbeit befasst sich mit der Erforschung des Interface zwischen Lochleiter und farbstoffbedeckten nanostrukturierten Metalloxide

---

Halbleiter. Der Einfluss der Oberflächenabdeckung des Farbstoffes und seinem Dipolmoment auf die Lage des  $\text{TiO}_2$  Leitungsband und damit auf die Leerlaufspannung wird erprobt. Des Weiteren wird die Beziehung zwischen der Farbstoffmolekülstruktur und der effizienten Ladungstrennung demonstriert. Schliesslich werden die vorteilhafte de-Aggregationsfähigkeit von spiro-MeOTAD durch optische Messungen dargestellt.

Hybrid organische-anorganische Blei-Iodid-basierende Perowskit  $\text{CH}_3\text{NH}_3\text{PbI}_3$  wird als Lichtsammelmaterial in mesoskopischen Feststoff-Solarzellen eingeführt und anhand IS untersucht. Wir entwickeln ein Modell für diese Perowskit-Typ-Zellen durch die Nutzung von vorhandenen Ersatzschaltbildern für Flüssig- und Feststoff-Farbstoffsolarzellen als Grundlage. Getrennte Merkmale werden identifiziert für die entsprechenden elektronischen und ionischen Leitfähigkeiten des Perowskit-Materials. Diese Eigenschaften sind stark abhängig von der Natur, Kristallinität und Morphologie des Perowskit-Materials.

Die leichte Verarbeitbarkeit dieser Materialien in Lösungen umgreift eine ihrer wichtigsten Vorteile. Der Formationprozess des Perowskit-Materials aus einer Mischung, in dessen Vorstufenkomponente in einem gemeinsamen Lösungsmittel aufgelöst sind, wird untersucht. Unsere Experimente zeigen, dass die Struktur und Form des gebildeten Perowskit-Films durch die Wahl des Lösungsmittels gesteuert werden kann. Die Zusammensetzung der Vorstufenlösung bestimmt die Natur des gebildeten Perowskits. Der Konvertierungsschritt wird durch das Erhitzen der abgeschiedenen Lösungsmischung erreicht und beeinflusst die Filmmorphologie stark. Bei Temperaturen von über  $120^\circ\text{C}$  gibt es zusätzlich eine Bildung von  $\text{PbI}_2$ . Dies wirkt wie ein Graben für Ladungen, wodurch die Injektion in und aus dem  $\text{TiO}_2$  begrenzt wird. Dies führt zu einer Abweichung von dem typischen Verhalten der chemischen Kapazität.

Schliesslich werden die thermischen Eigenschaften und das Verhalten von dem  $\text{CH}_3\text{NH}_3\text{PbI}_3$  Perowskit und seinen einzelnen Komponenten überprüft. Die Systeme, die aus gemischtem Halogenid bestehen, führen zur Bildung von überschüssigem organischem Material, das unter Erhitzung sublimiert. Infolgedessen werden die Enthalpie und Temperatur der Sublimation des organischen  $\text{CH}_3\text{NH}_3\text{X}$  ( $\text{X}=\text{Cl}$  oder  $\text{I}$ ) Bestandteiles bestimmt. Die Zersetzung des Perowskits folgt dem anfänglichen Verlust der organischen Komponenten – aufeinanderfolgender Verlust der Säure- und Aminekomponenten – und anschliessend dem Abbauverlust der anorganischen Spezies. Die Bildung des Perowskits  $\text{CH}_3\text{NH}_3\text{PbI}_3$  von verschiedenen Vorstufenlösungen führt zu feinen Unterschieden in der Kristallstruktur.

Die Studien dieser Arbeit stellen eine umfassende Untersuchung der wichtigsten Parameter der Betriebsprozesse von Feststoff-mesoskopischen Solarzellen dar. Das Wissen und der Einblick in die Betriebsabläufe und internen Oberflächen bieten einen wertvollen Beitrag zur Verbesserung und Entwicklung von Hochleistungssolarzellen.

**Schlüsselwörter:** Photovoltaik, Feststoff-Farbstoffsolarzelle, Lochleiter, spiro-MeOTAD, Hybrid Perowskit Solarzelle, organische-anorganische Blei-Iodid Perowskit, organische Farbstoff, Impedanzspektroskopie, thermische Eigenschaften.

# Contents

<b>Abstract (English/Français/Deutsch)</b>	<b>v</b>
<b>1 Introduction</b>	<b>1</b>
1.1 Sunlight . . . . .	1
1.2 Solar Energy . . . . .	3
1.2.1 Photovoltaic Effect . . . . .	4
1.3 Dye-Sensitized Solar Cell . . . . .	5
1.3.1 Electron-Transfer Processes . . . . .	8
1.3.2 Dye-Sensitized Solar Cell Components . . . . .	10
1.3.2.1 Nanostructured Metal Oxide Film . . . . .	10
1.3.2.2 Hole-Transport Material: Spiro-MeOTAD . . . . .	11
1.3.2.3 Sensitizer . . . . .	13
1.3.2.4 Back Contact . . . . .	15
1.4 Solar Cell Photovoltaic Characterization . . . . .	15
1.4.1 Current-Voltage Characteristics . . . . .	15
1.4.2 Quantum Efficiency Measurements . . . . .	18
1.4.3 Impedance Spectroscopy . . . . .	19
1.4.3.1 Ohm's Law: Resistance and Impedance . . . . .	19
1.4.3.2 Equivalent Circuits . . . . .	21
1.4.3.3 IS Model of Solar Cells . . . . .	24
1.4.3.4 Dye-Sensitized Solar Cells . . . . .	25
1.5 Motivations . . . . .	30
<b>2 Transport Properties of Spiro-MeOTAD in Solid-State DSSCs</b>	<b>33</b>
2.1 Introduction . . . . .	33
2.2 Establishing IS Equivalent Circuits . . . . .	35
2.3 Interpretation of IS Spectra: Temperature Effects . . . . .	38
2.3.1 High Frequency IS Response . . . . .	38
2.3.2 Contribution to Series Resistance by HTM . . . . .	38
2.3.3 Activation Energy for Hole-Transport in Spiro-MeOTAD . . . . .	40
2.3.4 Low Frequency IS Response . . . . .	42
2.4 Photo- <i>versus</i> Chemical Doping of HTM . . . . .	47
2.4.1 Back Contact and Spiro-MeOTAD . . . . .	47

## Contents

---

2.4.2	Distribution of Oxidized Spiro-MeOTAD . . . . .	49
2.4.3	Low Frequency IS Response . . . . .	51
2.4.4	Photovoltaic Performance . . . . .	51
2.5	Conclusions . . . . .	53
2.5.1	Temperature Dependence of Transport Properties . . . . .	53
2.5.2	Photo- <i>versus</i> Chemical Doping . . . . .	54
2.5.3	Perspectives . . . . .	55
<b>3</b>	<b>Molecular Sensitization for Solid-State Solar Cells</b>	<b>57</b>
3.1	Introduction . . . . .	57
3.2	Squaraine Sensitizers: Near-Infrared Light Absorption . . . . .	58
3.2.1	Optical Characterization of Squaraine Sensitizers . . . . .	59
3.2.1.1	Dye Aggregation . . . . .	59
3.2.2	Photovoltaic Performance . . . . .	61
3.2.2.1	Co-sensitization . . . . .	62
3.2.3	Transient and Impedance Characterization . . . . .	63
3.3	D- $\pi$ -A Sensitizers: Effect of the Donor Group . . . . .	65
3.3.1	Optical Characterization of D- $\pi$ -A Dyes . . . . .	67
3.3.2	Photovoltaic Performance . . . . .	68
3.3.3	Transient and Impedance Characterization: TiO <sub>2</sub> Conduction Band Shift	69
3.3.4	Computational Calculations . . . . .	70
3.3.4.1	Dipole Moment Phenomenon . . . . .	71
3.3.4.2	Calculated Interaction Geometries . . . . .	73
3.4	Ullazine Sensitizers: Role of Molecular Structure . . . . .	74
3.4.1	Optical Characterization of Ullazine Sensitizers . . . . .	74
3.4.2	Photovoltaic Performance . . . . .	79
3.4.3	Ullazine Dye Adsorption Mode . . . . .	81
3.4.4	Photoinduced Absorption Spectroscopy . . . . .	81
3.4.5	Time-Correlated Single Photon Counting: Injection Dynamics . . . . .	85
3.4.6	Transient and Impedance Characterization: Charge-Transfer Mechanisms	86
3.5	Conclusions . . . . .	88
3.5.1	Squaraine Sensitizers . . . . .	89
3.5.2	D- $\pi$ -A Sensitizers . . . . .	89
3.5.3	Ullazine Sensitizers . . . . .	90
3.5.4	Perspectives . . . . .	90
<b>4</b>	<b>Impedance Spectroscopic Analysis of Perovskite Solid-State Solar Cells</b>	<b>93</b>
4.1	Introduction . . . . .	93
4.1.1	Organic-Inorganic Hybrid Perovskite . . . . .	93
4.2	Considerations of the Systems and Impedance Spectroscopy . . . . .	97
4.3	Validation of Impedance Model . . . . .	108
4.3.1	Effect of Spiro-MeOTAD Overlayer Thickness . . . . .	108
4.3.2	Influence and Role of LiTFSI as Additive . . . . .	116

4.3.3 Influence and Role of 4- <i>tert</i> -butylpyridine as Additive . . . . .	121
4.4 Standard Devices Under Illumination . . . . .	125
4.5 Additional Discussion . . . . .	130
4.6 Conclusions . . . . .	131
4.6.1 Perspectives . . . . .	131
<b>5 Morphological Studies of CH<sub>3</sub>NH<sub>3</sub>PbI<sub>3</sub> Perovskite</b>	<b>133</b>
5.1 Introduction . . . . .	133
5.2 Perovskite Formation: Morphology, Structure and Composition . . . . .	133
5.3 Solvent Effects . . . . .	134
5.3.1 Perovskite Infiltration and Transport Mechanisms . . . . .	138
5.3.2 Solvent properties . . . . .	143
5.4 Perovskite Annealing Temperature . . . . .	144
5.4.1 Optical Characterization . . . . .	146
5.4.2 Scanning Electron Microscopy: Film Morphology . . . . .	147
5.4.3 X-ray Diffraction: Perovskite Conversion and Composition . . . . .	149
5.4.4 Photovoltaic Performance . . . . .	152
5.4.5 Impedance Spectroscopy: Deviation from Chemical Capacitive Behavior	153
5.5 PbI <sub>2</sub> Compositional Effects . . . . .	156
5.5.1 Scanning Electron Microscopy: Film Morphology . . . . .	158
5.5.2 X-ray Diffraction: Perovskite Composition . . . . .	158
5.5.3 Optical and Photovoltaic Characterization . . . . .	158
5.5.4 Impedance Spectroscopy: Confirmation of Chemical Capacitive Behavior	162
5.6 PbI <sub>2</sub> Content . . . . .	164
5.7 Conclusions . . . . .	165
5.7.1 Solvent Effects . . . . .	165
5.7.2 Perovskite Annealing Temperature . . . . .	165
5.7.3 PbI <sub>2</sub> Compositional Effects . . . . .	166
5.7.4 Perspectives . . . . .	167
<b>6 Thermal Analysis of Methyl Ammonium Lead-Trihalide Perovskite</b>	<b>169</b>
6.1 Introduction . . . . .	169
6.2 Thermogravimetric Analysis . . . . .	169
6.2.1 Precursor Materials . . . . .	170
6.2.2 Perovskite Mixtures . . . . .	175
6.2.3 Perovskite Powder . . . . .	180
6.3 Differential Scanning Calorimetry . . . . .	182
6.4 Conclusions . . . . .	184
6.4.1 Perspectives . . . . .	185
<b>7 General Conclusions and Summary</b>	<b>187</b>

## Contents

---

<b>8 Experimental Methods</b>	<b>193</b>
8.1 Materials and Synthesis . . . . .	193
8.2 Characterization Methods . . . . .	193
8.2.1 Optical Spectroscopy . . . . .	193
8.2.2 X-ray Diffraction . . . . .	194
8.2.3 Fourier Transformed Infrared Spectroscopy . . . . .	194
8.2.4 Photoinduced Absorbance . . . . .	195
8.2.5 Thermal Analysis . . . . .	195
8.3 Crystal Structure . . . . .	195
8.4 Solar Cell Fabrication . . . . .	195
8.4.1 Solid-State Dye-Sensitized Solar Cells . . . . .	195
8.4.2 Perovskite Based Solid-State Mesoscopic Solar Cells . . . . .	196
8.5 Solar Cell Characterization . . . . .	197
8.5.1 Photovoltaic Characterization . . . . .	197
8.5.2 Impedance Spectroscopy . . . . .	197
8.5.3 Transient Photocurrent and Photovoltage Measurements . . . . .	198
<b>A Appendix</b>	<b>199</b>
A.1 Molecular Structures . . . . .	199
A.2 Impedance Fitting Procedure for Perovskite Solar Cells . . . . .	200
<b>Nomenclature</b>	<b>201</b>
<b>Bibliography</b>	<b>216</b>
<b>Acknowledgements</b>	<b>217</b>
<b>Curriculum Vitae / List of publications</b>	<b>219</b>

# 1 Introduction

## 1.1 Sunlight

Sunlight is the electromagnetic radiation – denoted solar irradiance – given off by the sun and takes approximately 8.3 minutes to reach the earth. It spans most of the electromagnetic spectrum, from high energy x-rays at 100 nm wavelengths to radio waves at 1 mm. Approximately 50% of solar radiation is composed of infrared light while 40% and 10% are made up of visible and ultraviolet light respectively. Sunlight is the earth's primary source of energy, determining its warm and habitable climate, supporting and sustaining life on earth.

### *Solar Constants*

The *solar constant* is a measure of the flux density, corresponding to the solar irradiance when the distance between the sun and the earth is 1 AU<sup>1</sup>. It takes into account solar radiation over the entire spectrum, culminating in an integrated total of approximately 1361 W m<sup>-2</sup> which is susceptible to small annual variations resulting from solar activity and changes in the earth/sun distance. Solar simulators typically describe the solar irradiance in terms of 'suns' or % sunlight intensity where 1 sun or 100% sunlight intensity is defined as one solar constant.

### *Solar Spectrum*

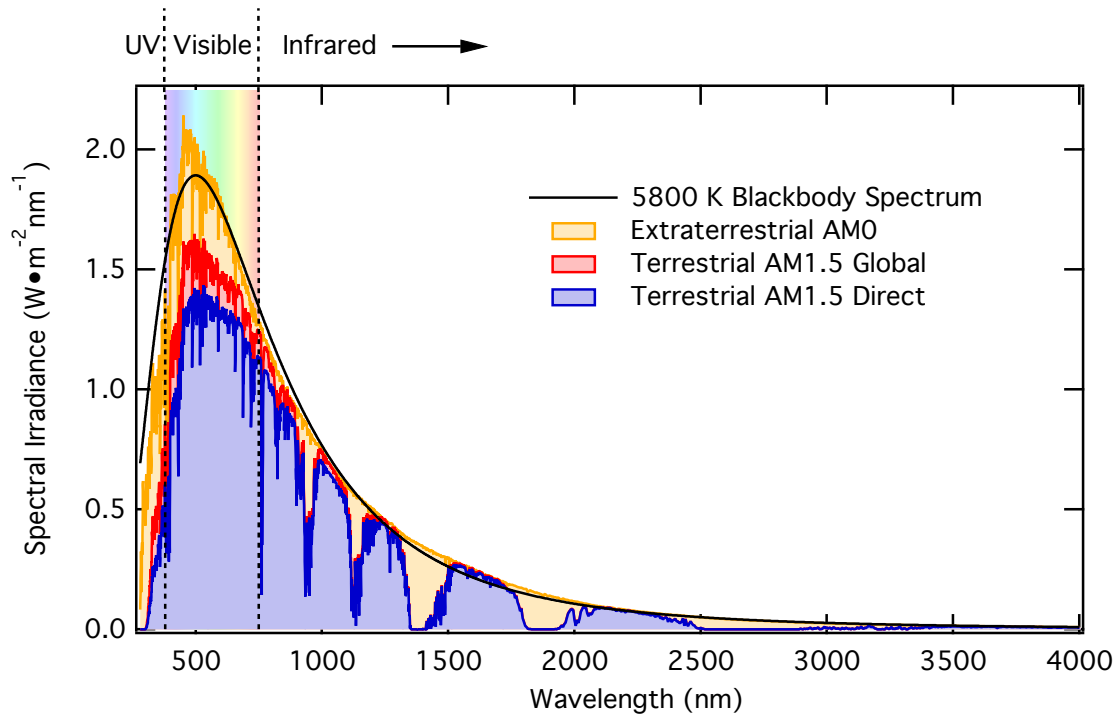
The surface temperature of the sun – the star at the centre of our solar system – is approximately 5800 K. Hence the resultant radiation spectrum is similar to a black body at the same temperature. The spectral radiance  $B$  of a black body in thermal equilibrium at an absolute temperature  $T$  as a function of wavelength  $\lambda$  is given by Planck's law, Equation 1.1:

$$B_{\lambda}(T) = \frac{2hc^2}{\lambda^5} \frac{1}{\exp\left(\frac{hc}{\lambda k_B T}\right) - 1} \quad (1.1)$$

where  $k_B$  is Boltzmann constant,  $h$  is Planck's constant and  $c$  is the speed of light. Integrating

---

<sup>1</sup> One astronomical unit – equivalent to a mean distance of 149 597 870 km.



**Figure 1.1.** Spectral distribution of the solar irradiance above the earth’s atmosphere (extraterrestrial spectrum – AM0) and on the earth’s surface (terrestrial – AM1.5) showing the difference between the direct and global irradiance. Additionally the blackbody radiation spectrum at 5800 K is displayed (black trace).

Planck’s law over all wavelengths gives the Stefan-Boltzmann law, Equation 1.2. This is a measure of the total power  $P$  radiated per unit of time per unit of surface area  $A$  by a black body at a temperature  $T$ :

$$P/A = \sigma T^4 \tag{1.2}$$

where  $\sigma$  is the Stefan-Boltzmann constant ( $\sigma \approx 5.67 \times 10^{-8} \text{ W m}^{-2} \text{ K}^{-4}$ ).

The solar spectrum has additional fine structure (Fraunhofer lines) due to the absorption by the peripheral solar gas which results in the deviation from the black body radiation spectrum shown by the extraterrestrial solar spectrum in Figure 1.1. The solar irradiance is standardized according to the American Society for Testing and Materials (ASTM) in terms of the *air mass coefficient* which defines the optical path length through the earth’s atmosphere, expressed as a ratio relative to the path length at the zenith (vertically upwards). Hence the extraterrestrial solar spectrum is denoted as Air Mass Zero (AM0) (meaning that the light has passed through ‘zero atmospheres’) and its integrated solar irradiance is equivalent to the solar constant.

The earth’s atmosphere acts as a filter for solar radiation, preventing the harmful wavelengths from reaching the surface of the earth. This attenuation of the solar irradiance results from the scattering and absorption processes of radiation by gases and chemicals in the atmosphere.



Rayleigh scattering of sunlight leads to the removal of high frequency radiation from direct sunlight. Consequently the high frequency radiation arrives to the observer *via* indirect scattered paths, resulting in the blue appearance of the sky while the direct sunlight gives the sun a yellow appearance. Atmospheric scattering also gives rise to the red appearance of the sun and sky at sunrise and sunset.

Ozone present in the upper atmosphere filters out ultraviolet radiation, seen in the reduction in the short-wavelength region of the solar spectrum at the earth's surface, the terrestrial solar spectrum. Water vapour, nitrogen, carbon dioxide and oxygen all contribute to the formation of absorption bands at various wavelengths, further confining the terrestrial solar spectrum between the near ultraviolet and far infrared region. The presence of pollutants such as aerosols, photochemical smog are also contributing factors, leading to significant amplification of atmospheric attenuation particularly in the lower layers of the atmosphere. The solar spectrum at sea level with the sunlight directly overhead (zenith=0°) after passing through the atmosphere is denoted as AM1 and corresponds to the solar irradiance in equatorial and tropical regions.

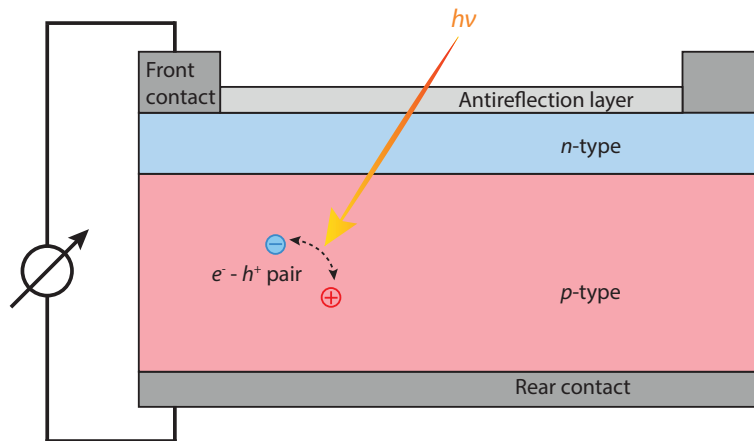
Generally the standard solar spectrum reaching the earth's surface is defined as AM1.5, consistent with an atmosphere thickness of 1.5 which coincides to a solar zenith angle of 48.2° as described by the ASTM G-173-03 standard. The corresponding integrated spectral irradiance calculated using Equation 1.2 is  $1000.4 \text{ W m}^{-2}$  for AM1.5 and gives a measure of its solar intensity. This is the global (G) spectral radiation taking into account the hemispherical irradiance consisting of direct and diffuse light reflected from the ground ('albedo effect') on the south (sun) facing surface tilted at 37° from the horizontal (towards the equator). This differs from the direct (D) normal irradiance which consists of only direct parallel radiation and excludes the diffuse contributions resulting in the observed decrease in the solar spectrum as seen in Figure 1.1.

The AM1.5G spectrum represents the solar irradiance for specific atmospheric conditions which is most commonly used as the standard solar spectrum to which solar simulators are matched.

## 1.2 Solar Energy

As previously mentioned, sunlight is crucial in establishing conditions in which life is possible. The earth's atmosphere, land and water surfaces absorb solar energy, increasing their temperature driving many of earth's key natural processes. As a direct result of solar energy hot air rises, creating atmospheric circulation and convection resulting in the earth's weather conditions. The evaporation of water, formation of clouds and subsequent cooling constitutes the earth's water cycle. Finally solar energy is converted to chemical energy by the process of photosynthesis by plants.

Solar energy is by far the most abundant energy resource available and it can be harnessed and



**Figure 1.2.** Basic configuration for a conventional  $p$ - $n$  junction type silicon solar cell.

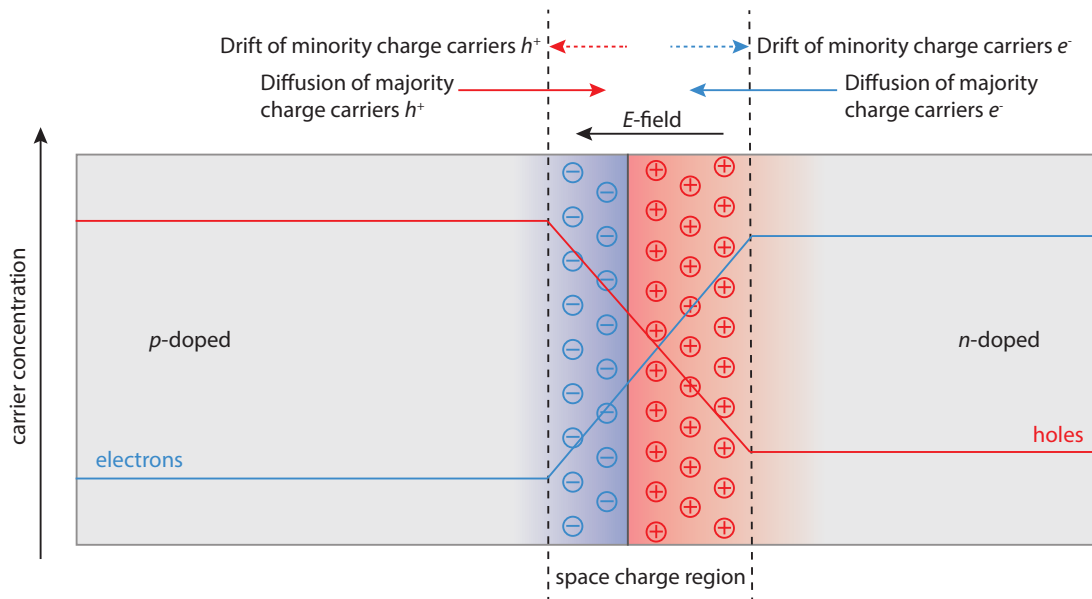
used by a wide range of ever-evolving technologies. All renewable energies (with the exception of geothermal and tidal) derive their energy from the sun. Even the energy extracted from the non-renewable resources of coal, oil and natural gas originally stemmed from light energy converted into chemical energy and stored as biomass.

### 1.2.1 Photovoltaic Effect

One of the most prominent and direct uses of solar energy is the direct conversion into electrical energy. This is achieved using a solar cell and the photovoltaic effect. A solar cell is a photoelectric cell that, under illumination, can generate and support an electric current without connection to an external voltage source. The photovoltaic effect was first observed by A. E. Becquerel in 1839, through the immersion of silver chloride in an acidic solution, which connected to platinum electrodes generated a photocurrent and photovoltage under illumination. Nowadays the most common materials used in photovoltaics are semiconductors (such as silicon) employing a  $p$ - $n$  junction configuration as depicted in Figure 1.2.

Conventional solar cells are composed of silicon in a  $p$ - $n$  junction configuration, by which  $p$ -type and  $n$ -type doped silicon are joined together. When no external bias is applied, the materials are in thermal equilibrium, where the electrons  $e^-$  from the  $n$  region near the junction diffuse into the  $p$  region and *vice versa* for holes  $h^+$  in the  $p$ -type region. The diffusion currents are balanced such that there is no net current through the junction. As a consequence of the majority charge carrier diffusion a *space charge region* is formed at the interface creating an electric field, see Figure 1.3. The potential difference formed across the junction by the equilibration of the Fermi levels between the  $p$ -type and  $n$ -type doped material is denoted the *built-in potential*.

In the standard photovoltaic effect, when such a solar cell is exposed to illumination, this results in the absorption of photons by the electrons in the valence band (VB) of the material



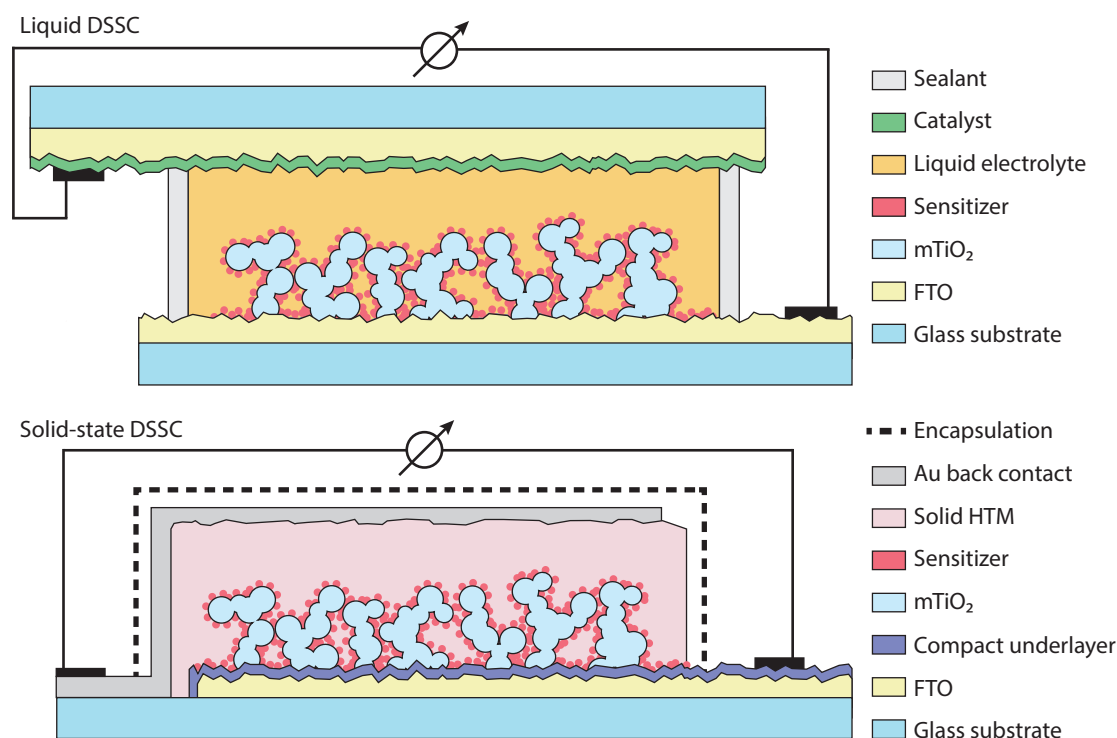
**Figure 1.3.** A  $p$ - $n$  junction in thermal equilibrium displaying the resultant electric field. The drift currents as a result of the electrostatic force on the charges and the diffusion currents are shown.

within the space charge region and their subsequent promotion to the conduction band (CB). These high-energy charge carriers are then charge separated by the built-in potential accelerating the drift of photogenerated minority charges – excited electrons and associated holes – in different directions leading to the conversion of light into electrical energy.

Since the first discovery of the photovoltaic effect there has been considerable advancement in the development and manufacture of solar cells, with solar cell efficiencies varying from 6% for amorphous silicon-based solar cells to 44% for multiple-junction concentrated devices [1]. A wide range of different materials and device configurations are presently used for photovoltaics. In recent years there has been significant progress in the use of abundant low-cost organic materials in photovoltaic technologies. Included in this category is the dye-sensitized solar cell, which imitates the natural process of photosynthesis by which plants convert solar energy into chemical energy.

### 1.3 Dye-Sensitized Solar Cell

The conventional dye-sensitized solar cell (DSSC), first reported in 1991 by O'Regan and Grätzel [2], takes its inspiration from the natural process of photosynthesis. The typical device configuration is presented in Figure 1.4. In this type of device the role of chlorophyll as a light harvesting material in plants is emulated by a molecular chromophore which is chemically anchored to a wide bandgap metal oxide semiconductor by the process described as sensitization. In addition to acting as a scaffold for the chromophore (or sensitizer), the metal oxide semiconductor adopts the role of electron transport material. Unlike any other



**Figure 1.4.** Schematic representation of the device configuration for a liquid and solid-state DSSC. The liquid DSSC adopts a sandwich configuration while the solid-state counterpart used in the course of this thesis has a monolithic architecture. Figure not to scale.

photovoltaic technology where one material has the dual role of light absorption and charge-transport, separate materials adopt the individual processes of light harvesting and charge-transport in DSSCs leading to the phenomenon of charge separation. The light harvesting element (the sensitizer) is excited upon light absorption and injects an electron into the conduction band (CB) of the metal oxide semiconductor resulting in the one electron oxidation of the sensitizer. The photogenerated electron is then transported through the mesostructured semiconductor to the transparent conductive oxide (TCO)<sup>2</sup> coated glass substrate which constitutes the current-collecting photoanode.

Following the photoinduced electron injection leading to charge separation, the oxidized sensitizer is regenerated by electron donation from a redox couple in the electrolyte which infiltrates the mesoporous structure of the metal oxide semiconductor. The concentration driven diffusion of the oxidized redox couple species away from the sensitized interface to the counter-electrode of the device where it is regenerated, completes the circuit of photovoltaic device.

In the solid-state counter part of the DSSC, the liquid electrolyte of the conventional liquid-based DSSC is replaced by a solid-state hole-transport material (HTM) and as a result of there

<sup>2</sup> The TCO used here is fluorine doped SnO<sub>2</sub> (FTO) deposited on glass – TEC15 (Pilkington, UK).

are some structural differences in the device design. The basic principles of device operation remain identical, where the oxidized dye is regenerated by hole injection into the solid HTM, which transports the holes to the back contact completing the external circuit. Unlike a liquid DSSC which has a sandwich configuration between two separate TCO substrates as electrodes, ssDSSCs are based on a monolithic design built on a single TCO substrate (etched to give the correct electrode configuration) with the back contact deposited by thermal evaporation of silver or gold directly on the solid HTM layer.

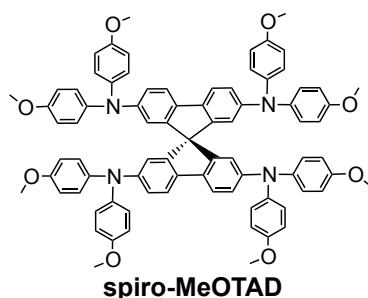
An additional advantage of separating the processes of light absorption and charge separation from charge-transport has allowed the individual components making up the DSSC to be optimized and improved. This has led to significant improvement in the solar-to-electrical power conversion efficiencies (*PCE*) of devices over the years as a direct result from the implementation of new and tailored materials. For the conventional DSSC configuration, the highest *PCE* of 12.3% was reported using a porphyrin dye in combination with a D- $\pi$ -A dye and a cobalt(II/III) complex redox couple [3].

In an effort to improve stability and the processability of DSSCs with the aim to allow efficient roll-to-roll manufacture, extensive research is being invested in the study of solid and quasi-solid alternatives for the liquid electrolyte. Efforts have focused on organic [4–8], inorganic [9–11] semiconductors and conducting polymers [12, 13] in order to meet all the requirements for a good hole-transport material. In the field of organic semiconductors, the *p*-type semiconductor 2,2',7,7'-tetrakis(*N,N*-di-*para*-methoxyphenylamine)-9,9'-spirobifluorene (spiro-MeOTAD) was first introduced by Bach *et al.* [14] in 1998 (Figure 1.5) as a HTM for solid-state DSSCs. This report used a ruthenium(III) complex as sensitizer and the spiro-MeOTAD was chemically *p*-doped with N(PhBr)<sub>3</sub>SbCl<sub>6</sub> to increase its charge carrier density culminating in a *PCE* of 0.74%.

Since then these initial low *PCEs* have been steadily improved from < 1% to > 7% [15] mainly through the use of new high molar extinction sensitizers [16, 17] and the introduction of organic molecular sensitizers [18–21]. However for such devices spiro-MeOTAD remains the material of choice as HTM to achieve high *PCEs*.

In recent years the introduction of organic-inorganic perovskite materials has led to a revolution in DSSCs. Chung *et al.* [10] employed the *p*-type CsSnI<sub>3</sub> perovskite as HTM in combination with a ruthenium(II) complex as sensitizer achieving up to 8.5%. The excellent optical properties of the lead-iodide based hybrid perovskite CH<sub>3</sub>NH<sub>3</sub>PbI<sub>3</sub> classified it as a promising candidate for light harvesting. However initial results implementing this material in combination with a liquid electrolyte displayed low *PCEs* due to problems associated with the corrosion and degradation of the perovskite material by the liquid electrolyte.

In contrast the use of solid-state HTM overcame these issues, improving the stability of the devices and has led to record breaking efficiencies of up to 16%.



**Figure 1.5.** Molecular structure of the *p*-type semiconductor 2,2',7,7'-tetrakis(*N,N*-di-*para*-methoxy-phenylamine)-9,9'-spirobifluorene (spiro-MeOTAD) used as HTM in ssDSSCs.

### 1.3.1 Electron-Transfer Processes

Unlike silicon solar cells where charge separation is driven by the built in electric field, in nanostructured bulk heterojunction such as DSSCs, this process is based on the kinetic competition between energy, electron transfer and charge-transport processes. As such the key for good photovoltaic performance lies in the relative timescales between the beneficial and unwanted electronic processes. The relevant photophysical and electron transfer processes involved in the operation of a DSSC are depicted schematically in Figure 1.6. The corresponding time-scales for the individual processes is also included.

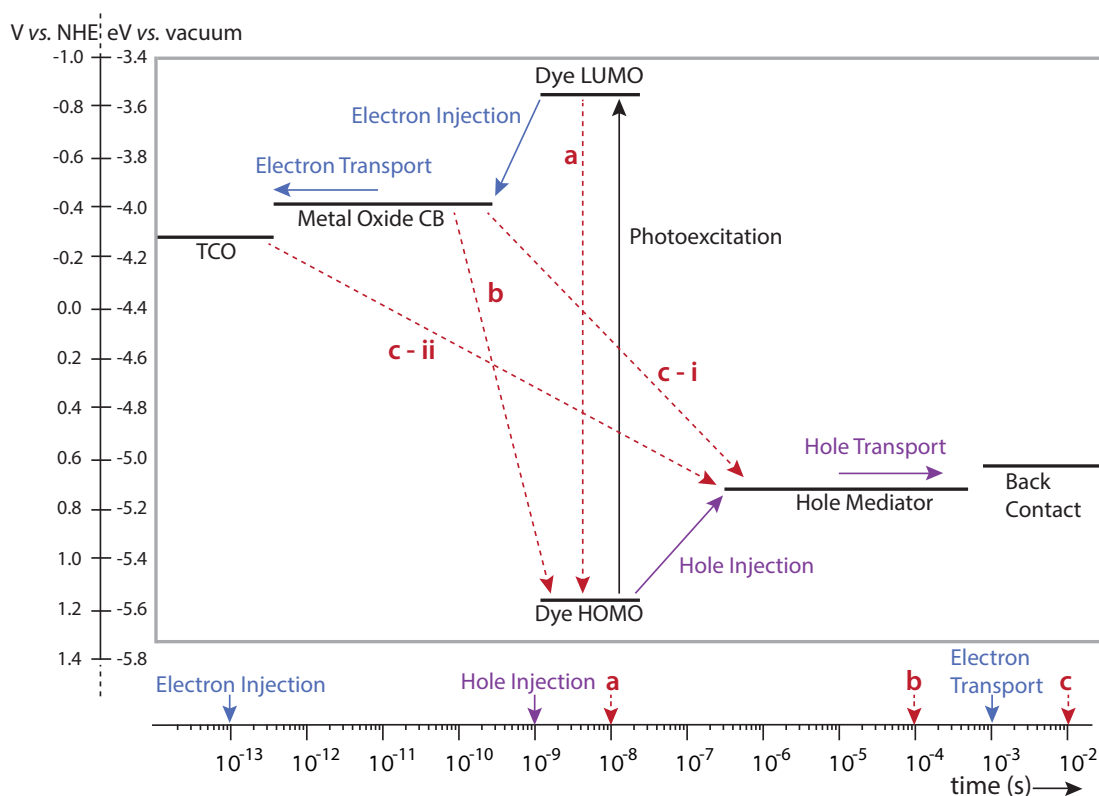
**Photoexcitation** – The light absorption by the adsorbed sensitizer molecule leads to the excitation of an electron from its highest occupied molecular orbital (HOMO) to its lowest unoccupied molecular orbital (LUMO). As such this photoexcitation (Equation 1.3) from the ground ( $S$ ) to the excited state ( $S^*$ ) of the sensitizer requires the incident photon to have an energy greater than or equal to the HOMO-LUMO gap. This process results in charge separation.



**Electron Injection** – The process of electron transfer from the photoexcited state of the sensitizer to the CB of the metal oxide semiconductor occurs on the femtosecond timescale. Consequently the excited state of the sensitizer is quenched, generating its oxidized species ( $S^+$ ) according to Equation 1.4. This process is quantified by the *charge injection efficiency*,  $\eta_{inj}$  which is a measure of the fraction of electrons that are injected into the  $\text{TiO}_2$  CB ( $e_{CB}^-$ ) after photoexcitation.



**Dye Regeneration** – Following charge separation and electron injection the oxidized sensitizer is reduced by the electron transfer from the hole-transport mediator, thus regenerating the sensitizer. In the case of ssDSSCs this process is referred to as *hole injection* as a hole is transferred to the HTM from the oxidized sensitizer.



**Figure 1.6.** Energy level schematic illustrating the electronic processes that occur in a DSSC. The desired electron transfer processes are indicated by the blue arrows, the hole transfer processes by purple and the unwanted recombination loss channels by dashed red. The approximate energy levels are given with respect to vacuum (in eV) and NHE – normal hydrogen electrode (in V). The dynamics of the electron transfer processes are presented below the schematic.

**Charge-transport** – The injected electron in the CB of the metal oxide,  $e_{CB}^-$ , is transported through the metal oxide to the current-collecting photoanode. Meanwhile in a liquid DSSC the oxidized redox active species formed following dye regeneration diffuses to the counter-electrode where it is reduced. In ssDSSCs the hole injected is transported through the HTM and collected at the back contact.

In the DSSC device operation possible electron transfer processes exist that lead to the loss of photogenerated charges. The photon-to-current conversion efficiency of the solar cell is governed by the kinetic competition between the initial photoinduced charge separation processes and the loss mechanisms. The following loss channels are illustrated by the red arrows in Figure 1.6:

**a. Excited State Deactivation** – A possible loss mechanism is the radiative or non-radiative relaxation of the photoexcited sensitizer back to its initial ground state instead of the electron injection into the CB of the metal oxide. However this process is typically considerably slower than the electron injection, ensuring quantitative charge separation.

**b. Back Electron Transfer** – This loss channel involves the recombination of electrons in the metal oxide CB with the oxidized sensitizer. This recombination pathway is in direct competition with the hole injection into the HTM.

**c. Electron-Hole Recombination** – Finally charges can recombine indirectly by the transfer of electrons from **c - i** the metal oxide CB and/or **c - ii** the TCO with holes in the HTM. In addition to process **b** these loss mechanisms typically occurs on a similar timescale as the electron transport in the metal oxide semiconductor and thus to achieve high *PCEs* this recombination process needs to be slower than the charge-transport. This is expressed by the *charge collection efficiency*,  $\eta_{coll}$  which is a measure of the fraction of charges that are collected at the photoanode relative to the total number of photogenerated charges and is determined from the relative rates of charge-transport  $k_{trans}$  and global recombination  $k_{rec}$ , Equation 1.5.

$$\eta_{coll} = 1 - \frac{k_{rec}}{k_{trans}} \quad (1.5)$$

The relative rates of the electronic processes occurring are strongly influenced by the choice of materials employed. Molecular engineering of the sensitizer and surface treatments of the metal oxide surface in particular are commonly used to modify the kinetics of the charge-transfer reactions.

### 1.3.2 Dye-Sensitized Solar Cell Components

The following section introduces and discusses the main general components of the DSSC. Particular emphasis is placed on the materials and property requirements necessary for application in the solid-state configuration of the DSSC which is the focus of the work conducted in this thesis.

#### 1.3.2.1 Nanostructured Metal Oxide Film

The nanostructured metal oxide layer in a DSSC conventionally consists of a mesoporous  $\text{TiO}_2$  structure. Ideally the metal oxide semiconductor should be covered by a monolayer of sensitizer molecules. The nature of the material must be such that it can transport electrons from its sensitized surface to the conductive substrate, while its nanostructure provides a large surface area to maximize the number of dye molecules present in the device, thus increasing the light harvested per unit of active area. Furthermore the metal oxide needs to be transparent in the visible region to prevent its competitive light absorption.

$\text{TiO}_2$ , with its wide bandgap of approximately 3.2 eV, is typically the material of choice to achieve high *PCEs* in solid-state and liquid DSSCs<sup>3</sup>. This semiconductor is intrinsically *n*-

---

<sup>3</sup> Other wide bandgap materials such as ZnO [22, 23] and  $\text{SnO}_2$  [24, 25] have been investigated.



doped by the presence of oxygen vacancies in its structure.

In order to harvest sufficient light to generate high photocurrents the metal oxide film is nanostructured to be highly porous, increasing the specific surface area of the mesoporous film. The average pore and particle size of the film need to allow for the facile infiltration of the solid HTM in the case of ssDSSCs and the efficient diffusion of the redox species in and out of the pores in the liquid electrolyte of liquid DSSCs. The short diffusion length of spiro-MeOTAD and the problems associated with its incomplete pore-filling limits the mesoporous TiO<sub>2</sub> (mTiO<sub>2</sub>) thickness to 2 – 3 μm in ssDSSCs. While the highest reported efficiencies have been achieved with mesoporous films, several different geometric configurations (i.e. nanowires and nanotubes [26, 27]) have been examined to improve the diffusion of charges within the nanostructured layer.

The electronic and optical modification of the metal oxide surface has been extensively examined through the implementation of surface treatments and/or application of overlayers using a wide range of techniques and materials. The widely used surface treatment is the TiCl<sub>4</sub> procedure by which a thin layer of insulating titanium oxide is deposited on top of the mesoporous TiO<sub>2</sub> [28–30]. Such treatments additionally influence the adsorption of the sensitizer on the metal oxide surface [31]. Even the simple adsorption of surface water plays a significant role in this process and must be controlled.

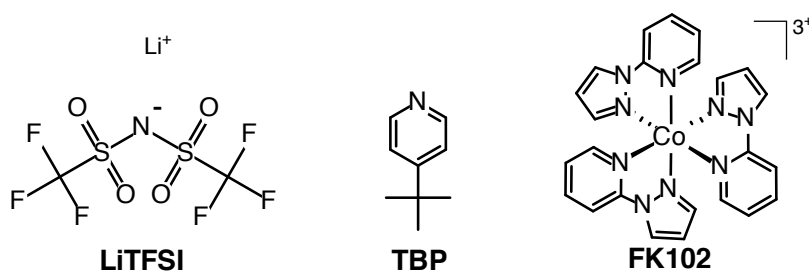
#### 1.3.2.2 Hole-Transport Material: Spiro-MeOTAD

In a liquid DSSC the hole-transport material is a liquid electrolyte containing a redox couple, such as I<sup>-</sup>/I<sub>3</sub><sup>-</sup> necessary to regenerate dye. Liquid electrolytes have traditionally been based on volatile solvents, but there has been significant research in the use of ionic-liquid based electrolytes or solid-state hole-transport materials.

In this work the amorphous organic *p*-type semiconductor 2,2',7,7'-tetrakis(*N,N*-di-*para*-methoxy-phenylamine)-9,9'-spirobifluorene (spiro-MeOTAD) is used as a solid-state HTM. Since its first report as a HTM in ssDSSCs more than 15 years ago it remains the material of choice to achieve high *PCEs* [14]. The HTM is infiltrated into the sensitized mesoporous metal oxide structure, the intimate contact with the oxidized dye molecules ensuring efficient dye regeneration, followed by the transport of the injected holes to the back contact of the solar cell.

For the solar cell to exhibit good photovoltaic performance the chosen material for application as a HTM in ssDSSC needs to fulfil the following basic property requirements:

**Energetics** – The HOMO level of the HTM must be above that of the sensitizer to ensure sufficient driving force for the hole injection from the latter into the HTM. Whilst a large driving force may increase the efficiency of hole injection this is opposed by the resulting reduction in the open-circuit potential,  $V_{OC}$ . The maximum possible  $V_{OC}$  is determined by the difference in the quasi Fermi level of the mTiO<sub>2</sub> and the redox potential of the HTM.



**Figure 1.7.** Molecular structure of the common additives – LiTFSI and TBP – used in the preparation of the HTM solution. The FK102 cobalt(III) complex employed as *p*-type dopant was used in the form of the  $\text{PF}_6^-$  salt.

The HOMO level of spiro-MeOTAD has been reported to lie at 0.72 eV *versus* NHE, which is suitable for most molecular dyes and sets the maximum theoretical  $V_{\text{OC}}$  at approximately 1.2 V (assuming the CB of  $\text{mTiO}_2$  lies at 0.5 eV).

**Transport Properties** – To allow for efficient and fast transport of holes away from the sensitized  $\text{mTiO}_2$  surface a suitable HTM requires good *p*-type conductivity and hole mobility. The charge-transport resistance of the material is inversely proportional to its conductivity and as such greatly depends on its charge carrier density which is heavily influenced by the presence of dopants, additives and/or impurities. In the case of spiro-MeOTAD, it has very low conductivity in its pristine, undoped form. It has been well established that spiro-MeOTAD needs to be partially oxidized to decrease the intrinsic charge-transport resistance of the bulk material. This has been achieved through the addition of chemical *p*-type dopants (so called chemical doping) or through the facile oxidation of the material in the presence of oxygen and light (photodoping). Furthermore common additives such as  $\text{Li}^+$  ions have been shown to also contribute to the oxidation and increased hole mobility of spiro-MeOTAD. The hole-transport within organic *p*-type semiconductors such as spiro-MeOTAD is typically described as a hole-hopping mechanism.

**Pore Infiltration** – For efficient hole injection from the dye to the the HTM, the two materials need to be in intimate contact. This necessitates good infiltration of the HTM into the pores of the  $\text{mTiO}_2$ . This in turn depends on the processability of the material. Typically spiro-MeOTAD is deposited from solution into the  $\text{mTiO}_2$  structure by spin-coating. This requires the choice of a suitable solvent to ensure good wettability of the surface, in addition to good infiltration and pore-filling of the HTM into the porous structure. Typically spiro-MeOTAD is dissolved in chlorobenzene, which is deposited onto the substrate, allowing the solution to infiltrate the pores by capillary action, any excess forming a reservoir on top of the  $\text{mTiO}_2$ . During the spin-coating procedure the solvent evaporates leading to reported pore-filling fractions between 60–70% [32–36]. The pore-filling fraction is a measure which determines the extent to which the HTM infiltrates and fills the pores of the  $\text{mTiO}_2$  structure. Relative to polymeric HTMs, spiro-MeOTAD demonstrates good pore-filling, however it remains a limitation to the *PCEs* of devices.

Several additives are typically added to the HTM solution prior to its deposition. As in the case of liquid DSSCs where they are added to the electrolyte solution, 4-*tert*-butylpyridine (TBP) and lithium bis(trifluoromethylsulfonyl)amide (LiTFSI) are commonly used in the preparation of the HTM solution, see Figure 1.7. The role of these additives on the device mechanism of both solid-state and liquid DSSC has been extensively investigated and is reportedly largely related to their adsorption to and subsequent electronic modification of the porous metal oxide surface. The presence of TBP is believed to be an upward shift of the CB of the mTiO<sub>2</sub> in addition to acting as a recombination blocking agent, thus resulting in an increase in the  $V_{OC}$  of the device [37–39]. The addition of LiTFSI has the opposite effect in that it pulls the mTiO<sub>2</sub> CB downwards, increasing the driving force for the electron injection resulting in an increase in the short-circuit current density,  $J_{SC}$ . In ssDSSCs the effect of LiTFSI on the device performance is more complex as it influences the transport properties of the bulk HTM. As previously mentioned Li<sup>+</sup> ions participate in the oxidation process of the spiro-MeOTAD in the presence of oxygen and light [40–43]. In an attempt to control the doping level of spiro-MeOTAD and in turn its bulk transport properties a chemical *p*-type dopant is sometimes also added to the HTM solution (cf. Chapter 2) an example of which is the cobalt(III) complex, tris(1-(pyridin-2-yl)-1H-pyrazol)cobalt(II) bis(hexafluorophosphate) (FK102) depicted in Figure 1.7.

#### 1.3.2.3 Sensitizer

The key component of DSSC type devices is the light absorbing species adsorbed on the metal oxide semiconductor. To ensure this sensitization of the metal oxide by the dye and to achieve high power conversion efficiencies certain properties of the sensitizer must fulfill specific requirements.

**Broad Absorption Spectrum** – The sensitizer should ideally have a broad absorption spectrum in the visible spectrum. Preferably extending into the red/infrared to ensure maximum overlap with the emission spectrum of the sun to harvest the maximum possible light.

**Energetics** – The energy levels of the sensitizer need to be appropriately positioned relative to the CB of the metal oxide semiconductor and the redox potential of the redox couple in the electrolyte (or HOMO of the HTM) to ensure efficient charge separation. The level of the excited state (LUMO) should lie above the CB of the metal oxide semiconductor to ensure electron injection from the sensitizer while hole injection into the hole-transport medium requires the redox potential of the ground state (HOMO) of the dye to lie lower than that of the HTM.

**Sensitization** – The sensitization of the metal oxide semiconductor requires the chemical adsorption of the sensitizer to establish the electronic connection necessary for efficient electron injection. As such the molecular structure of the species need to contain an anchoring group that can form a chemical bond with the semiconductor surface. Types of anchoring groups generally employed are carboxylic or phosphoric acid functionalities.

**Stability** – The sensitizer should be stable under illumination and in terms of electrochemistry (corresponding to the number of catalytic red/ox turnovers the dye can undergo under illumination<sup>4</sup>). Furthermore the attachment of the sensitizer to the semiconductor should be sufficiently strong to prevent desorption from its surface.

Generally DSSCs employed molecular dyes as sensitizers which can be classified into metal complexes and organic dyes. Ru(II)-based metal complexes were the first class of dyes that yielded high power conversion efficiencies [2, 16, 44]. However the molar extinction coefficient of this class of sensitizers is typically relatively low in the order of  $10^4 \text{ M}^{-1} \text{ cm}^{-1}$ , requiring thick active layers (between 10–20  $\mu\text{m}$ ) to ensure complete light absorption.

Organic sensitizers are composed of purely organic atoms which form large conjugated  $\pi$ -systems and have much higher molar extinction coefficients relative to the metal complex. As such they are the sensitizers of choice to achieve high *PCEs* in ssDSSCs which have a limited active layer thickness [15, 19, 26, 45].

A common configuration for organic sensitizers is based on the D- $\pi$ -A concept, in which the sensitizer is composed of an electron rich donor (D) and an electron deficient acceptor (A) connected by a  $\pi$ -conjugated bridge ( $\pi$ ) structure. This design allows facile molecular engineering by variation of the individual components, which has led to the large number of different structures reported [20, 46, 47]. The use of D- $\pi$ -A organic dyes in ssDSSCs is investigated extensively in Chapter 3.

Another class of organic sensitizers include porphin-based chromophores similar to the naturally occurring chlorophyll, termed porphyrins. Unlike the D- $\pi$ -A sensitizers that are made up of organic moieties that, isolated, are colorless, porphyrins are highly colored organic chromophores. These species consist of a divalent metallic cation (such as  $\text{Zn}^{2+}$ ) that coordinates to a tetradentate ligand forming a porphin macrocycle, that is attached to the semiconductor surface by an anchoring group. Even though they contain a metallic cation porphyrins are classified as organic dyes as the metal orbitals do not participate electronically in the light absorption.

Extensive research has been conducted in the molecular engineering of sensitizers, adapting their chemical and physical properties to improve the photovoltaic performance of DSSCs.

There has been a recent surge of progress in the field of thin film solar cells focusing on the integration of three-dimensional organic-inorganic hybrid perovskites in solar cell devices. The role of these types of material is reportedly complex; primarily as high extinction light absorbers [48, 49], where they adopt the role of the sensitizer, with additional contributions as hole[10] and electron transport material [50, 51]. Chapters 4 and 5 investigate the role of organic-inorganic lead-based perovskite  $\text{CH}_3\text{NH}_3\text{PbI}_3$  on the photovoltaic performance of solid-state mesoscopic solar cells.

---

<sup>4</sup> The calculated turnover number for dye molecules close to the illuminated front side of a DSSC is about  $10^8$  which corresponds to approximately 20 years of exposure to sunlight.

### 1.3.2.4 Back Contact

In liquid DSSCs the devices typically adopt a sandwich device configuration where the counter-electrode is a TCO substrate coated with a layer of catalyst (i.e. platinum, various forms of carbon or conducting polymers) suitable for the regeneration of the redox couple.

The device configuration of ssDSSC is monolithic, where the back contact is deposited by thermal evaporation of a high work function metal such as silver or gold. The higher reflectivity of silver makes it a cheaper alternative to gold in devices employing thin metal oxide films where the incident light is not completely absorbed and hence reflected at the back contact, enhancing the  $J_{SC}$  by increasing the optical path length [52].

## 1.4 Solar Cell Photovoltaic Characterization

In this section the most common techniques used to characterize and evaluate the photovoltaic performance of solar cells are presented. The most general methods include current-voltage and quantum efficiency measurements, classified as steady-state techniques. These are time-independent measurements where the charge density within the metal oxide semiconductor does not vary as a function of time. Hence the processes of photogeneration and charge-transport through the semiconductor are in equilibrium with the loss processes of charge recombination.

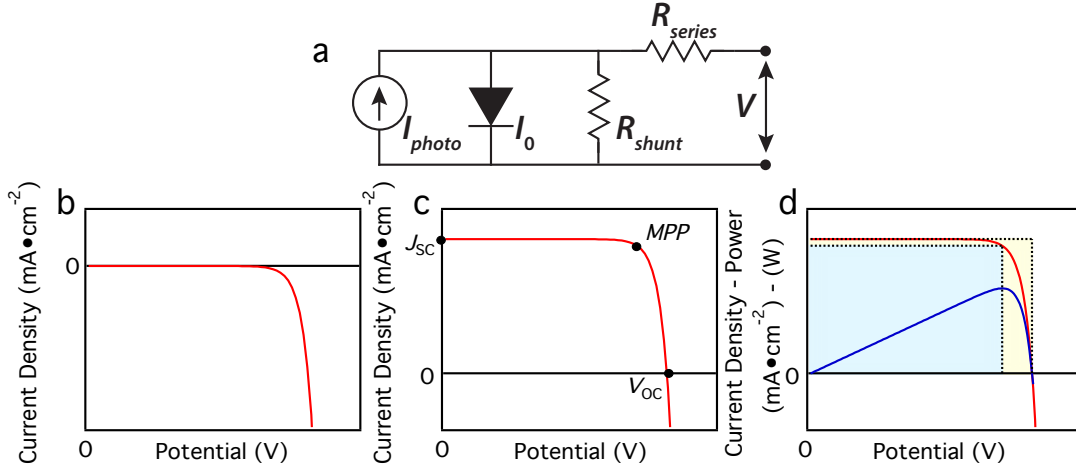
Moreover impedance spectroscopy (IS) is extensively used throughout this thesis to examine the interfaces and internal electrical process within the solar cell under operating conditions. This is a frequency-dependent technique that provides valuable insight into the working mechanisms of the solar cells.

### 1.4.1 Current-Voltage Characteristics

The most common technique used to evaluate the photovoltaic performance of solar cells is the measurement of the current density – voltage ( $J$ - $V$ ) characteristics, by which an external potential bias is applied and the resultant current response of the device is measured. This measurement is conducted in the dark (to determine the so-called *dark current*) and under illumination of different light intensities. Typically the measurement under 100% sunlight intensity at standard AM1.5G illumination ( $100 \text{ mW cm}^{-2}$ ) is used to classify the solar cell photovoltaic performance.

The potential can be applied in reverse bias, such that electrons are injected from the back contact, or forward bias, where they are injected from the photoanode into the device. Conventionally solar cells are characterized using an applied forward bias.

At its most basic a solar cell can be considered as a source of current ( $I_{photo}$ ) in parallel with a diode (with a reverse saturation current of  $I_0$ ) described by the ideal diode equation. Under



**Figure 1.8.** (a) Equivalent circuit of a solar cell. A typical  $J$ - $V$  curve (b) in the dark and (c) under illumination. The maximum power point (MPP), short-circuit current density  $J_{SC}$  and open-circuit potential  $V_{OC}$  are indicated. (d)  $J$ - $V$  curve under illumination (red trace) and corresponding power curve (blue trace).

illumination the total current  $I$  generated by the solar cell is described by Equation 1.6. This takes into account the current lost due to charge recombination losses ( $I_{shunt}$ ) and the diodic dark current (Equation 1.7) flowing through the device ( $I_{dark}$ ).

The non-ideal nature of a solar cell requires the correction by the ideality factor  $m$  where the deviation from  $m = 1$  describes the non-ideality of the solar cell. Additionally the resistive losses within the device is resolved by the inclusion of parasitic shunt and series resistances ( $R_{shunt}$  and  $R_{series}$  respectively). This is depicted in the equivalent circuit model of a solar cell presented in Figure 1.8 (a) and the modified diode Equation 1.8.

$$I = I_{photo} - I_{dark} - I_{shunt} \quad (1.6)$$

$$I_{dark} = I_0 \left[ \exp\left(\frac{eV}{k_B T}\right) - 1 \right] \quad (1.7)$$

$$I = I_{photo} - I_0 \left[ \exp\left(\frac{e(V + IR_{series})}{mk_B T}\right) - 1 \right] - \frac{V + IR_{series}}{R_{shunt}} \quad 1 \leq m \leq 2 \quad (1.8)$$

where  $e$  is an elementary charge,  $k_B$  is Boltzmann's constant and  $T$  is the temperature.

A typical  $J$ - $V$  curve measured in the dark and under illumination is presented in Figure 1.8 (b)–(d). In the dark, when a low potential forward bias is applied, the metal oxide semiconductor has low charge density and thus low conductivity. As a result little or no current flows through the device in these conditions. Increasing the applied potential increases the charge density within the metal oxide semiconductor, raising its quasi Fermi level. Upon further increasing the applied potential, the quasi Fermi level approaches the conduction band of the metal oxide semiconductor. The increase in conductivity of the metal oxide semiconductor is apparent in

the steep increase in the dark current as electrons freely flow to the hole mediator material (either HTM or liquid redox electrolyte). Consequently the dark current is governed by the recombination process between electrons in the metal oxide semiconductor and holes in the HTM.

Under illumination (Figure 1.8 (c)), the solar cell acts as a current source and the photocurrent generated flows in opposition to the dark current. The generation of photocurrent is based on the charge separation of electrons and holes, which is in direct competition with the reverse process; the recombination of electrons and holes (typically between electrons in the metal oxide semiconductor and holes in the HTM). This recombination dominates at high forward bias, leading to the rapid loss of photogenerated charges, visible in the steep decrease in the  $J$ - $V$  curve at this point. When the rates of photocurrent generation and electron-hole recombination are equivalent, all photogenerated charges recombine and the net current is zero. This condition is denoted as open-circuit and the associated potential is the open-circuit potential ( $V_{OC}$ ). When the applied external potential is zero this is denoted as short-circuit conditions and the associated photocurrent density is the short-circuit current density ( $J_{SC}$ ).

In addition to the  $V_{OC}$  and  $J_{SC}$  several other parameters are used to characterize the photovoltaic performance of a solar cell.

The power conversion efficiency ( $PCE$ ) is a measure of the fraction of incident solar power ( $P_{in}$ ) that is converted into electrical power ( $P_{max}$ ). Electrical power is determined using  $P = V \times I$  and as such can be calculated from a typical  $J$ - $V$  measurement as illustrated by the output power curve in Figure 1.8 (d).

The maximum of the power curve is referred to as the maximum power point (MPP), with the corresponding voltage and current ( $V_{MPP}$  and  $J_{MPP}$  respectively).  $PCE$  is accordingly determined by Equation 1.9.

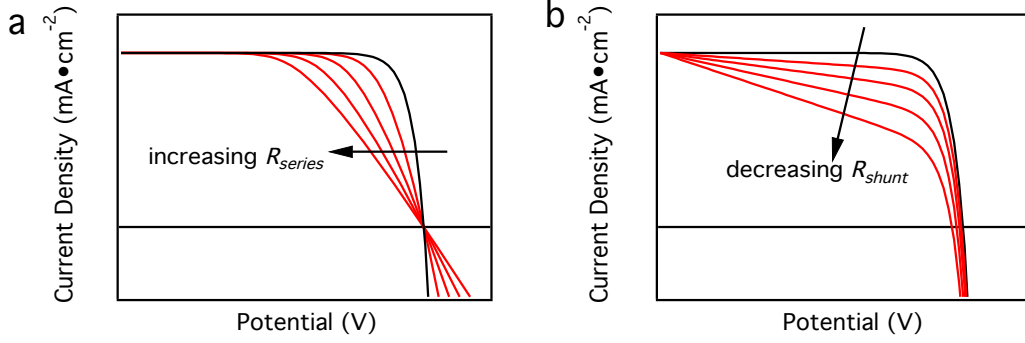
$$PCE = \frac{P_{max}}{P_{in}} = \frac{J_{MPP} V_{MPP}}{P_{in}} = \frac{J_{SC} V_{OC} FF}{P_{in}} \quad (1.9)$$

$$FF = \frac{J_{MPP} V_{MPP}}{J_{SC} V_{OC}} \quad (1.10)$$

The fill factor ( $FF$ ) is a parameter describes the 'squareness' of the  $J$ - $V$  curve and is defined according to Equation 1.10. It can be depicted as the ratio between the two rectangles defined by  $J_{MPP}$  and  $V_{MPP}$  and  $J_{SC}$  and  $V_{OC}$  as illustrated in Figure 1.8 (d).

Conventionally such a  $J$ - $V$  curve is measured from high forward bias to short-circuit conditions (at 0 V) where the applied bias is positive and the measured photocurrent response is negative.

The effect of  $R_{shunt}$  and  $R_{series}$  on the  $J$ - $V$  characteristics of a solar cell are depicted in Figure 1.9. In reality  $R_{series}$  is the sum of the dissipative series resistance contributions within the solar cell, mainly originating from the sheet resistance of the TCO and from the electrical



**Figure 1.9.** Influence of (a) increasing the series resistance  $R_{series}$  and (b) decreasing the parallel shunt resistance  $R_{shunt}$  on the shape of the  $J$ - $V$  curve.

connections made to the solar cell. In the case of solid-state DSSCs, the charge-transport resistance within the HTM also contributes to the net series resistance of the device.

$R_{shunt}$  decreases as a result of recombinative loss processes in the device which lead to leakage current. A possible cause of this could be through the presence of pinholes within the blocking layer on the TCO leading to the direct contact between the TCO and the HTM. Ideally to achieve high  $PCEs$  and reduce the losses, these parameters need to be optimized such that  $R_{series} \rightarrow 0$  and  $R_{shunt} \rightarrow \infty$ .

### 1.4.2 Quantum Efficiency Measurements

In the process of solar cell characterization, it is valuable to determine the fraction of incident photons which are converted into electrons collected in the external circuit. This is given by quantum efficiency of the solar cell which can be expressed as the external quantum efficiency ( $EQE$ ) or the internal quantum efficiency ( $IQE$ ).

The  $EQE$  – which is also referred to as the incident photon-to-electron conversion efficiency ( $IPCE$ ) – takes into account all photons incident on the device, making no distinction between those absorbed and those reflected or transmitted. It is determined from the ratio of the collected charges to the photons falling on the device. Practically this is done by the measurement of the photocurrent generated by the device illuminated by monochromatic light of known photon flux ( $J_0$ ). The  $IPCE$  can subsequently be calculated according to Equation 1.11 where  $J_{SC}(\lambda)$  is the short-circuit photocurrent density with respect to the wavelength of the monochromatic irradiation.

$$IPCE(\lambda) = \frac{J_{SC}(\lambda)}{eJ_0} \quad (1.11)$$

$$J_{SC} = \int_{\lambda_i}^{\lambda_f} eIPCE(\lambda)\phi(\lambda) d\lambda \quad (1.12)$$



The resulting plot of the *IPCE* as a function of the wavelength provides valuable information of the spectral response of the device and in the case of DSSCs typically is a signature of the sensitizer used. The integrated area under the *IPCE* curve yields the short-current density as specified by Equation 1.12, where  $\phi(\lambda)$  is the incident photon flux at a given wavelength.

Equation 1.13 expresses the *IPCE* in terms of the internal efficiencies corresponding to the electronic processes within the devices, where *LHE* is the light harvesting efficiency, and  $\eta_{inj}$  and  $\eta_{coll}$  are the electron injection and charge collection efficiencies respectively (as described previously in Section 1.3.1).

In contrast to the *IPCE*, the *IQE* – also referred to as the absorbed photon-to-current conversion efficiency (*APCE*) – only considers the fraction of photons absorbed by the device and as such is a measure of the efficiency of the direct generation of photoelectrons.

$$IPCE(\lambda) = LHE(\lambda) \times \eta_{inj}(\lambda) \times \eta_{coll}(\lambda) \quad (1.13)$$

$$APCE(\lambda) = \eta_{inj}(\lambda) \times \eta_{coll}(\lambda) \quad (1.14)$$

### 1.4.3 Impedance Spectroscopy

#### 1.4.3.1 Ohm's Law: Resistance and Impedance

An electrical circuit consists of individual components through which there can be a continuous flow of electrical current,  $I$ . The potential energy of the circuit to move electrons from one point to another corresponds to the voltage,  $V$  of the system. The opposition to the motion of electric current is a measure of its electrical resistance,  $R$  and is determined from the ratio between the voltage and the current. This is known as Ohm's Law:

$$R = \frac{V}{I} \quad (1.15)$$

This law assumes an ideal resistor case, where the resistance is constant, frequency independent, independent of the current (resulting in  $V \propto I$ ) and finally the alternate current and voltage are in phase with each other. As such an ideal conductor has zero resistance and an ideal dielectric (a material that does not conduct electricity) has infinite resistance. In order to extend this concept to alternating current (AC) circuits the voltage and current need to be treated as complex time dependent functions to take their phases,  $\phi_V$  and  $\phi_I$  respectively, into account,

$$V(\omega) = |V| \exp[i(\omega t + \phi_V)] \quad (1.16)$$

$$I(\omega) = |I| \exp[i(\omega t + \phi_I)] \quad (1.17)$$

$$\omega = 2\pi f \quad (1.18)$$

where  $\omega$  is the angular frequency.

## Chapter 1. Introduction

---

Electrical impedance  $Z$  is a measure of the opposition to current when a voltage is applied in an AC circuit and corresponds to the generalized resistance in AC circuits. Hence it is the complex ratio of the voltage and the current (Equation 1.19) and takes into account both magnitude and phase, where  $\varphi$  is the phase difference between the voltage and the current. For a direct current (DC) circuit, the resistance of the system can be taken as impedance with the same magnitude and zero phase angle.

$$Z(\omega) = \frac{|V| \exp[i(\omega t + \phi_V)]}{|I| \exp[i(\omega t + \phi_I)]} = |Z| \exp(-i\varphi) \quad (1.19)$$

$$= Z'(\omega) + iZ''(\omega) \quad (1.20)$$

$$\phi_V = \phi_I + \varphi \quad (1.21)$$

In AC circuits, in addition to the resistance present in DC circuits, two further impeding mechanisms must be taken into account: 1) the inductance by which voltages are induced in conductors by the magnetic fields generated by currents and 2) the capacitance, the electrostatic storage of charge induced by an applied voltage between conductors. Collectively the inductance and the capacitance form the imaginary part of the complex impedance  $Z''$ , Equation 1.20, which is referred to as the reactance while the resistance forms the real part  $Z'$ .

### **Small Perturbation Measurements**

Impedance spectroscopy (IS) is the measurement of the AC electrical current response of an electrical system after the application of a small voltage perturbation as a function of the angular frequency  $\omega$ . The small perturbation is necessary to maintain the linear relationship between  $V(\omega)$  and  $I(\omega)$ , resulting that  $Z(\omega)$  is independent of the amplitude of the perturbation.

An IS measurement is generally conducted by keeping the system in a fixed steady-state by applying the stationary constraints within the parameters of DC current and illumination intensity. The impedance is then measured over a range of frequencies,  $f = \omega/2\pi$ , typically from the mHz to the MHz range. Consequently the IS data provides information of the steady-state of the system at different frequencies, thus giving an insight into its dynamic properties. The IS measurement can be described in terms of an equivalent circuit composed of the basic electrical elements presented in Table 1.1.


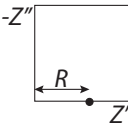

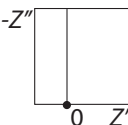

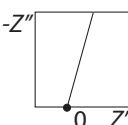

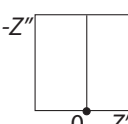
The capacitance can be determined from the measurement of the change in the electrical charge resulting from a small perturbation of the voltage. This frequency-dependent capacitance given by Equation 1.22 and displayed in Table 1.1 is used to determine the capacitance from the impedance measurement;

$$C(\omega) = \frac{I(\omega)}{i\omega V(\omega)} = \frac{1}{i\omega Z(\omega)} \quad (1.22)$$

This demonstrates the simplicity with which impedance data can be converted to different electrical representations (including complex capacitance, impedance and phase angle) which

## 1.4. Solar Cell Photovoltaic Characterization

**Table 1.1.** The defining relation and impedance corresponding to bulk electrical elements. Furthermore the corresponding electrical equivalent circuit symbols are presented. The graphical representation of the impedance is displayed in the Nyquist plots where  $Z'$  and  $Z''$  are the real and imaginary components respectively.

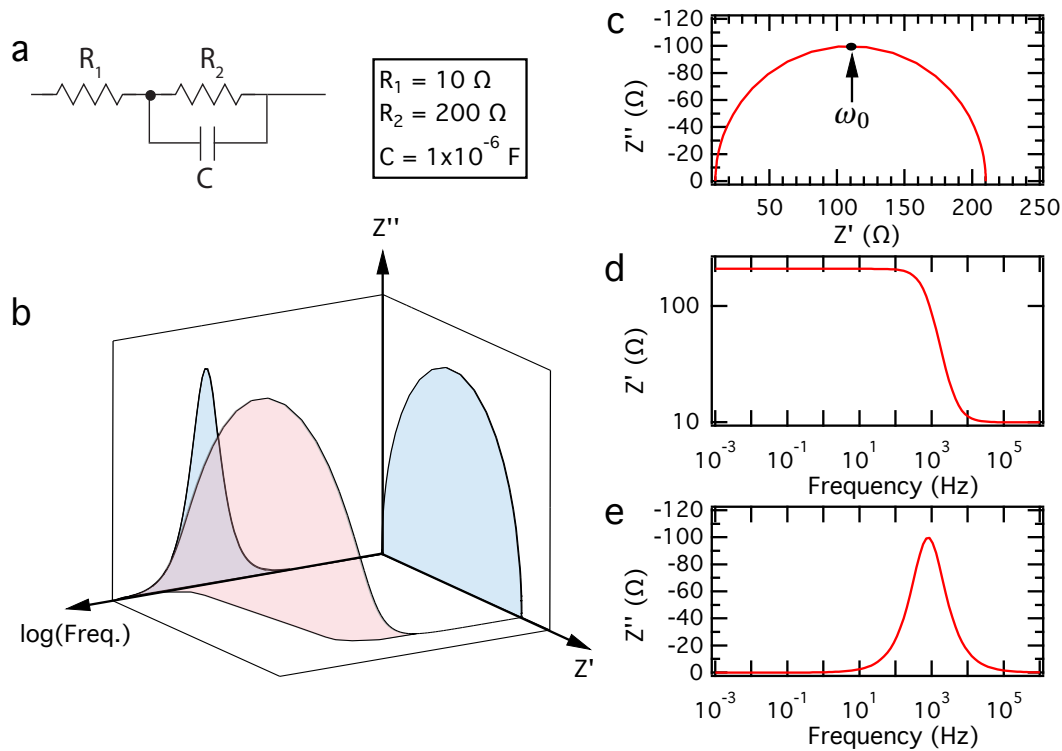
Element	Relation	Impedance	Symbol	Nyquist
Resistor $R$	$V = IR$	$Z_R = R$		
Capacitor $C$	$I = C \frac{dV}{dt}$	$Z_C = \frac{1}{i\omega C} = -\frac{i}{\omega C}$		
Constant Phase Element $Q$		$Z_{CPE} = -\frac{i}{(\omega)^n Q}$ $Q = \frac{1}{ Z }$		
Inductor $L$	$V = L \frac{dI}{dt}$	$Z_L = i\omega L$		

is useful in the interpretation and analysis of the IS measurements.

### 1.4.3.2 Equivalent Circuits

Table 1.1 presents the definition and impedance for the ideal resistor, capacitor and inductor electrical elements. In the case of an ideal resistor, its impedance has no imaginary component and is purely real while ideal inductors and capacitors are purely imaginary. As previously mentioned, for an ideal resistor the  $V$  and  $I$  waveforms are proportional and in phase. The impedance corresponding to capacitors decreases as the frequency increases while it increases in the case of inductors. Consequently for an applied sinusoidal voltage waveform, the generated sinusoidal current waveform is phase shifted by  $-90^\circ$  in the case of a capacitor where the current is leading the voltage by  $90^\circ$  while for an inductor it is shifted by  $+90^\circ$ , lagging behind the voltage.

Equivalent circuits are composed of electrical elements that are connected by low resistance wires. When connected in series the current passing through components is the same, while when in parallel they experience the same voltage as according to Kirchoff's circuit laws based on the principles of conservation of electrical charge and energy. Hence the impedance of elements in series is additive, and for parallel elements the total impedance is the inverse of the sum of the inverse impedances of the individual components. Consequently the impedance



**Figure 1.10.** (a) Equivalent Circuit. (b) 3D representation of simulated impedance data showing real, imaginary and frequency components. (c) Nyquist plot of imaginary as a function of real component. The maximum of the RC-arc takes place at the characteristic angular frequency  $\omega_0$  as indicated. Frequency dependence of (d) real and (e) imaginary parts of impedance. Simulation was conducted from 1 MHz to 1 mHz.

for the parallel combination of a resistor and a capacitor is given by Equation 1.23;

$$Z(\omega) = \left( \frac{1}{R} + i\omega C \right)^{-1} = \frac{R}{1 + i\omega RC} = \frac{R}{1 + i\omega\tau} \quad (1.23)$$

$$\tau = RC = \frac{1}{\omega_0} \quad (1.24)$$

The relaxation time  $\tau$  is given by Equation 1.24 and is a measurement of the characteristic frequency  $\omega_0$ . An equivalent circuit consisting of the parallel combination of a  $R$  and  $C$  element in addition to a simple series resistance  $R_1$  is shown in Figure 1.10 (a). The 3D representation of the impedance of such a system is shown in Figure 1.10 (b) displaying the relationship between the real and imaginary components as well as their dependence on frequency. Figures 1.10 (c)–(e) display the perspective of the individual planes.

The complex Nyquist plot (Figure 1.10 (c)) of the imaginary impedance component as a function of the real component manifests as an arc, often called RC-arc. The top of the arc occurs at the characteristic frequency  $\omega_0$  corresponding to the relaxation time  $\tau$ . The intercept of the arc on the real axis provides a measure of the magnitude of the resistance associated

with the system.

The addition of a series resistance,  $R_1$  results in the shift of the RC-arc along the real axis. Consequently the DC resistance of this system – corresponding to the low frequency intercept – is the sum of the individual resistors,  $Z(0) = R_{DC} = R_1 + R_2$ , which in this case is  $210 \Omega$ . Hence the data representation in the Nyquist plot is crucial to discern information about the contributions of various resistances within a system. Equation 1.22 demonstrates the inverse relationship between the capacitance of the system and its impedance. The capacitance is crucial in determining the origins of the individual resistances since different electrical elements, while they may have similar resistances, typically can be identified by their unique capacitive features.

The frequency dependence of the real and imaginary components presented in Figure 1.10 give first indication of the behavior of the magnitude  $|Z|$  and the phase  $\varphi$  of the impedance as a function of the frequency. These parameters are typically presented in Bode plots as a function of the frequency. This is useful in the identification of relaxation processes with different time constants, which therefore manifest at different frequencies.

### ***Deviation from Ideality***

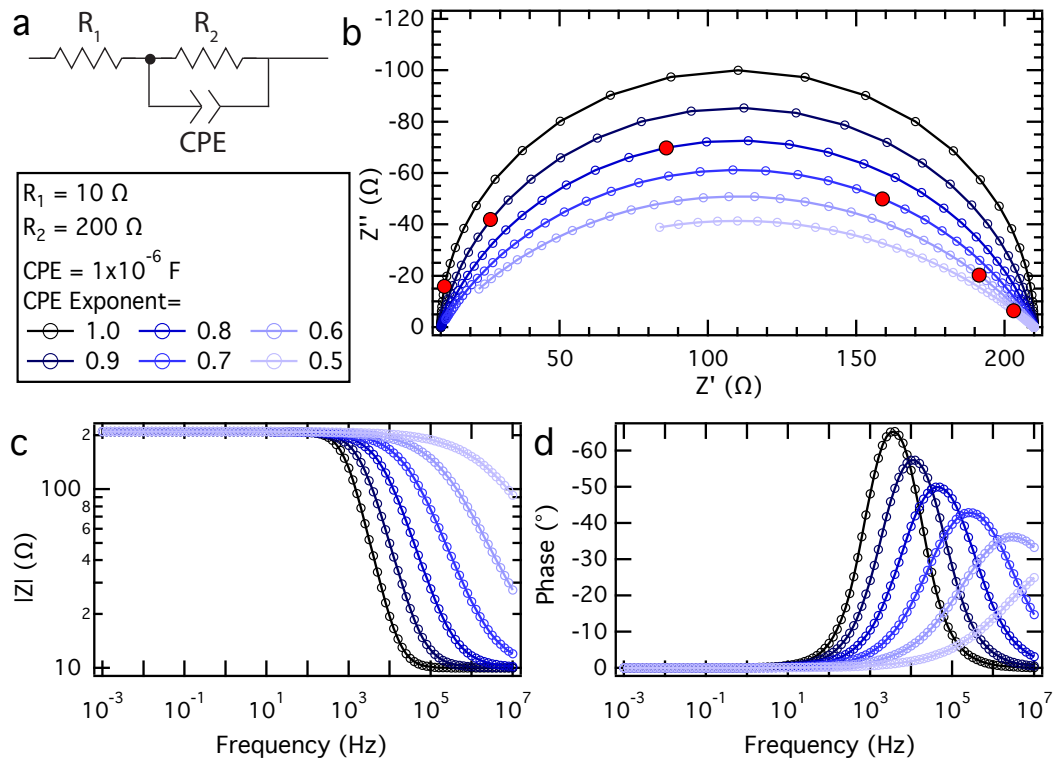
The definitions discussed above correspond to the ideal cases. To take the deviation from ideality into account constant phase elements (CPEs) are employed in place of ideal capacitors. The electrical symbol for a CPE is shown in Table 1.1 and Figure 1.11 (a). A CPE is typically used to describe a capacitive process which is accompanied by a frequency dispersion. The exponent,  $n$  accounts for the deviation from the ideal case where  $n = 1$  describes an ideal capacitor while  $n = 0$  corresponds to a pure resistor. The physical meaning for this deviation is attributed to the existence of anomalous diffusion taking place in the real systems.

In the fitting procedure of IS measurements the CPE exponent is typically fixed or left non-restricted, constraining it between 0.8 and 1. The deviation from ideality manifests in a suppression in the RC-arc in the Nyquist plot as depicted in Figure 1.11 (b). Furthermore a decrease in the exponent of the CPE results in slower response times of the capacitor as evident by the shift in the position of the 10 000 Hz mark in the Nyquist plot. This is reflected in a decrease in the characteristic frequency with increased deviation from ideality;

$$\omega_0 = \frac{1}{(RQ)^{1/n}} \quad (1.25)$$

where  $Q$  is the uncorrected capacitance associated to the CPE (also denoted as  $CPE_T$ ) and becomes equal to the real capacitance when the exponent  $n$  (also denoted  $CPE_p$ ) is equal to 1. To determine the correct capacitance  $C$  of the system the CPE capacitance needs to be corrected accordingly taking into account the associated resistance  $R$ ;

$$C = \frac{(R \times CPE_T)^{CPE_p^{-1}}}{R} \quad (1.26)$$



**Figure 1.11.** (a) Equivalent Circuit. (b) Nyquist and Bode, (c) magnitude and (d) phase, plots from simulation using the presented values for  $R_1$ ,  $R_2$  and CPE. The exponent of CPE was changed from the ideal case when it is equal to 1 to 0.5. The red points in the Nyquist plot correspond to the frequency 10 000 Hz. Simulation was conducted from 10 MHz to 1 mHz.

### 1.4.3.3 IS Model of Solar Cells

In order to use IS as a tool to examine real systems it is necessary to correlate its physical properties with electrical circuit elements. This allows the system to be represented by an equivalent circuit model that can be used to interpret and analyze the IS response of the system. To establish this relationship for solar cells, it is necessary to associate the potentials of the model circuit with the electrochemical potential of the charge carriers (electrons or holes) in the device.

The simplest IS model of a solar cell consists of the parallel combination of the recombination resistance and the chemical capacitance corresponding to the basic configuration of a light absorber between two selective contacts. The recombination resistance needs to be sufficiently large to allow the accumulation of charge carriers in the capacitive element. Selective contacts are essential to direct the flow of charges and prevent the internal short-circuiting of the device. The chemical capacitance is a measure of the charge density and is associated with the splitting of the Fermi levels, thus generating a photovoltage.

### 1.4.3.4 Dye-Sensitized Solar Cells

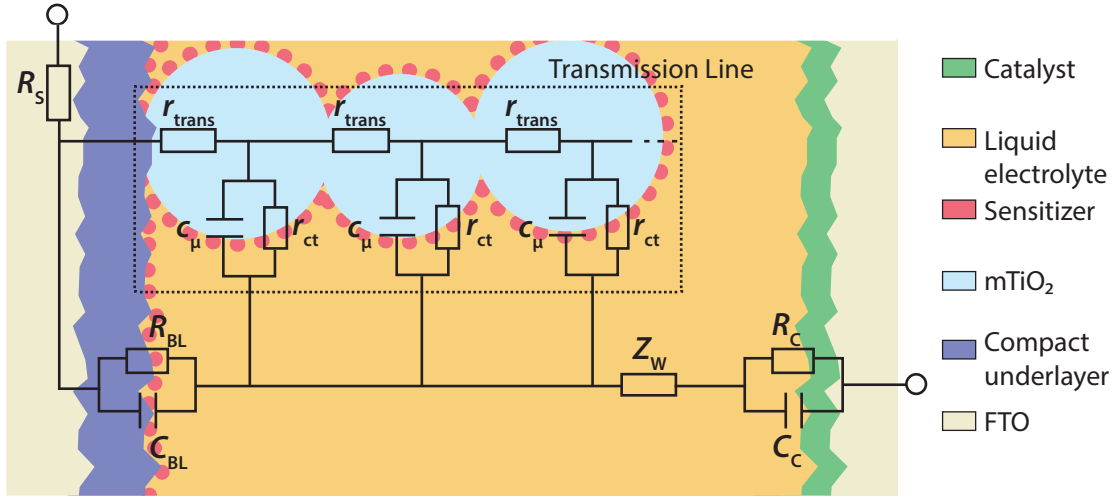
DSSCs have been extensively characterized by IS. The simplest IS model for a solar cell discussed above is further complicated by the complexity of electronic and ionic processes taking place in this system. Here the molecular dye takes the role of the absorber and the selective contacts are formed by electron- and hole-transport materials respectively. Conventionally the electron-transport material (ETM) is the nanostructured wide bandgap semiconductor  $\text{TiO}_2$ . The hole selective contact is formed by a HTM that easily conducts hole carriers and blocks the transport of electrons. The associated hole-transport resistance in the HTM introduces an additional series resistance to the system and thus a source of power loss. Typical HTMs used are either a redox couple in a liquid electrolyte or a solid HTM such as spiro-MeOTAD.

#### *Transmission Line Model*

The configuration of DSSCs employing nanostructured  $\text{TiO}_2$  requires the generated charges to travel a certain distance to reach the external contacts. As such this transport is in competition with the recombination process of the charges. Transmission line equivalent circuit models are used to describe the diffusion-recombination behavior within such structures such as nanostructured  $\text{TiO}_2$ . This model takes into account the additional impedances necessary to move carriers from one point to the next one, describing the macroscopic resistances of the system in terms of their spatially separated distributed components.

A transmission line connects two parallel channels associated to the transport of the electrons and holes. The general model used for a DSSC with a liquid electrolyte is illustrated in the enclosed dashed section of Figure 1.12. The top channel is much more conductive, leading to the short-circuit of the lower transport channel. For a DSSC the top channel describes the diffusion of electrons within the  $\text{mTiO}_2$  using the distributed transport resistance  $r_{\text{trans}}$  (measured per unit length per area). The transverse element describes the local recombination processes in terms of a parallel combination of the recombination resistance  $r_{\text{ct}}$  and chemical capacitance  $c_{\mu}$ . The macroscopic resistances and capacitances can subsequently be determined from the corresponding distributed components using the thickness and area of the active layer.

Consequently the macroscopic transport resistance  $R_{\text{trans}}$  and chemical capacitance  $C_{\mu}$  are respectively measures of the conductivity and the charge density of the nanostructured  $\text{TiO}_2$  film. The macroscopic charge-transfer (also termed recombination) resistance  $R_{\text{ct}}$  accounts for the recombination current at the interface between the  $\text{TiO}_2$  and the hole-transport medium. As such the charge collection efficiency, calculated from the relative rates of the charge-transport in the metal oxide and recombination loss mechanisms (cf. Equation 1.5 Section 1.3.1), can be determined from the resistances corresponding to these electronic processes. The rate and associated resistance of such processes are inversely proportional thus  $\eta_{\text{coll}}$  can be determined



**Figure 1.12.** The general transmission line equivalent circuit for DSSCs using  $m\text{TiO}_2$  and a liquid electrolyte as hole-transport medium. The section of the circuit enclosed by the dashed line corresponds to the transmission line component of the model.

using Equation 1.27.

$$\eta_{coll} = 1 - \frac{R_{trans}}{R_{ct}} \quad (1.27)$$

The impedance of a diffusion-recombination transmission line (shown in enclosed section of Figure 1.12) is simulated and presented in Figure 1.13. For an efficient DSSC it is necessary that the rate of transport of charges is greater than their recombination, implying that the corresponding transport resistance  $R_{trans}$  is smaller than the recombination resistance  $R_{ct}$ . This generates characteristic features in the impedance spectra of the diffusion-recombination model. The impedance is described according to Equation 1.28 and at low frequency manifests as a typical recombination arc from the parallel combination of  $R_{ct}$  and  $C_{\mu}$ .

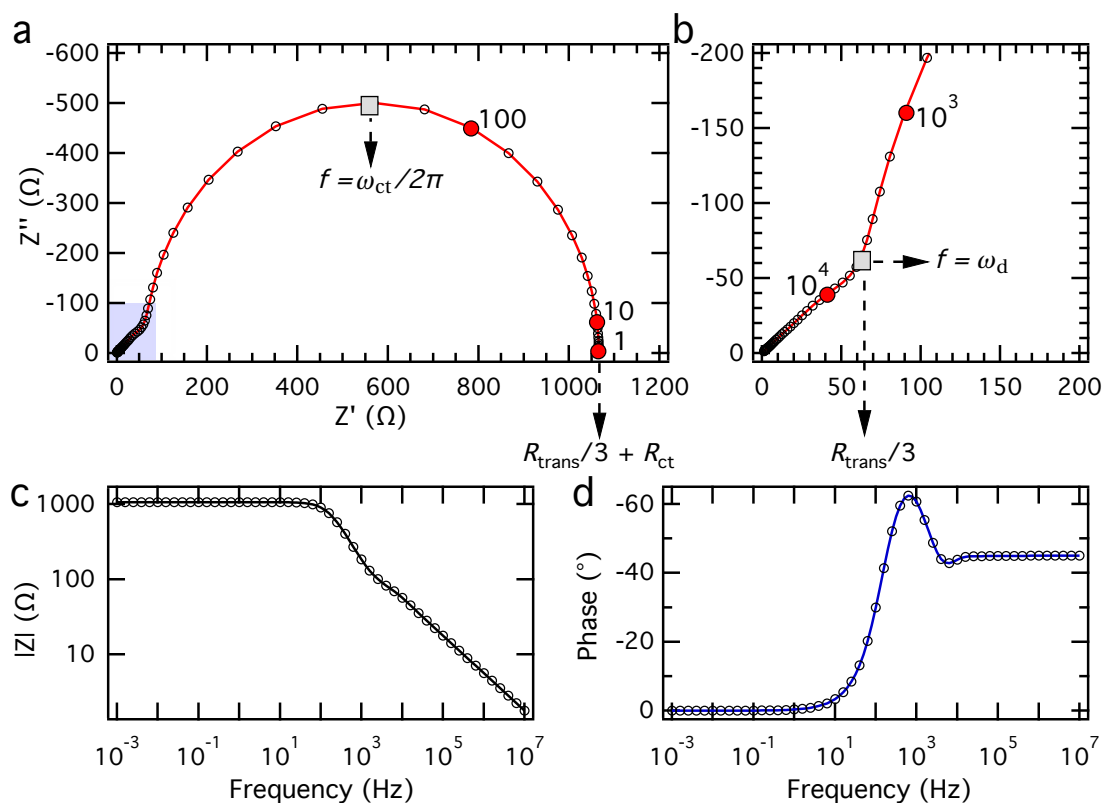
$$Z = \frac{R_{trans}}{3} + \frac{R_{ct}}{1 + i\omega/\omega_{ct}} \quad (1.28)$$

The competing processes of carrier diffusion across the active layer and the recombinative loss of carriers are illustrated by their corresponding characteristic frequencies:  $\omega_d$  and  $\omega_{ct}$ .

In the high frequency region the transmission line displays a  $45^\circ$  line in the Nyquist plot presented in Figure 1.13 (a)–(b).

This so-called Warburg impedance is further displayed in the associated phase which remains at  $-45^\circ$  in this frequency region (Figure 1.13 (d)). For systems with spatially limited diffusions such as the DSSC this straight line behavior changes at frequencies lower than the characteristic diffusion frequency  $\omega_d$ . In this low frequency regime the impedance is dominated by the recombination behavior of the active layer and the spectrum displays the typical recombination arc.





**Figure 1.13.** Simulated impedance spectra of a diffusion-recombination transmission line with reflecting boundary conditions using the following parameters:  $R_{\text{trans}} = 200 \Omega$ ,  $R_{\text{ct}} = 1000 \Omega$  and  $C_{\mu} = 1 \times 10^{-6} \text{ F}$  (a) Nyquist plot, (b) magnification of tinted region of (a) showing the straight line feature of the transmission line. The solid red markers show selective frequencies in Hz. The characteristic frequency of the low frequency recombination process and the frequency of the turnover between the straight line behavior at high frequency and the curvature of the recombination arc at low frequency are marked by grey squares in (a) and (b) respectively. Bode plots displaying (c) magnitude and (d) phase.

The transport resistance can be determined from the resistance at the turnover between the  $45^\circ$  Warburg impedance and the curvature of the capacitive element resulting from the recombination process as indicated by Figure 1.13 (b), from which the conductivity can subsequently be calculated. The recombination resistance is determined from the low frequency intercept of the recombination arc as shown in Figure 1.13 (a).

The transmission line model describes the diffusion-recombination behavior within the mesoporous  $\text{TiO}_2$  structure and at the interface with the hole selective contact. The various other interfaces within the liquid-based DSSC are accounted by additional electrical elements as shown in the complete equivalent circuit in Figure 1.12.

**Counter-electrode/Electrolyte Interface** –  $R_C$  and  $C_C$  represent the charge-transfer resistance and the associated interfacial capacitance at the interface between the counter-electrode and the electrolyte, corresponding to the process of the regeneration of the oxidized electrolyte

## Chapter 1. Introduction

---

species at the counter-electrode. This process occurs on a faster timescale relative to the other processes taking place in the solar cell operation and thus manifests in the highest frequency region of the IS spectra.

**TCO and/or Blocking Layer/Electrolyte Interface** – The resistance at the substrate needs to be sufficiently high to prevent current leakage through this interface. In contrast to the conventional liquid DSSC where the electron transfer from the TCO to the oxidized redox couple species is relatively slow, in the case of the ssDSSC this direct contact needs to be avoided. Hence the TCO substrate is generally covered by a blocking layer (BL) – typically  $\text{TiO}_2$  – to increase this ‘shunt’ resistance.  $R_{\text{BL}}$  and  $C_{\text{BL}}$  represent the charge-transfer resistance and capacitance for the interface between the blocking layer and the hole-transport mediator. The time constant for this process is similar to the charge-transfer at the interface between the metal oxide and the hole-transport mediator and thus the associated RC-arc manifests in the same low frequency range. The sheet resistance of the TCO contributes as a simple series resistance to the system given by  $R_s$  and corresponds to the displacement of the spectral features from the origin.

**Diffusion of Redox Species** – The diffusion of the redox species within the liquid electrolyte is given by the element  $Z_d$ , described as a Warburg diffusion element. The timescale of this process is typically relatively slow, thus it manifests at low frequencies.

As outlined the individual processes within this system have characteristic time constants and as a result the associated impedance spectral features manifest in specific frequency regions. Hence for this system the distribution of the spectral features in the frequency domain from high to low frequency corresponds to:

- Series resistance of wires/contacts and sheet resistance of TCO
- Counter-electrode/electrolyte interface RC-arc
- Metal oxide/hole-transport mediator diffusion-recombination transmission line – TCO and/or BL/electrolyte interface RC-arc
- Redox species Warburg diffusion element

which is used to identify and subsequently interpret the resulting IS response.

### ***Role of Applied Potential***

The IS response of a liquid-based DSSC is greatly dependent on the externally applied potential as this defines the position of the Fermi level and conductivity within the  $\text{mTiO}_2$ . Taking into account the changes in behavior of the IS, the general model presented in Figure 1.12 for a liquid DSSC can be simplified depending on the applied potential.

The charge-transfer at the counter-electrode/electrolyte interface occurs on a fast timescale, manifesting in the high frequency region. The corresponding RC-arc of this interface is

generally apparent across the entire potential range. The impedance of diffusion within the electrolyte ( $Z_d$ ) is a slow process and thus appears at the lowest frequencies as a deformation in the Nyquist plot or even as a separate arc (at high forward bias).

**Low Potential** – At low applied forward bias, the  $\text{TiO}_2$  acts as an insulator, thus both  $R_{\text{trans}}$  and  $R_{\text{ct}}$  are very large and the behavior is dominated by the interface between the electrolyte and the BL. The contribution from the  $\text{mTiO}_2$  is negligible and the transmission line section of the equivalent circuit can be disregarded.

**Intermediate Potential** – At intermediate potentials, the Fermi level in the  $\text{TiO}_2$  increases and therefore the electron density and thus the conductivity of the  $\text{TiO}_2$  increases. This latter aspect is reflected in the exponential increase in the chemical capacitance with increasing applied potential [53]. This is accompanied by an exponential decrease in the charge-transfer resistance at the  $\text{mTiO}_2$  interface with the hole mediator. In this region the complete unsimplified transmission line model is necessary to fit the data.

**High Potential** – Finally for high forward bias, the Fermi level in the  $\text{mTiO}_2$  approaches its CB, resulting in negligible  $R_{\text{trans}}$ . As a consequence the  $45^\circ$  transmission line feature disappears and the equivalent circuit reduces to a single RC contribution of the parallel coupling of the  $R_{\text{ct}}$  and  $C_\mu$ .

### ***Effect of Series Resistance***

The effect of the series resistance  $R_{\text{series}}$  on the  $J$ - $V$  curve have been presented in Section 1.4.1. Increasing  $R_{\text{series}}$  results in a decrease in the  $FF$  and hence in the  $PCE$  of the solar cell device.

$$R_{\text{series}} = R_S + R_C + \frac{1}{3}R_{\text{trans}} + W_d \quad (1.29)$$

$$V_C = V_{\text{app}} - \int R_{\text{series}} dI \quad (1.30)$$

The total series resistance of the device is related to the sum of the individual dissipative resistance contributions according to Equation 1.29 for a liquid DSSC where  $W_d$  is the resistance associated with the redox species Warburg diffusion element.

When a current passes through a solar cell, the potential is decreased due to the power losses resulting from the internal series resistance of the system. Consequently the applied potential  $V_{\text{app}}$  is not the same as that experienced at the interfaces within the device and needs to be corrected for this ohmic drop – the so-called IR drop. This is achieved by subtracting the integrated internal series resistance with respect to the current from  $V_{\text{app}}$  to give the corrected potential  $V_C$  (Equation 1.30). Consequently the larger  $R_{\text{series}}$  is, the larger the IR drop and associated drops in  $FF$  and  $PCE$ . As such evaluating  $R_{\text{series}}$  of a system provides valuable information on a critical limiting factor in solar cell performance and understanding its origins and effects can be utilized to ultimately improve the systems  $PCE$ .

Note that although the definition of the net series resistance (Equation 1.29) includes the

contribution from  $R_{\text{trans}}$ , this often leads to over estimation of the subsequently derived IR drop. Hence in the course of this thesis this element was not included in the calculation of the IR drop. This is justified by the treatment of the metal oxide semiconductor (here  $\text{TiO}_2$ ) and its associated  $R_{\text{trans}}$  as a separate entity.

### 1.5 Motivations

Since the first reports of the conventional DSSC, there has been extensive research and development in the area of the liquid electrolyte version, leading to *PCEs* of up to 13% at the time of the start of this thesis. In comparison to the liquid DSSC, the operating mechanisms and the limiting parameters of the solid-state analogue was poorly understood, resulting in poor reproducibility and low *PCEs* in the range of 3–6%. This was partly due to the direct application of results and knowledge pertaining to liquid DSSCs to ssDSSCs disregarding the different device mechanisms of the systems.

In this thesis I address the device mechanisms of solid-state mesoscopic solar cells using spiro-MeOTAD as HTM. The factors contributing to the photovoltaic performance are investigated and analyzed to gain a more complete fundamental understanding of the phenomena within the working solar cells.

Impedance spectroscopy, while it has become a toolbox technique in the characterization of liquid DSSCs, has been less popular in the case of ssDSSCs. This characterization method presents a good example where the procedures and knowledge from the liquid case have been generalized to the solid-state analogue without fully adapting for the inconsistencies and differences between the systems leading to poor understanding of the operating mechanisms of ssDSSCs. These issues are addressed through the course of this thesis where impedance spectroscopy (IS) is extensively utilized to carefully characterize solid-state mesoscopic solar cells and examine the internal electronic processes and interfaces of the devices under working conditions. New equivalent circuit models are developed and adapted to interpret and analyze the IS response. These investigations have been supported through the analysis of key operating parameters by a wide range of characterization techniques.

**Chapter 2** investigates the transport properties of the key component of ssDSSCs – the HTM – by IS. Different device configurations were investigated to differentiate the individual transport processes and interfaces of ssDSSCs. To simplify the complexity of the system no sensitizer was used in this investigation. An equivalent circuit model is developed to characterize such devices and gain better understanding of their internal working mechanisms. The influence of temperature on the IS response was investigated and the charge-transport within the HTM was further analyzed using the Arrhenius equation. Additionally increasing the conductivity of spiro-MeOTAD through doping procedures was investigated and correlated with a decrease in the transport resistance of the HTM by IS. Subsequently the method of photodoping in the presence of atmospheric oxygen and illumination was compared to chemical doping using a *p*-type dopant. Observed trends in device *PCEs* as a result of the doping methods were

associated to changes in the extracted IS parameters. This study highlights key components and parameters that can be used to understand and improve the photovoltaic performance of ssDSSC revealed through the development of a powerful characterization method.

**Chapter 3** presents individual studies on the photovoltaic performance of ssDSSC using molecular sensitizers. The physical and chemical properties of molecular dyes are investigated and correlated with the device mechanisms using various characterization techniques. The importance of the molecular structure of the dyes is highlighted and directly related to the photovoltaic device performance. Optical absorption studies revealed the de-aggregating ability of spiro-MeOTAD in reducing the aggregation of a squaraine dye adsorbed on TiO<sub>2</sub>. IS and transient measurements were used to examine the induced CB shift of the mTiO<sub>2</sub> resulting from the so-called *surface dipole effect* arising from the individual dipole moments of the adsorbed dye molecules. This was consequently related to the molecular structure of the individual dye components contributing to the dye-loading properties and dipole moment of the sensitizer. Furthermore IS in combination with photoinduced absorption (PIA) measurements were used to examine the charge-transfer mechanisms of ssDSSCs employing different sensitizers. This chapter presents the photovoltaic performance of ssDSSCs using different molecular sensitizers in addition to thorough, in depth investigations of the device working mechanisms.

**Chapters 4 and 5** are based on the use of the organic-inorganic hybrid perovskite CH<sub>3</sub>NH<sub>3</sub>PbI<sub>3</sub> instead of a molecular dye as sensitizer in conjunction with the amorphous organic semiconductor spiro-MeOTAD as HTM in the application for mesoscopic solid-state solar cells.

**Chapter 4** investigates the perovskite-sensitized solar cells using IS. The existing models used for liquid and solid-state DSSCs are expanded and elaborated to establish a model to interpret the frequency response of these type of devices. A similar approach is adopted as in Chapter 2. The influence of the additive concentrations of 4-*tert*-butylpyridine and LiTFSI in the HTM solution and varying the HTM overlayer thickness on top of the submicrometer thick TiO<sub>2</sub> on the extracted IS parameters are investigated. These studies tested and validated the developed IS model, allowing the in depth characterization of these devices and examination of pertinent factors affecting their photovoltaic performance. The IS response of these perovskite devices displays unique behavior – particularly under illumination. The complex nature of this behavior can be identified and separated by the presented model into individual features corresponding to the electronic and ionic conductivities of the lead-iodide perovskite material. The manifestation of the individual features were found to greatly depend on the morphology and nature of the perovskite material which define the electrical and transport properties.

**Chapter 5** follows on from the previous **Chapter 4** presenting a morphological study of the organic-inorganic hybrid perovskite CH<sub>3</sub>NH<sub>3</sub>PbI<sub>3</sub>. The photovoltaic performance of lead-iodide based perovskite-sensitized mesoscopic solid-state solar cells is greatly dependent on the film morphology, which in turn is dependent on the deposition techniques and subsequent treatments employed. In this chapter parameters influencing the perovskite film

formation, morphology and composition are investigated and correlated with the photovoltaic performance and device working mechanisms. The role of the chosen solvent, the effect of the annealing temperature used in the conversion process and the composition of the perovskite precursor solution are examined. Increasing the annealing temperature of the perovskite material was found to lead to significant morphological changes in the film structure in addition to the increased formation of pure  $\text{PbI}_2$ . IS measurements reveal a deviation from the typical chemical capacitive behavior of these types of devices when the  $\text{PbI}_2$  content within the material is increased (either by high annealing temperatures or increased  $\text{PbI}_2$  content in the precursor solution).

**Chapter 6** examines the thermal properties of the hybrid perovskite  $\text{CH}_3\text{NH}_3\text{PbI}_3$  using thermal gravimetric analysis (TGA) and differential scanning calorimetry (DSC). The individual components and precursor materials are analyzed in order to correctly identify their contributions to the thermal behavior of the perovskite material. The sublimation behavior of the isolated organic components is examined. Subsequently the formation of the perovskite material with the general formula  $\text{CH}_3\text{NH}_3\text{PbX}_3$  (where X=I or Cl) from mixed precursor solutions of  $\text{PbX}_2$  and  $\text{CH}_3\text{NH}_3\text{X}$  (where X can be I or Cl) is investigated to gain insight about the formation mechanisms of the perovskite. When a mixed halide solution is used (i.e. the inorganic and organic component contain different halide atoms) the resulting mixture contains an excess of organic material in addition to the perovskite formed. The role of the formation and presence of the excess organic component on the thermal behavior is examined through the comparison of TGA measurements of perovskite powder and solution. This study highlights the importance of the molar ratio between the organic and inorganic components in the perovskite precursor solution and the identity of the chosen halide for the respective constituents.

## 2 Transport Properties of Spiro-MeOTAD in Solid-State DSSCs

*The first section of this chapter is based on the publication Dualeh et al. ACS Nano, 2013, vol. 7, 2292–2301.*

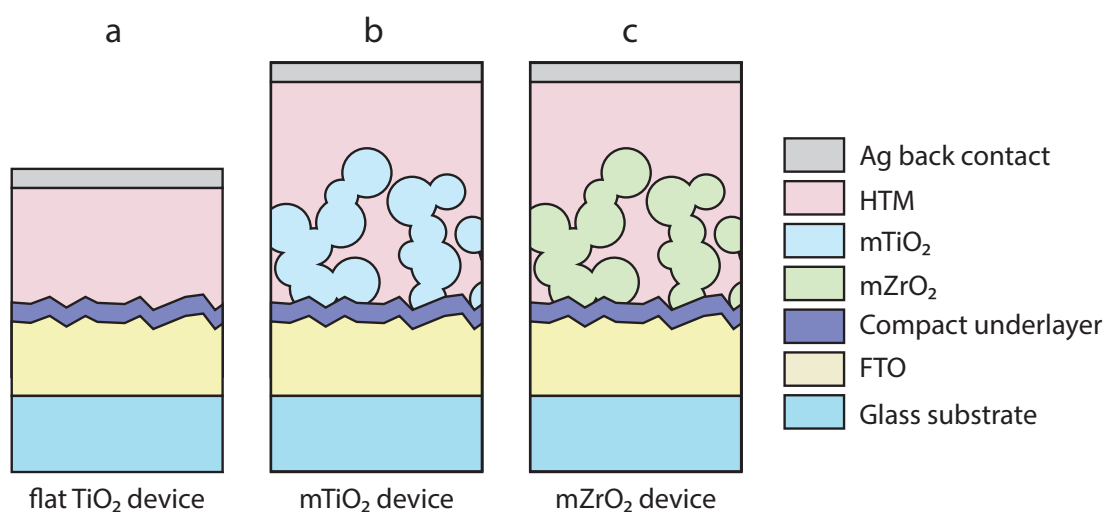
### 2.1 Introduction

In this chapter impedance spectroscopy is used to study the transport properties of the organic *p*-type semiconductor, spiro-MeOTAD, and its dependence on temperature [54]. The effect of temperature on the transport of spiro-MeOTAD and thus the overall device performance has significant importance. This is due to the large range of temperatures devices are subjected to in real-life application.

Previous studies [55, 56] have examined the effect of varying the temperature on the electrical parameters of liquid DSSCs and observed decreases in the electron lifetimes as a function of temperature. Furthermore temperature variations were found to have restoring effects [57] on the device performance of DSSCs with liquid and semi-solid electrolytes. In the case of DSSCs using solid-state electrolytes, the influence of environmental factors such as temperature on the electrical parameters of the device performance have been studied infrequently so far and are not fully understood.

IS has been used extensively to study liquid DSSCs [58–61] and the physical mechanisms of charge-transfer in this system are well understood. In the case where the liquid electrolyte is replaced by a solid-state hole-transport material the model used to fit liquid DSSCs is no longer completely sufficient and requires adjustment. Previous work [62–64] report the use of a two-channel transmission line model in order to consider the electron- and the hole-transport characteristics that appear when a more resistive electrolyte (such as a solid HTM) is employed. In this case the two channels correspond to the transport of electrons and holes respectively within the composite of HTM infiltrated into the mesostructured metal oxide.

In order to better understand the processes occurring within ssDSSCs, three different systems were investigated: compact TiO<sub>2</sub> with 1) spiro-MeOTAD deposited directly on top, and 2)



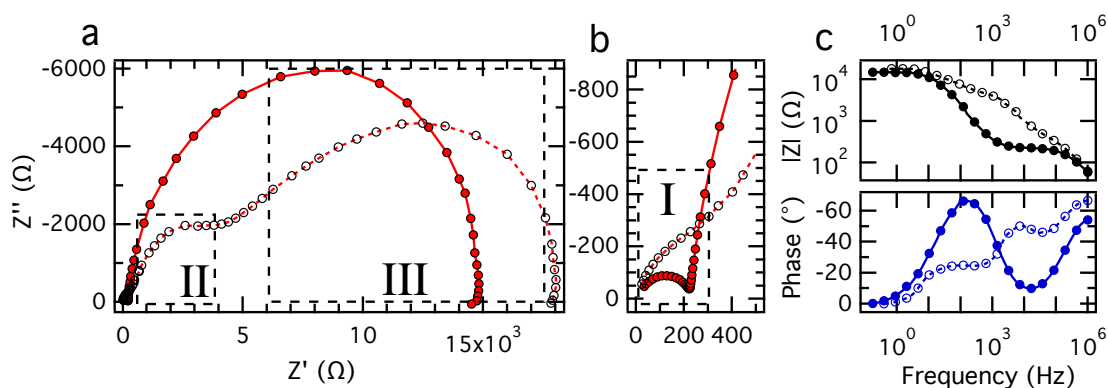
**Figure 2.1.** Schematic illustration of the device structures for compact  $\text{TiO}_2$  with (a) spiro-MeOTAD deposited directly and (b) mesoporous  $\text{TiO}_2$  or (c)  $\text{ZrO}_2$  infiltrated with spiro-MeOTAD. Fluorine doped tin oxide (FTO) glass substrates and silver back contacts (Ag BC) were used to complete the devices. Figure not to scale.

mesoporous  $\text{TiO}_2$  or 3) mesoporous  $\text{ZrO}_2$  infiltrated with the HTM, as depicted in Figure 2.1. The first-case scenario models the direct interface between the HTM and the semiconductor material (here  $\text{TiO}_2$ ). However in the case of real devices this simplistic model is further complicated due to the convoluted mesoporous structure of the nanocrystalline semiconductor. To simulate a three-dimensional HTM matrix, mesoporous  $\text{ZrO}_2$  was chosen because of its insulating character which prevents current flowing over the mesoporous matrix and thus simply acting as a scaffold for the HTM. Finally case 2) represents the real case scenario within working ssDSSCs where the HTM infiltrates a mesoporous  $\text{TiO}_2$  film. No sensitizer was used in these devices to simplify the interfaces being considered.

In its pristine state, spiro-MeOTAD has low conductivity and thus in order to achieve high efficiencies in ssDSSCs, the material needs to be *p*-doped to increase the charge carrier density. Whilst this occurs naturally during exposure to oxygen and light (so-called photodoping), a range of chemical dopants have been investigated to controllably oxidize the spiro-MeOTAD making it sufficiently conductive to achieve good power conversion efficiency [41, 65, 66].

$\text{Li}(\text{CF}_3\text{SO}_2)_2\text{N}$  (LiTFSI) is conventionally used as an additive to the HTM to increase its conductivity [41]. Recent studies have found that it further plays a significant role in the doping process of the spiro-MeOTAD [40, 42] where the  $\text{Li}^+$  is believed to be consumed during the oxidation process which may compromise the long-term stability of the device. In this work to achieve high *PCEs* under controlled conditions, in addition to the LiTFSI a cobalt(III) complex, coded FK102 (cf. Figure 1.7 Chapter 1) [15] was used to chemically *p*-dope the HTM during the manufacture of the devices. The effect of chemically doping spiro-MeOTAD on its transport properties was investigated.





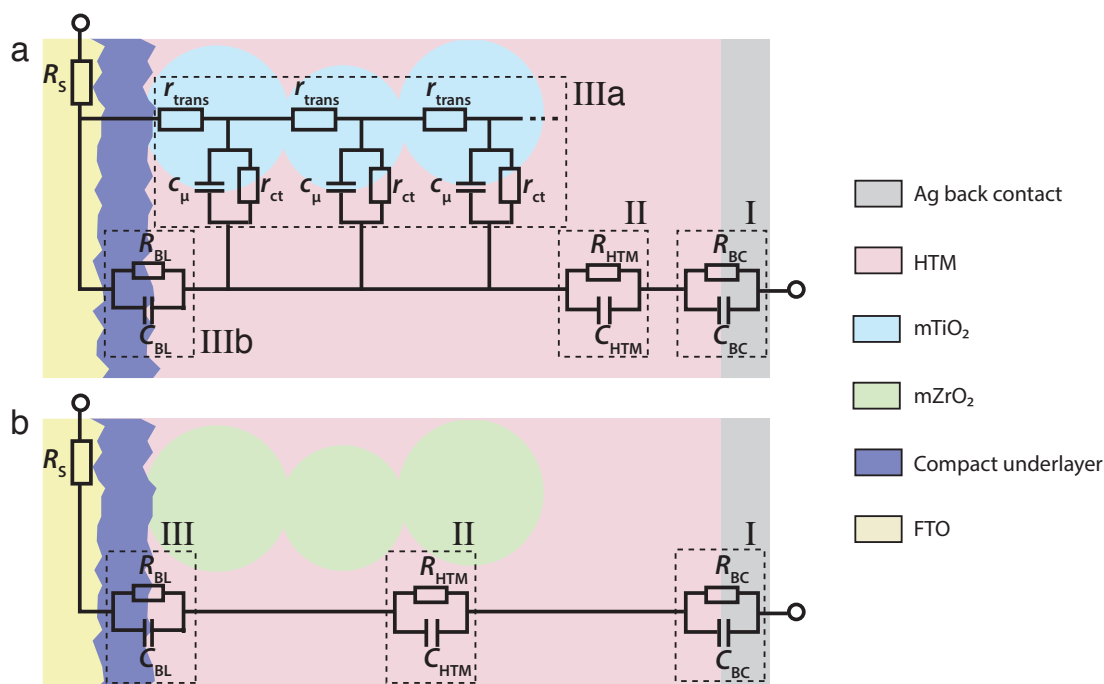
**Figure 2.2.** (a) Nyquist plots measured under dark at 0.65 V for devices using mesoporous TiO<sub>2</sub> infiltrated with doped (solid) and undoped (dashed) spiro-MeOTAD. (b) Detail of high frequency range of Nyquist plot. (c) Corresponding bode plots displaying the magnitude (black) and phase (blue). This measurement was conducted at 0°C.

## 2.2 Establishing IS Equivalent Circuits

Normally the general equivalent circuit used to model ssDSSCs uses an adapted transmission line to describe the diffusion-recombination limited transport within the mesoporous semiconductor and the transport within the HTM [63]. The model used in the work of Fabregat *et al.* [63] is the two-channel transmission line with both channels open, corresponding to the transport in the wide bandgap semiconductor and in the HTM respectively. These samples were not sealed and therefore the properties of the device components, especially the HTM can change rapidly during the IS measurement. In this study the channel for the HTM was not used and the transport of the HTM is simply modelled by a resistor. This is a very similar model as used by Boix *et al.* [67] for organic/inorganic hybrid solar cells using TiO<sub>2</sub>/Sb<sub>2</sub>S<sub>3</sub>/P3HT. The reasoning for this change in the fitting model is discussed in further detail below.

A representative example of the Nyquist plots is shown in Figure 2.2. The spectral features can be categorized into different frequency ranges (cf. Section 1.4.3.3 Chapter 1). The resistance of the conducting glass, contacts and wires –  $R_{\Omega}$  – can be determined from the intersection of the first arc at high frequency, labeled region I (see high frequency detail in Figure 2.2 (b)). The arc at high frequency was independent of applied bias regardless of the system under consideration and is associated to the charge-transfer resistance  $R_{BC}$  and the interfacial capacitance at the back contact (BC)/HTM interface. This is the solid-state DSSC analogue to the counter-electrode/electrolyte interface in the liquid DSSC (cf. Section 1.4.3.4). As in liquid-state the time constant for the charge-transfer at this interface is faster than the other processes occurring in the system, thus manifesting in the high frequency region.

The RC-arc at low frequency – region III – was identified as the recombination resistance  $R_{ct}$  of electrons in the TiO<sub>2</sub> and holes in the HTM and the corresponding chemical capacitance  $C_{\mu}$ . The arc at intermediate frequency – region II – was observed to merge with the low frequency arc as well as overlapping slightly with the high frequency arc. This feature has been ascribed

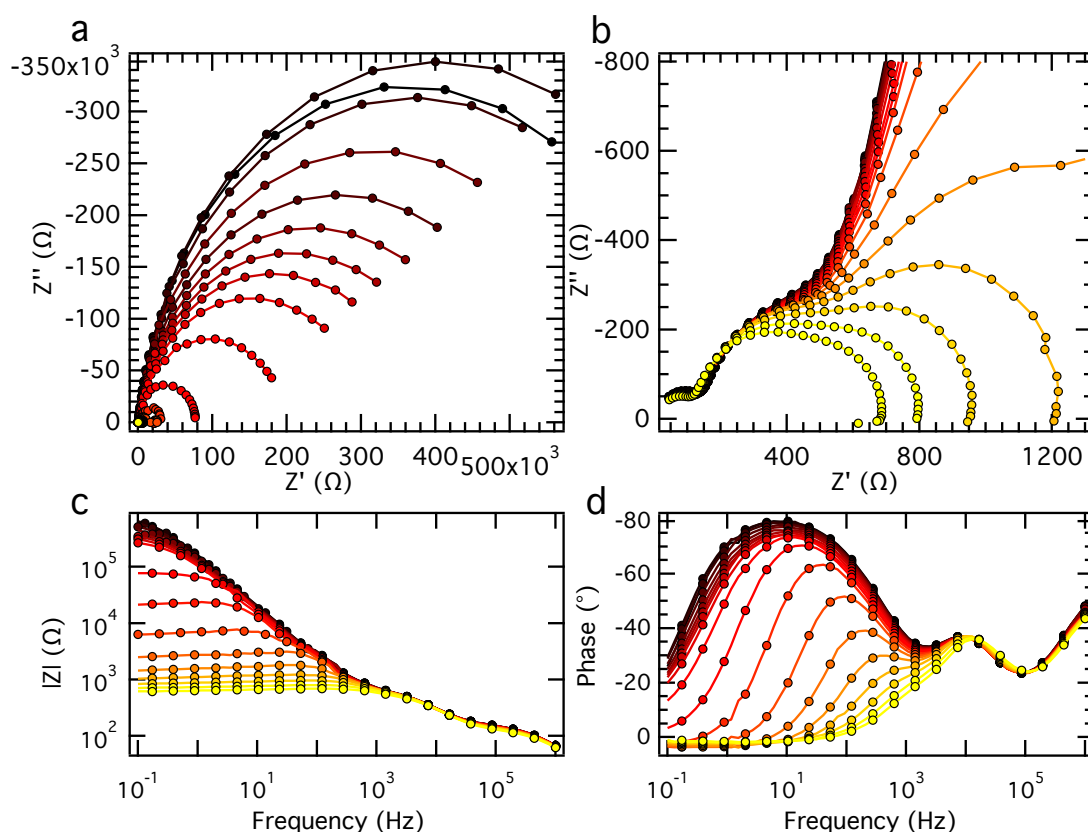


**Figure 2.3.** Equivalent circuit models used to fit the IS data for systems using the (a) mesoporous  $\text{TiO}_2$  and (b) mesoporous  $\text{ZrO}_2$ . BL = compact  $\text{TiO}_2$  blocking layer, BC = Ag back contact used as counter electrode.

to the charge-transport resistance  $R_{\text{HTM}}$  and capacitance of the HTM. This phenomena is clearly visible down to low potentials and as such it is not an artefact resulting from the fitting procedure, see Figure 2.4.

In the case of the mesoporous  $\text{TiO}_2$  samples, there is a straight line feature at the intersection between region II and III, which is attributed to the transmission line (see section IIIa in Figure 2.3 (a)) and appearing at high forward bias. The transport resistance of electrons in the  $\text{TiO}_2$  can be determined from this element. This feature was often observed to be partially hidden beneath the high degree of overlap between the arc corresponding to  $R_{\text{HTM}}$  (see Figure 2.2) and the recombination arc, making it difficult to fit the transport resistance of the  $\text{TiO}_2$  reliably. The section IIIb of the equivalent circuit model in Figure 2.3 (a) was used to fit the low forward bias region when the  $\text{TiO}_2$  is not conductive and the current flows over the compact  $\text{TiO}_2$  layer/HTM interface. Hence in this region the characteristic  $45^\circ$  transmission line is not present. At high forward bias only the capacitive element of the feature IIIb is still active.

In the case where devices were fabricated using mesoporous  $\text{ZrO}_2$  this straight line feature is not present at all due to the insulating character of the  $\text{ZrO}_2$ , see Figure 2.4. However the continued presence of an intermediate frequency arc indicates that the charge-transport resistance of the HTM can be modelled as a characteristic feature separate from the transmission line, validating the use of an additional RC-element in series to the transmission line



**Figure 2.4.** Nyquist plots measured at 0.05 V steps from 0 V (yellow) to 0.85 V (black) in the dark for a sample using mesoporous  $\text{ZrO}_2$  infiltrated with undoped spiro-MeOTAD. This measurement was conducted at 20°C.

for this parameter similar to the IS analysis of Boix *et al.* [67, 68], see section II Figure 2.3. The equivalent circuit presented in Figure 2.3 (b) also applies to the model used to fit the low forward bias region of devices with mesoporous  $\text{TiO}_2$ . This is based on the fact that under these conditions the  $\text{TiO}_2$  is insulating. This model is used for the entire potential range when the insulating scaffold of  $\text{mZrO}_2$  is used instead of  $\text{mTiO}_2$ .

Furthermore in this work the transport resistance of the electrons in the  $\text{TiO}_2$  – as a property that is associated with the material of the metal oxide semiconductor and not the HTM – is not of primary interest. Due to the deviation from ideality of these devices, constant phase elements were used instead of ideal capacitances to fit the data with the proposed model.

It was observed that upon *p*-doping the spiro-MeOTAD, the intermediate arc illustrated in region II of Figure 2.2 (a), decreased significantly in magnitude, indicating that the corresponding resistance decreased. This confirms the association of this feature with the transport within the HTM as the process of chemical *p*-doping leads to the creation of additional holes, increasing the doping inside the HTM. Hence its conductivity is enhanced accounting for the observed decrease of  $R_{\text{HTM}}$  to such degree that it is no longer visible.

### 2.3 Interpretation of IS Spectra: Temperature Effects

Using this developed model to analyze the IS spectra, the effect of temperature<sup>1</sup> on the individual processes was examined in order to gain a better understanding of the mechanisms within the working devices. The responses are examined according to their frequency region, which is used in the identification of the individual components.

#### 2.3.1 High Frequency IS Response

The trend observed for the charge-transfer resistance at the BC/HTM interface  $R_{BC}$  and the corresponding capacitance was found to be similar for the different systems, regardless if the film consisted of solely flat  $\text{TiO}_2$  or had an additional layer of mesoporous  $\text{TiO}_2$  or  $\text{ZrO}_2$  as illustrated in Figure 2.5. As previously stated  $R_{BC}$  was found to be mainly independent of the applied bias (with the exception of the high forward bias region), indicating that it does not depend on the Fermi level position. As such taking into account the potential drop due to the series resistance does not change the observed trends. Furthermore the magnitude of the resistance decreased with increasing temperature whilst the magnitude of the corresponding capacitance was found to increase as expected (see Figure 2.5).

In the region of high forward bias the IS parameters are no longer completely independent of the applied potential. While at low temperatures the resistance and capacitance are independent of the applied bias, where the resistance may display a slight decrease, at high temperature the resistance shows a slight increase at high applied potentials whilst a decrease in the capacitance is observed. The exception to this trend is the m $\text{TiO}_2$  with doped spiro-MeOTAD where the resistance at displays a decrease at high forward bias, regardless of the temperature and the capacitance remains independent of applied potential at low temperatures and only at 40°C presents an increase at high forward bias. However note that these changes at high forward bias are relatively small in magnitude.

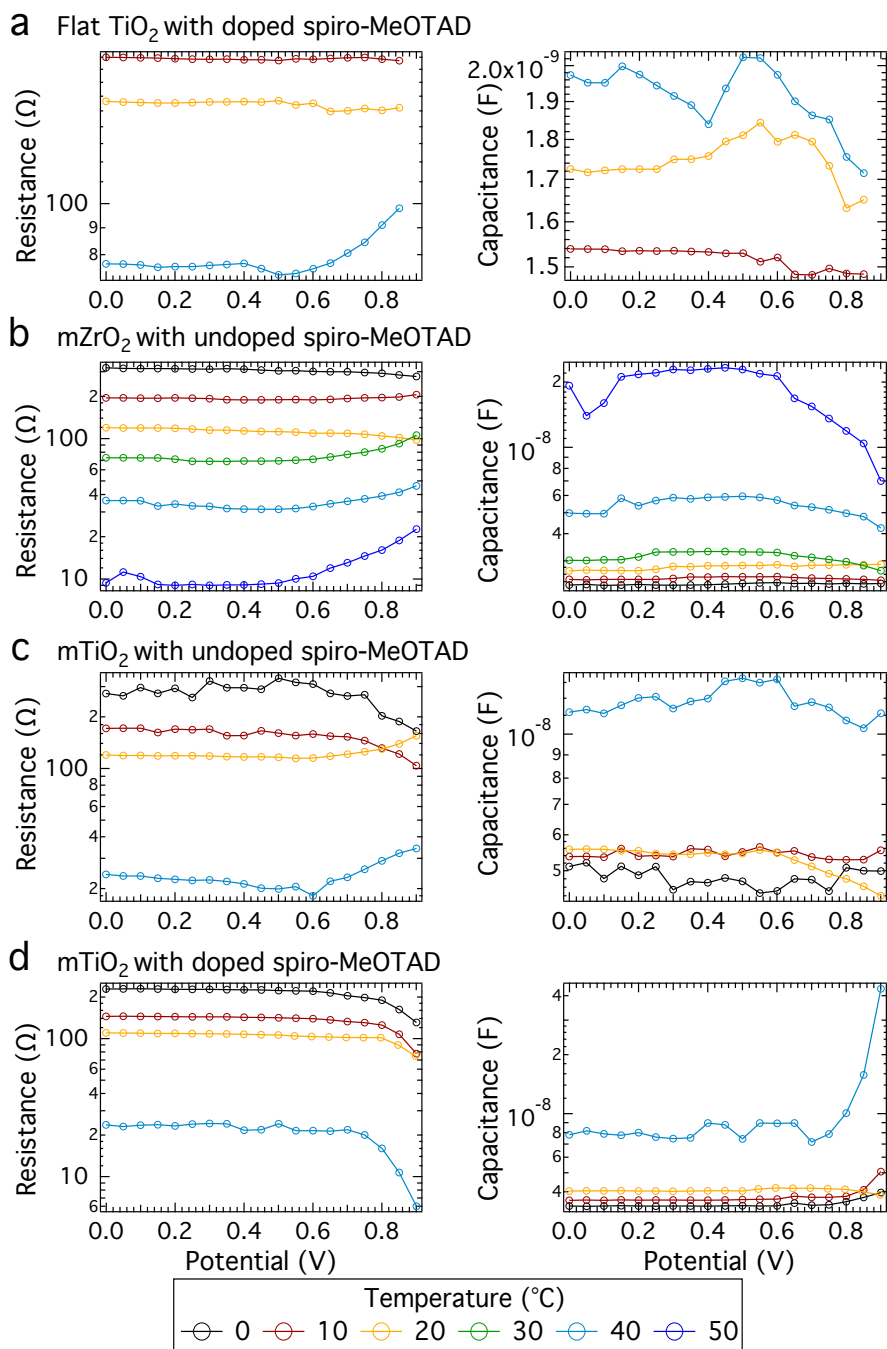
#### 2.3.2 Contribution to Series Resistance by HTM

The second arc, found at intermediate frequency (region II in Figure 2.2 (a)), representing the charge-transport resistance  $R_{HTM}$  and capacitance of the HTM, was found to substantially decrease and even disappear upon chemically *p*-doping the HTM, see Figure 2.2. The resistance corresponding to the hole-transport in spiro-MeOTAD contributes to the total series resistance of the devices, and hence greatly influences the fill factor (*FF*) of ssDSSCs. The decrease in  $R_{HTM}$  upon doping spiro-MeOTAD is a major factor in the observed increase in the *FF* upon doping the HTM [15]. Consequently it was not possible to determine the  $R_{HTM}$  for samples prepared with doped spiro-MeOTAD. In the cases of undoped samples, the magnitude of the resistance was found to remain relatively constant with applied potential, and decrease with increasing temperature, see Figure 2.6. Hence similarly to the case of the charge-transfer

---

<sup>1</sup> The temperature was controlled by placing the samples in a sealed oven in the dark.

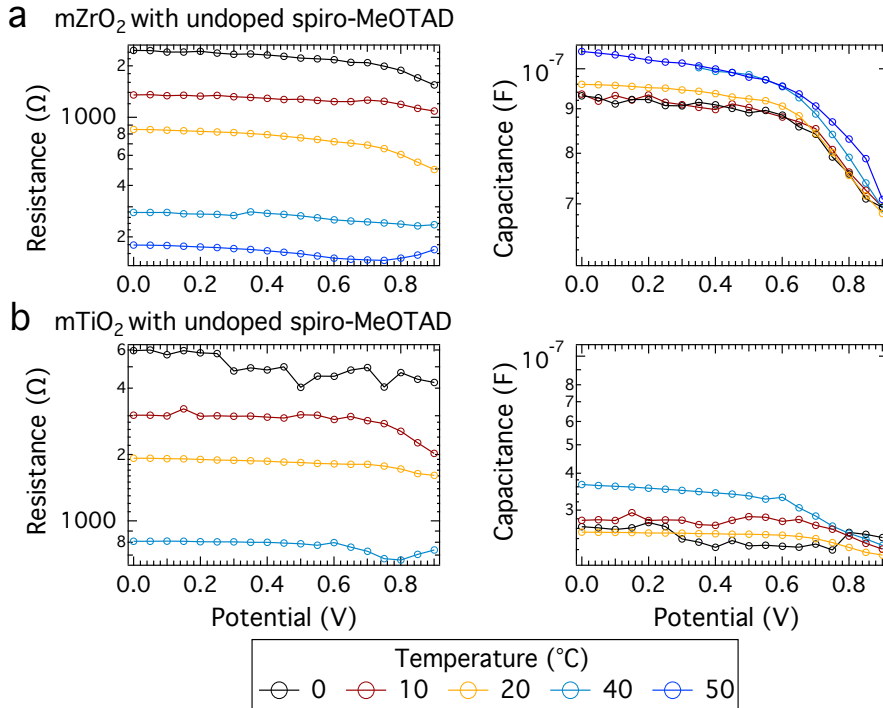
### 2.3. Interpretation of IS Spectra: Temperature Effects



**Figure 2.5.** The charge-transfer resistance and the corresponding capacitance at the BC/HTM interface for the different systems as a function of potential.

resistance at the BC/HTM interface, the observed trends do not change when the ohmic drop is taken into account and the corrected potential is used in place of the applied potential.

The associated capacitance was found to decrease slightly at high potentials (Figure 2.6), this



**Figure 2.6.** The charge-transport resistance,  $R_{\text{HTM}}$  and capacitance of the HTM for systems using mesoporous  $\text{ZrO}_2$  and  $\text{TiO}_2$  as a function of potential.

effect being more pronounced in the case of the mesoporous  $\text{ZrO}_2$  samples compared to the mesoporous  $\text{TiO}_2$ . Previous studies [19, 36] measuring the transport time of ssDSSCs by transient photovoltage and photocurrent decay showed this parameter to increase at high forward bias when conducted under high light intensities. A similar observation is made here, where  $R_{\text{HTM}}$  is seen to increase at high forward bias for measurements at higher temperatures. Whilst not fully understood, this effect appears only when the HTM is already very conductive, either due to increased temperatures or at higher light intensities, suggesting that in these conditions the transport resistance of the HTM increases at increased applied potential.

### 2.3.3 Activation Energy for Hole-Transport in Spiro-MeOTAD

The conductivity  $\kappa$  of materials is determined according to Equation 2.1;

$$\kappa = e\mu n \tag{2.1}$$

where  $e$  is the elementary charge,  $\mu$  is the mobility and  $n$  is the concentration of the charge carriers. Hence to achieve high *PCEs*, a good HTM requires good conductivity to minimize the charge-transport resistance, and high hole mobility to rapidly move the holes away from the sensitized metal oxide surface.

The charge-transport within organic semiconductors such as spiro-MeOTAD has been de-

### 2.3. Interpretation of IS Spectra: Temperature Effects

scribed in terms of the Gaussian disorder model within the Bässler formalism. This model considers that charge-transport occurs *via* hopping through localized states, randomly distributed in space and energy coordinates [69, 70]. The positional Gaussian disorder arises from fluctuations of the mutual orientation of neighbouring molecules or intermolecular distances (i.e. adjacent hopping sites) while the energetic disorder results from fluctuations of the energy levels. The Bässler model proposes an expression (Equation 2.2) that predicts a dependence of the charge-carrier mobility on the on temperature  $T$  and the electric field  $E$ :

$$\mu(T, E) = \mu_0 \exp \left[ - \left( \frac{2\sigma}{3k_B T} \right)^2 \right] \exp \left[ C_0 \sqrt{E} \left( \left( \frac{\sigma}{k_B T} \right)^2 - \Sigma^2 \right) \right] \quad (2.2)$$

where  $\mu_0$  is the mobility prefactor,  $\sigma$  and  $\Sigma$  are parameters describing the degree of energetic and spatial disorder,  $C_0$  is an empirical constant and  $k_B$  is the Boltzmann factor.

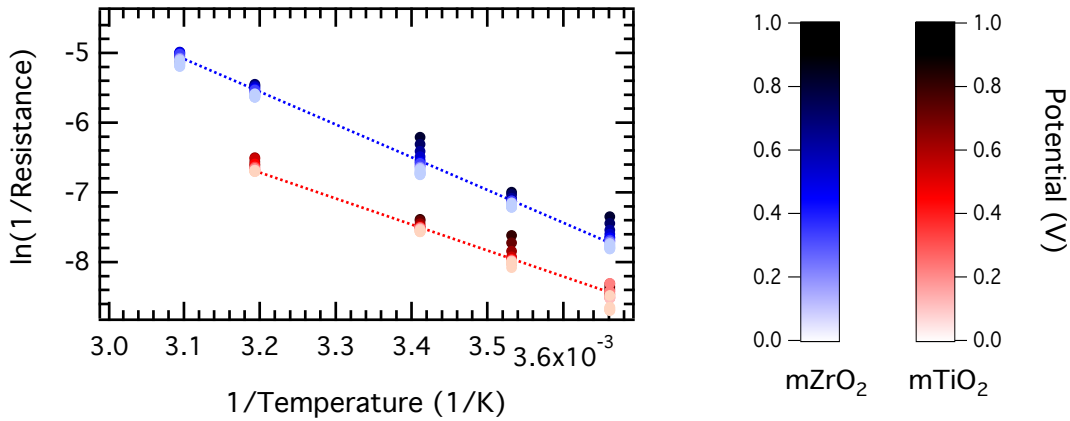
The hole-transport in spiro-linked triarylamine compounds, including spiro-MeOTAD, has been characterized as non-dispersive [70, 71]. For such disordered organic semiconductor systems the charge mobility is only weakly dependent on the electric field [69, 72] and has been treated as field independent [41]. Furthermore in this work the range of the applied potential is very small and hence it is justifiable to assume that for such low fields the conductivity is can be assumed to be approximately constant as has been reported by Li *et al.* [72].

Here the frequency of hole-hopping transport in the HTM is considered to be proportional to its conductivity. Assuming that the concentration of the charge carriers is constant, this frequency of hole-hopping  $k$  is inversely proportional to the charge-transport resistance of the HTM, which was determined by IS above. Hence the activation energy  $E_A$ , for the hole-hopping transport in spiro-MeOTAD can be determined using the Arrhenius equation:

$$k = A \exp \left[ - \frac{E_A}{k_B T} \right] \propto \frac{1}{R_{\text{HTM}}} \quad (2.3)$$

where  $A$  is the pre-exponential factor and  $T$  is the temperature.

In order to gain a better understanding of the transport properties of spiro-MeOTAD within ssDSSCs, the  $R_{\text{HTM}}$  values extracted from the IS measurements were used to produce an Arrhenius plot as shown in Figure 2.7. Both systems consisting of mesoporous  $\text{TiO}_2$  and  $\text{ZrO}_2$  show a clear linear trend between  $1/R_{\text{HTM}}$  and  $1/T$  (see Figure 2.7) indicating that the Arrhenius relationship holds true and allowing  $E_A$  to be determined. Consequently  $0.34 \pm 0.02$  and  $0.40 \pm 0.02$  eV were determined as  $E_A$  for the hole-transport within spiro-MeOTAD for the mesoporous  $\text{TiO}_2$  and  $\text{ZrO}_2$  systems respectively. These are in relatively good agreement with each other further indicating that the measured  $R_{\text{HTM}}$  extracted from the intermediate frequency arc originates from the same component – the HTM. Additionally these values are consistent with the reported value (0.315 eV) obtained by Rana *et al.* [73] through the study of the charge-transport properties of thermally evaporated thin films of spiro-MeOTAD.



**Figure 2.7.** Arrhenius plot using  $R_{\text{HTM}}$  determined from IS for devices using mesoporous  $\text{TiO}_2$  (red) or  $\text{ZrO}_2$  (blue) infiltrated with undoped spiro-MeOTAD. The measurements made at different potentials for each temperature are represented by the color scale.

### 2.3.4 Low Frequency IS Response

Finally the recombination resistance and the corresponding capacitance was determined from the low frequency arc in the IS Nyquist plots – section III in Figure 2.2 (a). The recombination resistance  $R_{\text{ct}}$  is the charge-transfer resistance related to the recombination of electrons at the  $\text{TiO}_2/\text{HTM}$  interface. At low potentials the  $\text{TiO}_2$  is an insulator and hence  $R_{\text{ct}}$  is high. As the applied potential increases, the electron density within the  $\text{TiO}_2$  increases, shifting its Fermi level closer to the lower edge of the conduction band, thus resulting in a decrease in  $R_{\text{ct}}$ . This behavior was observed for the different systems (mesoporous  $\text{ZrO}_2$ , flat and mesoporous  $\text{TiO}_2$ ) in Figure 2.8. Furthermore  $R_{\text{ct}}$  decreased as a function of the applied temperature. This same trend is reflected in the observed increase in the dark current as a function of temperature (Figure 2.8).

Taking into account the voltage drop due to the overall series resistance, a greater correction for samples with undoped HTM is observed since for these samples the  $R_{\text{HTM}}$  contribution to the series resistance is larger. The region of high forward bias presents the largest potential correction due to the higher current passing. This is visible in the change of the slope of the measured dark current in this potential region as shown in Figure 2.8.

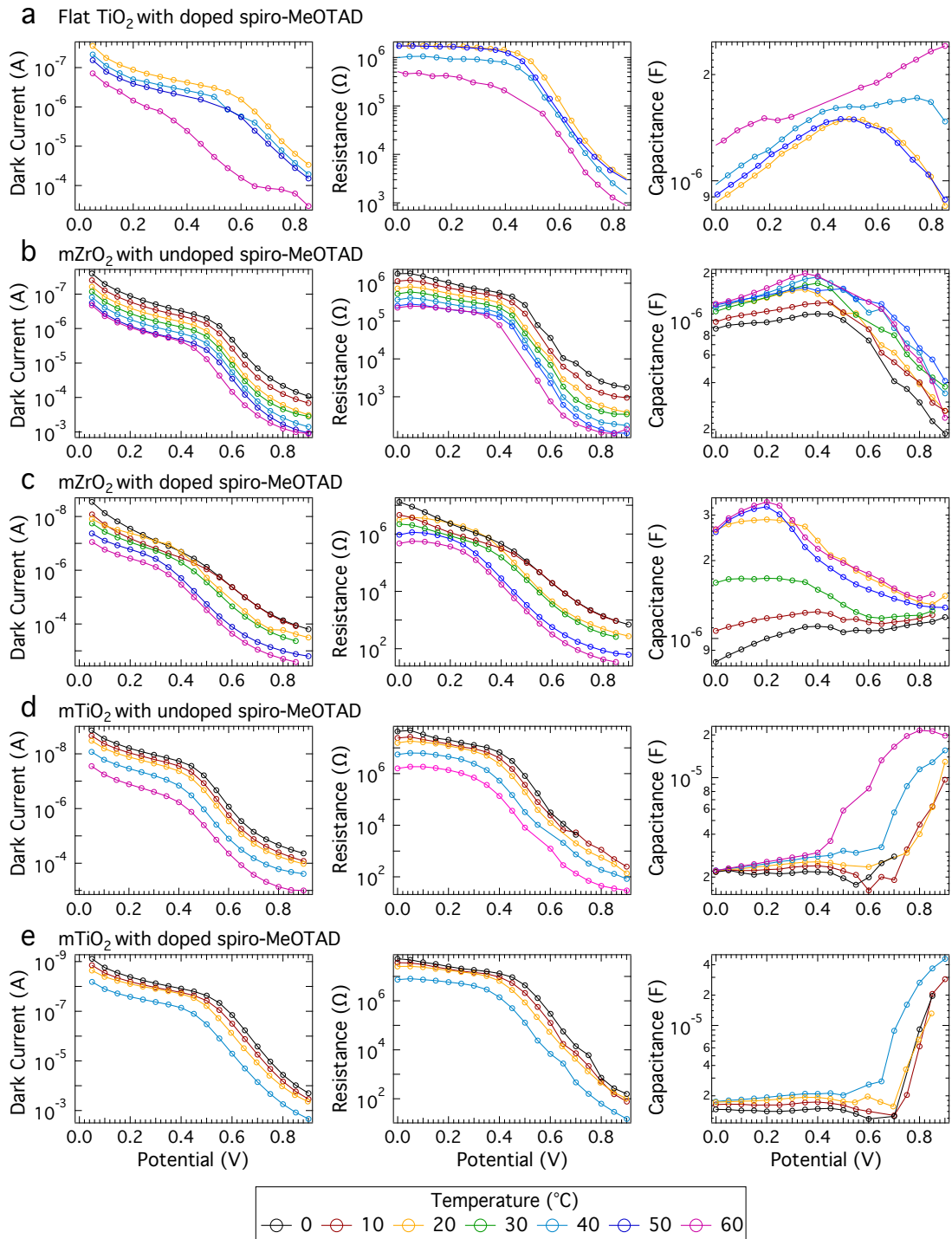
Qualitatively the dark current and  $R_{\text{ct}}$  determined are in good agreement. Quantitatively the recombination current  $I_{\text{ct}}$  of the devices can be calculated from the extracted IS  $R_{\text{ct}}$  parameter according to Equation 2.4;

$$I_{\text{ct}} = \int \frac{1}{R_{\text{ct}}} dV \quad (2.4)$$

Figure 2.9 shows the comparison of the experimentally measured dark current with the calculated current determined from  $R_{\text{ct}}$ . The calculated current coincides excellently with the

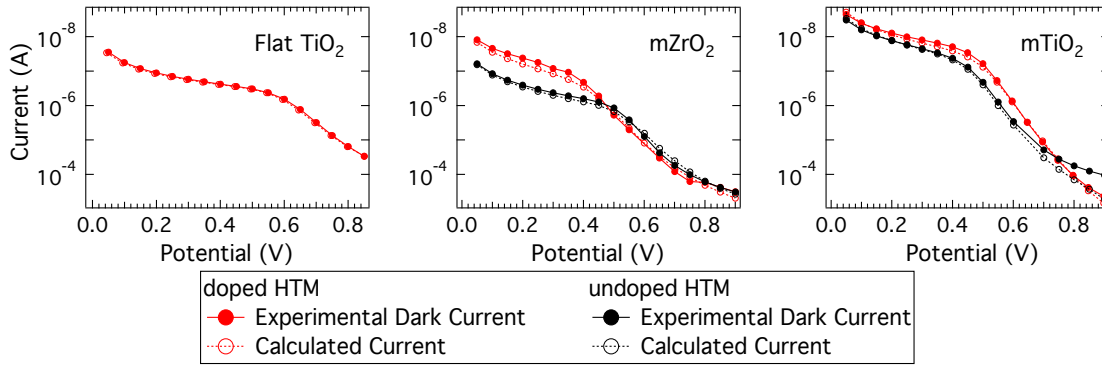


### 2.3. Interpretation of IS Spectra: Temperature Effects



**Figure 2.8.** Dark current measurement, recombination resistance and the corresponding capacitance extracted from IS conducted in the dark for the different systems as a function of potential.

experimentally measured dark current. The small deviations observed, particularly at high forward bias (as visible for the undoped  $\text{mTiO}_2$  samples), correspond to the contribution of



**Figure 2.9.** Dark current measurement (solid circles) and current calculated from  $R_{ct}$  from IS conducted in the dark (open circles) at 20°C for all systems under consideration. The results presented here correspond to undoped (black) and doped (red) spiro-MeOTAD.

the series resistances to the overall current that have not been included in this calculation here.

Doping the spiro-MeOTAD samples resulted in only a small reduction in  $R_{ct}$ . This is further highlighted when the electron lifetime  $\tau_n$  is considered in comparison to the chemical capacitance  $C_\mu$  (see Figure 2.10) which shows only a small difference. This indicates that the electron lifetime, which is calculated from the chemical capacitance and the recombination resistance according to Equation 2.5, and hence the recombination kinetics within the  $TiO_2$  are mainly unaffected by the  $p$ -doping of the spiro-MeOTAD.

$$\tau_n = R_{ct} \times C_\mu \quad (2.5)$$

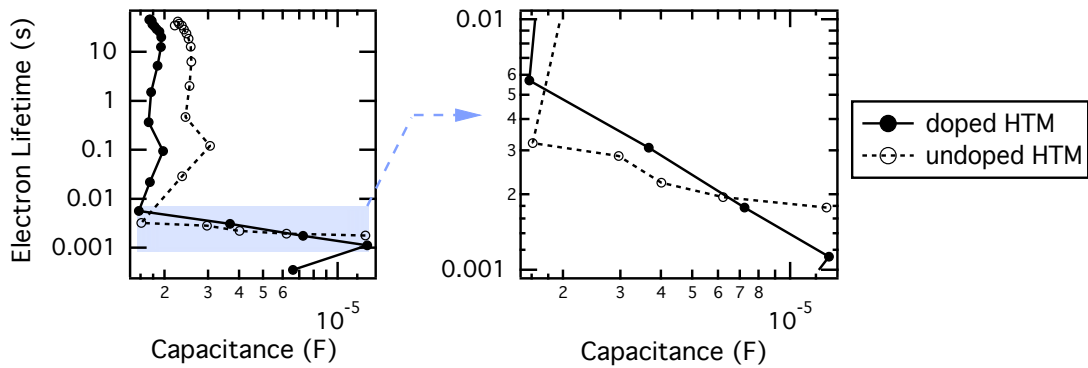
The capacitance associated with this resistance has been interpreted as the chemical capacitance  $C_\mu$  of the nanostructured materials [53] and has been characterized by an exponential dependence on the applied potential bias. This behavior has been observed experimentally for nanostructured semiconductors and DSSCs [61, 74, 75]. The chemical capacitance has been related to the total electron density  $n$  within the semiconductor by,

$$C_\mu = \frac{e^2}{k_B T} n \quad (2.6)$$

where  $e$  is the elementary electron charge. The chemical capacitance is a critical parameter necessary to understand the underlying mechanisms in DSSCs describing the storage of free energy by photogenerated carriers and the resulting production of current and voltage [53].

Considering the case of the mesoporous  $TiO_2$ , the experimentally determined capacitance is found to increase exponentially with potential as expected, displaying a small increase with temperature, see Figure 2.8. Hence this parameter can be interpreted as the chemical capacitance of the nanostructured  $TiO_2$ .  $C_\mu$  is proportional to the density of trap states (DOS)

### 2.3. Interpretation of IS Spectra: Temperature Effects



**Figure 2.10.** Calculated electron lifetime as a function of the chemical capacitance,  $C_\mu$  for devices using mesoporous  $\text{TiO}_2$  infiltrated with doped (solid line) or undoped (dashed line) spiro-MeOTAD. This set of data corresponds to measurements made at  $20^\circ\text{C}$ . Similar behavior was observed for measurements conducted at other temperatures.

according to the following Equation 2.7:

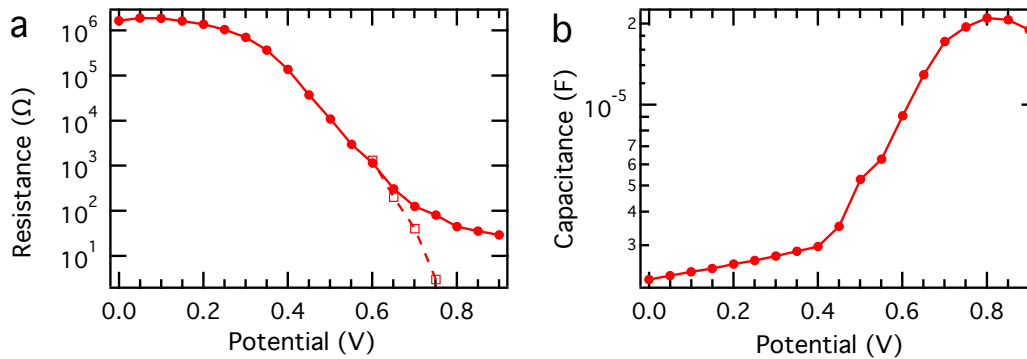
$$\text{DOS} = \frac{1}{e} \frac{C}{d(1-p)} \quad (2.7)$$

where  $d$  is the thickness of the mesoporous  $\text{TiO}_2$  film and  $p$  is its porosity.

In previous studies on liquid DSSCs  $C_\mu$  did not show a dependence on temperature [58]. In contrast a temperature dependence of the chemical capacitance is observed similar to the reported results from O'Regan *et al.* [76] and Wang *et al.* [77]. Thereby the depth of the DOS also depends on the temperature. However this effect is comparatively small in the temperature domain investigated, as visible by the small change in shape of the  $C_\mu$ . According to O'Regan *et al.* [76] the main reason for the change of  $C_\mu$  with temperature is the change in the ionic surrounding of the  $\text{TiO}_2$  at elevated temperatures leading to a displacement of the conduction band edge.

In the case of the  $\text{mZrO}_2$ , the capacitance corresponding to  $R_{\text{ct}}$  was observed to decrease with potential, while it still increased with temperature. At low temperatures samples using flat  $\text{TiO}_2$  showed a similar behavior, where the capacitance displayed a decrease at high potentials. Conversely, at higher temperatures the capacitance demonstrated an increase at high potentials. It is important to note that the change in magnitude of the capacitance as a function of potential for this system is small in comparison to the mesoporous systems.

This conflicting behavior can be attributed to the fact that the capacitance measured here is not the chemical capacitance. The interface between the compact  $\text{TiO}_2$  and HTM may lead to the formation of a  $p$ - $n$  junction which results in an additional capacitance [78, 79]. This is visible in all systems as a small increase followed by a drop in the capacitance at approximately 400 mV. This underlayer capacitance dominates at short-circuit conditions. At high forward bias this type of  $p$ - $n$  junction lets charge flow out, preventing further accumulation of charge and thus



**Figure 2.11.** (a) Recombination,  $R_{ct}$ , (solid circles), transport resistance,  $R_{trans}$ , (dashed open squares) and (b) associated capacitance extracted using the transmission line model. These measurements correspond to a mesoporous  $TiO_2$  sample with undoped spiro-MeOTAD conducted at  $60^\circ C$ .

leading to a decrease in the capacitance. In the case of devices using mesoporous  $TiO_2$ , this underlayer capacitance is visible only at lower temperatures, otherwise it is overlaid by the several orders of magnitude larger chemical capacitance (density of states) of the mesoporous  $TiO_2$ , which increases exponentially as a function of the applied potential.

The transport of electrons within the nanostructured metal-oxide semiconductor in DSSCs has been expressed in terms of the diffusion-recombination transmission line model [61, 62, 80]. The transport resistance  $R_{trans}$  can be determined from the turnover between the diffusion feature, observed as a  $45^\circ$  line at high frequency, to the curvature of the low frequency recombination arc [61]. It has been observed that the intermediate arc, corresponding to the hole-transport in spiro-MeOTAD, merges with the recombination resistance feature at low frequency (region III in Figure 2.2 (a)) for the samples considered here. This suggests that the timescales for these processes are relatively close, consequently frequently partially hiding the straight line feature corresponding to the electron transport.

An example of the electron transport resistance determined using the transmission line model is presented in Figure 2.11. The transmission line is often clearly visible only at one or two potentials and therefore the error associated with  $R_{trans}$  is large. As previously described, section IIIb of the equivalent circuit model in Figure 2.2 (c) was used to fit the low forward bias region when the  $TiO_2$  is not conductive and recombination occurs *via* the compact  $TiO_2$  blocking layer/HTM interface. At high forward bias recombination occurs across the transmission line as shown in section IIIa. In the case of  $ZrO_2$ , the conduction band position is assumed to be sufficiently high that there is no injection of electrons from the spiro-MeOTAD.

### 2.4 Photo- versus Chemical Doping of HTM

To achieve high *PCEs* it is necessary to oxidize the HTM, as spiro-MeOTAD in its intrinsic state has very low conductivity. While there have been reports of the use of various chemical *p*-dopants, several publications of high efficiency ssDSSCs tend to improve the conductivity of the undoped spiro-MeOTAD through the facile oxidation of the material in the presence of molecular oxygen and under illumination – so-called photodoping [6, 19, 26, 42].

As observed in the previous Section 2.3, when the HTM is chemically *p*-doped the intrinsic resistance of the HTM is drastically decreased, reducing the IS response of the HTM to such an extent that it can not be accurately resolved. Here this effect is examined in more detail and compared to the effects resulting from the photodoping process where spiro-MeOTAD is oxidized in the presence of oxygen and light.

In order to reduce the complexity of the system, mZrO<sub>2</sub> is again used in place of mTiO<sub>2</sub> to ensure that the mesoporous film is electronically inactive in the device working mechanisms and hence only acts as a scaffold for the HTM. The devices were prepared in the absence of oxygen under an inert atmosphere and red light<sup>2</sup> and the HTM was doped following two procedures: 1) After fabrication under inert atmosphere the complete devices were exposed to 1 sun illumination in the presence of oxygen (dry conditions) for varying amounts of time and 2) Increasing aliquots of a cobalt complex *p*-type dopant<sup>3</sup> were added to the HTM solution in the preparation process to give between 0 to 2.2%<sup>4</sup>. Only very small doping concentrations are necessary to increase the conductivity of spiro-MeOTAD sufficiently as has been reported by the use of only 0.16% of an antimony salt as dopant [41]. For both doping procedures considered here, the assembled devices were sealed after the completion of fabrication and doping procedures.

#### 2.4.1 Back Contact and Spiro-MeOTAD

The complete devices were characterized by IS measurements conducted in the dark and fitted according to the model developed in the previous Section 2.3. Figure 2.12 presents the resistance and associated capacitance extracted from fitting the high frequency region of the IS measurements, corresponding to the interface between the BC and the HTM. Both the resistance and the capacitance are independent of the applied potential and the trends observed as a function of the doping level in the HTM are similar regardless of the doping procedure applied.

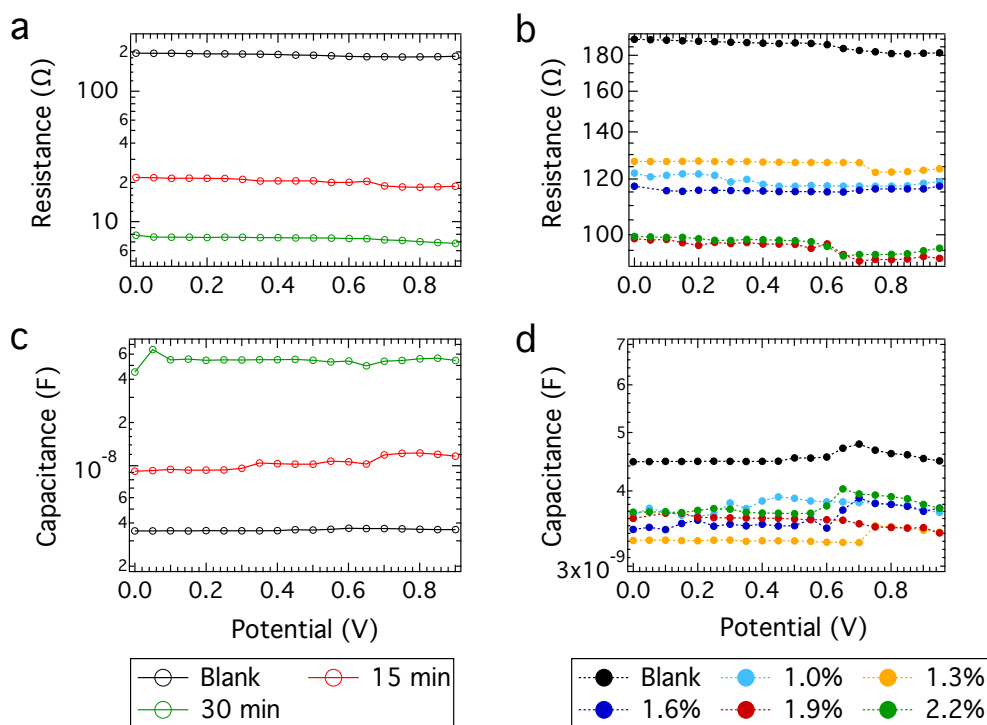
As the doping level of the HTM is increased (either by increased exposure to light and oxygen or by addition of larger amounts of chemical dopant) the resistance is observed to decrease in magnitude as seen in Figure 2.12 (a)–(b). In the case of photodoping the capacitance is

---

<sup>2</sup> To minimize the amount of light exposure. Red light was provided by an array of LEDs.

<sup>3</sup> Code name FK102 – cf. Figure 1.7 Chapter 1.

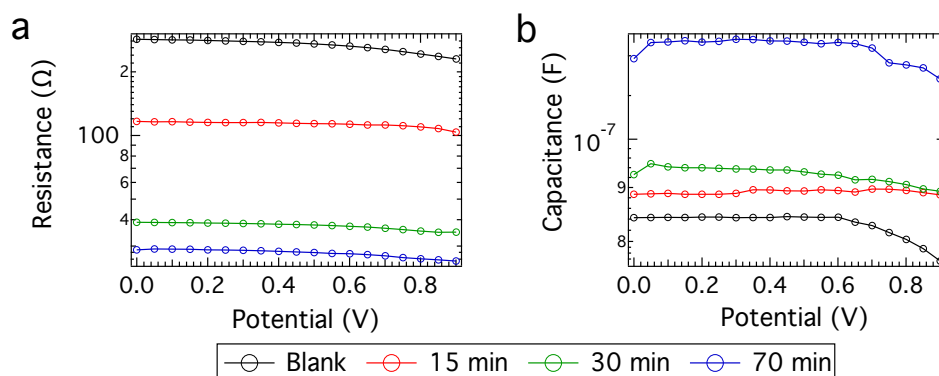
<sup>4</sup> Percentile of molar ratio between dopant and spiro-MeOTAD.



**Figure 2.12.** (a)–(b) The charge-transfer resistance and the (c)–(d) corresponding capacitance at the BC/HTM interface devices exposed to controlled photo- or chemical doping.

observed to increase with increased exposure, while the magnitude remains relatively similar for all chemically doped devices (Figure 2.12 (d)) lying between  $3.3$  and  $4.8 \times 10^{-9}$  F for the entire potential range. This implies an inherent difference between the effect of the doping procedures. When the system is photodoped, it is clear that the interface between the BC and the HTM is much more affected, resulting in a strong dependence of the capacitance on the time of exposure to oxygen and light. On the other hand when the system is chemically doped, the capacitance of this interface is relatively insensible to the level of chemical dopant added. From this it is possible to conclude that there is a considerable change in the electronic environment at this interface when the system is exposed to illumination in the presence of oxygen, which does not take place in the same manner when the HTM is chemically *p*-doped.

Similarly while the observed trends in the resistance are identical for the different doping methods, their associated magnitudes interestingly show significant difference. In both cases the blank devices which have not been exposed to oxygen or light and contain no chemical dopant, display similar resistances between  $180$  and  $195 \Omega$ . This value is decreased to  $7$ – $8 \Omega$  after  $30$  minutes of photodoping and becomes too small to resolve upon further exposure to oxygen and light. In the case of the devices where the HTM has been chemically doped, this same resistance decreases from approximately  $185 \Omega$  (blank device) to  $88$ – $90 \Omega$  when  $2.2\%$  of dopant has been added to the HTM solution. This resistance is more than an order of magnitude larger relative to the devices that have been photodoped.



**Figure 2.13.** (a) The charge-transfer resistance,  $R_{\text{HTM}}$  and the (b) capacitance of the HTM for devices with different levels of photodoping.

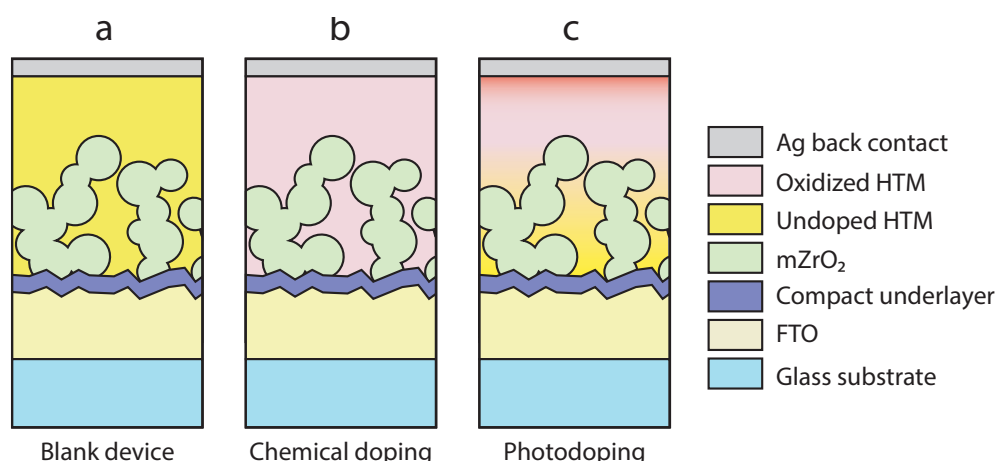
The back contact used here was silver which has been suggested to lead to the formation of a silver oxide interlayer between the pure Ag back contact and the HTM when exposed to oxygen [52]. This may act as an efficient hole collection layer due to the  $p$ -type conductivity of the silver oxide semiconductor, resulting in the observed decrease in the associated charge-transfer resistance at this interface for photodoped devices exposed to oxygen and light. Similarly time-evolution measurements of ssDSSCs have been reported to suggest that the exposure to oxygen improves the ohmic contact between undoped spiro-MeOTAD and the silver back contact [81]. The improved contact between the HTM and the back contact would result in effectively reducing the charge-transfer resistance at this interface as seen here.

As was observed in the previous section, when the HTM is chemically  $p$ -doped, its associated resistance  $R_{\text{HTM}}$  is reduced to such an extent that it is not possible to accurately resolve it in the Nyquist plots (cf. Figure 2.2). This is not the case when photodoping is used to oxidize the HTM. The charge-transport resistance of the HTM  $R_{\text{HTM}}$  is observed to decrease from 230–290  $\Omega$  (blank device) to 25–28  $\Omega$  after 70 minutes exposure to oxygen and light (Figure 2.13). Similar to the capacitance associated with the BC/HTM interface the capacitance associated with the HTM is observed to increase with longer photodoping exposure.

#### 2.4.2 Distribution of Oxidized Spiro-MeOTAD

The differences observed in the magnitudes of the resistances associated with the individual components and interfaces of the devices as a result of the two HTM doping procedures provide valuable insight to their working mechanisms. The HTM is deposited on the mesoporous scaffold by spin-coating, leading to the infiltration of the material into the pores and the formation of a dense overlayer on top of the mesoporous layer as illustrated in Figure 2.14 (a). The two doping methods examined here will most likely result in different distribution and concentration of oxidized spiro-MeOTAD within the active layer.

The typical procedure to chemically dope the HTM is the addition of the dopant to the HTM



**Figure 2.14.** Schematic illustration of device configuration consisting of (a) a blank device with undoped spiro-MeOTAD, (b) a photodoped device (oxidized spiro concentration gradient from red to yellow) and (c) a device with spiro-MeOTAD chemically doped using a cobalt(III) complex. These representations correspond to the situation when no sensitizer is present.

solution prior to deposition. As such it is assumed that this leads to a uniform distribution of oxidized HTM throughout the deposited HTM layer as depicted in Figure 2.14 (b). This is supported by the observed color change of the HTM solution upon addition of the chemical dopant from pale yellow to deep red as the spiro-MeOTAD<sup>+</sup> species is formed. As a result the conductivity of the HTM is inferred to increase homogeneously throughout the deposited film, which is reflected in the considerable decrease of  $R_{\text{HTM}}$ . This resistance rapidly becomes indiscernible at low doping levels indicating that the HTM is sufficiently oxidized and highlights the importance of increasing the conductivity of the bulk material. It is important to note here that it is unlikely that the doping level of the solution after addition of the chemical dopant is the same in the HTM film formed after processing within the device.

When the samples are exposed to illumination in the presence of oxygen, the distribution of the oxidized spiro-MeOTAD is not as straightforward. Considering first the simplified case when the HTM is infiltrated into the electronically inactive mZrO<sub>2</sub> scaffold without the presence of any adsorbed sensitizer. In this situation it is probable that the doping of the HTM takes place mainly at the surface of the HTM which is exposed to air. Due to the presence of the dense HTM overlayer, it is possible to assume that the material deep in the pores does not undergo the same extent of oxidation, thus resulting in a distribution profile, where the concentration of oxidized HTM is highest at the interface to the BC (Figure 2.14 (c)).

Including a molecular sensitizer in the system significantly increases the complexity as in this case light is absorbed by both the HTM and the dye species. Consequently in addition to the direct photooxidation of the HTM by molecular oxygen, the photoexcited dye molecules are believed to participate in the photodoping process. This is expected to result in changes in the distribution profile of the oxidized HTM depicted in Figure 2.14 (c) which most probably depend on the properties of the sensitizer and its interaction with the HTM.



### 2.4.3 Low Frequency IS Response

The dark current measurements, recombination resistance and associated capacitance extracted from the IS conducted in the dark for the devices under investigation are presented in Figure 2.15. Considering the devices exposed to photodoping, the dark current is observed to decrease for low doping levels (15 minutes exposure) relative to the blank device while it increases for high doping levels (30–70 min). Furthermore the dark current measured for highly doped devices was similar. No such clear trend is observable for the chemically doped devices. However in the high forward bias region, with the exception of the devices containing 1.6% dopant, the dark current is relatively similar for all doping levels.

The trends observed in the dark current measurements are clearly reflected in the extracted recombination resistance (see Figure 2.15 (c)–(d)). The associated capacitance displayed in Figure 2.15 (e)–(f), show the same decrease at high forward bias as observed for similar devices utilizing mZrO<sub>2</sub> presented in Section 2.3.4 which has been attributed to the underlayer capacitance. This decrease in capacitance at high forward bias is greater for low doping levels. Samples with higher doping levels and thus increased conductivity display capacitances that are relatively independent of the applied bias, showing only a small peak at approximately 400–600 mV.

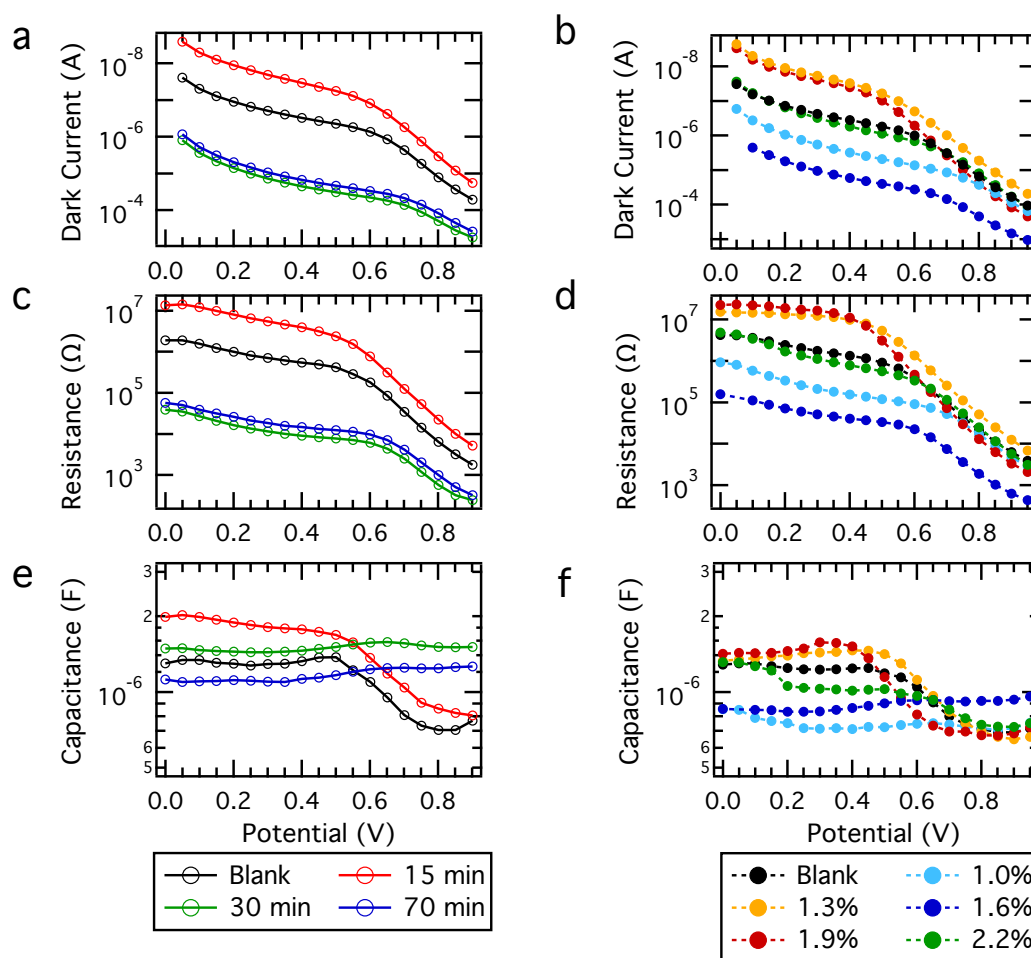
### 2.4.4 Photovoltaic Performance

In order to correlate the observed trends in the impedance parameters with the photovoltaic performance, ssDSSCs were fabricated using the D- $\pi$ -A organic dye Y123<sup>5</sup> as sensitizer and mTiO<sub>2</sub>. The three extreme cases are presented here; 1) a blank device where the spiro-MeOTAD has not been chemically *p*-doped or exposed to controlled photodoping, 2) a device which has been exposed to 1 sun illumination in the presence of dry air for 15 minutes prior to sealing and 3) a device where the HTM solution was chemically *p*-doped through the addition of 1.5% cobalt(III) complex. The photovoltaic performance measured under simulated AM1.5G solar irradiance (10 and 100 mW cm<sup>-2</sup> light intensity) is presented in Figure 2.16 with the relevant parameters summarized in Table 2.1.

The *J*-*V* behavior of the devices demonstrate a clear improvement in the *PCE* when the HTM is doped in comparison to the blank device. The 'blank' device displays a very poor *FF* arising from a large series resistance, as evident in the shallow slope of the *J*-*V* curve. These are attributed to the high series resistance contributions from the unoxidized HTM and the poor contact between the BC and HTM.

The IS measurements revealed the reduction in the charge-transport resistance of the spiro-MeOTAD in addition to improving the ohmic contact at the BC/HTM interface when the HTM is doped. Regardless of the doping method used, the reduction of these resistances manifest as an improvement in the photovoltaic performance. In particular the *FF* is seen to improve

<sup>5</sup> cf. Section 3.3 Chapter 3 for molecular structure.



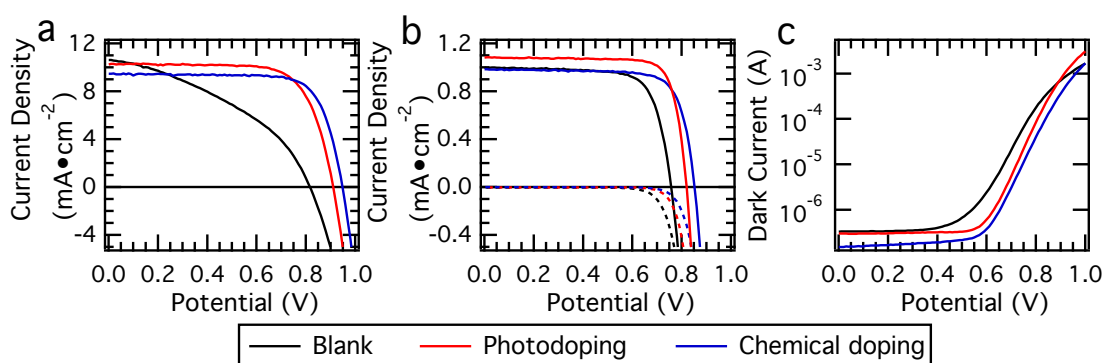
**Figure 2.15.** (a)–(b) Dark current measurements, (c)–(d) recombination resistance and the (e)–(f) corresponding capacitance for devices exposed to controlled photo- or chemical doping.

from 0.4 for a blank device to over 0.7 for both cases when the HTM is doped. Moreover the poor  $FF$  of the blank device is light dependent, displaying a  $FF$  of 0.73 at a lower light intensity of  $10 \text{ mW cm}^{-2}$  (Figure 2.16 (b)) indicating the presence of a photoshunt limiting the photovoltaic performance.

The  $PCE$  of the doped devices is found to be similar for the two different doping techniques (6.74 and 6.77% for photo- and chemical doping respectively). Nevertheless small differences in the individual photovoltaic characteristics are observed. Photodoped devices generally display slightly higher  $J_{SC}$  while chemical doping leads to slightly higher  $V_{OC}$ . This is attributed to a lower Fermi level for the spiro-MeOTAD when the  $p$ -dopant is added, thus allowing higher  $V_{OC}$  to be achieved. The observed reduction in  $J_{SC}$  when the HTM is chemically doped is most likely due to the parasitic light absorption of the oxidized spiro-MeOTAD species at 520 nm, thus acting as a filter, reducing the amount of light harvested by the molecular sensitizer.

**Table 2.1.** Photovoltaic parameters extracted from  $J$ - $V$  measurements of ssDSSC devices under simulated AM1.5G solar irradiance at 10 and 100  $\text{mW cm}^{-2}$  intensity.

Dye	Sun Intensity ( $\text{mW cm}^{-2}$ )	$V_{OC}$ (mV)	$J_{SC}$ ( $\text{mA cm}^{-2}$ )	$FF$	$PCE$ (%)
No doping	10	757	0.94	0.73	5.55
	100	816	10.6	0.40	3.45
Photodoping	10	819	1.00	0.80	7.05
	100	910	10.0	0.72	6.74
Chemical doping	10	851	0.93	0.77	6.42
	100	948	9.4	0.76	6.77

**Figure 2.16.**  $J$ - $V$  characteristics measured under simulated AM1.5G solar irradiance with an intensity of (a) 100  $\text{mW cm}^{-2}$ , (b) 10  $\text{mW cm}^{-2}$  and in the dark. (c) Logarithmic representation of the dark current measurements. All devices were masked to achieve an illuminated active area of  $0.2025 \text{ cm}^{-2}$ .

Finally the higher  $V_{OC}$  is accompanied by a higher  $FF$  (0.76 relative to 0.72 for the photodoped procedure).

## 2.5 Conclusions

This chapter examines the working device mechanisms of ssDSSCs employing spiro-MeOTAD as HTM. Using IS the transport properties of the HTM were investigated in addition to the role of doping the HTM wherein the effect of two procedures, photo- *versus* chemical doping, on the IS response and photovoltaic performance are compared. Particular emphasis was placed upon understanding the transport properties of the HTM within such devices and the role of doping the organic semiconductor.

### 2.5.1 Temperature Dependence of Transport Properties

The charge-transport resistance of spiro-MeOTAD was found to decrease significantly upon chemically  $p$ -doping the material. Using the Arrhenius relationship a value for the activa-

tion energy corresponding to the hole-hopping transport in undoped spiro-MeOTAD was determined. These were found to be in good agreement with values found in literature, thus demonstrating the validity of the chosen model used to fit the IS data for these types of systems.

The charge-transport resistance of the HTM  $R_{\text{HTM}}$  contributes to the overall series resistance of the devices and consequently to their fill factor. Gaining further understanding of the transport properties of the HTM and methods of its characterization allows more targeted approaches to improve device performance of such ssDSSCs. IS analysis provides a valuable tool with which the properties of individual components of ssDSSCs and their impact on the photovoltaic performance can be investigated. In order to isolate the transport properties of spiro-MeOTAD as a HTM in ssDSSCs, the analyzed devices did not contain any sensitizer.

The choice of mesoporous  $\text{ZrO}_2$  as a scaffold for the HTM further allowed the interface between the compact  $\text{TiO}_2$  underlayer and the HTM to be scrutinized in a setup identical to nearly working device conditions employing a mesoporous structure. The overall chemical capacitance of the devices was found to show a small increase at approximately 0.4 V originating from the interface between the compact  $\text{TiO}_2$  underlayer and the HTM. This is further confirmed by similar behavior observed for the devices utilizing flat  $\text{TiO}_2$ . These findings suggest the formation of a  $p$ - $n$  junction between the compact  $\text{TiO}_2$  underlayer and the HTM which contributes to the overall device capacitance but is frequently masked by the exponential increase in the chemical capacitance arising from the DOS of the mesoporous  $\text{TiO}_2$  in convention working ssDSSCs.

### 2.5.2 Photo- versus Chemical Doping

Finally the technique of chemically doping the HTM was compared to the method of photodoping the HTM by oxidation in the presence of oxygen and light. The methods of doping the HTM demonstrate similar effects on decreasing the resistance of the HTM through the formation of oxidized spiro-MeOTAD species. However this effect is enhanced significantly when a chemical dopant is employed as this most likely leads to a relatively uniform distribution of oxidized material throughout the film, increasing the conductivity of the bulk HTM and thus decreasing its contribution to the net series resistance. When the HTM is photodoped, the exposure to oxygen and light is assumed to lead to the formation of the oxidized spiro-MeOTAD species mainly at the BC/HTM interface. Consequently while the bulk resistance is not as greatly reduced as in the case of chemical doping, the exposure to oxygen improves the ohmic contact between the BC and the HTM, leading to a reduction in the charge-transfer resistance at this interface. This is further reduced by the possible formation of a silver oxide layer.

Furthermore the effect of the doping methods on the photovoltaic performance was investigated. High *PCEs* were achieved for both procedures, stemming mainly from an improvement in the *FF* resulting from overall reduction in series resistance of the system. This demonstrates that photodoping can successfully be implemented to achieve high *PCEs*, however this technique is susceptible to changes in the atmospheric conditions and thus may lead to

problems with the reproducibility and stability of the devices. Moreover the overall doping level of the HTM is unknown following this procedure. Chemically *p*-doping the organic HTM has been found to allow better control over the conductivity in the HTM, improving the reproducibility of the photovoltaic results and the stability. The role of this chemical *p*-doping of spiro-MeOTAD using this cobalt(III) complex has been studied more extensively elsewhere [15].

### 2.5.3 Perspectives

This chapter probed the behavior of the organic semiconductor spiro-MeOTAD used as HTM in ssDSSCs by IS, establishing a working model that can be applied to such systems. Furthermore the IS analysis revealed subtle differences between the doping procedures, thus providing valuable insight into the working mechanism of ssDSSCs employing spiro-MeOTAD as a HTM and its doping requirements.

The investigations conducted within this chapter mostly considered the simplified system without any sensitizer. However as outlined, the process of photodoping is believed to not be insensible to the presence of a molecular light harvesting species. Future work should elucidate the possible role of the sensitizing species on the doping mechanism of the HTM and its impact on the efficiency of the process.

The following chapters will examine the role and effect of different sensitizing systems on the IS response of solid-state mesoscopic solar cells and correlate the results with the measured photovoltaic performance.



# 3 Molecular Sensitization for Solid-State Solar Cells

*This chapter is based on the following published works:*

*Shi et al. Angewandte Chemie, 2011, vol. 123, 6749–6751;*

*Dualeh et al. Applied Physics Letters, 2012, vol. 100, 173512;*

*Dualeh et al. Journal of Physical Chemistry C, 2012, vol. 116, 1572–1578;*

*Dualeh et al. Advanced Energy Materials, 2013, vol. 3, 496–504.*

## 3.1 Introduction

Since the pioneering report in 1991 [2], dye-sensitized solar cells (DSSCs) have been the focus of extensive research as an attractive alternative in the efficient generation of low-cost power from solar energy. Recently, power conversion efficiencies (*PCEs*) as high as 12.3% have been reported using a liquid cobalt(II/III)-based redox electrolyte and a porphyrin sensitizer [3]. In solid-state dye-sensitized solar cells, the liquid electrolyte is replaced by a solid hole-transport material (HTM) to overcome the leakage problems associated with volatile solvents and corrosive electrolytes. The aim is to improve the longevity and stability of the devices while offering the advantage of large-scale processability. Despite the many different HTMs reported [4, 34, 82–84], the amorphous organic semiconductor spiro-MeOTAD [14] remains the material of choice to achieve desirable, high *PCEs* [15, 19]. In combination with an organic donor- $\pi$  bridge-acceptor dye (coded Y123) and spiro-MeOTAD as HTM, *PCEs* of 7.2% were reported for ssDSSCs [15].

A major drawback which limits the device performance is the short electron diffusion length and the poor pore-filling of the mesoporous TiO<sub>2</sub> layer with the HTM [34]. Consequently, TiO<sub>2</sub> thicknesses are restricted to around 2–3  $\mu\text{m}$ . To overcome the limitation imposed by the thin titania layer and achieve sufficient light absorption for high *PCEs*, sensitizers with high molar extinction coefficients and broad absorption over a wide range of wavelengths are of great interest [20].

D- $\pi$ -A sensitizers consists of individual organic moieties that can be engineered and adapted

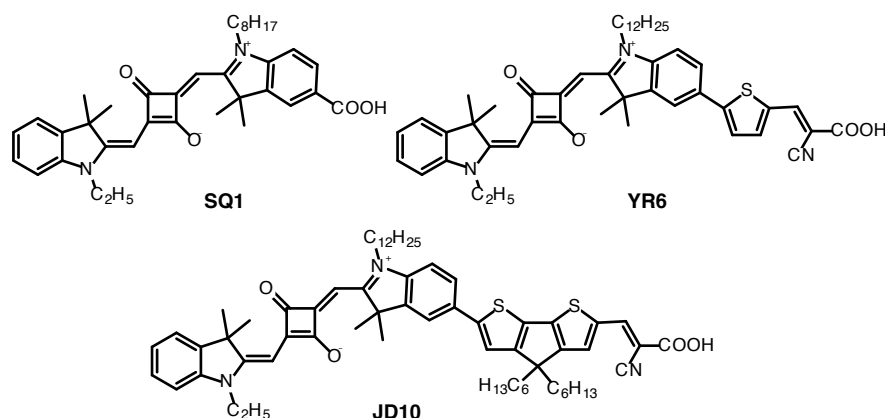


Figure 3.1. Molecular structures of squaraine-based sensitizers

changing the physical and chemical properties of the species. They are designed such that following light absorption an intramolecular charge-transfer state is created by the transfer of electron density from the HOMO, which is dominantly located on the donor unit, to the LUMO, mainly localized on the acceptor unit. Thus the electron flow is vectorial from the light harvesting donor moiety to the surface of the semiconductor *via* the acceptor moiety which typically is also the anchoring group. To further facilitate this electron flow, a strong conjugation should exist across the entire structure and there should be good electronic coupling between the LUMO of the dye and the CB of the TiO<sub>2</sub> semiconductor surface.

Ideally the adsorption of the sensitizer on the mesoporous metal oxide semiconductor should result in a monolayer of neatly aligned dye molecules. In reality the detrimental formation of aggregates takes place on the surface and dye molecules are not uniformly aligned. The individual functional components of dyes are engineered taking into account the necessary criteria for their application as sensitizers in DSSCs, resulting in vast numbers of different dyes being reported.

This chapter explores several different classes of molecular sensitizers and examines their influence on the photovoltaic performance in ssDSSCs using spiro-MeOTAD as HTM. The physical and chemical properties of the dyes are subsequently correlated with the investigated device mechanisms.

### 3.2 Squaraine Sensitizers: Near-Infrared Light Absorption

To date, the most successful sensitizers for ssDSSCs have fulfilled the necessary requirement of high molar absorptivity, but in general light absorption has been restricted to the visible region (< 600 nm). As such, sensitizers with increased light harvesting in the near-infrared (NIR) are of great interest in achieving the ideal panchromatic light-absorber. Squaraine-based sensitizers [85–87] are thus good candidates due to their characteristic strong absorption in the long-wavelength visible and NIR region of the spectrum. The unsymmet-



## 3.2. Squaraine Sensitizers: Near-Infrared Light Absorption

rical squaraine dye 5-carboxy-2-[[3[(1,3-dihydro-3,3-dimethyl-1-ethyl-2*H*-indol-2-ylidene)-methyl]-2-hydroxy-4-oxo-2-cyclobuten-1-ylidene]methyl]-3,3-trimethyl-1-octyl-3*H*-indolium was developed – code named SQ1, the molecular structure of which is presented in Figure 3.1. In order to increase the *PCEs* when employed as sensitizer in DSSCs, the physical and chemical properties of SQ1 were tuned by further molecular engineering. The targeted modifications included a bathochromic shift of the absorption maximum to longer wavelengths, increasing the molar extinction coefficient and the formation of a narrower optical bandgap to improve the photon harvesting. Furthermore new structures were developed to increase the electronic coupling between the excited state of the dye and the TiO<sub>2</sub> CB and thus electron injection, reducing the non-radiative recombination losses.

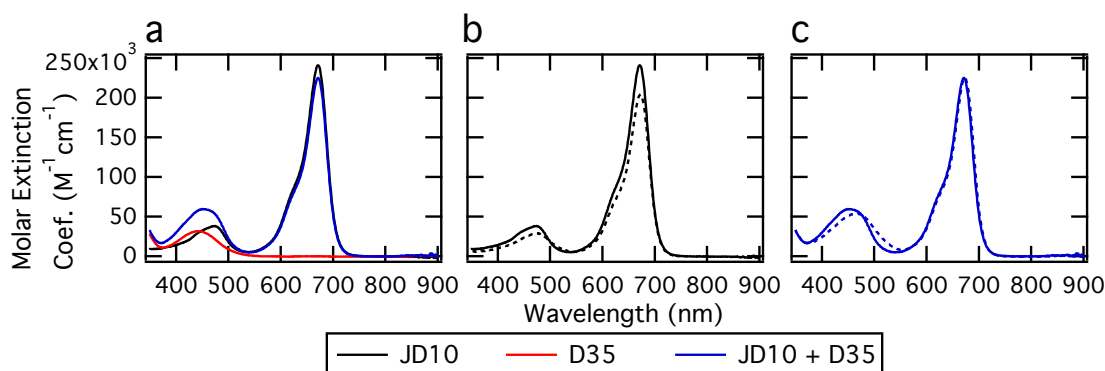
As a result of these molecular optimizations, the molecular sensitizers coded YR6 and JD10 (see Figure 3.1) were developed. In this section the photovoltaic performance of these sensitizers in ssDSSCs is investigated and correlated with their properties and behavior as molecular sensitizers [88].

### 3.2.1 Optical Characterization of Squaraine Sensitizers

The squaraine dye SQ1 has a narrow, intense absorption band at 647 nm with a corresponding molar extinction coefficient  $\epsilon$  of 292 000 M<sup>-1</sup> cm<sup>-1</sup> [85]. This absorption maximum is red-shifted for the subsequently designed dyes YR6 and JD10 due to the extended  $\pi$ -system of the molecular structures. Further molecular engineering increased the light absorption in the visible spectrum range between 400 and 550 nm in which SQ1 displays no absorption. JD10 was designed based on the record efficient squaraine dye YR6, replacing the thiophene unit by a di-*n*-hexyl substituted cyclopentylidithiophene (CPDT) bridge to aid in absorbing in the visible part of the spectrum and in reducing dye aggregation [86]. The solution absorption spectrum of JD10 shows a strong maximum at 672 nm with  $\epsilon = 250\,000$  M<sup>-1</sup> cm<sup>-1</sup> (see Figure 3.2). In addition, the ultraviolet-visible (UV-vis) absorption spectrum displays a high-energy absorbance with a higher molar extinction coefficient when compared to the analogous squaraine sensitizer YR6 [86]. The increased absorbance strength at 474 nm has been attributed to the inclusion of the CPDT bridge [89].

#### 3.2.1.1 Dye Aggregation

With regard to DSSC devices, the dye properties on sensitized TiO<sub>2</sub> films are of greater importance to the photovoltaic performance than the dye properties measured in solution. As such, the optical density of JD10 on 2  $\mu$ m TiO<sub>2</sub>-sensitized films was determined (Figure 3.3). As previously noted, a secondary prominent peak near 620 nm appears upon adsorption of the dye onto the mesoporous metal oxide [87, 89]. This characteristic development of a higher energy charge-transfer band with respect to the maximum absorbance is often attributed to the formation of undesirable H-aggregates [7, 85, 87]. The high-energy absorbance peak resulting from aggregation decreases in intensity upon addition of the deaggregating agent



**Figure 3.2.** UV-Vis spectra of (a) JD10, D35 and a 1:1 molar mixture of JD10:D35 solutions in ethanol. Effect of CDCA addition (dashed) on absorption spectra of (b) JD10 and (c) 1:1 molar mixture of JD10:D35 solution in ethanol.

chenodeoxycholic acid (CDCA)<sup>1</sup> [7, 86]. Furthermore, the addition of CDCA to the dye solution prior to the adsorption onto the mesoporous film leads to a narrowing of the absorption spectra peaks as observed in Figure 3.3 (a). This deaggregating agent has no significant effect on the absorption spectra of the dye in solution (Figure 3.2 (b)–(c)).

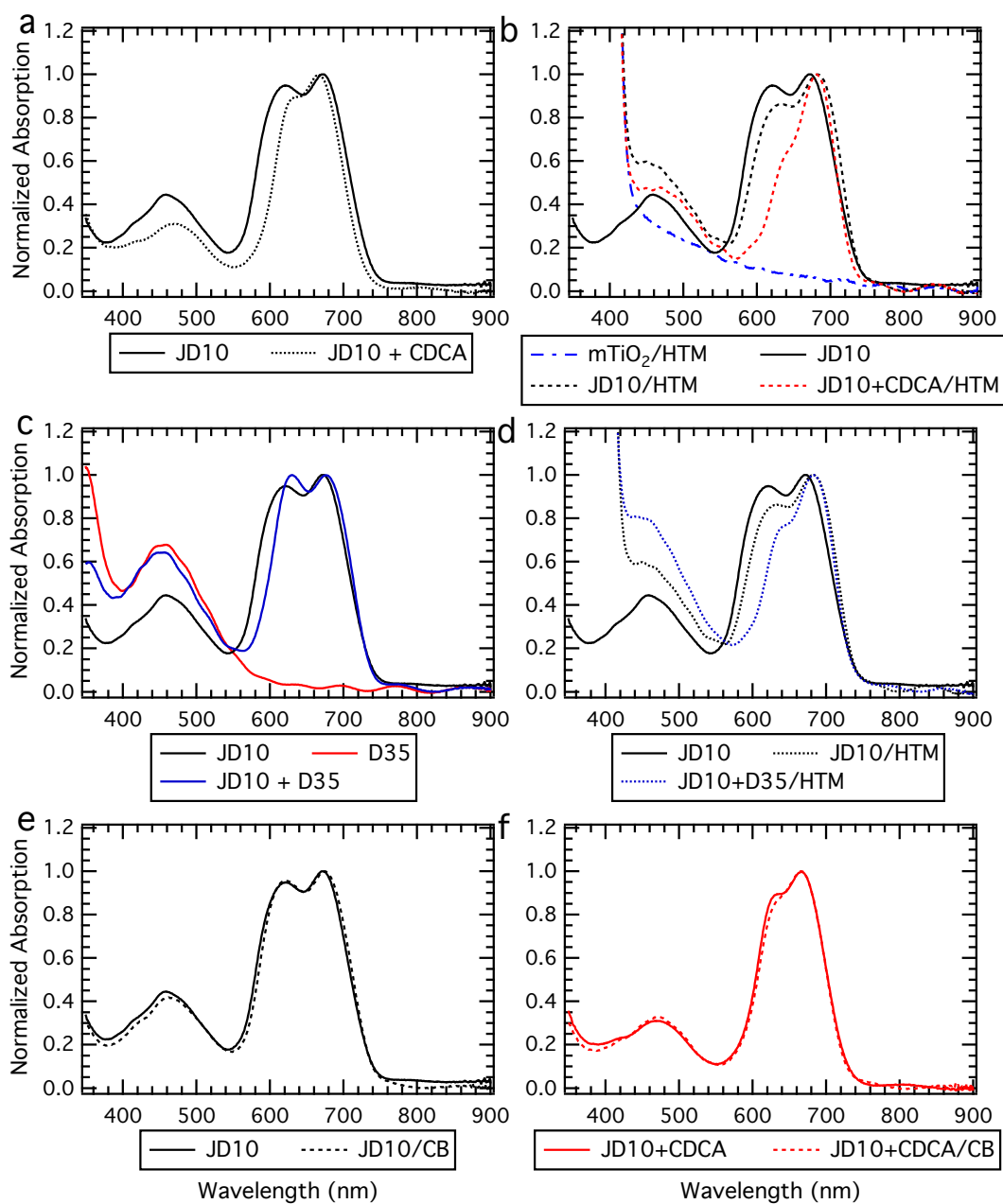
Aggregation is a common phenomenon associated with squaraine dyes and influences the device performance. In addition to accelerating the rate of electron-hole recombination, the formation of dye aggregates results in the self-quenching of the photoexcited state of the dye thus reducing the efficiency of electron injection into the mTiO<sub>2</sub> [90]. The adverse effects of aggregation are even more pronounced in the case of ssDSSCs where the presence of dye aggregates hinder the infiltration of the HTM into mTiO<sub>2</sub> pores. Accordingly, many regions within the mTiO<sub>2</sub> film contain dye molecules that are not in contact with the HTM and are consequently not effectively regenerated by the HTM.

Interestingly, the addition of spiro-MeOTAD has a similar effect to CDCA on the absorption spectra (Figure 3.3 (b)). The aggregation peak at 620 nm is decreased and the absorption peaks are slightly red-shifted. The process of depositing the HTM by spin-coating may lead to 1) the removal of aggregates not firmly attached to the mTiO<sub>2</sub> surface, or 2) the disruption of dye aggregates by the HTM [7].

Figures 3.3 (e)–(f) shows that there is no significant decrease in the aggregation peak when the pure solvent (chlorobenzene) is spin-coated onto films, sensitized with either pure JD10 (Figure 3.3 (e)) or the mixture of JD10 and CDCA (Figure 3.3 (f)) in ethanol. This indicates that the observed effect of aggregation suppression likely arises due to interaction between the dye sensitized-TiO<sub>2</sub> surface and the spiro-MeOTAD molecules. Significantly, CDCA and spiro-MeOTAD work synergistically to almost completely dissipate the high-energy aggregation peak as displayed in Figure 3.3 (b) (red dashed trace).

<sup>1</sup> cf. Appendix Figure A.1 for molecular structure.

### 3.2. Squaraine Sensitizers: Near-Infrared Light Absorption



**Figure 3.3.** Normalized optical density spectrum of sensitized  $2 \mu\text{m}$   $\text{TiO}_2$  films prepared by immersion in an ethanol solution of: (a) 0.05 mM JD10 with and without 20 mM CDCA, (b) 0.05 mM JD10 with spin-coated spiro-MeOTAD. Background reference of only  $\text{mTiO}_2$  and spin-coated spiro-MeOTAD is displayed (dot-dash blue). (c) Films sensitized with 0.05 mM JD10, 0.1 mM D35 and 0.05:0.05 mM JD10:D35 mixture. (d) Normalized spectra for sensitized films with spin-coated spiro-MeOTAD. (e) Films sensitized with 0.05 mM JD10 without and (f) with the addition of 20 mM CDCA to the dye solution. Dashed traces correspond to sensitized  $\text{mTiO}_2$  films treated with spin-coated chlorobenzene (CB).

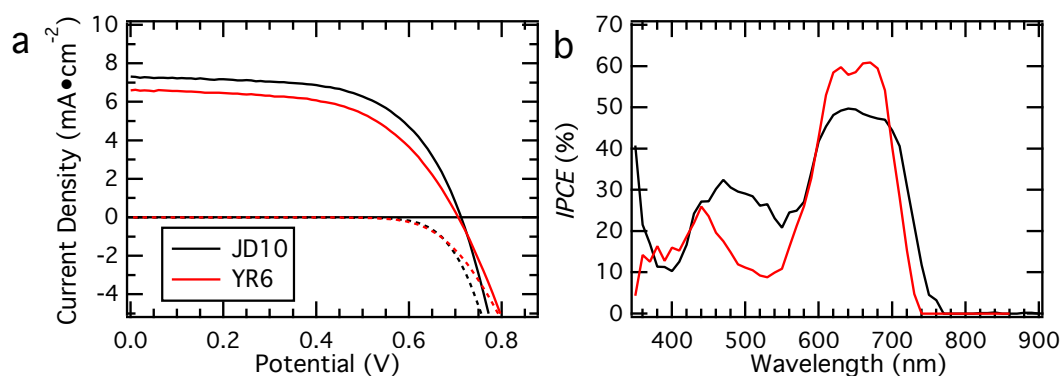
#### 3.2.2 Photovoltaic Performance

The  $J$ - $V$  performance of ssDSSCs measured under 100% sunlight intensity ( $100 \text{ mW cm}^{-2}$  standard AM1.5G illumination) using the squaraine sensitizers, YR6 and JD10, are presented

## Chapter 3. Molecular Sensitization for Solid-State Solar Cells

**Table 3.1.** Photovoltaic parameters determined from  $J$ - $V$  measurements of ssDSSC devices under simulated AM1.5G solar irradiance ( $100 \text{ mW cm}^{-2}$ ). All devices were masked to achieve an illuminated active area of  $0.2025 \text{ cm}^{-2}$ . Integrated current densities determined from the overlap of the  $IPCE$  spectrum with the AM1.5G solar photon flux.

Dye	Integrated Current Density ( $\text{mA cm}^{-2}$ )	$V_{OC}$ (mV)	$J_{SC}$ ( $\text{mA cm}^{-2}$ )	$FF$	$PCE$ (%)
YR6	6.9	706	6.61	0.58	2.69
JD10	7.8	712	7.32	0.61	3.16
D35	6.4	906	6.44	0.72	4.23
JD10:D35	9.9	741	9.94	0.59	4.42



**Figure 3.4.** (a) Photovoltaic performance of YR6 (red) and JD10 (black) sensitized ssDSSC measured in the dark and under  $100 \text{ mW cm}^{-2}$  AM1.5G solar irradiation and (b) corresponding  $IPCE$  spectra.

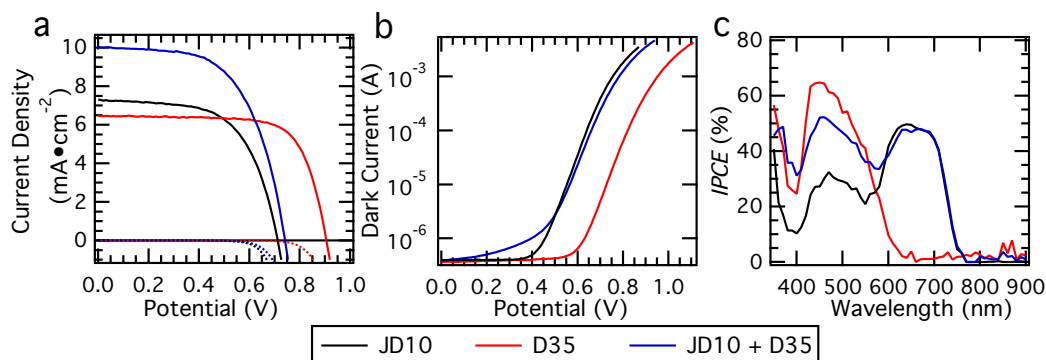
and summarized in Figure 3.4 and Table 3.1 respectively. At full sunlight intensity JD10 sensitized devices gave a  $PCE$  of 3.16%. This higher value relative to the 2.69% achieved by YR6 is mainly due to an increase in  $J_{SC}$  (7.32 and  $6.61 \text{ mA cm}^{-2}$  respectively), which is reflected in the slightly broader  $IPCE$  spectrum and the significantly stronger signal between 400 and 550 nm (Figure 3.4 (b)) for JD10.

The relatively low  $FF$  displayed by all the ssDSSCs employing a squaraine sensitizer arises due to the high series resistance within the device resulting from the presence of dye aggregates hindering the infiltration of the HTM into the  $\text{TiO}_2$  pores.

### 3.2.2.1 Co-sensitization

Co-sensitization involving dyes with complementary spectral responses is an effective strategy to broaden and intensify the light absorption spectra [3, 91, 92]. The high-energy absorbance of JD10 has been improved compared to previous squaraines; however, to further increase the light harvested in this region, devices were fabricated using JD10 co-sensitized with the

### 3.2. Squaraine Sensitizers: Near-Infrared Light Absorption



**Figure 3.5.** (a) Photovoltaic performance of JD10 with CDCA (black), D35 (red) and JD10:D35 co-sensitized with CDCA ssDSSCs measured in the dark and under 100 mW cm<sup>-2</sup> AM1.5G solar irradiation. (b) Dark current displayed on logarithmic scale. (c) *IPCE* spectra.

organic dye D35<sup>2</sup> [93, 94]. D35 exhibits a strong complementary high-energy absorption with a maximum at 442 nm and corresponding extinction coefficient of 31 800 M<sup>-1</sup> cm<sup>-1</sup> in ethanol (Figure 3.2 (a)). As a result, the cocktail dye solution containing a 1:1 molar ratio of the two sensitizers – JD10 and D35 – in ethanol, shows a doubling in absorption strength in the high-energy visible region of 400–550 nm. A similar effect is observed during optical density measurements for TiO<sub>2</sub>-sensitized films (Figure 3.3 (c)–(d)).

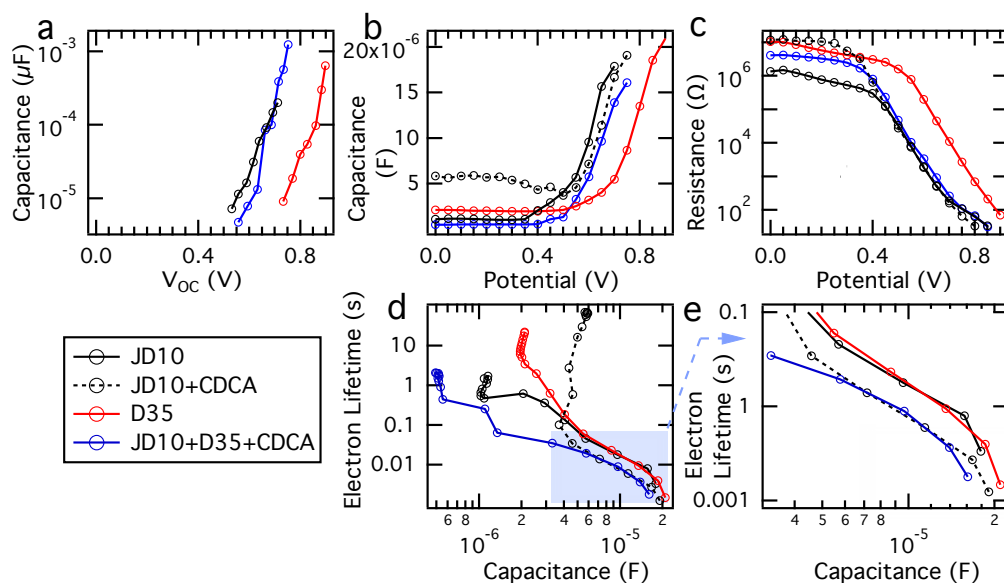
The photovoltaic characteristics of JD10, D35 and JD10:D35 co-sensitized ssDSSC devices are shown in Figure 3.5 (a)–(b) and the corresponding parameters are summarized in Table 3.1. From the *IPCE* (Figure 3.5 (c)), it is clear that D35 contributes strongly to the light harvested in the 400–550 nm visible region. The increased light absorption consequently leads to a considerable increase in the photocurrent of the co-sensitized devices, which is higher than that of devices sensitized with JD10 or D35 individually. The *IPCE* of the co-sensitized photovoltaic devices approaches the ideal panchromatic shape with peak efficiencies of 52% and 48% at 450 and 670 nm respectively. The *IPCE* peaks correspond to the maximum absorption of D35 and JD10.

Finally, the co-sensitized ssDSSC gave a *PCE* of 4.42% which is the highest value reported to date for a squaraine dye co-sensitized with an organic dye. Similar to the other squaraine-sensitized devices, the co-sensitized device, containing the sensitizer JD10, has a significantly lower *FF* as is typical for squaraine sensitized solar cells.

#### 3.2.3 Transient and Impedance Characterization

Photocurrent and photovoltage transient decay measurements were conducted to study the internal electrical parameters of these ssDSSC devices [95, 96]. The devices were held at steady-state open-circuit conditions (where the *V*<sub>OC</sub> is determined by the light intensity). The

<sup>2</sup> cf. Appendix Figure A.3 for molecular structure.



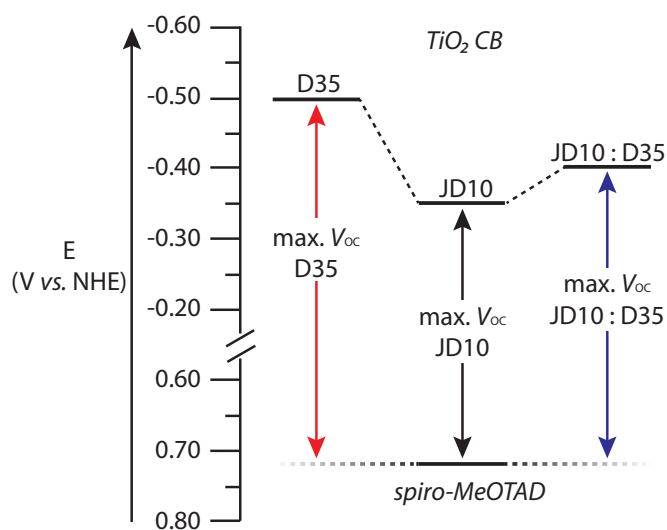
**Figure 3.6.** (a)  $V_{\text{OC}}$  dependence on the capacitance determined from transient measurements. (b) Chemical capacitance, (c) recombination resistance and (d)–(e) calculated electron lifetime extracted from IS measurements conducted on devices in the dark.

system was perturbed using a short red pulse (cf. Experimental Methods Chapter 8) leading to a small increase in the  $V_{\text{OC}}$ . This response was monitored at different light intensities and the transient photovoltage data were used to determine the capacitance  $C_{\mu}$  at  $V_{\text{OC}}$ , from which the DOS can be calculated using Equation 2.7.

The results depicted in Figure 3.6 (a) exhibit a shift of about 50 mV between the JD10 and JD10:D35 co-sensitized devices. Additionally, there is an approximate shift of 160 mV in the capacitances for the D35 sensitized device relative to the JD10 sensitized device. This shift in the CB is in good agreement with the differences in  $V_{\text{OC}}$  determined from the  $J$ – $V$  measurements.

To further examine this phenomenon, impedance spectroscopy (IS) measurements were conducted for complete devices in the dark. The fits determined from the measurements are presented in Figure 3.6 (b)–(c) and reveal that the chemical capacitance extracted indicate an upward shifts of the CB by approximately 170 mV and 30 mV respectively for D35 and JD10:D35 co-sensitized devices relative to the JD10 device, which is in excellent agreement with the transient and  $J$ – $V$  measurements. The relative shifts in the CB for the different systems are shown schematically in Figure 3.7.

The bulky alkoxy groups of the organic D– $\pi$ –A sensitizer D35 have been reported to efficiently reduce the rate of recombination [47] in liquid-based DSSCs employing cobalt-based redox mediators. These constituents of the D35 dye molecules prevent the formation of dye aggregates and inhibit electron-hole recombination by protecting the  $\text{TiO}_2$  surface. It is possible



**Figure 3.7.** Schematic displaying the differences in the CB potentials reflecting the shifts in the CB band found by IS and transient photovoltage decay measurements. The CB potential of D35 sensitized TiO<sub>2</sub> was taken at -0.5 V for comparison purposes. The maximum  $V_{OC}$  is represented as the difference between the relative CB potential and the first oxidation potential of spiro-MeOTAD [15] for films sensitized with D35 (red), JD10 (black), and JD10:D35 (blue).

that the adsorption of this species effectively prevents the direct contact between HTM and the TiO<sub>2</sub>, thus reducing the amount of adsorbed species (i.e. Li<sup>+</sup> ions) that may shift the TiO<sub>2</sub> CB downwards. This results in the observed relative upward shift of the CB of D35 with respect to the pure JD10. In the latter case the readily aggregating sensitizer results in ‘exposed’ TiO<sub>2</sub> surface, allowing the direct contact between the HTM and the TiO<sub>2</sub>, facilitating charge recombination.

It can be inferred that while the use of JD10 greatly improves the photocurrent of the devices due to the extended light absorption in the NIR region of the visible spectrum, there are still extensive loss mechanisms that adversely influence the  $V_{OC}$ . The calculated electron lifetime determined from the recombination resistance and the chemical capacitance display a slightly longer lifetime for the devices using pure JD10 or D35 at high forward bias, Figure 3.6 (e). Devices where CDCA was added exhibit shorter lifetimes for similar DOS.

### 3.3 D- $\pi$ -A Sensitizers: Effect of the Donor Group

Although the squaraine class of sensitizers examined in the section above have strong absorption in the NIR, problems associated with dye aggregation and poor light absorption in the visible region of the spectrum result in relatively low  $PCEs$ . Their characteristic narrow, intense light absorption cause them to be very selective photon absorbers, and thus inappropriate for the mono-sensitization of DSSCs using a single dye. The record  $PCEs$  have been achieved with high molar extinction coefficient organic dyes with strong light absorption across the entire visible spectrum [3, 15].

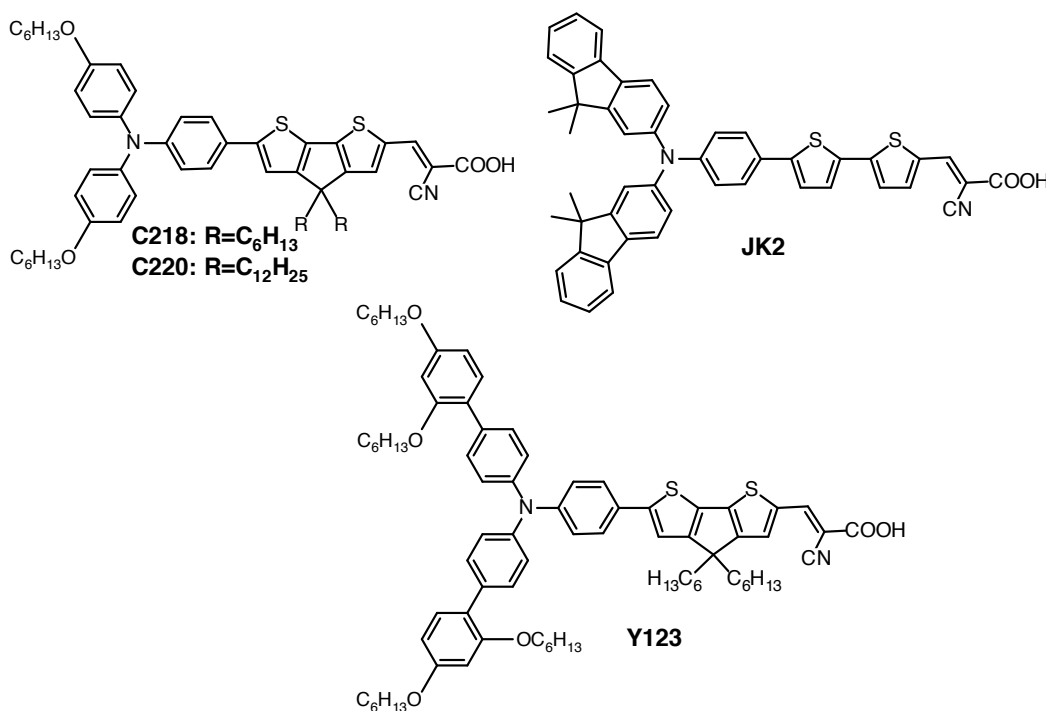


Figure 3.8. Molecular structures of C218, C220, JK2 and Y123.

This section examines the use of different organic D- $\pi$ -A dyes with high molar extinction coefficients and their role on the photovoltaic performance of ssDSSCs and in particular on the  $V_{OC}$ . Furthermore the differences in the molecular structure of the donor group is correlated with the  $PCE$  and device mechanism through IS analysis [45].

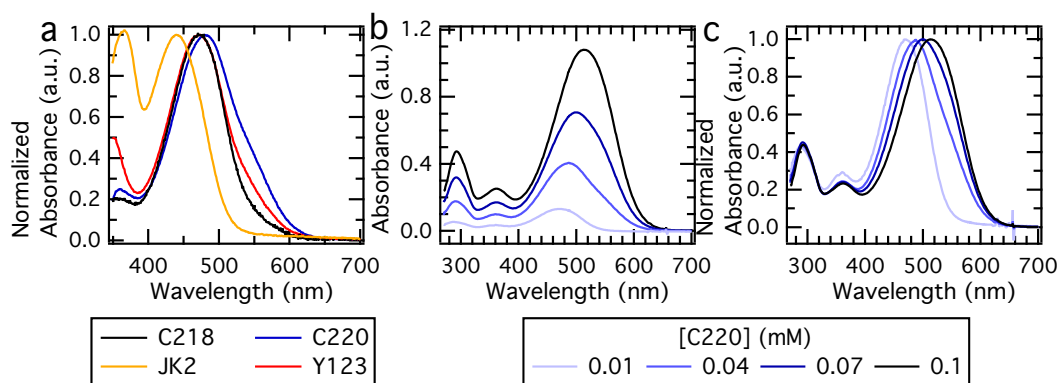
The  $V_{OC}$  of ssDSSCs is determined by the difference between the quasi Fermi level in the semiconductor ( $TiO_2$ ) under illumination and the oxidation potential of the HTM. The value of the oxidation potential of spiro-MeOTAD in solution has been found to be 0.72 V *versus* NHE [15]. Assuming a value of -0.5 V *versus* NHE for the  $TiO_2$  CB edge, one is limited to the theoretical value for the  $V_{OC}$  of about 1.2 V.

Variations in the  $V_{OC}$  can be caused by an increased concentration of holes (e.g. due to doping), resulting in a lower Fermi level in the HTM. Alternatively it can be affected by an upward shift in of the CB edge of the semiconductor. In this study the devices were all fabricated following the same procedure hence it is assumed that any shift there may be in the HTM Fermi level is the same for all the constructed devices.

Solid-state dye-sensitized solar cells were fabricated using spiro-MeOTAD as a hole conductor and high molar extinction coefficient organic D- $\pi$ -A dyes, coded C218, C220, JK2 and Y123, the molecular structures of which are presented in Figure 3.8.

In combination with a Co(III)/Co(II) redox electrolyte,  $PCEs$  of 9.6% have been achieved with Y123 in liquid DSSC [97]. Y123 and its analogue, C220, have been reported as record





**Figure 3.9.** (a) Normalized UV-vis spectra of C218, C220, JK2 and Y123 in a 1:1 solvent mixture of acetonitrile and *tert*-butanol. (b) UV-vis spectra for different concentrations of C220 in a 1:1 solvent mixture of acetonitrile and *tert*-butanol. (c) Normalized UV-vis spectra from (b).

performing dyes in ssDSSCs, achieving 7.2% [15] and 6.1% [19] respectively. Finally the highest  $V_{OC}$  of over 1 V in ssDSSCs was reached using the JK2 sensitizer [18].

In addition to the conventional additives – LiTFSI and TBP – a cobalt(III) complex<sup>3</sup> [15] was added to the HTM solution as a *p*-type dopant prior to deposition. As discussed in the previous chapter, pure spiro-MeOTAD has low conductivity and thus in its intrinsic form is an unsuitable hole conductor. The conductivity of the HTM is dependent on the charge carrier density and their mobility, which can be easily controlled through the addition of dopants.

### 3.3.1 Optical Characterization of D- $\pi$ -A Dyes

The UV-vis spectra of C218, C220, JK2 and Y123 in a 1:1 solvent mixture of acetonitrile (MeCN) and *tert*-butanol (*t*-BuOH) exhibit similar absorption maxima and  $\epsilon$  of 45, 34, 35 and  $29 \times 10^3 \text{ M}^{-1} \text{ cm}^{-1}$  at 471, 481, 440 and 472 nm respectively (Figure 3.9). These values are blue-shifted due to the influence of the polar solvent, which results in the deprotonation of the dye, when compared to the values found in chloroform ( $55 \times 10^3 \text{ M}^{-1} \text{ cm}^{-1}$  at 521 nm for C220 [19]).

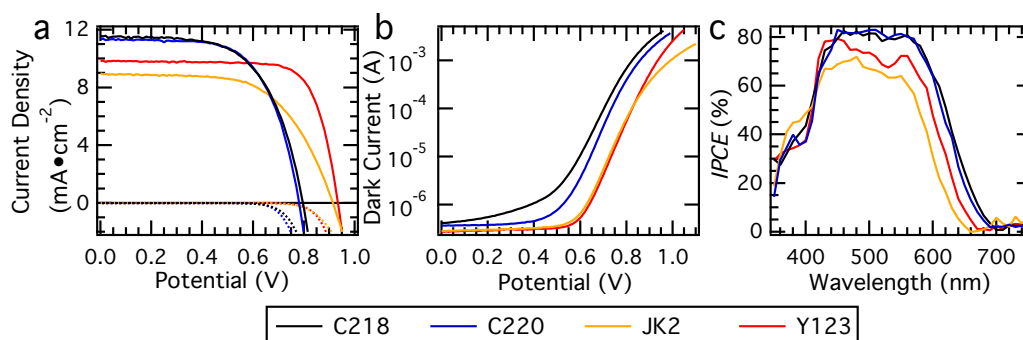
This blue-shift in the absorption spectra as a result of the deprotonation of the dye molecules is similarly observed when the concentration of the dye solution is decreased in Figure 3.9 (b)–(c). As the concentration of the dye solution is decreased from 0.1 mM to 0.01 mM the absorption maxima is shifted from 513 to 470 nm. This is clearly displayed in the normalized absorbance spectra depicted in Figure 3.9 (c). Similar observations were made upon the formation of the deprotonated species by reductive electrolysis [98] and simulated step-wise deprotonation [99] of Ru(II) metal complex dyes.

At lower dye concentrations the deprotonated species and the associated proton are more

<sup>3</sup> Code name FK102 – cf. Figure 1.7 Chapter 1.

**Table 3.2.** Photovoltaic parameters determined from  $J$ - $V$  measurements for ssDSSCs using C218, C220, JK2 and Y123 measured under simulated AM1.5G solar irradiance ( $100 \text{ mW cm}^{-2}$ ). Integrated current density determined from overlap of the  $IPCE$  and solar spectrum.

Dye	Integrated Current Density ( $\text{mA cm}^{-2}$ )	$V_{OC}$ (mV)	$J_{SC}$ ( $\text{mA cm}^{-2}$ )	$FF$	$PCE$ (%)
C218	11.9	796	11.6	0.61	5.6
C220	11.7	781	11.5	0.64	5.7
JK2	9.2	914	8.9	0.60	4.9
Y123	10.1	934	9.8	0.75	6.9



**Figure 3.10.** (a)  $J$ - $V$  characteristics of C218, C220, JK2 and Y123 sensitized ssDSSCs. (b) Dark current displayed on logarithmic scale. (c) Corresponding  $IPCE$  spectra as a function of monochromatic wavelength.

readily stabilized by the polar solvent, thus resulting in the observed blue-shift of the absorption spectra. Furthermore the lower concentration of dye directly correlates with a lower concentration of available protons, which drives the formation of the deprotonated species.

### 3.3.2 Photovoltaic Performance

The  $J$ - $V$  characteristics of ssDSSCs fabricated using the sensitizers JK2, C218, C220 and Y123 measured at 1 sun illumination under standard global AM1.5G conditions ( $100 \text{ mW cm}^{-2}$ ) and in the dark are shown in Figure 3.10 (a)–(b) with the corresponding photovoltaic parameters summarized in Table 3.2. The ssDSSC device using the Y123 dye gave an impressive  $PCE$  of 6.9%, which can be attributed to the high voltage of 934 mV and  $FF$  of 0.75. Devices made with JK2 and C220 yielded  $PCE$ s of 4.9 and 5.7% respectively. The performance of devices with C218 is similar to C220.

The increase in  $J_{SC}$  in the order  $JK2 < Y123 < C220 < C218$  arises from improved light harvesting which is further evident in the  $IPCE$  spectra shown in Figure 3.10 (c). The similarities in the spectra reflect comparable light absorption qualities of the dyes and lie between 70–80% from 450 to 570 nm, with the maximum achieved at the plateau for C218 and C220 followed by Y123 and JK2. Additionally the  $IPCE$  spectra are enhanced most in the red regions for C218/C220

and the least for JK2. The projected current density values calculated by integration of the *IPCE* spectra over the AM1.5G standard solar emission spectra are presented in Table 3.2 and are in good agreement with the  $J_{SC}$  values obtained from the standard photovoltaic characterizations. In the case of JK2, the lower light harvesting abilities of the dye leads to lower  $J_{SC}$  and thus *PCE*.

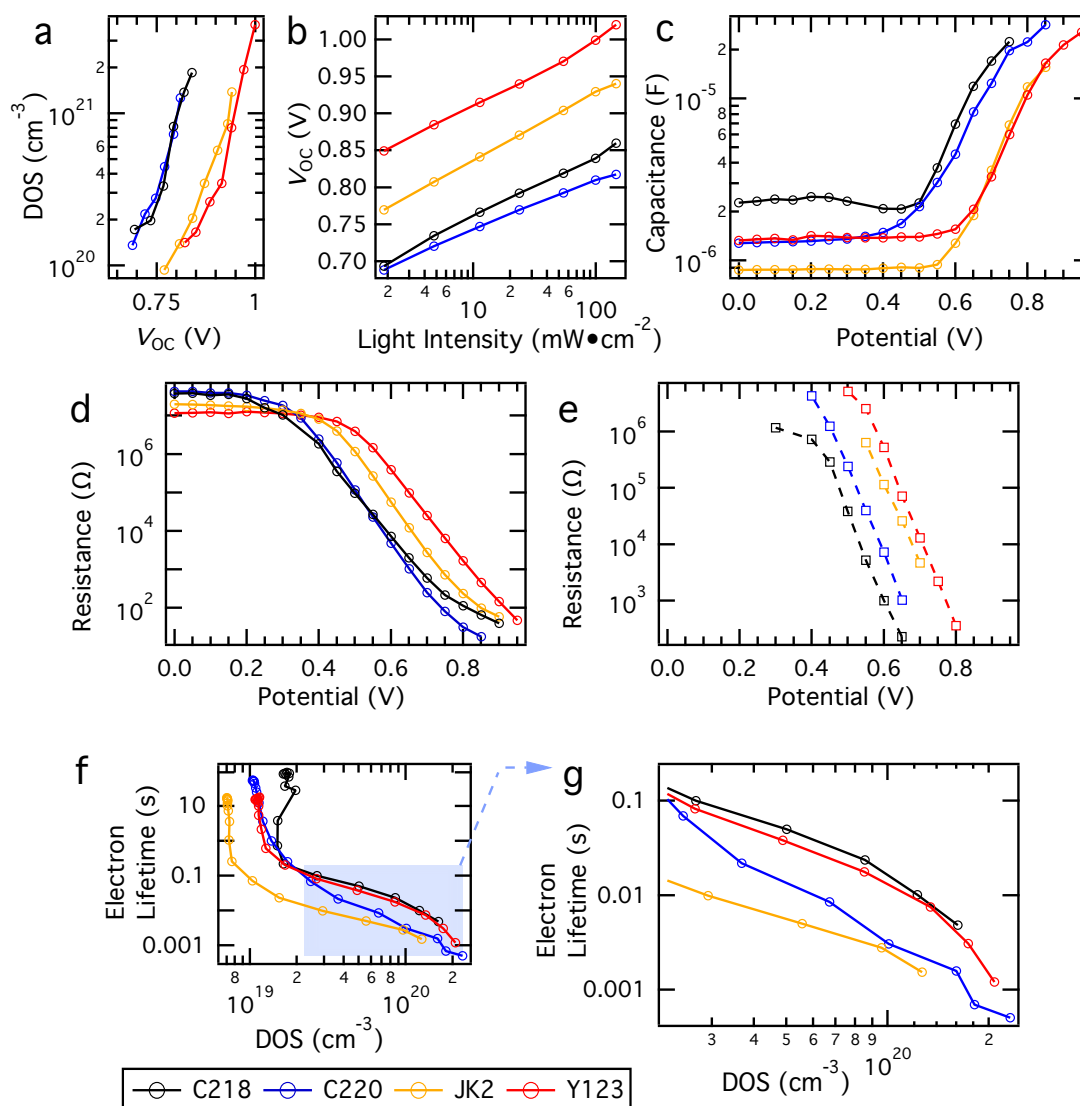
#### 3.3.3 Transient and Impedance Characterization: TiO<sub>2</sub> Conduction Band Shift

The DOS was determined from the capacitance extracted from transient photovoltage decay measurements at  $V_{OC}$  [95, 96] using Equation 2.7. The results presented in Figure 3.11 (a) show a shift of 150 and 130 mV in the DOS for Y123 and JK2 respectively relative to C220 sensitized devices. These values are in good agreement with the differences in  $V_{OC}$  observed for these devices. Figure 3.11 (b) shows a plot of the  $V_{OC}$  as a function of the logarithm of the light intensity for the different devices. The diode ideality factor  $m$  obtained from the slope was found to be 86, 72, 90 and 80 mV dec<sup>-1</sup> for C218, C220, JK2 and Y123 respectively, indicating that these devices show similar deviation from ideal diode behavior. Consequently recombination takes place mainly between electrons in the titania layer and holes in the spiro-MeOTAD, and any back reaction *via* the FTO substrate is negligible due to the diode properties of the compact TiO<sub>2</sub> underlayer [100].

To further investigate the internal electrical characteristics of the ssDSSCs IS measurements were conducted in the dark. The transmission line model [62] was used to analyze the low frequency region of the IS spectra, the results of which are presented in Figure 3.11 (c)–(e). The devices made with C218, C220 and Y123 display superimposable trends in the IS spectra. The displacement between the recombination  $R_{ct}$  and transport  $R_{trans}$  resistances relative to the potential corresponds to 170 and 150 mV between Y123 and C220 (Figure 3.11 (d)–(e)). C218 only shows a significant negative shift of 50 mV in  $R_{trans}$  and is otherwise indistinguishable from C220. In the case of JK2 the resistances,  $R_{ct}$  and  $R_{trans}$  are displaced by 100 mV relative to C220. However a faster decrease in  $R_{ct}$  with applied potential suggests a faster rate of recombination.

The DOS is directly proportional to the chemical capacitance, hence the latter can be used as an indirect measure of the former. The chemical capacitance presented in Figure 3.11 (c) shows an upward shift in the CB of the TiO<sub>2</sub> of approximately 150 and 130 mV for devices using Y123 and JK2 relative to C220 respectively. This is in good agreement with the shift observed in the DOS determined from the transient decay measurements.

From the extracted IS fit results the electron lifetime  $\tau_n$  within the TiO<sub>2</sub> was calculated [62] and displayed in Figure 3.11 (f)–(g). The electron lifetime results from the amount of electrons in the CB, which in turn depends on the rate of trapping and detrapping of electrons in localized states within the bandgap of the TiO<sub>2</sub>. Thus the electron lifetime strongly depends on the applied voltage. In the high forward bias regime (Figure 3.11 (g)) the electron lifetime at similar electron density is longest for ssDSSCs with Y123 which is reflected in its high  $V_{OC}$ .

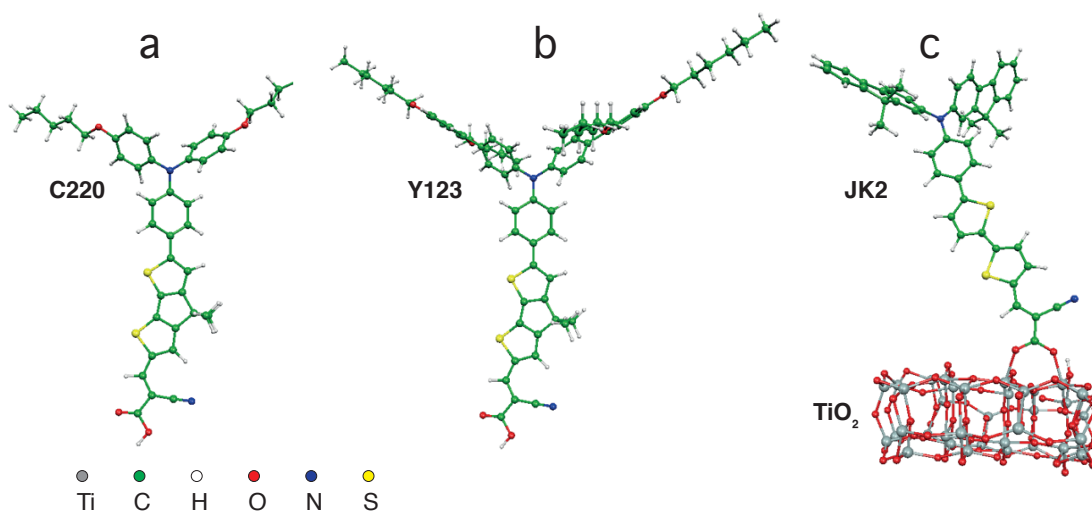


**Figure 3.11.** (a) DOS as a function of the  $V_{OC}$  and (b)  $V_{OC}$  dependence on light intensity determined from transient measurements of C218, C220, JK2 and Y123 sensitized ssDSSCs. (c) Chemical capacitance, (d) recombination resistance and (e) transport resistances for C218, C220, JK2 and Y123 sensitized ssDSSCs extracted from IS measurements conducted in the dark. (f) Calculated electron lifetime as a function of the DOS calculated from the chemical capacitance. (g) High forward bias region.

### 3.3.4 Computational Calculations

DFT/TDDFT<sup>4</sup> calculations were performed on C220 and Y123 to gain insight into their electronic and optical properties. For simplicity the alkyl chains on the CPDT moiety were replaced by methyl groups.

<sup>4</sup> All calculations were carried out using a 6-31G\* basis set.



**Figure 3.12.** Optimized geometries of (a) C220 and (b) Y123 dye molecules. (c) Adsorption geometry of JK2 on  $\text{TiO}_2$ .

The optimized geometries of the C220 and Y123 dyes in their ground states<sup>5</sup> are reported in Figure 3.12. The two dyes show a planar arrangement of the conjugated phenyl-CPDT-cyanoacrylic acid moiety, while the two aromatic moieties bound to the nitrogen donor are displaced out of plane to minimize steric repulsion.

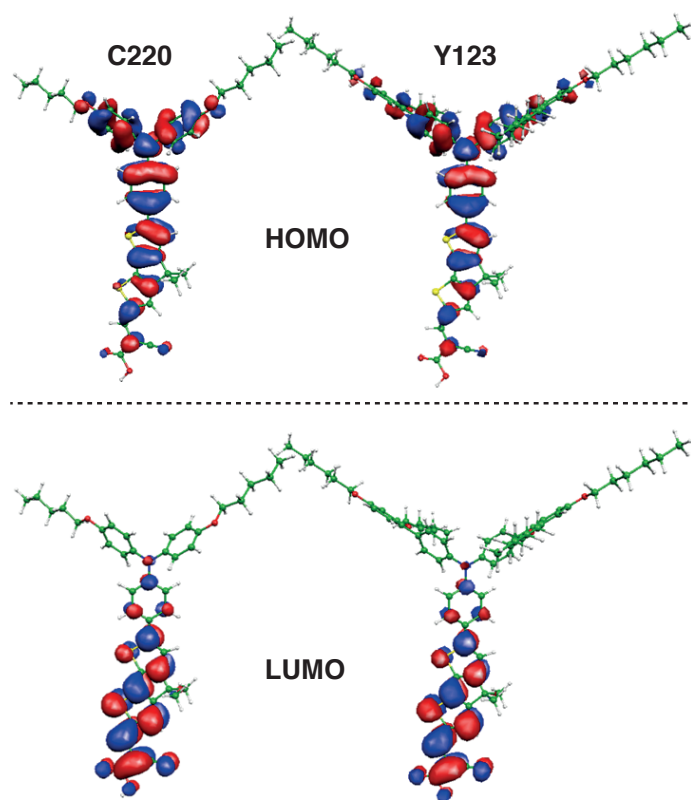
From the isodensity plot of the HOMOs and LUMOs for C220 and Y123 shown in Figure 3.13 it is clear that they share a common electronic structure. They display the typical HOMO-LUMO pattern characteristic of these push-pull dyes, whereby the HOMO is mainly localized on the donor and bridge portion of the molecules, while the LUMO is mainly localized on the bridge and on the anchoring/acceptor moiety. The lowest TDDFT transition wavelengths for the protonated C220 and Y123 dyes are calculated at 521 and 519 nm. Both transitions originate from HOMO-LUMO excitations.

Taking into account the expected blue-shift of the absorption as a result of the deprotonation of the terminal carboxylic group [102] this is in good agreement with the corresponding experimental data presented above.

#### 3.3.4.1 Dipole Moment Phenomenon

The adsorption of dipolar molecules onto the  $\text{TiO}_2$  surface has been shown to influence the position of the CB edge [103] – the so-called *net dipole effect*. Studies examining such surface modification techniques have led to improvement of the  $V_{\text{OC}}$  of liquid DSSCs [104]. Furthermore the presence of dipoles on the surface have been shown to act as surface blocking layers, suppressing the dark current in ssDSSCs and leading to a change in the band alignment at the sensitized semiconductor/HTM interface [105]. Hence it is clear that the dipole moment

<sup>5</sup> Carried out in vacuo using the B3LYP exchange-correlation functional [101]



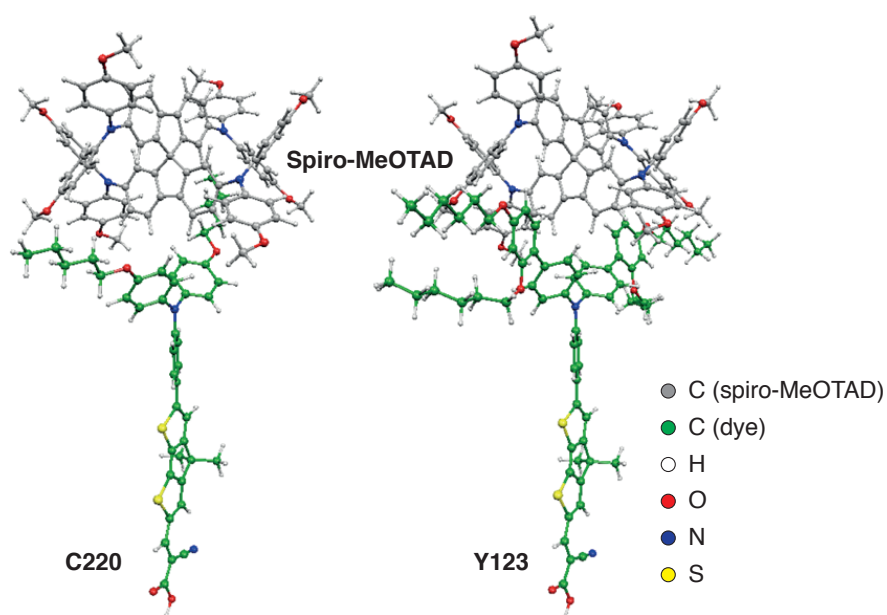
**Figure 3.13.** Isodensity plots of the HOMOs and LUMOs for the C220 and Y123 dyes.

of the adsorbed dye molecules has a strong effect on the charge distribution and consequently influences the position of the semiconductor CB. The total dipole moments for C220 and Y123 calculated from the optimized geometries are 10.6 and 11.5 D respectively and are found to be oriented along the main push-pull molecular axis, pointing from the cyanoacrylic acceptor to the N-substituted donor.

As previously mentioned the dipole moment of the adsorbed molecule at the  $\text{TiO}_2$  surface is possibly responsible for the observed shifts in  $\text{TiO}_2$  CB. To evaluate the dipole component of the adsorbed molecule normal to the  $\text{TiO}_2$  semiconductor surface, the geometry of Y123 and C220 adsorbed on the  $(\text{TiO}_2)_{38}$  cluster<sup>6</sup> was optimized. A similar adsorption geometry was found for Y123 and C220 as previously reported for the JK2 dye [18] consisting of a dissociative bidentate adsorption mode and a proton transferred to the  $\text{TiO}_2$  surface, Figure 3.12 (c).

From the calculated adsorption geometry, the dipole component normal to the  $\text{TiO}_2$  surface for Y123 and C220 was determined to be 8.8 and 8.6 D respectively. The similarity of the dipole moments in addition to the same adsorption mode determined for the two dyes indicates that if a dipole shift of the  $\text{TiO}_2$  CB is at work, it has to be related to different extents of dye

<sup>6</sup> The  $\text{TiO}_2$  semiconductor was modelled using a neutral stoichiometric anatase  $(\text{TiO}_2)_{38}$  cluster exposing the majority (101) surfaces [106, 107].



**Figure 3.14.** Optimized geometries of the C220 and Y123 adducts with spiro-MeOTAD. Carbon atoms belonging to the spiro-MeOTAD molecule are displayed in grey for clarity.

coverage. In the case of Y123 the dye coverage was found to be 23% higher in comparison to C220 ( $2.80$  and  $3.45 \times 10^{-6}$  mol m $^{-2}$  for C220 and Y123 respectively)<sup>7</sup>. The longer dodecyl alkyl chains of C220 reduce the close packing of the molecules on the surface as well as increase the solubility in solution. Employing the calculated dipole moments and the experimentally available dye coverages, a TiO $_2$  CB upshift of approximately 100 mV for Y123 with respect to C220 was calculated which is comparable to the experimental values. Considering the similar adsorption mode and dipole moment calculated for JK2 (previously reported as 7.7 D [18]), along with the measured dye coverage (21% higher relative to C220) a similar shift for JK2 is predicted, in line with the experimental findings.

#### 3.3.4.2 Calculated Interaction Geometries

In addition to the dipole moment effect, the influence of the different donor groups in C220/C218 and Y123 must be considered. Since the dye donor group is mainly responsible for the dye interaction with the spiro-MeOTAD hole conductor – the acceptor being firmly anchored to the TiO $_2$  surface – the interaction of the C220 (or C218) and Y123 dyes with a spiro-MeOTAD molecule was investigated<sup>8</sup> and the corresponding dye/spiro-MeOTAD adducts presented in Figure 3.14.

<sup>7</sup> Dye was desorbed from sensitized mTiO $_2$  films by immersion in 0.01 M solution of tetrabutylammonium hydroxide in *N,N*-dimethylformamide (DMF). Subsequently dye coverage was calculated from the UV-vis spectrum of the solution using Beer-Lambert law cf. Chapter 8 Experimental Methods.

<sup>8</sup> The interaction between the dye and the spiro-MeOTAD molecule were evaluated using second order (MP2) Møller-Plesset single point calculations using the DFT optimized geometries.

The calculated interaction geometries between C220 and Y123 with spiro-MeOTAD are rather similar, with a calculated distance between the dye N-donor and the spiro-MeOTAD carbon of 8.74 and 8.80 Å respectively. However the calculated interaction energies<sup>9</sup> are substantially different for the two dyes, with C220 showing an adduct formation energy of 14.1 kcal mol<sup>-1</sup>, while this quantity reduces to 9.5 kcal mol<sup>-1</sup> for Y123. Thus, by virtue of the more bulky donor group of Y123, a reduced interaction energy with spiro-MeOTAD is computed for this dye compared to C220.

A reported analysis of solid-state DSSC devices [35] has shown that a reduced filling of the TiO<sub>2</sub> pores by spiro-MeOTAD is a major limiting factor towards the achievement of high photovoltaic efficiencies in solid-state devices. At low pore-filling fraction (PFF) parasitic recombination between the oxidized hole-transporter and injected electrons into TiO<sub>2</sub> is responsible of considerable photovoltaic losses, while at high PFF improved hole-injection efficiency, reduced recombination and increased diffusion are observed. These results lead to the speculation that a strong dye/spiro-MeOTAD interaction might be responsible for incomplete pore-filling, whereby the spiro-MeOTAD molecules would prefer to strongly bind to the dye donor groups rather than binding among themselves to form a well-dispersed film. This might be the case for the increased recombination observed experimentally for C220 dye-sensitized solar cells compared to those based on the Y123 dye. Furthermore the addition of hexyloxy groups in Y123 are likely to also play a role in limiting the direct contact between spiro-MeOTAD and TiO<sub>2</sub> thus hindering the back reaction of electrons in the TiO<sub>2</sub> with holes in the HTM.

### 3.4 Ullazine Sensitizers: Role of Molecular Structure

This section presents a class of dyes that are reported for the first time as sensitizers in ssDSSCs using spiro-MeOTAD [108]. These ullazine molecules, presented in Figure 3.15, are a type of heteroarene based on an indolizino[6,5,4,3-*aij*]quinoline core [109, 110]. Four 3,9-disubstituted derivatives were examined to study the influence of the donor group on the device performance. In addition the position of the cyanoacrylic acid anchoring group for two of the derivatives was investigated.

Altering the donor group allows the modest tuning of the spectral response of the dyes and furthermore plays a critical role in determining the type of interaction with the HTM and consequently on the device performance. In this study ssDSSCs using the ullazine dyes have been extensively characterized, correlating the dye structures with the device performance.

#### 3.4.1 Optical Characterization of Ullazine Sensitizers

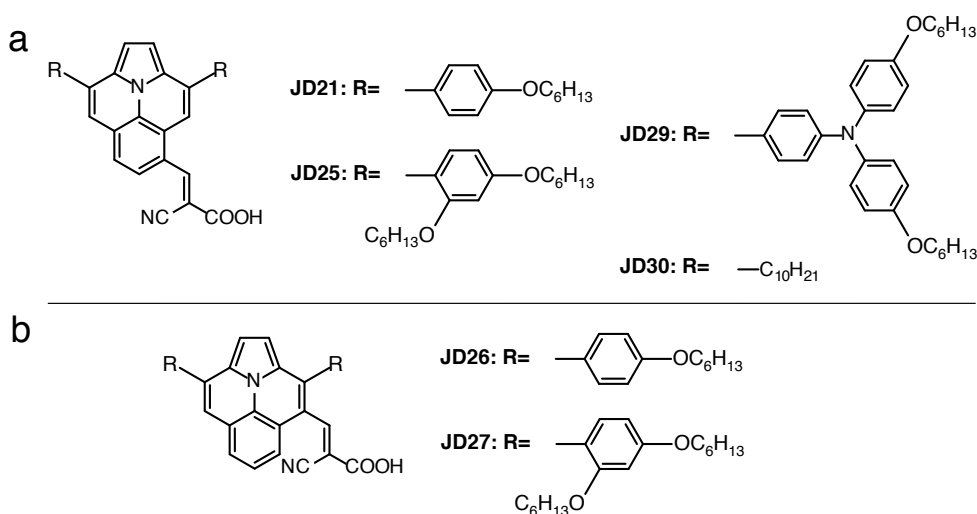
The absorption spectra of the dyes in 1:4 v/v tetrahydrofuran:ethanol (THF:EtOH) solution are shown in Figure 3.16 (a) and the corresponding parameters are listed in Table 3.3.

---

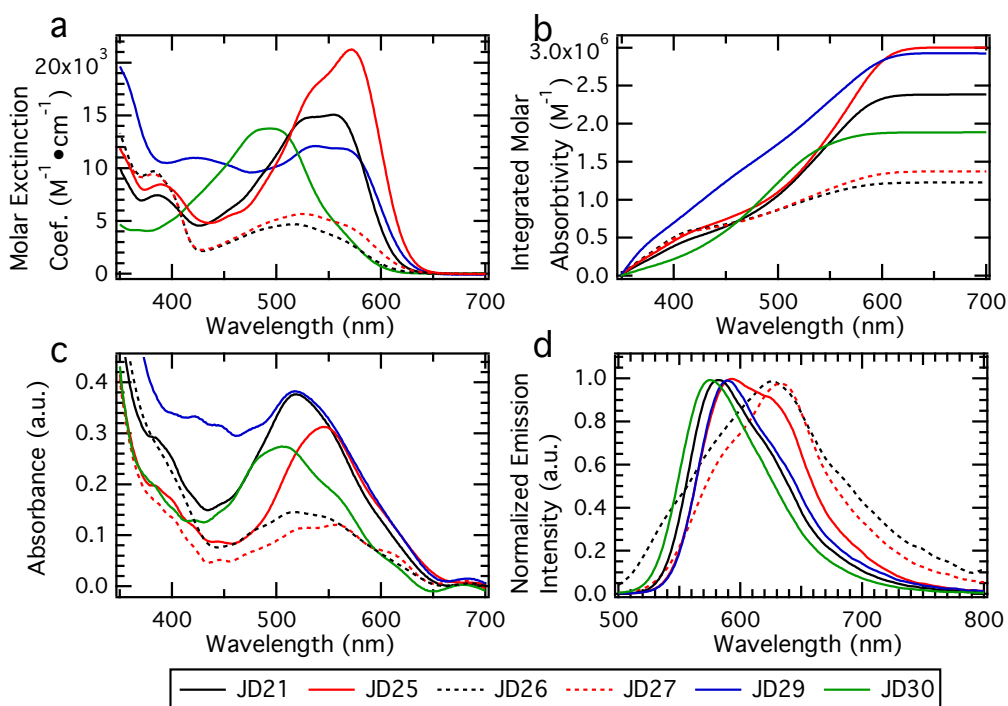
<sup>9</sup> Calculated using MP2 perturbation method.



### 3.4. Ullazine Sensitizers: Role of Molecular Structure



**Figure 3.15.** Molecular structures of ullazine sensitizers.



**Figure 3.16.** UV-vis spectra of dyes in (a) 1:4 v/v THF:EtOH solution with (b) the corresponding integrated absorption curve area and (c) adsorbed onto mTiO<sub>2</sub> films. The spectra have been normalized with respect to the film thickness. (d) Normalized emission spectra in 1:4 v/v THF:EtOH solution.

For this series of sensitizers the absorption spectra of JD25 is furthest red-shifted with the highest molar extinction coefficient  $\epsilon$  of  $21\,260\text{ M}^{-1}\text{ cm}^{-1}$  at 572 nm. While  $\epsilon$  for JD29 ( $12\,108\text{ M}^{-1}\text{ cm}^{-1}$  at 537 nm) is considerably lower, it shows increased absorption in the 400–500 nm region

### Chapter 3. Molecular Sensitization for Solid-State Solar Cells

**Table 3.3.** Experimental data for optical properties and bandgap energies for dyes JD21, 25, 26, 27, 29 and 30.

Dye	$\lambda_{abs-max}$ (nm) <sup>a</sup>	$\epsilon_{max}$ (M <sup>-1</sup> cm <sup>-1</sup> )	$\lambda_{em-max}$ (nm) <sup>a</sup>	$E_g$ (eV) <sup>b</sup>
JD21	555 (517)	15 070	580 (720)	2.17
JD25	572 (544)	21 260	592 (710)	2.12
JD26	516 (514)	4 700	630 (710)	2.17
JD27	525 (555)	5 670	638 (700)	2.12
JD29	537 (517)	12 110	588 (706)	2.14
JD30	491 (505)	13 770	575 (687)	2.26

<sup>a</sup> Absorption and emission maxima measured in 1:4 v/v THF:EtOH and (in parenthesis) measured on 2  $\mu$ m TiO<sub>2</sub> films.

<sup>b</sup> Measured at the intersection of the absorbance and emission spectra in solution.

and a broader absorption peak. This is reflected in the integrated absorption curve area (Figure 3.16 (b)) which shows JD29 and 25 reaching similar maximum values, followed by JD21, 30 and finally JD27 and 26.

Changing the position of the anchoring group of JD21 and 25 from the 5-position to the 4-position on the ullazine core gave the analogue structures coded JD26 and 27 respectively. JD26 and 27 show similar absorption spectra with the latter displaying a slight red-shift of 10 nm and an increased relative  $\epsilon$ , consistent with the difference between JD21 and 25. Comparing the two pairs of sensitizers, the absorption spectra of JD26 and 27 show a blue-shift of approximately 40 nm relative to JD21 and 25. Additionally JD26 and 27 display a drastic reduction in  $\epsilon$  (from 15 067 M<sup>-1</sup>cm<sup>-1</sup> for JD21 to 4 700 M<sup>-1</sup>cm<sup>-1</sup> for JD26) suggesting that changing the position of the anchoring group results in a decrease in the light harvesting capabilities in the visible region. The 4-position anchor results in a loss in planarity of dye molecule structure, where the anchoring group is twisted perpendicular to the ullazine core. This decreases the coordination, hence depressing the intramolecular charge-transfer (ICT) and culminating in the observed reduction of the molar absorptivity. Finally, the spectrum for JD30 is most blue-shifted of the series, with an absorption maxima at 491 nm ( $\epsilon = 13 770$  M<sup>-1</sup>cm<sup>-1</sup>).

The absorption spectra and corresponding  $\epsilon$  of the sensitizers were determined in a 1:4 v/v THF:EtOH solvent mixture and the peak maxima are blue-shifted by approximately 20 nm with respect to the case when measured in chloroform [110]. Furthermore, when compared to chloroform, the spectra measured in THF:EtOH solvent mixture displayed depressed  $\epsilon$  and appear more broad by extending further into the blue region. The change in the solvent polarity results in a higher proportion of sensitizer molecules in the basic form relative to the acidic form in the polar THF:EtOH solvent mixture, leading to greater absorption in the blue-region of the spectrum. This phenomenon was examined in more detail in Section 3.3.1. Upon the adsorption of the dyes onto the TiO<sub>2</sub> surface the blue-shifts of the peak maxima are further enhanced and have been attributed to the deprotonation of the terminal carboxylic group.

### 3.4. Ullazine Sensitizers: Role of Molecular Structure

**Table 3.4.** Experimental and relative dye coverage for dyes JD21, 25, 26, 27, 29 and 30.

Dye	$\Gamma$ ( $10^{-10}$ mol cm $^{-2}$ )	$\Gamma_0^a$	$\Gamma_1^b$
JD21	1.65	0.93	0.70
JD25	0.82	0.46	0.46
JD26	1.40	0.79	0.85
JD27	0.77	0.44	0.58
JD29	1.77	1.00	1.00
JD30	1.41	0.80	0.63

<sup>a</sup> Dye coverage determined from desorption and normalized relative to JD29.

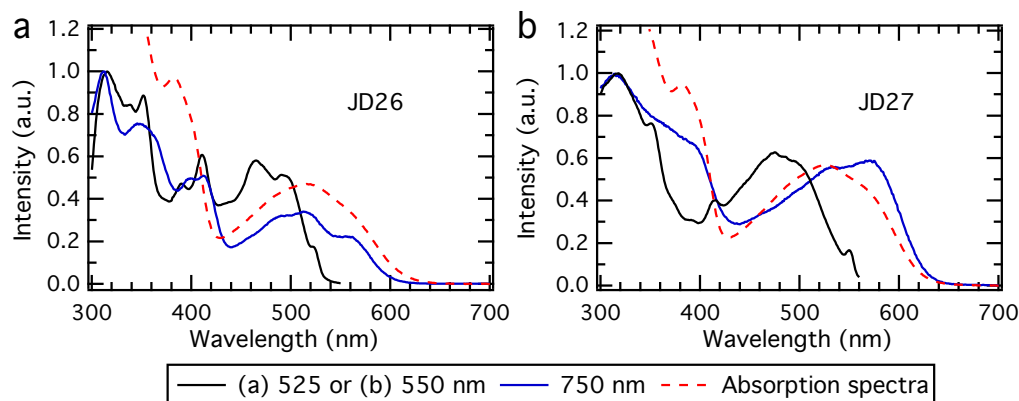
<sup>b</sup> Dye coverage calculated from the measured  $\epsilon$  and absorbance measurements on TiO $_2$  and normalized relative to JD29.

The bandgap energy  $E_g$  of the ullazine dyes were determined from the intersection of the absorbance and emission curves measured in solution and presented in Table 3.3. The values found are in good agreement with those determined in dichloromethane previously reported [110].

With regards to their application in DSSCs, it is important to consider the optical properties of the dyes when adsorbed onto TiO $_2$  in addition to the case in solution. The UV-vis spectra of these sensitizers adsorbed onto mTiO $_2$  films are presented in Figure 3.16 (c) and show distinct blue-shifts of the absorption maxima relative to the spectra measured in solution. The small feature visible between 650 and 700 nm is attributed to interference effects of such thin film samples. Furthermore these optical measurements reflect the extent of dye loading which strongly influences the device performance.

In order to gain a better understanding of the light harvesting properties of the completed devices, the extent of dye coverage  $\Gamma$  on the sensitized TiO $_2$  films was determined by dye desorption (cf. Chapter 8 Experimental Methods), the results of which are presented in Table 3.4. It is interesting to note that JD29, with the bulkiest donor group, showed the highest amount of dye uptake. In the case of JD25 and JD27, these sensitizers indicated the lowest dye uptake. The relative dye coverage of the ullazine sensitizers calculated from  $\epsilon$  and the absorbance measurements on TiO $_2$  (see Figure 3.16 (c)) are in good agreement with the dye loading determined by desorption as presented in Table 3.4.

JD25 shows only 46% of dye coverage relative to JD29. Excluding JD29, this can be explained by increased steric hindrance close to the TiO $_2$  surface introduced by the presence of the additional alkoxy chains on the ortho position of the phenyl group of the donor structure, resulting in relative  $\Gamma$  values of JD21 > JD25 and JD26 > JD27. In the case of JD29, while it does have a bulky donor structure, there is a greater distance between the alkoxy chains of the group and the TiO $_2$  surface. Furthermore it is possible that the structure of the triphenylamine (TPA) donor group directs the sterically blocking alkoxy groups away from the TiO $_2$



**Figure 3.17.** Excitation spectra determined at 750 and (a) at 525 nm for JD26 or (b) at 550 nm for JD27. The absorption spectra have been added for comparison purposes (red dashed)

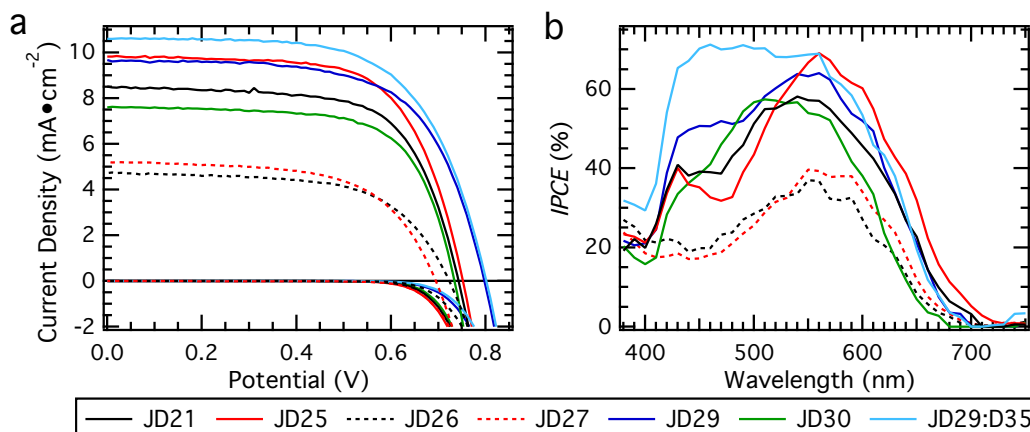
surface. Consequently the JD29 molecules may pack more homogeneously and efficiently on the TiO<sub>2</sub> surface leading to better dye adsorption and hence higher surface coverage relative to the sensitizers where the alkoxy groups are closer and/or directed towards the TiO<sub>2</sub> surface.

The Stokes shift (difference between position of the maxima of the absorption and emission spectra corresponding to the same electronic transition) of JD29 and 30 were determined to be 51 and 50 nm respectively which are considerably greater than JD21 and 25 (25 and 20 nm respectively). This suggests that there is significantly more structural reorganization upon photoexcitation for the former pair. This can be attributed to the extended donor group of JD29 which results in greater structural rearrangement upon emission. JD30 is not expected to have any significant electronic rearrangement energy based on the donor group. However unlike the other ullazine dyes, which, upon excitation, have some delocalization of the HOMO orbital across the aryl components of the donor groups, for JD30 the orbital exists only upon the ullazine core [110] leading to a lot of bond length changes on the ullazine core.

The unusual emission profile of dyes JD26 and 27 displayed in Figure 3.16 (d) suggest the degradation of the dye molecules in the solution. Consequently it is not possible to clearly determine the Stokes shift for JD26 and 27 due to the combined contribution from decomposition product and the dye molecules present in the dye solution to the emission profile. The presence of an aldehyde precursor resulting from a possible decomposition pathway for electron rich, sterically hindered aryl substituted cyano acrylic acids such as JD26 and 27 [111] was confirmed by thin layer chromatography (TLC).<sup>10</sup>

Figure 3.17 displays the excitation spectra of JD26 and JD27 respectively probed at 525 or

<sup>10</sup> In addition to the bands associated with the ullazine dyes the TLC measurement revealed the formation of less polar, orange bands which had retardation factors ( $R_f$ ) corresponding to the starting aldehyde of the ullazine dyes. Furthermore these bands displayed the same color and fluorescence under long wave UV illumination (365 nm) as the starting aldehyde materials on silica gel. The decomposition product was not formed in large enough quantity to be observed by NMR.



**Figure 3.18.** (a)  $J$ - $V$  characteristics measured under dark and  $100 \text{ mW cm}^{-2}$  AM1.5G solar intensity and the corresponding (b) IPCE spectra of ssDSSCs using ullazine dyes as sensitizers.

550 nm emission wavelength. The spectra show significant differences relative to those probed at 750 nm emission wavelength. This confirms the presence of a decomposition product in addition to the dye molecules, each species exhibiting different fluorescence profiles. The excitation spectra determined at 750 nm are similar to the absorption spectra for JD26 and 27, indicating that this species corresponds to the original sensitizer molecules, assuming that the dye dominates the absorption spectra. The excitation profile determined at 525 or 550 nm for JD26 and 27 respectively show similar features, suggesting that this is the same species for either dye, believed to be the aldehyde precursor resulting from the dye degradation.

### 3.4.2 Photovoltaic Performance

The  $J$ - $V$  characteristics measured under standard AM1.5G illumination ( $100 \text{ mW cm}^{-2}$ ) of ssDSSCs made using these ullazine dyes as sensitizers are presented in Figure 3.18 (a). The corresponding photovoltaic performance parameters are summarized in Table 3.5.

JD29 displays the highest  $PCE$  of 4.95% which can be attributed to its significantly higher  $V_{OC}$  of 797 mV. In the previous Section 3.3 the effect of the donor group of D- $\pi$ -A sensitizers on the  $V_{OC}$  was examined. One of the factors contributing to the  $V_{OC}$  was determined to be the extent of dye coverage which is confirmed here.

With the exception of JD25, which suffers from poor dye loading, a direct relationship between the surface coverage and the  $V_{OC}$  was observed. JD29 not only displays the highest  $V_{OC}$ , but also the highest dye coverage. In contrast the lowest  $V_{OC}$  and surface coverage were observed for JD27. While JD25 has a lower  $V_{OC}$ , it has similarly high  $J_{SC}$  of  $9.7 \text{ mA cm}^{-2}$ , leading to a marginally lower  $PCE$  of 4.88%. The low dye coverage is compensated by the higher  $\epsilon$  resulting in a high  $J_{SC}$ . The contrary is observed in the case of JD27, where its low  $\epsilon$  and dye coverage produce a lower  $J_{SC}$  of  $5.2 \text{ mA cm}^{-2}$ , which together with a  $V_{OC}$  of 694 mV and a  $FF$

### Chapter 3. Molecular Sensitization for Solid-State Solar Cells

**Table 3.5.** Photovoltaic performance parameters extracted from  $J$ - $V$  measurements of ssDSSC devices using JD21, 25, 26, 27, 29 and 30 as sensitizers. InteAll devices were masked to achieve an illuminated area of  $0.2025 \text{ cm}^2$ . Integrated current densities determined from the overlap of the  $IPCE$  spectrum with the AM1.5G solar photon flux.

Dye	Integrated Current Density ( $\text{mA cm}^{-2}$ )	$V_{OC}$ (mV)	$J_{SC}$ ( $\text{mA cm}^{-2}$ )	$FF$	$PCE$ (%)
JD21	7.8	743	8.5	0.66	4.19
JD25	8.8	752	9.7	0.66	4.88
JD26	4.8	723	4.7	0.62	2.11
JD27	5.0	694	5.2	0.61	2.19
JD29	8.7	797	9.7	0.64	4.95
JD30	6.8	733	7.5	0.68	3.78
JD29:D35 <sup>a</sup>	10.2	801	10.6	0.64	5.40

<sup>a</sup> 7:5 v/v ratio of JD29 and D35 in 0.1 mM dye solutions in THF:EtOH 1:4 v/v solvent mix.

of 0.61 generate a  $PCE$  of 2.19%. In the case of JD26, which shows higher dye coverage, a net surface dipole effect could explain the higher  $V_{OC}$  of 723 mV. The lower  $\epsilon$  and blue-shift of the UV-vis spectrum of JD26 suggest that it has the poorest light harvesting ability which is in good agreement with the low  $J_{SC}$  of  $4.7 \text{ mA cm}^{-2}$  from the  $J$ - $V$  and  $IPCE$  measurements, see Figure 3.18 (b).

In comparison to JD25 and 29, the performance of JD21 and 30 are inferior at 4.19 and 3.78% due to slightly lower current densities of  $8.5$  and  $7.5 \text{ mA cm}^{-2}$  and  $V_{OC}$  of 743 and 733 mV, respectively. The  $FF$  showed some variation between 0.61 (JD27) and 0.68 (JD30) for the different devices.

The  $J_{SC}$  increased in the order JD26 < 27 < 30 < 21 < 25 = 29 which is dependent on the light harvesting and adsorption properties of the dyes, and is further reflected in the  $IPCE$  spectra shown in Figure 3.18 (b). As previously observed the poor light absorption qualities of JD26 and 27 (discernible in their low  $\epsilon$ ) account for their low current densities. In the case of JD30, its UV-vis spectra is considerably shifted to the blue compared to JD21. The  $IPCE$  spectra is strongest in the red region and achieves the highest maxima of 70% at 560 nm for JD25. Subsequently, excluding JD26 and 27, the spectra decrease in intensity and are increasingly blue-shifted for JD29, 21 and finally 30 with a maximum of 57% at 510 nm. For JD26 and 27 the  $IPCE$  does not reach a maximum above 40% at 550 nm.

The projected current density values calculated by integration of the  $IPCE$  spectra over the AM1.5G standard solar emission spectra are presented in Table 3.5 and are found to be in good agreement with the current density values determined from the  $J$ - $V$  characterization and furthermore reflect the differences observed in the  $IPCE$  spectra.

As clearly evident from the  $IPCE$  spectra, the light harvesting abilities of the ullazines is lower in the 400–500 nm range. In order to increase the amount of photons harvested, devices were

fabricated using the organic D- $\pi$ -A sensitizer D35<sup>11</sup> as a co-sensitizer. D35 has been shown to absorb well in this region of the visible spectrum [94] and thus is a suitable candidate to increase the amount of light harvested. The  $J$ - $V$  characteristics of such a device is shown in Figure 3.18 (a) and the corresponding parameters are included in Table 3.5. Solid-state DSSCs made using a cocktail solution containing 7:5 v/v ratio of 0.1 mM JD29 and D35 each, provided an overall  $PCE$  of 5.40%.

JD29 was selected as the best performing ullazine sensitizer and its high  $V_{OC}$ . The increase in  $PCE$  of the co-sensitized device can be attributed to an increase in  $J_{SC}$  due to increased light harvesting which is reflected in the  $IPCE$  spectra (see Figure 3.18 (b)). This co-sensitized device has a peak  $IPCE$  value of above 67% from 440–560 nm, which is a considerable improvement in comparison to the JD29 sensitized device which reaches a maximum of approximately 64% at 540–560 nm.

#### 3.4.3 Ullazine Dye Adsorption Mode

The anchoring properties of the dyes were examined using fourier transform infrared spectroscopy (FTIR) measurements carried out on sensitized  $TiO_2$  films. In the region corresponding to the signals arising from the anchoring groups, the spectra (Figure 3.19) are similar for all the samples. In particular they all show peaks at approximately  $1607\text{ cm}^{-1}$  and  $1385\text{ cm}^{-1}$  which are associated to the asymmetric and symmetric stretch of the carboxylate group [94, 112], indicating similar binding to the titania surface. Thus it appears that the change of the position of the anchoring group between JD21/25 and JD26/27 does not result in any change in the binding mode of the dyes. No peak was observed at  $1700$ – $1750\text{ cm}^{-1}$  associated with the carbonyl group, indicating that the dyes coordinate to the  $TiO_2$  surface using a bidentate binding mode [113].

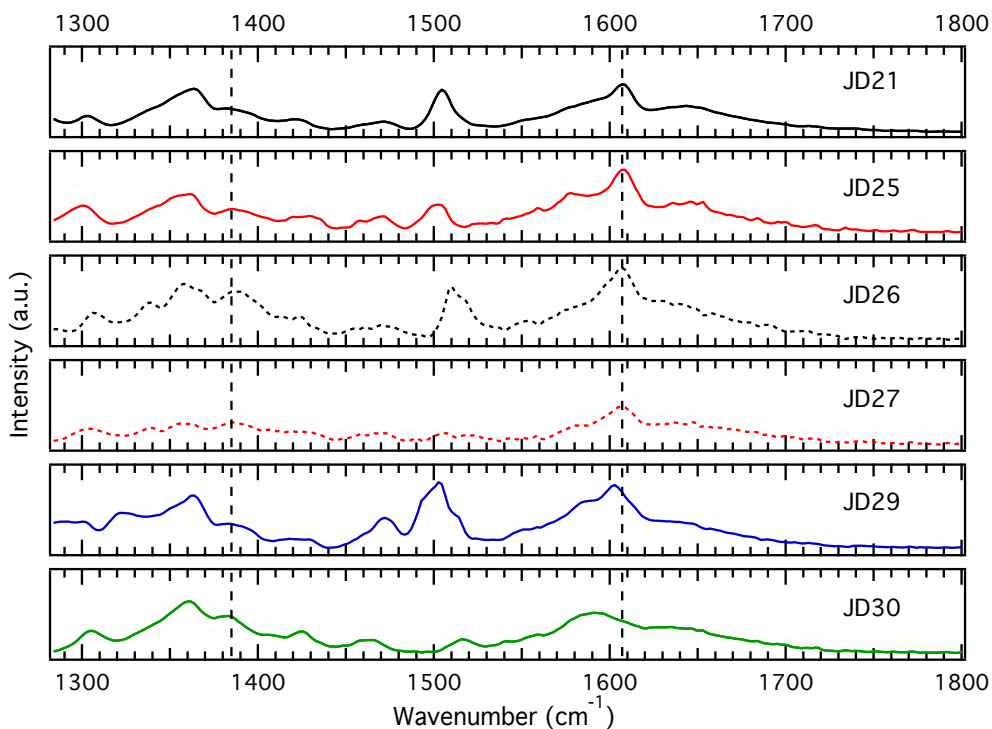
#### 3.4.4 Photoinduced Absorption Spectroscopy

To gain further understanding of the processes governing the photovoltaic performance, the role of the various donor groups and the position of the anchoring group in these ssDSSC, photoinduced absorption (PIA) spectroscopy [114, 115] measurements<sup>12</sup> were conducted (Figure 3.20). Here the transmission  $T$  through the samples was monitored in addition to any small changes in the transmission  $\Delta T$  induced by the application of a frequency-modulated monochromatic light beam. From this the change in absorbance  $\Delta A$  can be determined using  $-\Delta T/T = \ln 10 \times \Delta A$ .

Figure 3.20 (e) shows the PIA spectrum of the nanostructured  $TiO_2$  film sensitized with JD29 in the presence and absence of spiro-MeOTAD. In the absence of the HTM (blue dashed trace)

<sup>11</sup> cf. Appendix Figure A.3 for molecular structure.

<sup>12</sup> Measurements employed the same device structure as for the photovoltaic experiments, without the silver counter electrode to allow the transmission of light and using a glass microscopic slide substrate instead of FTO-coated glass.



**Figure 3.19.** FTIR spectra of ullazine dyes on  $\text{TiO}_2$ .

the absorption peak is clearly visible at 780 nm and a strong negative signal – corresponding to a bleach of the main absorption band – appears below 700 nm. Thus the PIA spectrum is believed to reflect the differential spectrum of the sensitizer upon the formation of its oxidized form.

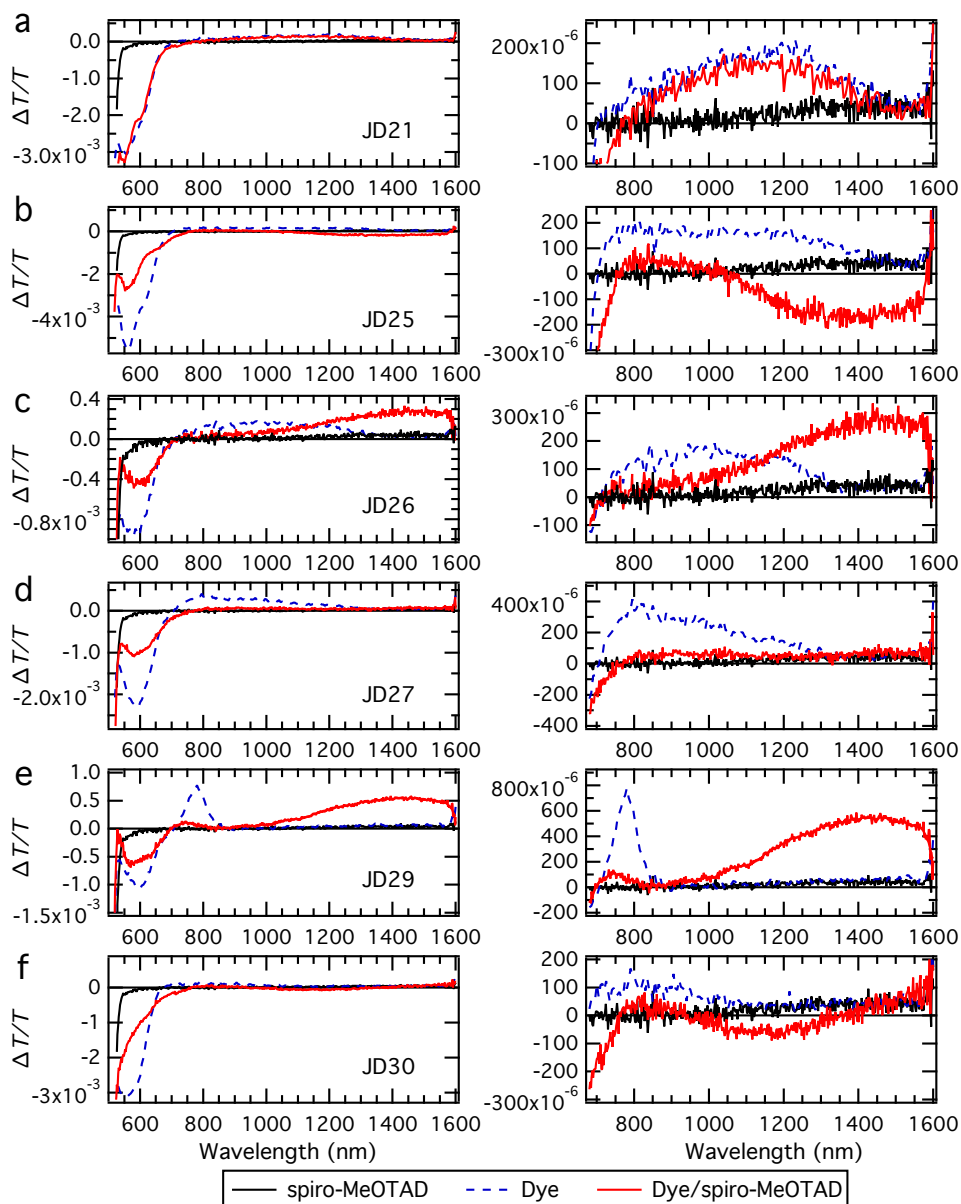
Upon the addition of the HTM (red trace), the strong peak at 780 nm is quenched, accompanied by a broad absorption around 1400 nm. This broad feature is attributed mainly to the electrons in the  $\text{TiO}_2$  and the formation of the oxidized spiro-MeOTAD (spiro-MeOTAD<sup>+</sup>) species which is known to have an absorption at approximately 1300 nm. This indicates that the oxidized dye is reduced in the presence of the spiro-MeOTAD, which is itself oxidized giving rise to the formation of spiro-MeOTAD<sup>+</sup>.

$\text{TiO}_2$  films infiltrated with spiro-MeOTAD in the absence of any sensitizer (black trace) showed little change in absorbance at  $\lambda > 600$  nm. Below 600 nm there is a bleach which originates from the absorbance of the unoxidized spiro-MeOTAD which has a very strong absorption band at 350 nm. This suggests that in the absence of dye molecules, the HTM does not inject any electrons directly into the  $\text{TiO}_2$  which would lead to a change in the oxidation state of the spiro-MeOTAD.

Similar PIA spectra were observed for JD26 (Figure 3.20 (c)), however in this case the peak



### 3.4. Ullazine Sensitizers: Role of Molecular Structure



**Figure 3.20.** PIA spectra for the  $\text{TiO}_2$  sensitized films in the presence (red solid) and the absence of spiro-MeOTAD (blue dashed). PIA spectra of  $\text{TiO}_2$  infiltrated with spiro-MeOTAD without any sensitizer (black solid). Magnification of 680–1600 nm region. The excitation wavelength used was 470 nm.

for the oxidized dye species is not as distinct as for JD29. In the presence of spiro-MeOTAD the broad absorption feature present for the sensitized film disappeared with the appearance of the broad signal at 1400 nm as in the case of JD29. In the case of JD21 (Figure 3.20 (a)) no difference was seen between the PIA spectra in the presence or absence of spiro-MeOTAD, implying that the regeneration of the dye taking place is not detected as this would lead

to a change in the spectrum arising from the spiro-MeOTAD. JD27 (Figure 3.20 (d)) shows a disappearance of a broad absorption feature in the presence of spiro-MeOTAD, but no increase in the spectrum at long wavelengths characteristic of the formation of spiro-MeOTAD<sup>+</sup> upon dye regeneration. In the cases of JD25 and 30 (Figures 3.20 (b) and 3.20 (f)) there is even a decrease in the PIA to give rise to negative peaks in this region.

Possible explanations for the lack of a clear peak that can be identified as the dye cation are 1) there is poor electron injection into the TiO<sub>2</sub> from the dye, thus any excited dye molecules immediately relax back to their ground state, 2) after electron injection, there is rapid recombination between the electrons in the TiO<sub>2</sub> and the oxidized dye and/or 3) with the spiro-MeOTAD on a timescale that is not detected by the experimental set up. Previous studies [110] determined that the cation generated for JD21, 25 and 30 is localized on the ullazine core.

In the case of JD29, it was found that it has the same affinity for a cation on the TPA donor group as on the ullazine core. This may account for the difference in the PIA spectra for the dyes adsorbed onto TiO<sub>2</sub> where the cation located on the ullazine core has a broad absorbance and no characteristic peak. The signature PIA behavior, characterized by a distinct oxidation peak is only detectable for JD29 where the cation can be localized on the TPA donor group. This may further account for better charge separation and reduced recombination upon photoexcitation, contributing to the superior device performance of JD29. For the other dyes this signal may not be distinguishable or too low in intensity.

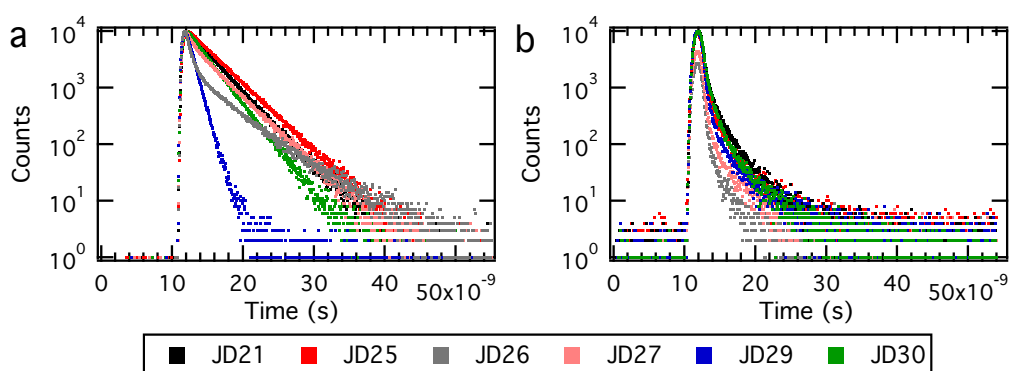
The spiro-MeOTAD is *p*-doped prior to deposition on the sensitized films during the sample preparation. Consequently, the unexpected negative signal at long wavelength for JD25 and 30 could be a result of a fast rate of recombination between holes in the oxidized spiro-MeOTAD already present in the sample and the electrons in the TiO<sub>2</sub> or even from the excited dye, relative to the rate of dye regeneration. To a lesser extent this could also pertain to JD21 and 27 where the rates of dye regeneration and recombination of electrons with spiro-MeOTAD<sup>+</sup> are similar thus resulting in no apparent change in the PIA spectrum due to the formation of oxidized HTM.

As a result, the PIA measurements indicate different extents of electron regeneration and recombination depending on the sensitizer used. Furthermore the amount of dye loading on the surface will also influence the PIA spectra. JD29, with the highest dye loading, has PIA spectra exhibiting the expected behavior. Lower dye loading allows spiro-MeOTAD to come in direct contact with TiO<sub>2</sub> increasing the rate of recombination between electrons in the TiO<sub>2</sub> and holes in the HTM. This is in agreement with the PIA spectra observed for JD21, 25, 27 and 30, where fast recombination explains the lack of a clear dye cation peak and lack or decrease of the features attributed to the spiro-MeOTAD<sup>+</sup> species. This reveals that the dye molecules also act as a blocking layer, reducing the channel of recombination between the TiO<sub>2</sub> and the HTM.

### 3.4. Ullazine Sensitizers: Role of Molecular Structure

**Table 3.6.** Fluorescence lifetimes calculated from TCSPC measurements of JD21, 25, 26, 27, 29 and 30 in solution (THF:EtOH 1:4 v/v solvent mix) and adsorbed onto TiO<sub>2</sub>. Injection yields were calculated using Equation 3.1.

Dye	$\tau_{sol}$ (ns)	$\tau_{TiO_2}$ (ps)	$\eta_{inj}$ (%)
JD21	3.2	142	> 95.5
JD25	3.6	127	> 96.5
JD26	4.4	126	> 97.1
JD27	3.5	90	> 97.4
JD29	0.9	105	> 86.4
JD30	2.6	181	> 95.1



**Figure 3.21.** TCSPC fluorescence histograms of ullazine dyes (a) in solution (THF:EtOH 1:4 v/v solvent mix) and (b) adsorbed onto TiO<sub>2</sub>.

#### 3.4.5 Time-Correlated Single Photon Counting: Injection Dynamics

Time-correlated single photon counting (TCSPC) measurements were conducted to study the excited state lifetimes of the ullazine dyes in solution and adsorbed onto TiO<sub>2</sub> films. Lifetimes in solution  $\tau_{sol}$  reflect the fluorescence lifetime of the molecules and are typically found to be on the nanosecond timescale. Once adsorbed onto the TiO<sub>2</sub>, the excited dye molecules can inject an electron into the conduction band of the semiconductor providing an alternate relaxation pathway, thus quenching the fluorescence measured and significantly decreasing the lifetime  $\tau_{TiO_2}$ . Consequently a limit for the injection efficiency  $\eta_{inj}$  can be determined from the relationship,

$$\eta_{inj} = 1 - \frac{\tau_{TiO_2}}{\tau_{sol}} \quad (3.1)$$

Injection efficiency is a crucial element in the characterization of the cell performance. For efficient device performance this process must be faster than the decay of the excited state to the ground state. The reverse reaction, the recombination of injected electrons in the TiO<sub>2</sub> and the dye cation, presents one of the major loss mechanisms to this system. Both injection and recombination kinetics have been found to depend strongly on the relative energy levels

of the conduction band of the semiconductor and the oxidation potentials of the ground and excited state dye [116–118].

Lifetimes of the excited species in solution were found to be around 3–4 ns for the ullazine dyes, with the exception of JD29, which had a considerably shorter lifetime of 0.9 ns, see Table 3.6. The fluorescence decay was found to be monoexponential for JD21, 25, 29 and 30 which is expected for such organic sensitizers in solution as is displayed in Figure 3.21 (a). However in the cases of JD26 and 27, they exhibited biexponential decay, which strongly suggests the presence of additional species with different excited state lifetimes. This further confirms the degradation of JD26 and 27 leading to the presence of a decomposition product in addition to the dye molecules as previously observed in the emission spectra.

From the excitation profiles measured at high (550 nm) and low (750 nm) energy (Figure 3.17) it is deduced that the short-lived species, dominating at high energies, is ascribed to the aldehyde precursor – identified as the decomposition product – whilst the long lived species is attributed to the original sensitizer molecules. This degradation of the dye molecules was only observed for the ullazine sensitizers with the anchor group in the 4-position of the ullazine core.

As a result of the electron injection into the semiconductor the lifetimes decreased significantly in the case where the dye molecules are adsorbed onto the  $\text{TiO}_2$  surface as shown in Figure 3.21 (b). For JD21, 25, 26 and 30 this parameter was found to range between 130 and 180 ps, whilst  $\tau_{\text{TiO}_2}$  for JD27 and 29 was considerably shorter at 90 and 105 ps respectively. The resulting injection efficiency calculated using Equation 3.1 varied between 95 and over 97% for all ullazine dyes with the exception of JD29. This suggests that after excitation almost all electrons are injected into the  $\text{TiO}_2$  rather than following the radiative decay pathway.

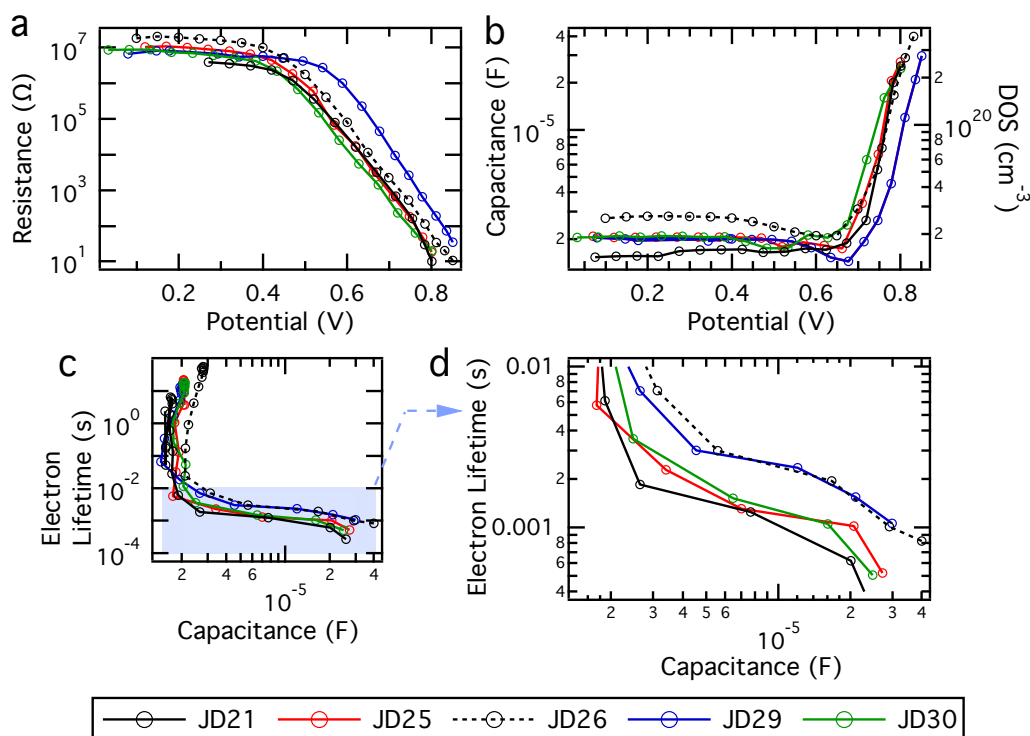
In the case of JD29, due to the inherent short-lived fluorescence lifetime of the dye molecules in solution, a smaller value for  $\eta_{inj}$  of 86.4% was found. The similarity of the results for the remaining dyes suggest the differences in the device performance may be explained by the recombination processes or the charge collection efficiency. This is in agreement with the results previously found with the PIA measurements suggesting that the rates and modes of charge recombination vary greatly depending on the sensitizer used and the extent of dye coverage.

#### 3.4.6 Transient and Impedance Characterization: Charge-Transfer Mechanisms

IS measurements carried out in the dark reveal that the charge-transfer resistance  $R_{ct}$  of devices employing JD29 as sensitizer is approximately an order of magnitude higher than JD21 (Figure 3.22 (a)). Relative to JD21, JD30 shows slightly lower resistance, whilst JD26 displays a  $R_{ct}$  shifted to slightly higher values.

The observed behavior of  $R_{ct}$  appears indistinguishable between JD21 and JD25. In order to correlate these observations with the photovoltaic performances, the cell chemical capaci-

### 3.4. Ullazine Sensitizers: Role of Molecular Structure



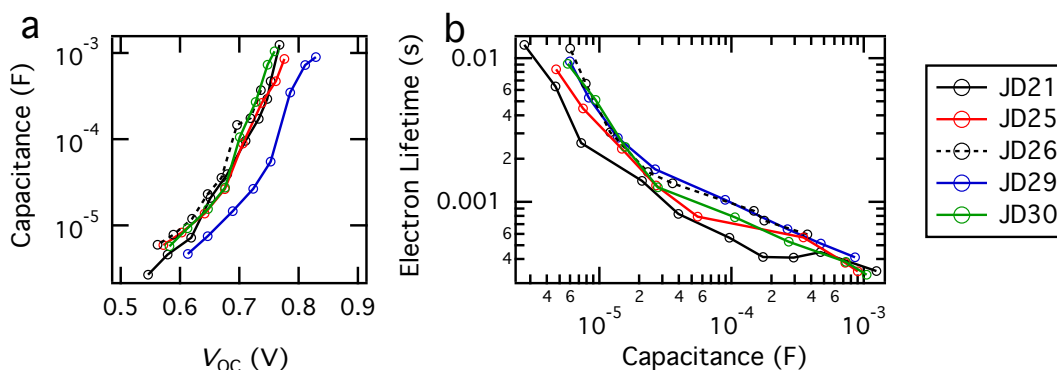
**Figure 3.22.** (a) Recombination resistance and (b) chemical capacitance obtained from IS measurements in the dark. (c) Calculated electron lifetime as a function of the capacitance and (d) high forward bias region.

tance  $C_{\mu}$  of the devices needs to be taken into account. As seen in Figure 3.22 (b), there is a clear shift in the capacitances indicating an upward shift of the CB of 40 mV for JD29 and a downward shift of 30 mV for JD30 relative to JD21. JD25 and 26 show similar cell capacitances as JD21. In the case of JD30 the shift in the conduction band relative to JD21 is reflected by a 20 mV shift in  $R_{ct}$ . This is in good agreement with the photovoltaic data which shows a difference of 10 mV in  $V_{OC}$  between devices using JD21 and 30, suggesting that this arises from a shift in the conduction band.

The shifts in the CB can be correlated with the extent of dye coverage, where the upward shift of JD29 is reflected by higher dye coverage and the downward shift for JD30 is seen in a lower dye coverage relative to JD21. Previous studies [104] and the work presented in Section 3.3 have shown the influence of the dipole moment of adsorbed molecules on the  $V_{OC}$  of DSSCs.

The devices were further characterized using transient photovoltage and photocurrents decay measurements, which demonstrated similar shifts in the CB of the  $TiO_2$  (Figure 3.23) as observed in the IS measurements.

JD29 shows a shift of approximately 90 mV in  $R_{ct}$  with respect to JD21, which when taking the CB shift of 40 mV into account leaves a difference of 50 mV which is in good agreement



**Figure 3.23.** (a) Capacitance as a function of open circuit potential and (b) electron lifetime as a function of the cell capacitance measured by transient photovoltage decay measurements.

with the difference in  $V_{OC}$  for JD21 and 29 sensitized devices. This suggests that the rate of recombination for devices using JD29 is lower in comparison to the other ullazine dyes. A similar phenomena is observed for JD26, which shows similar CB position as JD21, but a shift in  $R_{ct}$  of 20 mV. However in this case this is not reflected in the photovoltaic data, where the  $V_{OC}$  of JD26 is 20 mV lower than that of JD21. In the case of JD29, the upward shift of the CB in tandem with the increased recombination resistance, leads to the higher observed  $V_{OC}$ , consequently resulting in a decrease in driving force for the electron injection into the  $TiO_2$  from the excited state of the dye, contributing to the lower  $\eta_{inj}$  observed. In the case of JD29 the hole  $h^+$  is stabilized by to the localization of the cation on the TPA donor unit as previously determined by PIA measurements. This results in the improved charge separation and reduced recombination observed here.

In order to take into account the differences in the CB position of the devices, the electron lifetime calculated from the recombination resistance and chemical capacitance extracted from the IS measurement is plotted as a function of the chemical capacitance depicted in Figure 3.22 (c). At similar DOS, which is directly proportional to the capacitance, the electron lifetime is longest for devices using JD29 and 26 due to lower rates of recombination which is translated to a higher  $V_{OC}$  for JD29. The same trends are observed in the electron lifetime determined from the transient photovoltage decay measurements, see Figure 3.23. The reasons for the unexpectedly low  $V_{OC}$  of JD26 remain unclear, however it is possible to correlate its lower dye loading with a lower net surface dipole moment.

### 3.5 Conclusions

In this chapter the device mechanisms of complete solid-state DSSCs were investigated using different types and classes of molecular sensitizers. The photovoltaic performance of the devices was examined and correlated with the chemical and physical properties of the dyes utilized.

### 3.5.1 Squaraine Sensitizers

The dye self-assembled aggregation for the squaraine dye JD10 on mTiO<sub>2</sub> films was examined in conjunction with different additives. Both the de-aggregating agent, CDCA and the HTM, spiro-MeOTAD were found to decrease the absorption band attributed to the presence of dye aggregates. The two de-aggregating components were found to work synergistically in reducing the aggregation of JD10 on TiO<sub>2</sub> films.

Within the class of squaraine sensitizers, JD10 displays an outstanding *PCE* of 3.16% in ssDSSC devices. The performance was further improved to 4.42% in combination with a metal-free dye, D35. The increase in efficiency was achieved predominately through an increase in the photocurrent, which is the result of greater light absorption in the 400–550 nm visible region. The *IPCE* of the co-sensitized photovoltaic devices clearly displays the contributions from the individual sensitizers.

Independent measurements techniques (IS and transient photovoltage decay) showed a downward shift in the CB for the co-sensitized device relative to the D35 device, which is in agreement with the *J–V* measurements. Furthermore, the increased charge-transfer resistance determined for the D35 and co-sensitized devices in comparison to the JD10 sensitized device suggest that D35 has a lower recombination rate and its incorporation into the JD10 devices retards this process slightly.

### 3.5.2 D- $\pi$ -A Sensitizers

The photovoltaic performance of organic D- $\pi$ -A dyes in ssDSSCs and the influence of the donor group on the  $V_{OC}$  was explored. The DOS derived from photovoltage transient decay and impedance spectroscopy measurements are in good agreement with the photovoltaic performance and show that the increase in  $V_{OC}$  can be attributed to an upward shift of the CB of the TiO<sub>2</sub> for Y123 and JK2 relative to C220 or C218. The presence and length of the alkyl substituents on the bridge segment of the dye molecules plays an important role in dye surface coverage, which influences the net surface dipole effect and contributes to the observed CB shift.

The different donor groups, having different extents of interaction with the HTM, lead to different charge-transfer rates at the spiro-MeOTAD/dye interface. It is further believed that the different donor groups influence the pore-filling of the solid HTM and its interconnectivity when it is deposited out of solution by spin-coating, thus affecting the transport properties of the spiro-MeOTAD. The upward CB shift of Y123 relative to C220 or C218 is believed to originate from a contribution of the higher net surface dipole moment effect arising from higher dye coverage and a higher surface blocking effect resulting from a lower spiro/dye interaction energy due to its donor group which is believed to lead to reduced recombination.

### 3.5.3 Ullazine Sensitizers

Ullazine dyes are presented as sensitizers in ssDSSCs with *PCEs* of up to 5%. It was found that the rates of recombination was greatly influenced by the dye donor molecular structure. The localization of the cation on the TPA unit and the extended structure of the donor group of JD29 improved charge-separation and hindered the direct recombination of electrons from the excited dye species with the ground state. Furthermore the dye structure also hinders the recombination of electrons from the TiO<sub>2</sub> and the oxidized dye or the oxidized HTM. The reduction in recombination is reflected in a high *V*<sub>OC</sub>. Additionally the dye coverage for JD29 is highest of this series of ullazine sensitizers, which could lead to higher net surface dipole effect, leading to an upward shift in the CB. Consequently JD29 was reported with the highest *PCE* of 4.95% for this series of sensitizers, which can be mainly attributed to its high *V*<sub>OC</sub>. The *J*<sub>SC</sub> was further improved by increasing the light harvested through the use of D35 as a cosensitizer, leading to a *PCE* of 5.40%.

The donor groups and the position of the anchoring groups, which is also the acceptor, not only influenced the rates of recombination, but greatly effected the optical properties of the dyes, which play a crucial role in the device performance. Changing the position of the anchoring group for the dyes JD21 and 25 from the 5-position to the 4-position to give the analogue structures JD26 and 27, introduced considerable steric hindrance and additionally resulted in the group being twisted perpendicular to the ullazine core. Their low performance can thus be attributed to their extremely low molar extinction coefficients, and in the case of JD27, the low dye coverage resulting from the steric hindrance originating from the additional alkyl chain. This latter effect is also observed in the case of JD25 which has shows a low dye coverage which contributes to a lower recombination resistance and hence *V*<sub>OC</sub>.

### 3.5.4 Perspectives

This chapter highlights the importance of careful and targeted design of the individual components to optimize the physical and chemical properties of the molecular sensitizers used in ssDSSC. The light-harvesting, dye-loading properties and the stability of the sensitizers play a critical role for the photovoltaic performance.

Furthermore as has been shown here each sensitizer has unique properties that may be beneficial or detrimental to the photovoltaic performance in ssDSSCs. High molar extinction coefficient dyes absorbing light across a wide spectral range in the visible region are crucial to generate the high *J*<sub>SC</sub> necessary to achieve high *PCEs*. ‘Black dyes’ have been developed in an attempt to achieve these requirements, displaying near panchromatic absorption across the visible region, but due to their inherently low molar extinction coefficients they require thick mTiO<sub>2</sub> layers to harvest sufficient light. As such they are inappropriate for the use in ssDSSC, where the mTiO<sub>2</sub> thickness is limited due to the poor pore infiltration of the HTM. The technique of co-sensitization is a noteworthy alternative to circumvent the need of a singular dye that has this ideal absorption profile.



The near-infrared light absorption of squaraine dyes classifies them as good candidates for co-sensitization with complimentary absorption profiles. Furthermore their characteristic narrow and intense light absorption makes them valuable as selective photon absorbers as might be the case for tandem cells or in conjunction with energy relay dyes.

IS was used to successfully analyse the internal workings of the ssDSSCs and correlate the photovoltaic performance with the molecular structure of the dye sensitizers.



# 4 Impedance Spectroscopic Analysis of Perovskite Solid-State Solar Cells

*The chapter is based on the publication Dualeh et al. ACS Nano, 2014, vol. 8, 362–373.*

## 4.1 Introduction

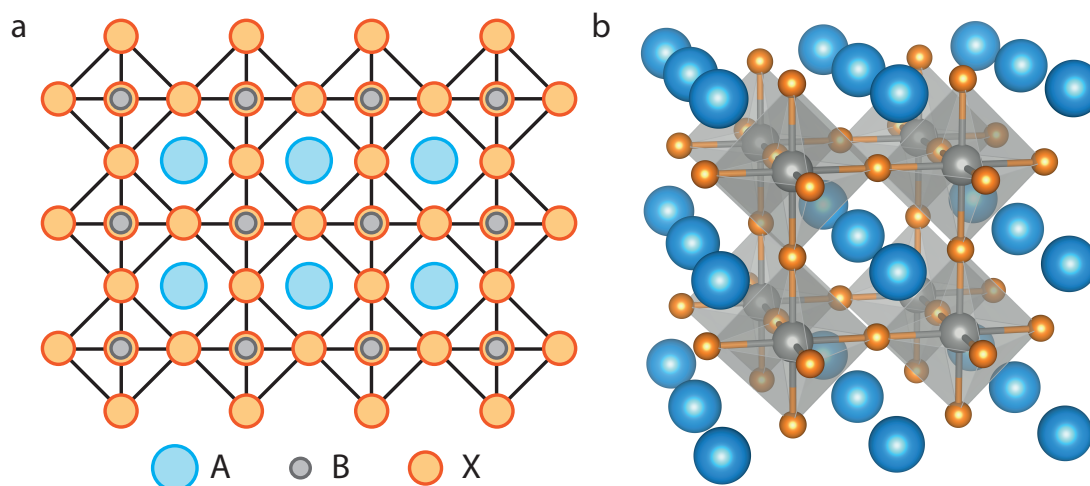
One of the main limitations of the solid-state mesoscopic solar cell system is the fast electron-hole recombination. As the recombination resistance scales inversely with film thickness, the nanostructured metal oxide layer is typically restricted to less than  $3\ \mu\text{m}$  to ensure the maximum possible charge collection. Similarly problems arising from incomplete pore infiltration of the  $\text{mTiO}_2$  by the HTM limit the film thickness. However reducing the film thickness also limits the amount of light harvested by the system and thus the photocurrent generated.

High molar extinction coefficient molecular sensitizers have been implemented to overcome this problem (cf. Chapter 3), but even for the best performing ssDSSCs there is still room for improvement to achieve complete light absorption.

As such there has been considerable interest in the development and implementation of materials with higher light absorption abilities such as inorganic semiconductor quantum dots [119–122]. More recently organic-inorganic hybrid perovskites have gained significant interest, leading to a paradigm shift in the field of solid-state nanostructured solar cells and for the first time since its conception, the solid-state analogue out performs its liquid-state counterpart.

### 4.1.1 Organic-Inorganic Hybrid Perovskite

Perovskite is a calcium titanium oxide mineral – specifically calcium titanate,  $\text{CaTiO}_3$  – named after the Russian mineralogist Lev Perovski. This name is now used to describe the class of compounds that have the same crystal structure, characterized by the general formula  $\text{ABX}_3$  where A and B are cations (the ionic radius of A is larger than B) and X is an anion that bonds to both cations. The ideal perovskite structure has cubic-symmetry, where the A cation is



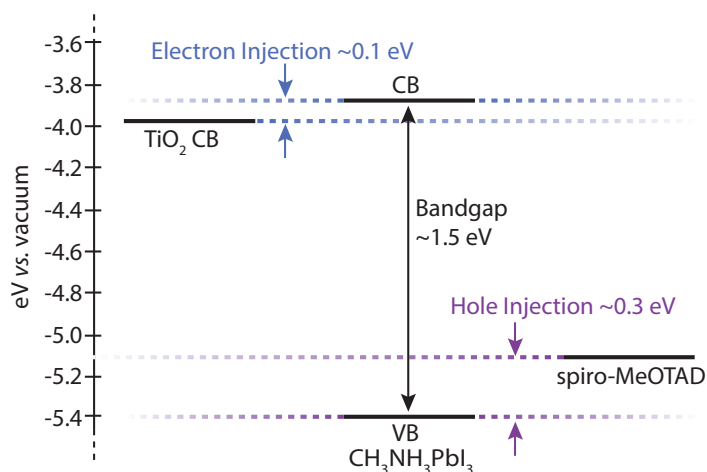
**Figure 4.1.** (a) Perspective and (b) projected view of the 3D  $ABX_3$  perovskite structure.

12-fold coordinated by the X anion in a cuboctahedral arrangement and the B cation is 6-fold coordinated by X in an octahedral configuration as depicted in Figure 4.1. Hence the A cation is positioned in the corner positions of the unit cell (0, 0, 0), B is at the body centred position (1/2, 1/2, 1/2) and the X anions sit in the face centered positions (1/2, 1/2, 0). The result is corner sharing  $BX_6$  octahedra with the A cation placed at the centre of the cube formed.

The organic-inorganic hybrid perovskite materials have long been of interest due to their unique optical, electronic and magnetic properties which can be further tailored by manipulation of the individual organic and inorganic components [123–125]. The general formula of the class of organic-inorganic hybrid perovskite material of interest here is  $RNH_3MX_3$ , where  $RNH_3$  ( $R = C_nH_{2n+1}$ ) is the organic component and  $MX_3$  ( $M = \text{metal such as Pb or Sn, X = I, Br or Cl}$ ) is the inorganic component [126]. The small monovalent organic component adopts the role of the A cation in the general perovskite structure. The divalent group 14 metal ion of the inorganic component constitutes the B cation and the X anion are the associated halides. The relative size requirements of the individual ionic components determines the stability of the cubic structure of the material, where deviation from the ideal structure produces lower-symmetry versions and phases.

Depending on the relative size of the two cationic species, the three-dimensional (3D) ideal cubic structure is distorted generating the tetragonal and orthorhombic phases or even the two-dimensional (2D) layered structure. For the latter case the 3D structure is broken into 2D layers of corner sharing  $BX_6$  octahedra separated by a double layer of organic cations with the general formula  $A_2BX_4$ . For the hybrid organic-inorganic perovskites discussed here this occurs when the relative size of the monovalent organic cation is increased [126–129].

The properties of the methyl ammonium lead-iodide perovskite  $CH_3NH_3PbI_3$  fulfill the necessary requirements that make it an attractive light absorbing material for application in photovoltaics. It has a direct bandgap of 1.54 eV with its valence and conduction bands positioned



**Figure 4.2.** Energy schematic illustrating the relative position of the conduction and valence bands of  $\text{CH}_3\text{NH}_3\text{PbI}_3$  with respect to the CB of  $\text{TiO}_2$  and the HOMO level of spiro-MeOTAD.

respectively at  $-5.4$  eV and  $-3.9$  eV *versus* vacuum [49, 130]. These energetics provide suitable driving force for electron injection into the  $\text{TiO}_2$  CB (approximately 0.1 eV) and hole injection into the HOMO level of the spiro-MeOTAD (approximately 0.3 eV) as illustrated in Figure 4.2. Furthermore it is relatively air stable, however due to the presence of the hygroscopic organic cation it is moisture sensitive and thus undergoes degradation in humid conditions. Finally its good solubility makes this material very attractive for solution-processing techniques.

While Lee *et al.* [50] showed that a mixed-halide perovskite on a mesoporous  $\text{Al}_2\text{O}_3$  photoanode acts both as light absorber and electron conductor, Etgar *et al.* [131] demonstrate that the pure iodide perovskite can act as a hole conductor. Similar to Etgar *et al.*, Chung *et al.* [10] showed that the perovskite material,  $\text{CsSnI}_3$ , also functions as a hole conductor.

This demonstrates the interesting property of perovskites in that they do not only act as light absorbers but also participate in charge conduction. Furthermore the perovskite halides show another interesting effect since they do not only possess electronic charge conduction but additionally exhibit ionic charge conduction. Perovskite-type oxide materials are important ionic conductors in the field of lithium ion batteries and in solid oxide fuel cells as fast ion conductors [132], in lead zirconium titanate (PZT) applications [133] or as ferroelectrics (i.e.  $\text{BaTiO}_3$  [134]). In the case of a perovskite-type oxide  $\text{La}_{2/3}\text{TiO}_3$ , lithium ion conduction has been observed when lithium is partially substituted for lanthanum and the measured conductivity was one of the highest for lithium ion conductors chemically stable at ambient atmospheric conditions [135]. In this structure 1/3 of the A-sites of the perovskite structure are vacant, allowing the Li ions (which are substituted for La in A-sites) to move through the vacancies.

Ionic conduction has also been reported for perovskite-type halides such as  $\text{CsPbCl}_3$ ,  $\text{CsPbBr}_3$  and  $\text{KMnCl}_3$  [136] and believed to be a result of the migration of halide-ion vacancies. The ionic

conductivity of the halide ions can be significantly enhanced through doping as demonstrated by increasing fluoride ion conductivity resulting from the partial replacement of F in  $\text{KCaF}_3$  by oxygen [137, 138].

The ease with which these organic-inorganic hybrid perovskite materials can be prepared and processed from solution [124, 139] whilst simultaneously providing desired device characteristics have made them an attractive alternative to amorphous silicon in the field of semiconductors. The relationship between the organic and the inorganic components and its impact on the material structure and properties can be exploited to design and develop materials for targeted applications [140–142]. Generally the relatively simple organic component in these hybrid structures has been found to play a secondary role in determining the physical properties and serve more to define the crystal structure of the material. This is the case for the conducting tin(II)-halide based perovskite where the high conductivity arises due to the high mobility of the tin-iodide layers while the organic component define the structure [129]. Alternatively the use of oligothiophene chromophores as the organic component in combination with lead(II) halide layers allowed charge-transfer between the separate components and thus not only defined the dimensionality of the lead(II) halide layers, but determined the photoluminescent properties of the material [141]. Chang *et al.* [143] examined not only the electronic and structural properties of the lead-halide based organic-inorganic perovskite  $\text{CH}_3\text{NH}_3\text{PbX}_3$  (X=Cl, Br, I) but determined that the physical coupling between the organic and inorganic components is weak, allowing easy rotation of the organic  $\text{CH}_3\text{NH}_3^+$  constituent. Unlike other composite materials where inorganic and organic components are often either randomly arranged or any order is only short-ranged, this hybrid perovskite class of materials display long-range order in the crystal structure [129, 141].

At elevated temperatures above  $56^\circ\text{C}$  the crystal structure of  $\text{CH}_3\text{NH}_3\text{PbI}_3$  adopts the ideal cubic perovskite phase. In this phase the organic  $\text{CH}_3\text{NH}_3^+$  constituent undergoes rapid reorientation and can occupy up to 24 different disordered states due to the weak physical coupling between the organic cation and the inorganic framework [144]. Distortion of the inorganic framework at lower temperatures leads to phase transitions to the common non-cubic variants. Between  $54$  and  $-121^\circ\text{C}$  the degree of symmetry of the structure is reduced assuming the tetragonal crystal phase, decreasing the number of disordered states available for the organic cation to 8. At temperatures below  $-121^\circ\text{C}$  the perovskite crystal phase becomes orthorhombic, fixing the  $\text{CH}_3\text{NH}_3^+$  in place.

A further advantage of these materials is the possibility to tune their light harvesting capabilities by chemical management as shown by Noh *et al.* [145]. This further allows more freedom and improved matching between the perovskite and the HTM used [146–148].

The system investigated in this chapter uses the lead-iodide based perovskite  $\text{CH}_3\text{NH}_3\text{PbI}_3$  as light absorbing material in a solid-state mesoscopic heterojunction style solar cell employing the amorphous organic *p*-type semiconductor spiro-MeOTAD as the hole-transport material. The lead-iodide perovskite used here is deposited by spin-coating from a 1:1 molar ratio

## 4.2. Considerations of the Systems and Impedance Spectroscopy

---

solution of  $\text{PbI}_2$  and  $\text{CH}_3\text{NH}_3\text{I}$  in  $\gamma$ -butyrolactone (GBL) directly onto the mesoporous  $\text{TiO}_2$  films following the procedure reported by Kim *et al.* [49]. These films are subsequently annealed at  $100^\circ\text{C}$  for 10 minutes, leading to the formation of crystallites of the organic-inorganic lead-iodide based perovskite,  $\text{CH}_3\text{NH}_3\text{PbI}_3$ .

The versatility of this organic-inorganic hybrid perovskite materials and the multitude of deposition methods, treatments and device architectures reported for  $\text{CH}_3\text{NH}_3\text{PbI}_3$  alone have resulted in the rapid improvement of the photovoltaic performance of corresponding solar cells and multiple record breaking *PCEs* of up to 16% [149, 150]. This incredible development is mainly a result of optimized and improved perovskite material films. The importance of the material composition, crystal structure and film morphology will be discussed in further detail in Chapters 5 and 6.

## 4.2 Considerations of the Systems and Impedance Spectroscopy

Impedance spectroscopy measurements are conducted in order to investigate the internal electrical processes and to quantitatively and qualitatively analyze the associated parameters of perovskite-based solid-state solar cells. This study aims to interpret the IS measurements of these devices, using the established equivalent circuits used for DSSCs as a starting point and basis for the development of a well-defined model.

In general IS is nowadays one of the most utilized techniques to analyze liquid DSSC devices. Although it is a relative long procedure from performing the initial measurement, fitting of the resulting impedance spectra to the analysis of the extracted data, this technique rewards the investigator with deep insights about the fabricated devices.

The equivalent circuit model employed for a liquid DSSC in the dark consists of a one channel transmission line model (describing the chemical capacitance and the recombination and transport resistance in the  $\text{TiO}_2$ ) in series with an RC element for the counter electrode and, depending on the applied potential, a Warburg diffusion resistance for the ionic transport in the electrolyte (cf. Figure 1.12 Chapter 1) at intermediate and higher forward biases. At low forward bias when the mesoporous  $\text{TiO}_2$  is insulating, an RC element for the FTO or compact  $\text{TiO}_2$  underlayer of the photoanode in contact with the electrolyte has to be employed instead of the transmission line branch for the  $\text{mTiO}_2$ . A modified but similar model is used to simulate the impedance response of ssDSSCs [54, 68] (cf. Chapter 2). In the ssDSSC equivalent circuit an additional RC element has to be implemented instead of the Warburg impedance element. The additional RC –  $R_{\text{HTM}}$  and  $C_{\text{HTM}}$  – represents the transport of charges inside the HTM if the hole conductor is not doped sufficiently or the hole mobility is too low.

At the time when this work was conducted there was only one investigation of perovskite-based solar cells by IS reported [151]. It provides valuable information on the capacitive behavior inside these devices though the behavior of parameters like recombination resistance or transport resistance still remains unclear. In this chapter a thorough analysis is presented

from which all the resulting information and subsequent conclusions can be drawn [152].

The device configuration of the perovskite-based solid-state solar cell shares similarities with the well-known liquid electrolyte-based DSSC as is depicted in Figure 4.3. Instead of a layer of dye molecules adsorbed on the surface of the  $\text{mTiO}_2$  as in the liquid and solid-state DSSCs, the perovskite material will cover major areas of the  $\text{mTiO}_2$  with several nanometer thick layers or crystallites. The impact of the degree of  $\text{mTiO}_2$  coverage by the perovskite material is unclear and a point of major interest for several reasons. The recombination of electrons from the  $\text{mTiO}_2$  with holes in the HTM may involve an additional step through the perovskite layer. Furthermore the conduction band position and/or the charge-transport in the  $\text{mTiO}_2$  can be affected either due to the hindered accessibility for TBP or  $\text{Li}^+$  ions, normally crucial for the performance of especially the ssDSSCs, or due to the change of the ionic environment by the perovskite coverage.

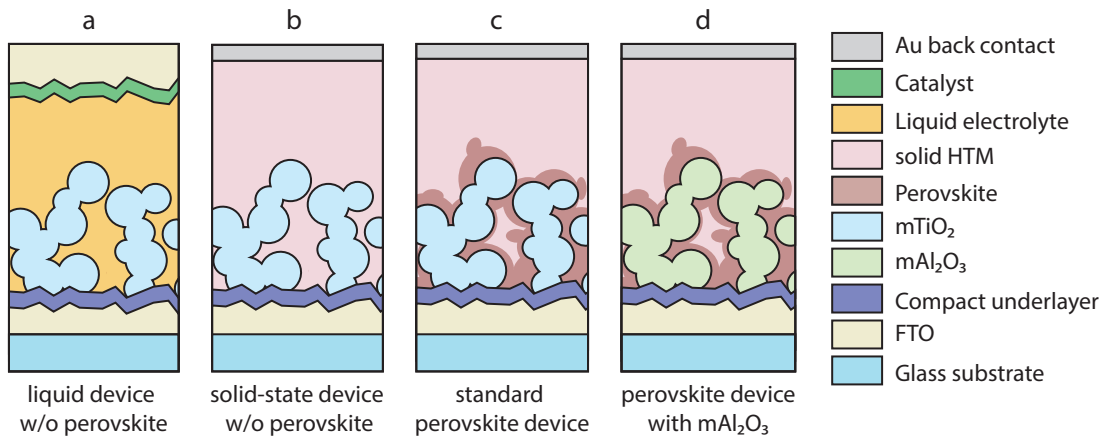
In the case of its solid-state analogue – the ssDSSC – the thickness of the  $\text{mTiO}_2$  layer is limited by the pore infiltration of the organic hole-transport material and its short diffusion length of charge carriers. Consequently ssDSSCs generally use thinner  $\text{mTiO}_2$  films of 2–3  $\mu\text{m}$  compared with the liquid-state alternative, which use up to 15 or even 20  $\mu\text{m}$ . In the case of the perovskite-based solar cells, 300–600 nm of  $\text{mTiO}_2$  film thickness is generally employed, representing a further reduction of 10 to 30 times relative to the solid-state and liquid DSSC systems. The pore-filling of the  $\text{mTiO}_2$  with the HTM is expected to be higher and thus is expected to not be a limiting or irreproducible step.

Due to the reduction of the  $\text{mTiO}_2$  film thickness to the submicrometer scale the relation between the interface of the compact blocking layer/ $\text{mTiO}_2$  and the surface area of the latter is considerably altered. Consequently the influence of the underlayer is much more pronounced for this system using such thin film thicknesses. The complexity of this system is underlined by its various capacitances; 1) the space-charge capacitance of the blocking layer, 2) ionic capacitances in the HTM/blocking layer and HTM/ $\text{mTiO}_2$  interfaces and 3) the chemical capacitance of the  $\text{mTiO}_2$  which is relatively small due to the low active film thickness. As a result of the change in the active layer thickness the interplay of these capacitances will differ from the conventional ssDSSC.

In order to build an equivalent model for this system it is necessary to determine the DC current and IS characteristics for devices utilizing such small active layer thicknesses. The typical photoanode for a standard perovskite device consists of 300–600 nm thick  $\text{mTiO}_2$  film deposited on a compact  $\text{TiO}_2$  blocking layer on FTO coated glass substrate. To elucidate the behavior of these thin active layers, liquid and solid-state DSSC type devices using an iodine electrolyte and spiro-MeOTAD were fabricated (without any perovskite or dye adsorbed) using the same type of submicrometer photoanode. These devices were subsequently analyzed using the well established existing equivalent models described above and compared to a standard perovskite device. The device configuration of the different systems under consideration are depicted in Figure 4.3.



## 4.2. Considerations of the Systems and Impedance Spectroscopy

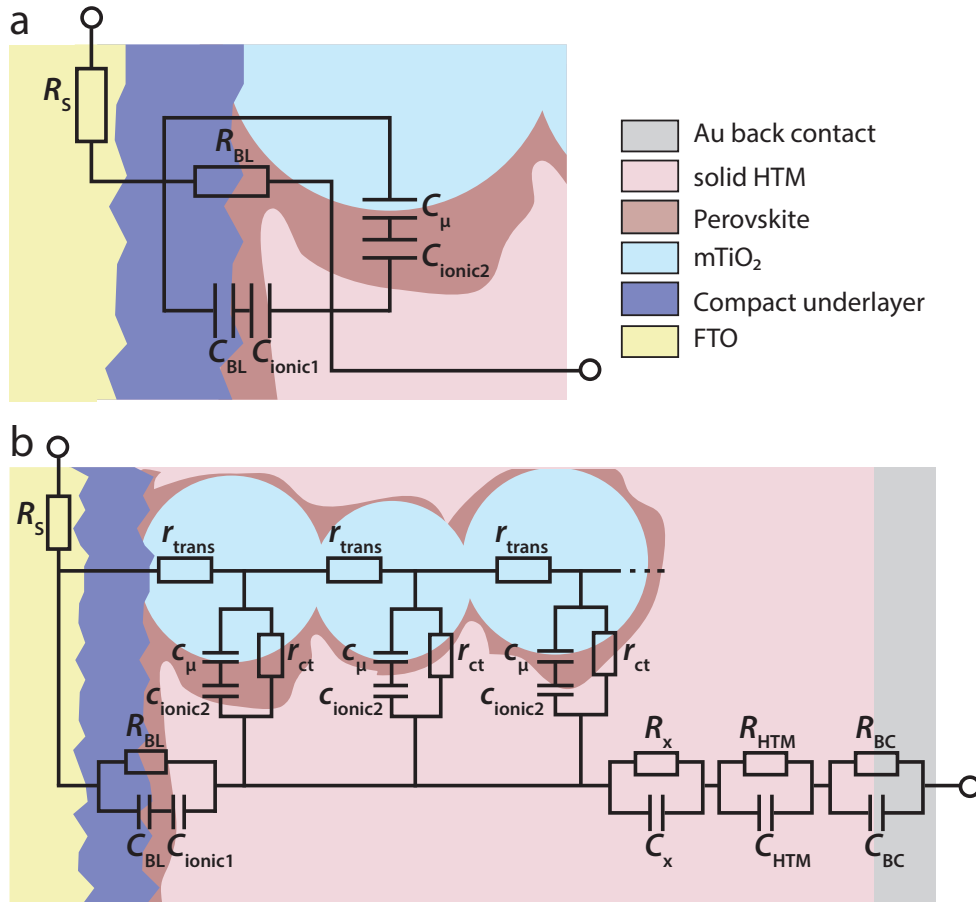


**Figure 4.3.** Device configuration for the different systems under consideration, not drawn to scale. (a) liquid iodine device; (b) solid-state device without perovskite, (c) solid-state device with perovskite, (d) solid-state device with perovskite using  $m\text{Al}_2\text{O}_3$  in place of  $m\text{TiO}_2$ . Figure not to scale.

In the conventional DSSC, the role of the dye sensitizer is to absorb the light and then separate the charges by injecting the electron into the  $m\text{TiO}_2$  and transferring the hole to the reduced species of the redox couple in the electrolyte which is then regenerated at the counter electrode. The corresponding situation in the perovskite solar cell is not as straightforward, where electron injection into the  $m\text{TiO}_2$  is seemingly not essential to achieve high *PCEs* due to the perovskite's ability to transport charges itself, demonstrated by the reported use of  $m\text{Al}_2\text{O}_3$  [50].

To clarify the role of the  $m\text{TiO}_2$ , perovskite devices using  $m\text{Al}_2\text{O}_3$  instead of  $m\text{TiO}_2$  (Figure 4.3 (d)) were built and similarly analyzed. The DC current response of the different device architectures is presented in Figure 4.5 (a). In the low forward bias region the current voltage characteristic is dominated by the interface between the photoanode blocking layer (BL) (here a compact  $\text{TiO}_2$  layer) and the electrolyte or HTM. The blocking character of this interface with respect to the iodine or triiodide reduction is apparent in the lower observed dark current response in this potential region. Furthermore the importance and necessity of the blocking layer for the solid-state devices is emphasized. At higher forward bias from about 400 mV onwards the dark current curve is governed by the current flow over the now conducting  $m\text{TiO}_2$ . However it is necessary to note that in this case the magnitude of the currents cannot be compared directly since the Fermi level  $E_F$  at 0 V differs in between the different devices. As stated above, this parameter is affected by the ionic environment and hence will be different for the iodine liquid electrolyte compared to the solid-state HTM spiro-MeOTAD or when perovskite is present.

In the simplest case the low forward bias region can be fitted by an RC element for the back contact (BC) or counter electrode in series with another simple RC accounting for the interface of the compact  $\text{TiO}_2$  blocking layer with the hole-transporting agent. Due to the similar time scales for the charge-transfer at these two interfaces, their IS response manifests in the same frequency range, leading to significant overlap in the Nyquist plot making it difficult to



**Figure 4.4.** (a) Full equivalent circuit model of the BL/HTM interface with a mesoporous non-conducting metal-oxide at low forward bias.  $R_{BL}/C_{BL}$  – charge-transfer resistance and capacitance at the FTO or BL;  $C_{ionic}$  – the ionic capacitance at the BL interface (ionic1) and at the mesoporous metal oxide interface (ionic2). (b) Full model of a solid-state device with perovskite.  $R_{trans} = L \times r_{trans}$  – transport resistance;  $R_{ct} = L \times r_{ct}$  – charge-transfer/recombination resistance, where  $L$  is the thickness of the active layer;  $R_x/C_x$  – resistance and capacitance associated with perovskite;  $R_{HTM}/C_{HTM}$  – charge-transport resistance and capacitance of the HTM;  $R_{BC}/C_{BC}$  – charge-transfer resistance and capacitance at BC/HTM. Depending on applied bias the model has to be changed accordingly, see text.

differentiate between them.

The capacitance at the underlayer/hole-transport agent interface is, in the liquid DSSC, in reality set together out of two capacitances in series; the space-charge capacitance in the BL and the Helmholtz capacitance in the electrolyte. The Helmholtz capacitance is about 10 to 100 times higher and is hence usually disregarded. This simplification of the capacitance at the interface BL/hole-transport (HT) media in the case of the liquid DSSC can not be generalized to the situation in the solid-state counterpart. While the capacitance of the underlayer for the solid-state devices can also be split into two parts, since there is no liquid electrolyte present, there is no ‘Helmholtz’ capacitance. Instead the presence of ions (mainly Li<sup>+</sup> from the LiTFSI

## 4.2. Considerations of the Systems and Impedance Spectroscopy

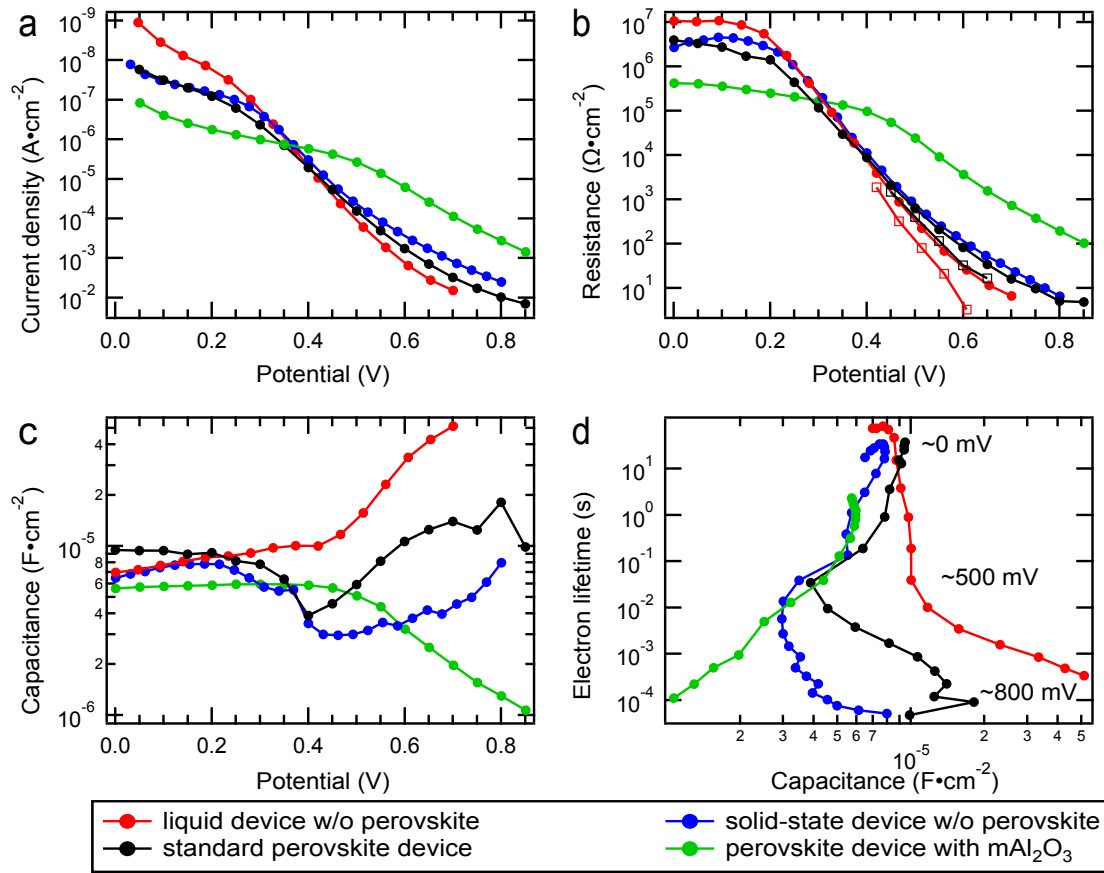
---

additive) in the HTM may lead to the formation of a capacitance at this interface. This ionic capacitance is probably in the same order of magnitude as the space-charge capacitance of the BL, consequently its contribution cannot be considered negligible and it cannot be simply discarded in a similar fashion to the Helmholtz capacitance in the liquid DSSC case. Also, even though the  $m\text{TiO}_2$  is still insulating in this potential region, and its chemical capacitance  $C_\mu$  is thus still very low, the interplay between  $C_\mu$  and the capacitance at the interface photoanode blocking underlayer/electrolyte or HTM might play a role. This fact is normally discarded in the equivalent circuit description of a liquid DSSC (cf. Figure 1.12 Chapter 1) due to its minor influence on the final results. However in the perovskite solar cells using a solid HTM, this contribution may be significant and thus needs to be considered in the analysis of the IS measurements.

The full equivalent model for the BL/HTM interface is presented in Figure 4.4 (a), taking into account all the components for a perovskite solid-state device. Additionally the considerations regarding capacitances at the BL/HTM interface can also be applied to the  $m\text{TiO}_2$ /HTM interface. Here too it is questionable if the ionic capacitance in the HTM is high enough to justify discarding it. However while Figure 4.4 (a) might be the accurate model it tends to over parameterize the fitting region for this interface. Consequently this easily leads to physically meaningless fits of the impedance data. To avoid these complications it is more practical to adopt a simpler model where the individual capacitances in series are not treated separately but fitted by a single capacitor. The extracted parameter is subsequently analyzed and interpreted taking into account that in reality it is the combination of two capacitances in series.

The transport resistance within the  $m\text{TiO}_2$  increases proportionally with the thickness of the active layer while the recombination resistance scales inversely. Hence in comparison to the liquid and solid-state DSSC devices, the use of the submicrometer thin  $m\text{TiO}_2$  layers in the perovskite solar cells results in substantial reduction in the associated transport resistance.

The first simplified system to be investigated by IS is the liquid electrolyte-based device with a similar photoanode used for the perovskite devices. In the low forward bias region (black trace in Figure 4.6 (a)–(b)) two semicircles can be identified – the high frequency one attributed to the counter electrode and the low frequency arc relating to the charge-transfer through the BL/electrolyte contact. At higher forward bias the transport resistance is visible as the  $45^\circ$  straight-line characteristic of the transmission line as seen for the measurement conducted at 560 mV, green trace in Figure 4.6 (a)–(b). The transmission line merges towards lower frequencies into the arc representing the recombination resistance and the chemical capacitance of the  $m\text{TiO}_2$ . At even higher forward bias (red trace in Figure 4.6 (b)) the Warburg diffusion impedance for the diffusion of the ions in the electrolyte appears at low frequencies. Though the thickness of the  $m\text{TiO}_2$  is changed by a factor of about 30 relative to the standard liquid DSSC, the general equivalent circuit model applied for this system is observed to keep its validity.



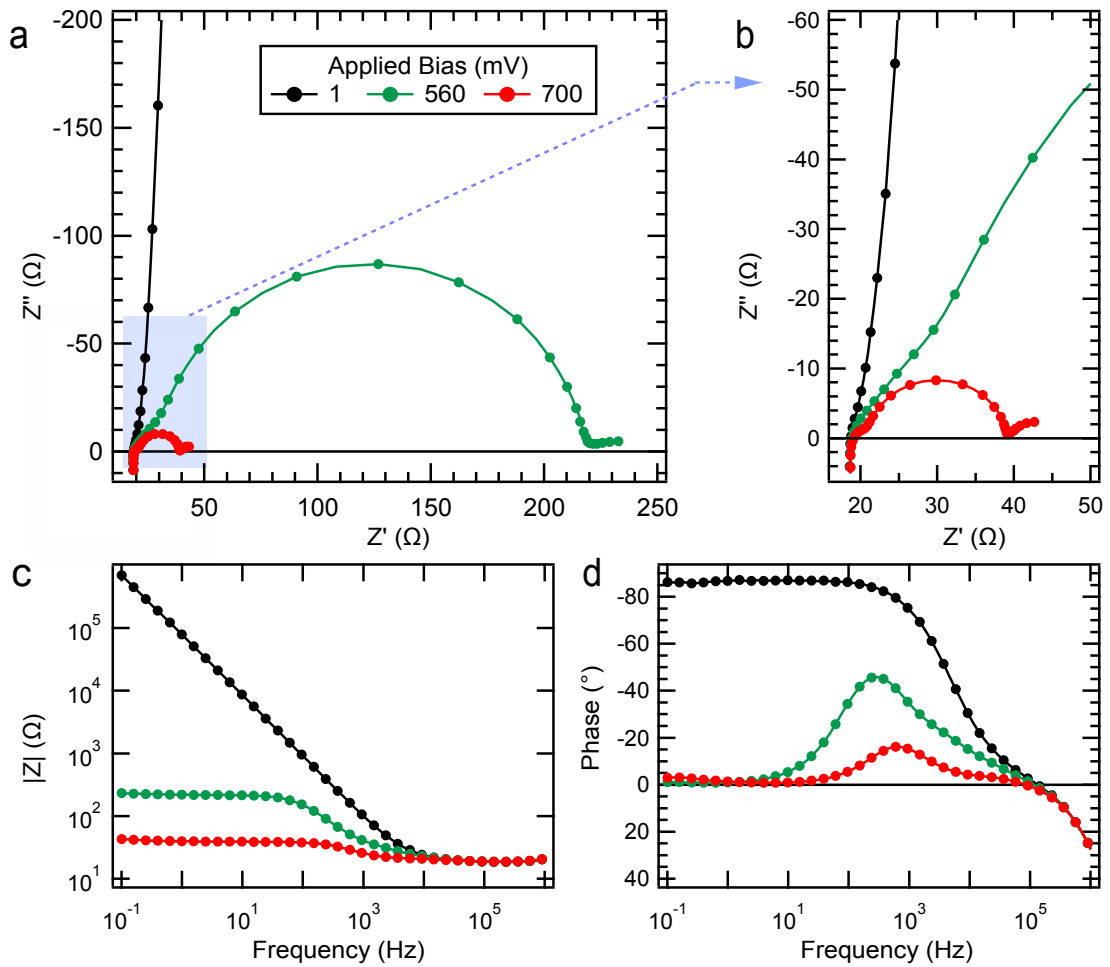
**Figure 4.5.** (a) Dark current plotted in log scale against the potential, (b) transport  $R_{trans}$  (open squares) and recombination resistance  $R_{ct}$  (solid circles), (c) chemical capacitance (dashed circles) and (d) calculated electron lifetime as a function of the capacitance of a liquid device (red) and solid-state devices with (black) and without (blue) perovskite with a similar photoanode and (green) a perovskite solid-state device with mesoporous  $Al_2O_3$  instead of mesoporous  $TiO_2$ .

When considering the Nyquist plots of the solid-state devices (Figures 4.7 and 4.8, here for the case with perovskite and spiro-MeOTAD as HTM) a similar transmission line behavior at intermediate potentials is observed (Nyquist plot measured at 550 mV in Figure 4.7). Consequently as in the case of the liquid DSSC, it can be concluded that the transmission line model can also be applied as a basic skeleton for an equivalent circuit model for the solid-state device. Naturally the underlying model has to be adjusted according to the bias applied.

In the high frequency region, the solid-state devices display the response from the back contact (BC) at the gold/HTM interface, which is similar to the counter electrode interface in the liquid electrolyte device (Figures 4.7 and 4.8 (c)). This BC element is visible over the whole potential range, with its associated resistance staying mainly unchanged in the low forward bias region until it begins to decrease in magnitude around the maximum power point MPP.

At lower forward bias, the samples with the perovskite absorber showed an additional RC

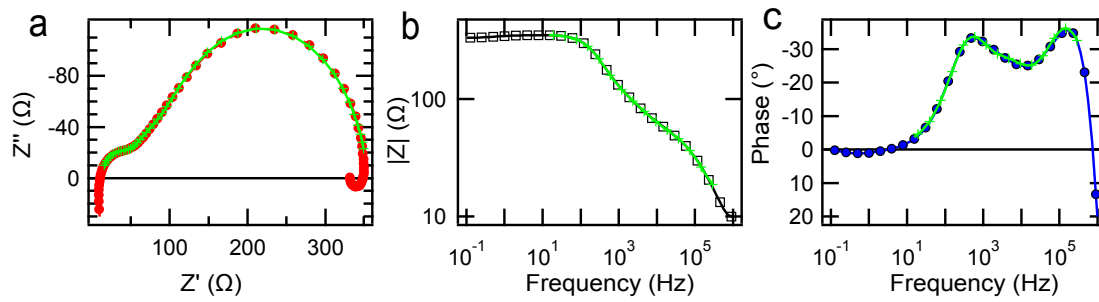
## 4.2. Considerations of the Systems and Impedance Spectroscopy



**Figure 4.6.** (a) Nyquist plot of the liquid device measured at 700 (black), 560 (green) and 1 mV (red). (b) Inset of Nyquist in high frequency region. Corresponding Bode plots displaying the (c) magnitude and (d) phase as a function of the frequency.

element in between the low and high frequency semicircles (Nyquist plot measured at 150 mV Figure 4.8 (b)). Such an effect could originate from a poor contact between the compact underlayer and the  $m\text{TiO}_2$ , which would lead to an additional RC element in series to the chemical capacitance in Figure 4.4 (a). Since this element at intermediate frequencies was not visible in the case of the liquid and, more importantly, in case of the solid-state devices without the perovskite, it is possible to exclude a poor contact between the substrate and the  $m\text{TiO}_2$  and deduce its direct relation to the perovskite material. The evolution of this intermediate resistance with potential is normally constant as long as the current flows over the BL/HTM contact. At higher forward bias when dark current start to flow over the  $m\text{TiO}_2$  the resistance decreases steeply and normally vanishes.

Three maxima are visible in the Bode plot in Figure 4.8 (e) clearly indicating the individual features contributing to the IS response at this applied bias; 1) the high frequency response



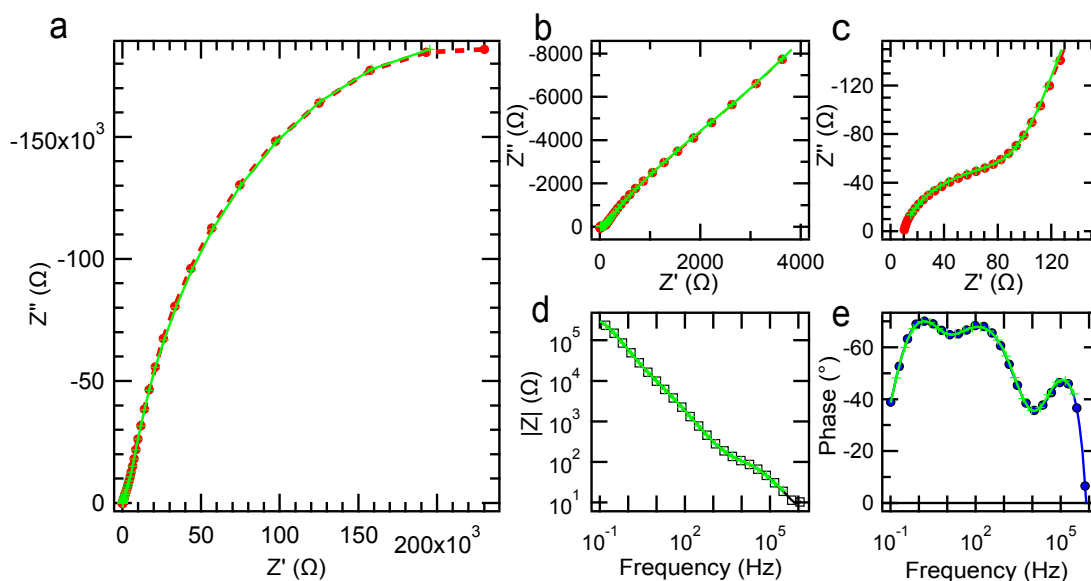
**Figure 4.7.** (a) Nyquist and Bode plot, (b) magnitude and (c) phase, of a standard solid-state perovskite-based device at 550 mV forward bias. The fit was performed with all parameters non-restricted with the exception of the exponent of the CPE of the BL. This was fixed to 1 as long as the transmission line was used since no parallel resistance exists for this element and hence no ‘real’ capacitance can be calculated.

from the BC/HTM interface, 2) the intermediate frequency response from the perovskite material and finally 3) the low frequency recombination component.

The deposition technique of the perovskite from a solution mixture of  $\text{PbI}_2$  and  $\text{CH}_3\text{NH}_3\text{I}$  precursors in GBL used here shows the formation of distributed crystallites of the absorber on the  $\text{TiO}_2$ . As such the control over the perovskite crystallization, stoichiometry and morphology is poor. However contrary to Ball *et al.* [51] no conformal film on top of the  $\text{mTiO}_2$  film is present though coverage is believed to be high with a high fraction of pore-filling. As a result charge-transport can flow *via* the ‘known’ mechanism from ssDSSC, *via* the perovskite itself or *via* a combination of both pathways. In the case when the pure triiodide perovskite material  $\text{CH}_3\text{NH}_3\text{PbI}_3$  is formed from the direct deposition of a precursor mixture in solution in the device configuration described here, the hole-transport is believed to be directed mainly by the hole conductor, spiro-MeOTAD. This is not the case when the mixed halide perovskite is prepared using  $\text{PbCl}_2$  [50, 51] in place of  $\text{PbI}_2$  or when the device architecture is changed, resulting in significant charge-transport within the perovskite material itself.

In the potential region with forward biases near  $V_{\text{OC}}$ , when the  $\text{mTiO}_2$  is in its conductive state and the transmission line has vanished, a two RC response is expected for the different device types. The high frequency response represents the BC interface and the second RC response – at low frequencies – corresponds to the  $\text{mTiO}_2/\text{HTM}$  interface.

A known discrepancy between the liquid and solid-state type devices manifests in the low frequency region at high forward bias. For liquid type devices, there is a Warburg element representing the diffusion of the ions in the electrolyte. For solid-state devices – lacking a liquid electrolyte – this feature is absent, and instead a slow time constant phenomenon is observed at high forward bias in the low frequency range. This feature can appear as a so-called ‘negative capacitance’ or as an additional small semicircle at frequencies in the low Hz or mHz range (see Figure 4.7 (b)) which may have a similar origin as the negative capacitance. The origin of such a negative capacitance is normally assumed to be based on an imbalance



**Figure 4.8.** (a) Nyquist plot, (b)–(c) showing intermediate and high frequency range, and Bode plots, (d) magnitude and (e) phase, of a standard solid-state perovskite-based device measured at 150 mV forward bias. The green line represents the fit by 3 RC elements in series. All elements have been fitted with non-restricted numbers. The exponent of the CPEs was for all the devices clearly above 0.8. For the perovskite solid-state devices in the case of the mid frequency RC-arc the exponent was 0.78, hence still acceptable. If this value was fixed to 0.8 it did not obviously change the other parameters.

(or a non-ohmic behavior) at one of the extracting contacts [153, 154]. It sometimes leads to cross-over or roll-over effects in the  $J$ - $V$  curves [155]. In most of the cases this feature appears at high electron density in the semiconductor. Since it is associated with a slow time constant it might be related to the reorganization of mobile ions at one of the interface.

In case of the devices with perovskite, at higher applied potential, an additional intermediate semicircle is sometimes visible in the mid frequency region, between the BC and the recombination RC features (similar to the case of low forward bias). Since there is no clear indication if and how these two elements in the mid frequency range are related, they were treated simply as an additional RC element in series ( $R_x$  and  $C_x$  in Figure 4.4 (b)). Further observation on how these two elements behave may elucidate their origin and thus require modification of the model.

To further study the samples and their IS response the proposed models were applied for the fitting procedure, omitting the ionic capacitances and the element related to the HTM unless stated otherwise.

Returning to the examination of the three model systems – liquid device without perovskite and solid-state devices with and without perovskite – as implied by the current characteristics, there is similarity in the IS behavior of all three samples. The main feature observed to change is the behavior of the chemical capacitance (see Figure 4.5 (c)). Initially at low forward bias

the determined low frequency resistance (the charge-transfer at the BL/HT media interface) clearly resembles the tendencies of the dark current, Figure 4.5 (a–b). The capacitance in this potential region (low forward bias) is dominated by the capacitance at the BL/HT media interface. The extracted values for this parameter for the different device systems are all in the same order of magnitude. The capacitance of the liquid device increases slightly with increasing forward bias as long as the dark current is channeled over the BL. In the case of the solid-state devices the capacitance first increases before it suddenly drops. The drop in capacitance near 400 mV forward bias for the two types of solid-state devices was also observed for solid-state dye-sensitized solar cells (cf. Chapter 2) and can be explained by a drop of the capacitance at the BL/HTM interface. For comparison the low frequency arc capacitance for a device with  $\text{mAl}_2\text{O}_3$  instead of  $\text{mTiO}_2$  (see green trace in Figure 4.5) was also determined. In this case the capacitance decreased with increasing forward bias exhibiting the plane evolution of the capacitance at this interface without the overlaid increase of the chemical capacitance of the  $\text{mTiO}_2$ .

As the chemical capacitance in the  $\text{mTiO}_2$  increases – at an applied forward bias  $> 400\text{mV}$  – and the transport resistance becomes visible. The chemical capacitances of the three devices display distinctly different behavior relative to the increase in potential. The increase of the capacitance observed at higher forward bias is most pronounced in the liquid device type. In the case of the solid-state devices, for the system with perovskite, the increase in the capacitance is steeper relative to the system without perovskite. This is a clear indication that the ionic environment of the  $\text{mTiO}_2$  is different for each device type. This can lead to changes in the shape of the density of trap states (DOS) inside the  $\text{mTiO}_2$  and therefore of the chemical capacitance. This chemical capacitance  $C_\mu$  is directly proportional to the DOS, dependent on the dimension specifications of the mesoporous  $\text{TiO}_2$  film (cf. Equation 2.7 Chapter 2). In this context, the difference of  $C_\mu$  between the two solid-state devices is particularly interesting indicating that the perovskite obviously has an influence on the shape and population of the DOS.

The electron lifetime  $\tau_n$  can be determined from the recombination resistance and the chemical capacitance using  $\tau_n = R_{\text{ct}} \times C_\mu$ . Electron lifetimes for the different types of devices are presented in Figure 4.5 (d). The lifetimes are plotted against chemical capacitance of the  $\text{mTiO}_2$  since the direct comparison of the lifetimes against the applied voltage is not suitable under such conditions. The conduction band position and the redox potential of the HT media differ for the different systems under consideration. Normally, under the assumption of a similar distribution of bulk traps inside the  $\text{TiO}_2$ , the chemical capacitance of the  $\text{mTiO}_2$  or the DOS can be used as an indirect measure of the Fermi level  $E_F$  or more precisely as a measure of the distance between  $E_F$  to the conduction band. However this assumption is not valid for the systems investigated in Figure 4.5. The perovskite and the presence of additives such as lithium ions or TBP change the CB position and the ionic surroundings of the  $\text{mTiO}_2$  and can therefore also change the distribution of the DOS as shown in Figure 4.5 (c). Alternatively the conductivity of the  $\text{mTiO}_2$  can be used to compare different samples since (under certain conditions) it represents the same number of mobile charge carriers in the CB.



## 4.2. Considerations of the Systems and Impedance Spectroscopy

---

The conductivity is calculated from the transport resistance of charges within the  $m\text{TiO}_2$  which is also greatly influenced by the ionic surrounding (screening) of the  $m\text{TiO}_2$  and can only be determined in a small potential range, which results in a very small window to compare the properties of the investigated samples. As such the chemical capacitance is the best approach to determine an approximation of the relation between the electron lifetime and  $E_F$ , taking into account the described restrictions discussed here.

In the low forward bias region all four samples (including the  $m\text{Al}_2\text{O}_3$  sample) possess very similar electron lifetimes since the current flows over the BL which is more or less similar for all devices. Considering the region in which the  $m\text{TiO}_2$  is active, the lifetime is the longest for the devices with the liquid electrolyte in combination with the iodine redox system. It is followed by the lifetime in solid-state devices with perovskite and finally the lowest lifetime for the solid-state device with only spiro-MeOTAD/ $\text{TiO}_2$  interface (without perovskite). The data presented in green is the electron lifetime with a device with  $m\text{Al}_2\text{O}_3$  instead of the  $m\text{TiO}_2$  where all the dark current can only be driven over the compact  $\text{TiO}_2$  BL/HTM interface.

The  $m\text{Al}_2\text{O}_3$  sample clearly shows no increase of the capacitance with higher forward bias (see Figure 4.5 (c)). On the contrary the capacitance drops at higher potential. Such behavior was already observed for ssDSSC type devices using  $\text{ZrO}_2$  in place of  $m\text{TiO}_2$ , however in this case the mesoporous films were considerably thicker [54, 153, 154].

On the basis of these results it is possible to conclude that charge (electron) transport is channeled over the mesoporous oxide as evidenced by the observation of the chemical capacitance of the mesoporous  $\text{TiO}_2$ . This capacitance belongs to the low frequency arc in the Nyquist plot and the relation between this RC element and the  $m\text{TiO}_2$  is further substantiated by the fact that its resistance scales with the  $\text{TiO}_2$  thickness as previously shown in the publication of Kim *et al.* [49]. This is further confirmed by charge extraction measurements presented by Abrusci *et al.* [156] which indicate the capacitance is much smaller for the case in which the electrons are not injected into a  $m\text{TiO}_2$  but a fullerene layer.

One can also observe that the BL dominates the observed lifetimes to different extents (Figure 4.5 (d)). The easier the recombination over the BL at lower potential the more current is driven over this interface and the more forward bias has to be applied to 'activate' the mesoporous oxide (see the case of the solid-state device without perovskite where the increase in chemical capacitance is at a higher forward bias compared to the sample with perovskite).

The investigation of these model systems allowed the identification and analysis of the individual components contributing to the IS response. A procedure and appropriate models were developed that can be used to fit the data generated with perovskite samples (cf. Appendix A.2 for a full description of this fitting procedure).

### 4.3 Validation of Impedance Model

In the previous section, model systems were investigated to examine the behavior and response of the individual solar cell components from which an equivalent model was developed and established. In order to assess and validate the suggested procedure to fit the impedance data the influence of various factors were investigated. These include the impact of the variation of the additive LiTFSI salt and TBP concentration in the HTM solution as well as the spiro-MeOTAD overlayer thickness on top of the perovskite-sensitized mesoporous TiO<sub>2</sub>.

#### 4.3.1 Effect of Spiro-MeOTAD Overlayer Thickness

Previous studies [32, 33, 35, 157] have investigated the mechanism of pore-filling of mTiO<sub>2</sub> films with spiro-MeOTAD and its influence on the power conversion efficiency (*PCE*) of ssDSSCs. It is believed that during the initial soak time after deposition of the HTM, the spiro-MeOTAD solution rapidly infiltrates the mTiO<sub>2</sub> by capillary force, with excess solution forming a reservoir on top of the film. During the spin-coating procedure the excess solvent evaporates, increasing the concentration of spiro-MeOTAD inside the pores until the molecules become immobile [36]. Similar to the pore-filling fraction of the HTM, the formation of an overlayer of spiro-MeOTAD is dependent on the deposition conditions and has been found to have considerable influence on the performance of ssDSSCs [158]. However both these aspects have not been explored for the case using submicrometer perovskite-sensitized mesoporous films, where the device mechanisms are not yet fully understood.

Herein, the overlayer thickness was controlled by varying the concentration of the spiro-MeOTAD solution used in the deposition stage from approximately 30 mM to 73 mM (the latter of which corresponds to 50% of the standard spiro-MeOTAD solution concentration used for ssDSSCs<sup>1</sup>). Additionally the spinning speed utilized in the deposition of the HTM on the perovskite-sensitized mTiO<sub>2</sub> was varied for each concentration of HTM solution used. Using scanning electron microscopy (SEM) to accurately determine the overlayer thickness (cf. Figure 4.9 and summarized in Table 4.1) it was found that varying these critical parameters in the deposition of the HTM allowed the overlayer thickness to be tuned between 0 and 271 ± 15 nm. Hence the overlayer thickness was correlated with the power conversion efficiency of the devices, increasing from a *PCE* of 4.41% when there is no visible overlayer to a maximum at 7.55% attained for an overlayer thickness of 136 ± 6 nm.

The *J-V* characteristics of devices with different overlayer thicknesses depending on the spin-coating speed and the concentration of the HTM solution were measured under standard AM1.5G illumination (100 mW cm<sup>-2</sup>), see Figure 4.10 (a). The corresponding parameters are summarized in Table 4.2. The pore-filling of the mTiO<sub>2</sub> and the thickness of the overlayer is known to depend on the viscosity of the HTM solution and the spin-coating conditions. Previous studies have shown that the overlayer thickness increases linearly with increasing

---

<sup>1</sup> The standard spiro-MeOTAD solution concentration used for conventional ssDSSC is 147 mM which corresponds to 180 mg in 1 ml of chlorobenzene

### 4.3. Validation of Impedance Model

**Table 4.1.** Overlayer thickness (in nm) determined from SEM images and their dependence on spin-coating speed (in rpm) and HTM solution concentration.<sup>a</sup>

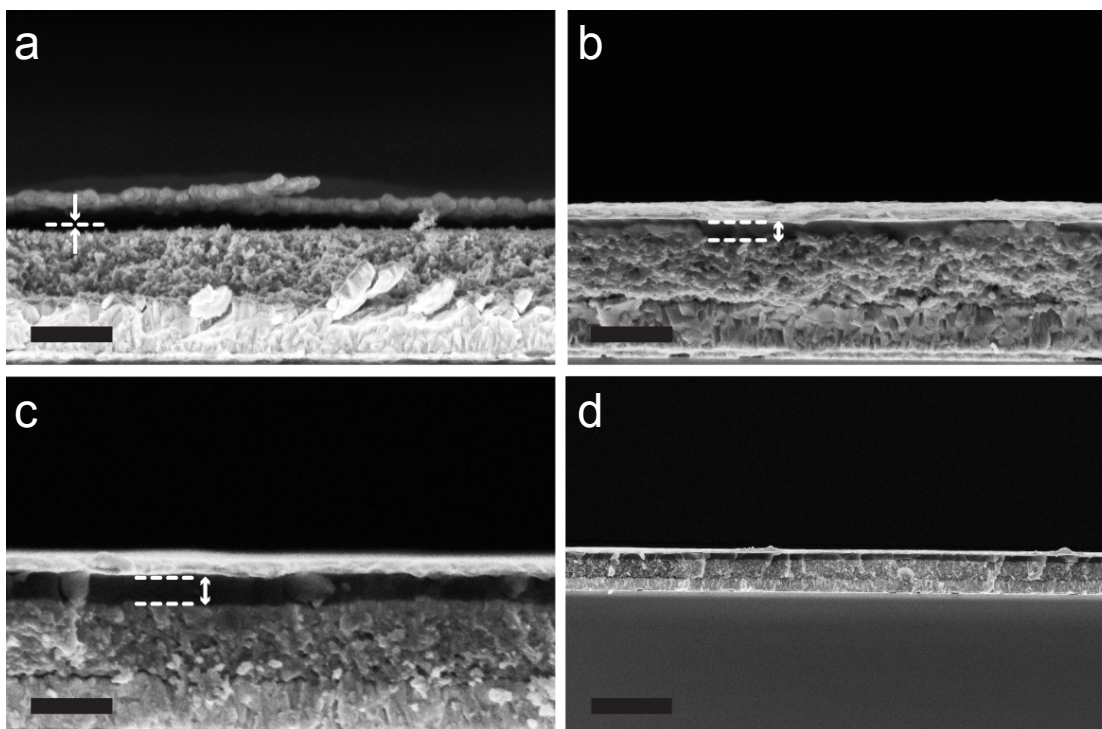
HTM concentration (mM)	2000	4000	5200
29	87±5	51±5	0
44	94±15	82±8	76±5
59	160±10	136±6	99±17
73	271±15	239±9	198±16

<sup>a</sup> Associated error determined from standard deviation of the average of measurements made at three different points of samples.

the soaking time of the HTM solution [158] prior to spin-coating, which is a consequence of the solvent evaporation increasing the viscosity of the solution. For the conventional ssDSSC, the concentration of the spiro-MeOTAD solution used is 147 mM (180 mg in 1 ml of chlorobenzene) and is deposited at a spin-coating rate of 2000 rpm. However in the case of  $\text{CH}_3\text{NH}_3\text{PbI}_3$  as sensitizer, the  $\text{mTiO}_2$  film used is considerably thinner at approximately 400–500 nm compared to the 2  $\mu\text{m}$  films used for ssDSSCs. Consequently the same conditions result in a HTM overlayer thickness of more than 800 nm and very poor performance.

There is a clear correlation between the device performance and the overlayer thickness. Both the  $J_{\text{SC}}$  and the  $V_{\text{OC}}$  display a gradual increase as the HTM overlayer increases from 0 nm, reaching a maximum at approximately 87 nm for the  $J_{\text{SC}}$  with a value of  $15.0 \text{ mA cm}^{-2}$  and at 136 nm for a  $V_{\text{OC}}$  of 819 mV. As the overlayer thickness increases further the  $V_{\text{OC}}$  decreases and the  $J_{\text{SC}}$  stabilizes following a small drop in magnitude at approximately  $13.6 \text{ mA cm}^{-2}$ . The  $FF$  was observed to be low between (0.59 and 0.61) for overlayer thicknesses up to 87 nm as well as for overlayers greater than 160 nm ( $FF$  between 0.56 and 0.57). For the range in between 87 and 136 nm the  $FF$  increased to lie between 0.63 and 0.66. As a result the overall  $PCE$  shows an increase from 4.41% to 7.55% at 136 nm overlayer thickness before dropping down to 5.20% at 271 nm. The peak performance at 136 nm is largely due to the high  $V_{\text{OC}}$  but  $PCEs$  of approximately 6% and greater are displayed for devices with overlayer thicknesses between 82 and 160 nm. These trends are depicted graphically in Figure 4.10 (b). The drop in  $FF$  towards higher thicknesses of the HTM overlayer can be readily explained by the increase in path length for the charge carriers. This should result in an increased resistance for the charge-transport within the HTM and in an overall higher series resistance. For no or very thin HTM overlayers a more slanted  $J$ - $V$  curve resulting in lower  $FF$  is observed and is indicative of partial but not complete device shunting. This is contrary to what would be observed with ssDSSCs sensitized with a molecular dye.

The trends of the  $J_{\text{SC}}$  and the  $V_{\text{OC}}$  against overlayer thickness are clearly related. Below 80 nm HTM overlayer the gold will be, in major areas, directly on the uncovered mesoporous surface and consequently be quite similar to the device structure of Etgar *et al.* [131], albeit with lower photocurrent. Still the small influence of the shunt is another indication that the perovskite

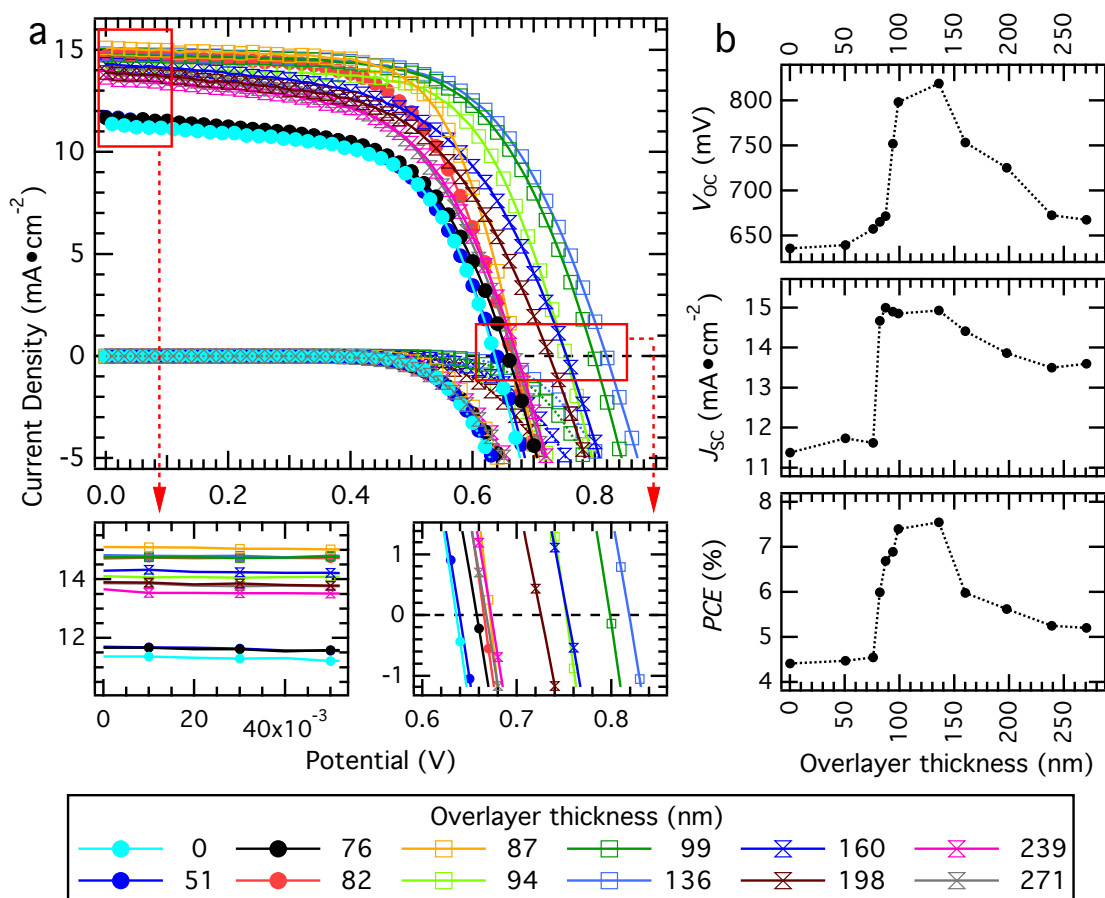


**Figure 4.9.** Cross sectional SEM images of devices made following different HTM deposition conditions to give (a) no visible overlayer, approximately (b) 100 nm and (c) 200 nm thick overlayers. When no overlayer was present the Au counter electrode frequently flaked off the surface during sample fracturing for SEM imaging. (d) Low magnification SEM image showing long-range uniformity of the film structure. Arrows indicate the HTM overlayer. Black scale bars indicate (a–c) 500 nm and (d) 2  $\mu\text{m}$ .

forms a relatively conformal layer around the  $\text{mTiO}_2$  preventing the direct contact with the gold BC. Especially in the case where no visible overlayer of the HTM is observed in SEM, the evaporated gold can penetrate deeply in the thin mesoporous film. This could lead to a more Schottky type device with a primarily active gold/perovskite interface. This would explain the different current and voltage behavior for the thin HTM overlayers and could result in an inactive  $\text{mTiO}_2$  where there is no charge injection.

In previous work (cf. Chapter 2) [54] the transport properties of spiro-MeOTAD as HTM for solid-state dye-sensitized solar cells was investigated. The charge-transport resistance of the spiro-MeOTAD was shown to manifest itself as a RC-arc at high to intermediate frequencies in the Nyquist plots. Furthermore it was observed to decrease significantly in magnitude upon chemically *p*-doping the spiro-MeOTAD. In this study using  $\text{CH}_3\text{NH}_3\text{PbI}_3$  in place of a molecular dye sensitizer and submicrometer thick  $\text{mTiO}_2$  the spiro-MeOTAD was chemically *p*-doped to a lesser extent. As a consequence the charge-transport resistance of the spiro-MeOTAD could be resolved for the devices with large spiro-MeOTAD overlayers and was found to be smaller than previously reported for the pristine, undoped spiro-MeOTAD [54].

The established model described above is used to analyze the IS Nyquist spectra for these



**Figure 4.10.** (a)  $J$ - $V$  characteristics of devices with varying overlayer thicknesses measured under standard AM1.5G illumination ( $100 \text{ mW cm}^{-2}$ ) (solid) and in the dark (dotted). Insets show the short- and open-circuit regions in detail. (b) Dependence of  $V_{OC}$ ,  $J_{SC}$  and  $PCE$  on HTM overlayer thickness.

devices. The first arc at high frequency appears deformed which is consistent with the RC-arc for the charge-transfer resistance at the BC/HTM interface overlapping partially with the RC-arc for the charge-transport resistance of the HTM  $R_{HTM}$ . The transport in the HTM is modelled by a resistor (see Chapter 2) [54]. The intersection of this high frequency arc corresponds to the resistance of the conducting glass, contacts and wires,  $R_S$ . The magnitude of the following RC-arc at high to intermediate frequencies was observed to be strongly influenced by changes in the spiro-MeOTAD overlayer thickness. Hence this feature is attributed to the transport resistance of the HTM  $R_{HTM}$ .

The resistance and associated capacitance extracted from the first high frequency RC element as a function of potential for devices with overlayer thicknesses from 0 to 271 nm is shown in Figure 4.11 (a) and (b). This resistance was found to remain relatively constant for low to intermediate forward bias and then to decrease at high potentials. As the overlayer thickness increases, the resistance displays an increase in magnitude from 50 to 2000  $\Omega$  as shown in

## Chapter 4. Impedance Spectroscopic Analysis of Perovskite Solid-State Solar Cells

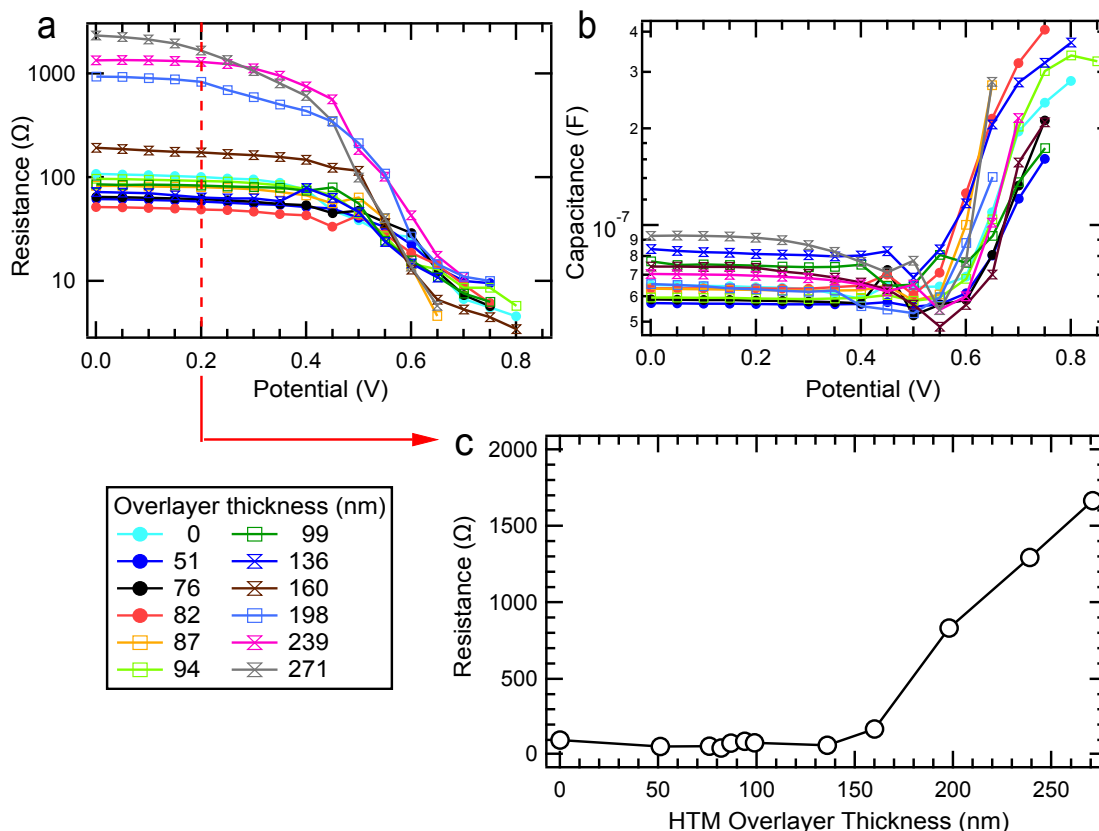
**Table 4.2.** Photovoltaic performance parameters extracted from  $J$ - $V$  measurements of devices with different overlayer thicknesses. All devices were masked to achieve an illuminated area of  $0.285 \text{ cm}^2$ .

Overlayer thickness (nm)	[HTM] (mM)	Spin-coating speed (rpm)	$V_{OC}$ (mV)	$J_{SC}$ ( $\text{mA cm}^{-2}$ )	$FF$	$PCE$ (%)
0	29	5200	636	11.4	0.61	4.41
51	29	4000	639	11.7	0.60	4.47
76	44	5200	657	11.6	0.59	4.55
82	44	4000	665	14.7	0.61	5.99
87	29	2000	671	15.0	0.66	6.69
94	44	2000	752	14.9	0.65	6.89
99	59	5200	798	14.9	0.63	7.40
136	59	4000	819	14.9	0.63	7.55
160	59	2000	753	14.4	0.56	5.98
198	73	5200	725	13.8	0.56	5.62
239	73	4000	673	13.5	0.57	5.25
271	73	2000	667	13.6	0.56	5.20

Figure 4.11 (c). For devices with overlayers less or equal than 140 nm, the magnitude of this resistance is similar and is thus mostly attributed to the charge-transport resistance at the BC/HTM interface, the charge-transport resistance of the HTM being too small to resolve for such thin overlayers. For overlayers greater than 140 nm the high frequency resistance shows considerable increase in magnitude, its main contribution arising from the hole-transport within the HTM,  $R_{HTM}$ . Consequently for thin spiro-MeOTAD overlayers up to 140 nm the BC/HTM interface dominates, while for devices with greater overlayer thickness the magnitude of  $R_{HTM}$  increases sufficiently to become the main contribution to the high frequency resistance. This high frequency resistance, comprising these two components, ultimately contributes to the total series resistance of the devices and thus affects their fill factor. This is reflected in the slight drop in  $FF$  observed for devices with overlayers greater than the optimum 136 nm. Further increasing the HTM overlayer thickness leads to drastic decreases in the  $FF$ , greatly reducing the  $PCE$ .

Devices with overlayers less than the optimum 136 nm show a slight shunt in their  $J$ - $V$  characteristics, which is similarly reflected in the lower  $FF$  values. While the HTM overlayer appears to be homogeneous across the  $\text{mTiO}_2$  surface in the SEM images (Figure 4.9), this may not universally be the case due to irregularities and defects on the top of the mesoporous film or regions that are not completely covered by HTM and are thus exposed to the back contact directly. As such, the optimum HTM overlayer thickness is achieved at the minimum HTM thickness that forms a continuous, uniform film on top of the perovskite sensitized  $\text{TiO}_2$ .

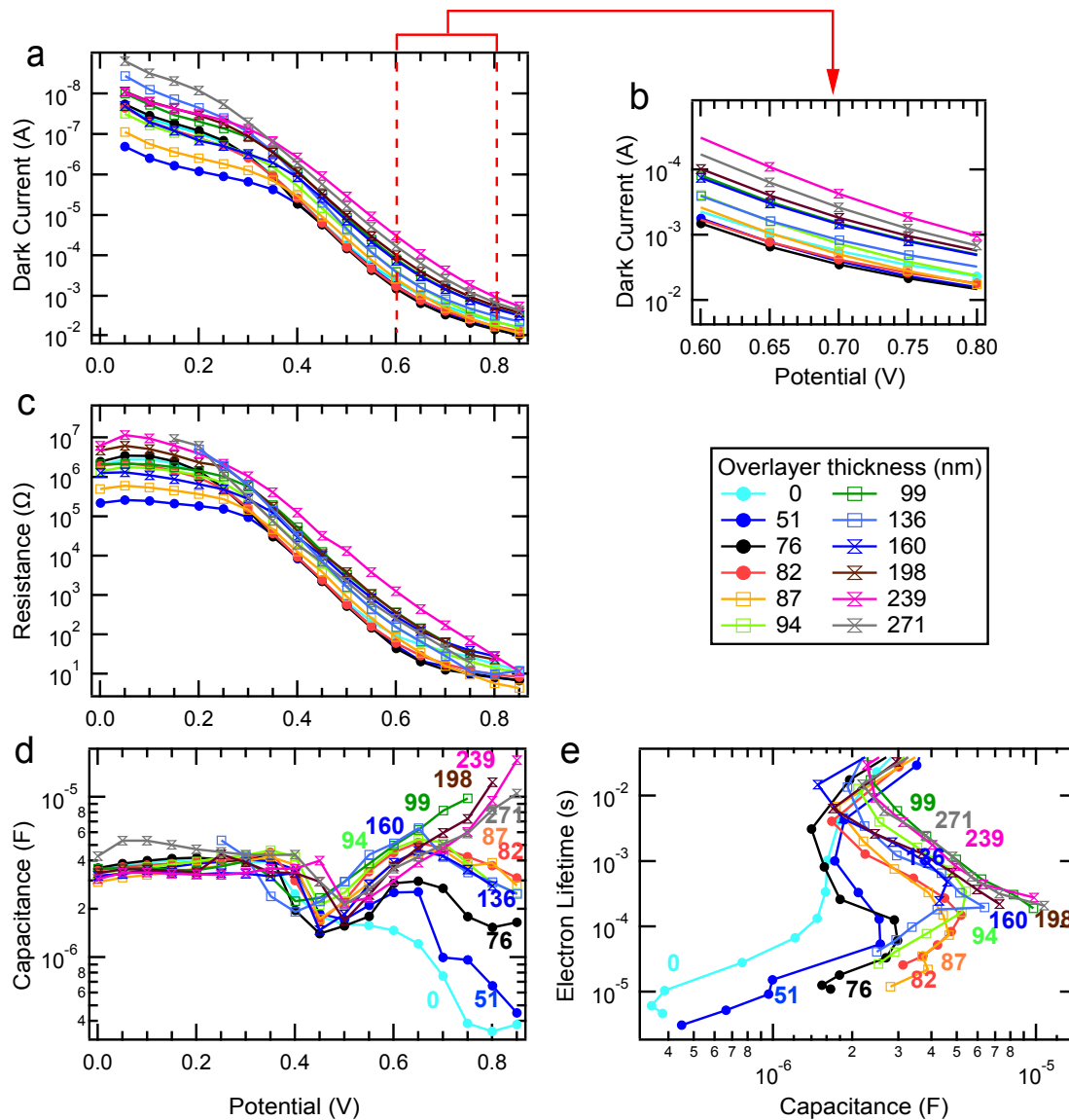
In addition to the increase in  $R_{HTM}$ , the recombination resistance  $R_{ct}$  which manifests in the lower frequency region is also influenced by the increasing overlayer thickness (Figure 4.12 (c)). In the potential range when the  $\text{TiO}_2$  is conductive and the recombination resistance decreases



**Figure 4.11.** (a) High frequency resistance and (b) associated capacitance as a function of the corrected potential determined from IS measurements conducted on complete devices in the dark. (c) Magnitude of high frequency resistance determined at a corrected potential of 0.2 V as a function of the HTM overlayer thickness.

rapidly, the shift in  $R_{ct}$  was found to be relatively constant between devices with different overlayer thicknesses. However there is a similar shift observed in the corresponding chemical capacitance  $C_{\mu}$  of  $R_{ct}$  (Figure 4.12 (d)). This shift is also observed in the dark current measurements for the devices (see Figure 4.12 (b)), which exhibit the same tendencies as the recombination resistance with applied potential.

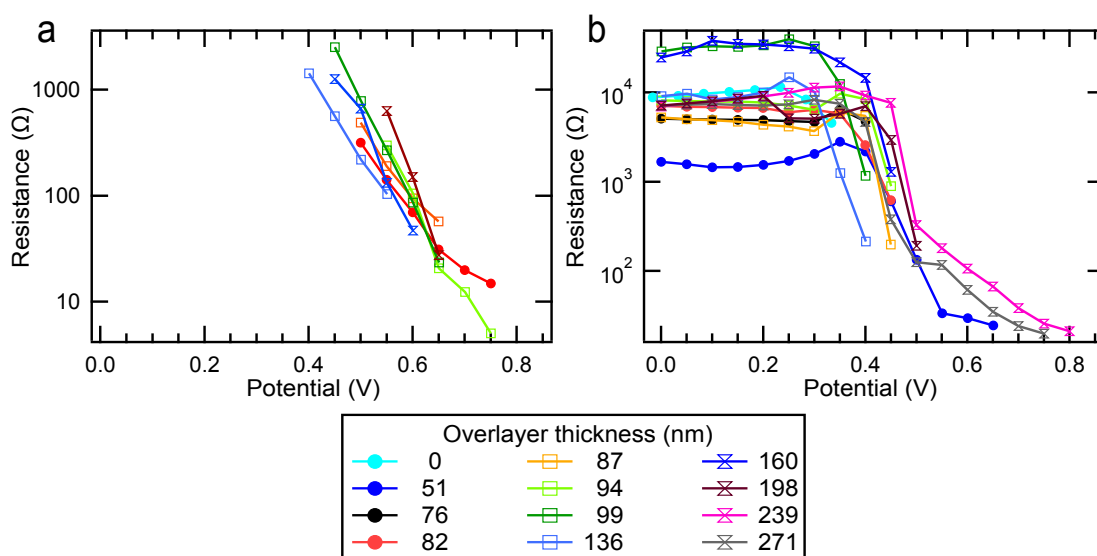
The chemical capacitance is observed to behave similarly for all devices at low forward bias, when the current flows over the BL. At approximately 400 mV it displays the typical decrease associated with the BL/HTM interface that has been described in more details above. Subsequently it increases at high forward bias as expected for mesoporous semiconductors. In the case of devices with thin spiro-MeOTAD overlayers, this increase is seemingly reduced, or even nearly completely suppressed. This suggests that in these instances the system cannot increase the charge density within the mesoporous film and as a result the DOS is not increased. Another possibility would be that in these instances the charges flow through the perovskite rather than the  $mTiO_2$ . In this case the  $mTiO_2$  would act more as a simple scaffold for the perovskite material, and not participate electronically.



**Figure 4.12.** (a) Dark current measurement of devices with varying spiro-MeOTAD overlayer on top of the mTiO<sub>2</sub>, (b) inset showing variation in current response between 0.6 and 0.8 V. (c) Recombination resistance  $R_{ct}$  and (d) corresponding chemical capacitance  $C_{\mu}$  as a function of potential determined from IS measurements conducted in the dark. (e) Electron lifetime calculated from IS measurements.

In the case of the transport resistance  $R_{trans}$  (Figure 4.13 (a)), there is an inherent large error associated with extracting this parameter, as such the magnitude of the relative shift for different devices may result in misrepresentation. However in this case, as suggested by the decreasing chemical capacitance for the device with no visible overlayer, the mTiO<sub>2</sub> participation is small. Similarly, no transmission line was visible when no spiro-MeOTAD overlayer was present, further emphasizing this point. As a HTM overlayer forms, the transport resistance within the mTiO<sub>2</sub> increases, which may explain the apparent shift observed in the





**Figure 4.13.** (a) Transport resistance,  $R_{trans}$  and (b) resistance associated with the perovskite as a function of potential determined from IS measurements conducted on complete devices with different HTM overlayer thickness in the dark.

transport resistances.

The relative shifts in  $C_{\mu}$  has been directly associated with the shift in the conduction band position of the  $\text{TiO}_2$  [53, 79, 159]. In order to better compare these parameters the electron lifetime is presented. As outlined above, the electron lifetime, when presented against the chemical capacitance, provides a comparison as a function of the rise of the Fermi level, taking any shifts in the conduction band into account. This comparison introduces the restriction of a similar DOS for the different devices, which may not necessarily be the case as evident by the variations in the shape of the chemical capacitance. However this assumption still allows an approximate comparison of the electron lifetime for the system under consideration. For the devices with very thin spiro-MeOTAD overlayer, the electron lifetime is observed to be lower, becoming longer for thicker overlayers, Figure 4.12 (e). This can explain the increase in voltage for the thin to medium thicknesses but the reasons for the decrease observe for thicker overlayers stays unclear. This unexpected behavior in the  $V_{OC}$  shows that the dark analysis by IS in this case does not lead to conclusive results since the lifetime for the devices with overlayers from around 90 nm onwards stays mainly unchanged.

At low forward bias up to 400 mV the intermediate resistance, attributed to the perovskite material, appears independent of the applied potential. Its absolute size varies over one order of magnitude for the different devices. This could be a result of differences in the coverage of the  $\text{mTiO}_2$  surface by the perovskite and the amount of perovskite material present. In this region of low forward bias the high transport resistance is due to the inherent low conductivity of the material in the dark. Once the applied potential is sufficiently high, the conductivity of the perovskite greatly increases and the resistance drops. This decrease is comparable for all

devices investigated, independent of the HTM overlayer thickness, Figure 4.13 (b).

To summarize the variation of the thickness of the spiro-MeOTAD overlayer on top of the mTiO<sub>2</sub> was investigated using IS. The suggested equivalent circuit model was used to fit the data, verifying the physical meaning of the individual IS parameters. This analysis was then used to correlate and explain the changes in the device performance as a function of the overlayer thickness. Between 0 and 136 nm, the HTM forms a conformal overlayer, blocking the direct contact between the perovskite and the gold back contact, thus leading to an increase in the  $V_{OC}$  and the  $J_{SC}$ . As the HTM overlayer is increased above this value, the increase in series resistance arising from the large  $R_{HTM}$  values leads to a decrease in the  $FF$  and thus in the overall cell  $PCE$ , reflected in the drop in  $J_{SC}$  and  $V_{OC}$ .

### 4.3.2 Influence and Role of LiTFSI as Additive

LiTFSI is a common additive to the spiro-MeOTAD HTM solution in solid-state DSSCs. In this section the influence of the variation of the LiTFSI concentration in the HTM solution employed in solid-state devices using perovskite sensitized mTiO<sub>2</sub> was investigated. The Li<sup>+</sup> concentration has been varied between 0, 1 and 10 times the standard [33, 54] concentration (corresponding to 0, 0.009 and 0.090 M Li<sup>+</sup> respectively). The spiro-MeOTAD concentration used here was 0.059 M in chlorobenzene<sup>2</sup>. One has to note here that the mechanism for the spiro-MeOTAD doping is accelerated or catalyzed by the presence of Li<sup>+</sup> ions [40]. A lower doping level of the HTM manifests in an increased transport resistance. This resistance may be evolve visibly in the impedance response even though the overlayer thickness if the spiro-MeOTAD is thin and a cobalt(III) complex<sup>3</sup> is added as chemical *p*-dopant. In addition to its role on the doping of the HTM, the Li<sup>+</sup> ions also participate in the screening of the negative charge of the electrons inside the mTiO<sub>2</sub>, enabling a facilitated charge-transport [160] and induce a downward shift of the conduction band of the mTiO<sub>2</sub> in liquid and ssDSSCs.

In Figure 4.14 (a) the dark current characteristics of solid-state perovskite devices with different Li<sup>+</sup> content are presented. In the low forward bias region the interface between the BL and HTM dominates and all devices display low dark current, the lowest currents measured for samples with high LiTFSI content. At higher forward bias the current is higher for the device with standard Li<sup>+</sup> content (0.009 M) followed by the one with the highest Li<sup>+</sup> content. The lowest dark current is observed for the solid-state device without any Li<sup>+</sup>. Furthermore a slower rate of increase in the current characteristics when there is no Li<sup>+</sup> indicates a higher series resistance relative to the devices containing Li<sup>+</sup>.

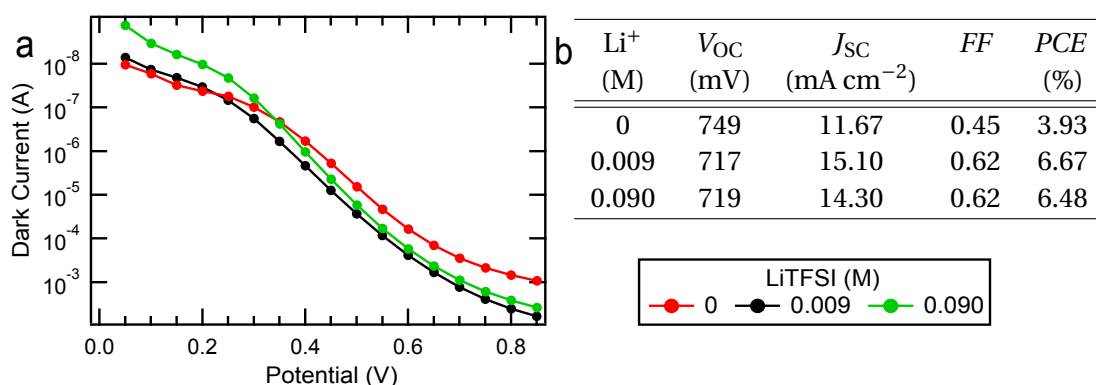
Figure 4.14 (b) presents the photovoltaic performance parameters exhibiting the following trends: The  $V_{OC}$  is reduced if the solid-state devices contain Li<sup>+</sup> ions while the  $J_{SC}$  is increased, indicating that more charges are extracted. These effects are both related since the addition of Li<sup>+</sup> ions results in a downward shift of the conduction band, leading to lower overall  $V_{OC}$ . The

---

<sup>2</sup> This corresponds to 40% of the standard spiro-MeOTAD solution concentration used for conventional ssDSSCs.

<sup>3</sup> Denoted FK209 – cf. Appendix Figure A.2 for molecular structure.

### 4.3. Validation of Impedance Model



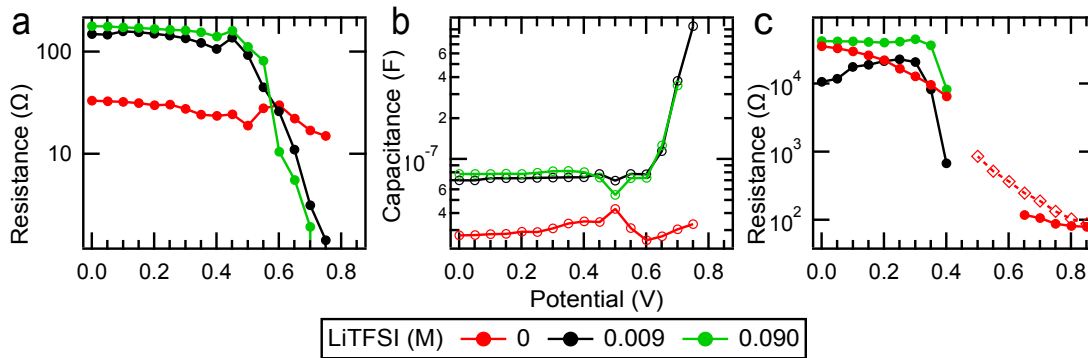
**Figure 4.14.** (a) Dark current measurement of the samples with different Li<sup>+</sup> concentration; 0 (red), 0.009 (black) and 0.09 M (green) LiTFSI. (b) Photovoltaic performance parameters extracted from *J*-*V* measurements under standard AM1.5G illumination (100 mW cm<sup>-2</sup>). All devices were masked to achieve an illuminated area of 0.285 cm<sup>2</sup>.

*FF* increases upon addition of Li<sup>+</sup> ions, which is a result of the previously mentioned higher doping of the HTM – increasing its conductivity – and/or a facilitated charge-transport due to the better screening at the perovskite/mTiO<sub>2</sub> interface.

The impedance spectra were fitted according to the model proposed in the previous section (and in more detail in Appendix Section A.2). In several regards the sample without any added lithium salt displayed strong deviation from the expected behavior. The devices without Li<sup>+</sup> exhibited – at low potential and in the low frequency domain – in addition to the expected 3 RC features, a feature resembling a 45° diffusion line as generally observed in the case of an open Warburg impedance (explained in further detail below). This component could not be fitted with sufficient accuracy and was therefore omitted. This additional low frequency response is related to the diffusion of the ions through the perovskite to the BL. Possible origins of these ions are from the additives such as the cobalt(III) complex used for doping the HTM or even iodide ions liberated from the perovskite structure.

In the high frequency domain at higher forward bias when the potential is greater than 600 mV another semicircle clearly evolves. The transmission line for the charge-transport inside the mTiO<sub>2</sub> is no longer clearly visible since it is partially concealed by this additional feature. Furthermore this semicircle at higher potentials represents the series resistance revealed in the dark current characteristics.

The absence of Li<sup>+</sup> ions facilitates the charge-transfer at the interface between the BC and the HTM at low forward bias as visible by the reduced resistance in this region, see Figure 4.15 (a). Furthermore the associated capacitance of the BC showed a lower magnitude when no LiTFSI is present (Figure 4.15 (b)). This indicates that this interface is not the origin of the additional series resistance leading to the observed reduction in the dark current. Hence logically it represents the HTM since it will be less oxidized and therefore the bulk transport resistance in this material will be higher.



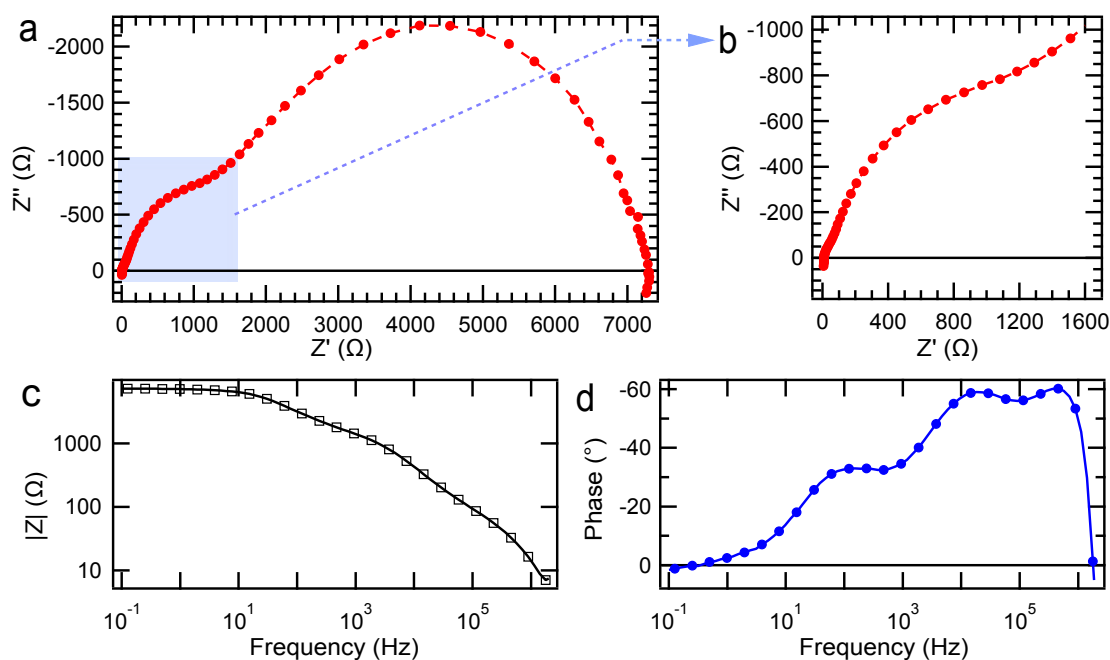
**Figure 4.15.** (a) Charge-transfer resistance at the BC/HTM interface, (b) the associated capacitance extracted by IS measurements in the dark for devices with 0 (red), 0.009 (black) and 0.09 M (green) LiTFSI. (c) Resistance (solid) extracted from the RC feature at intermediate frequencies. At high forward bias the additional resistance is given in case of the 0 M Li<sup>+</sup> ion content (red dotted open diamonds).

The samples with LiTFSI content show similar values of capacitance at the BC interface (Figure 4.15 (b)) across the entire the potential range. Moreover the charge-transfer resistances of these devices are similar, implying that after sufficient addition of ions this interface does not undergo any further change.

The Nyquist spectra (see Figure 4.16) for the device without any Li<sup>+</sup> ions show an additional resistive element (see dotted trace in Figure 4.15 (c)). This semicircle represents a pure series resistance which contributes to the observed low *FF* in the *J-V* characteristics. It is believed to be related to the transport resistance in the HTM  $R_{HTM}$ . It has been demonstrated that in the case of thick overlayers of doped HTM (see Section 4.3.1) the response from the hole conductor overlays with that of the BC at high frequencies. However in this case the absence of Li<sup>+</sup> ions affects the mobility as well as the doping density of the HTM. This consequently culminates in a slower reaction time for the charge carriers inside the HTM and thus shifts the impedance element associated with the HTM to lower frequencies. This is revealed in the different characteristic frequencies for the individual processes.

The resistance assigned to the perovskite is extracted at intermediate frequencies and displayed in Figure 4.15 (c). While this resistance is in the same order of magnitude in the low forward bias regime for all devices regardless of LiTFSI concentration, it is observed to decrease more rapidly with applied bias for devices containing Li<sup>+</sup> ions.

Figure 4.17 (a)–(b) presents the influence of the Li<sup>+</sup> content on the recombination resistance and the chemical capacitance. At 0 V the capacitances – which is related to the BL and the mTiO<sub>2</sub> – of the samples with Li<sup>+</sup> show similar values while that for the case without Li<sup>+</sup> is clearly lower (Figure 4.17 (b)). This implies that the simplest model – a simple RC element for the BL/HTM interface – has to be treated with care since there is an obvious influence of the Li<sup>+</sup> ions on this interface, increasing its complexity. In case of samples with Li<sup>+</sup> there is a slight decline of the capacitance with increasing forward bias while the current flows over the BL.

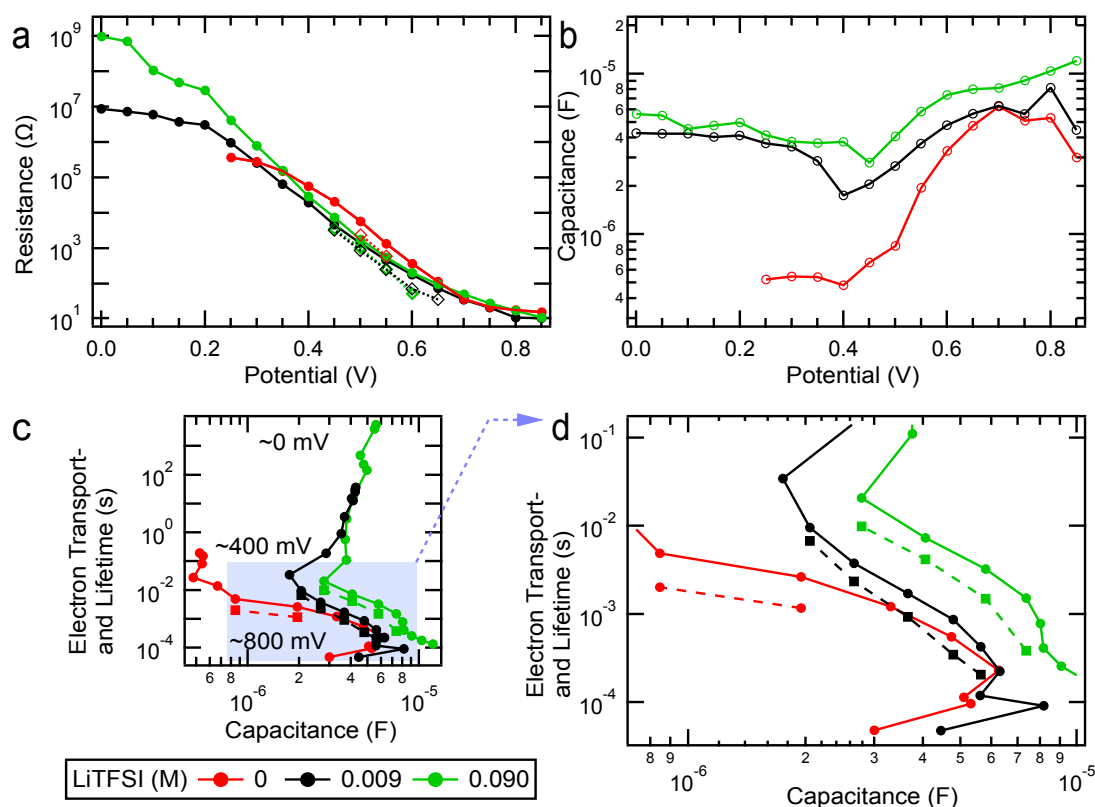


**Figure 4.16.** (a) Nyquist plot, (b) high frequency region, and Bode plots, (c) magnitude and (d) phase, for a solid-state perovskite device with no LiTFSI measured at an applied potential of 500 mV.

All of the samples show the expected drop of the capacitance at around 400 mV before the current starts to be channeled over the  $m\text{TiO}_2$ .

Above 400 mV the  $m\text{TiO}_2$  starts to become conductive and its chemical capacitance increases. As has been observed for the liquid DSSCs or ssDSSCs, the chemical capacitance shifts to lower forward biases with increasing content of lithium salt for the perovskite solid-state devices. However it is important to recall that a lower doping level of the spiro-MeOTAD is expected for devices without any  $\text{Li}^+$  content. The shape of the capacitance is dependent on the presence/absence of  $\text{Li}^+$ , exhibiting a steeper rise for the sample without  $\text{Li}^+$  ions as a function of applied forward bias. At approximately 700 mV bias the capacitance decreases again for the devices with 0 and 0.009 M  $\text{Li}^+$ . This effect does not appear in the case of high  $\text{Li}^+$  content (0.090 M), suggesting that this response is related to the two capacitances in series at the mesostructured surface; the chemical capacitance of the  $m\text{TiO}_2$  and the ionic capacitance at its surface. This latter parameter is strongly dependent on the presence and concentration of ionic species such as  $\text{Li}^+$ . In the case of devices with low or no content of  $\text{Li}^+$  in the HTM, the chemical capacitance in the  $m\text{TiO}_2$  equilibrates more rapidly with the capacitance in the surrounding media.

The recombination resistances reflect the shape of the dark current characteristics (see Figures 4.14 (a) and 4.17 (a)). There are no major differences visible in the behavior of this extracted IS parameter for the three different device types. However while the recombination resistance for the system with high  $\text{Li}^+$  content (0.090 M) displays a similar value relative to



**Figure 4.17.** (a) Recombination resistance,  $R_{ct}$  (solid circles), transport resistance,  $R_{trans}$  (open circles) and (b) the chemical capacitance,  $C_{\mu}$  of the  $mTiO_2$  determined from IS measurements. (c)–(d) Calculated electron (solid) and transport (dotted) lifetimes as a function of the chemical capacitance of the  $mTiO_2$ . Measurements were conducted in the dark on complete devices with different LiTFSI content; 0 (red), 0.009 (black) and 0.090 M (green) LiTFSI.

the case with standard  $Li^+$  concentration (0.009 M), its chemical capacitance is shifted to lower forward bias. This indicates a longer lifetime for the devices with higher concentration, 0.090 M, of LiTFSI.

The transport resistance could not be reliably determined for the case without  $Li^+$ . For samples containing any quantity of  $Li^+$ ,  $R_{trans}$  shows nearly no shift. This is unexpected since this parameter depends on the electrons in the conduction band, and consequently should be similar in magnitude only at the same chemical capacitance or DOS. Such a situation could arise due to similar screening by the charges in the surrounding media of the nanoparticles. Obviously this condition is not fulfilled in this comparison where varying  $Li^+$  concentrations are expected to result to different extents of charge screening.

The electron lifetime – determined from the recombination resistance  $R_{ct}$  – and represented against the chemical capacitance (Figure 4.17 (c)–(d)) normally shows the dependence of the lifetime against the rise in the Fermi level. However this direct comparison requires a similar DOS which is not necessarily the case as revealed here by the different shape of the chemical

capacitance for samples without  $\text{Li}^+$  (Figure 4.17 (b)). Nevertheless such a representation still provides a better comparison than when  $\tau_n$  is represented *versus* the applied potential since this latter situation omits to account for the shift caused by different doping levels of the HTM. At low forward bias when the current flows over the BL, the lifetime is dominated mainly by the change in recombination resistance exhibiting a strong electron lifetime change with nearly similar capacitance.

Generally the electron lifetime and the transport time for electrons inside the  $\text{mTiO}_2$  increase with increasing  $\text{Li}^+$  content. The  $V_{\text{OC}}$  for the devices with  $\text{Li}^+$  displayed a nearly similar value though a shift in the chemical capacitance to lower forward bias is visible for the higher  $\text{Li}^+$  content samples due to the increased electron lifetime. The transport time is observed to increase to a smaller extent leading to a mutual cancellation of the two effects and hence similar  $V_{\text{OC}}$  values.

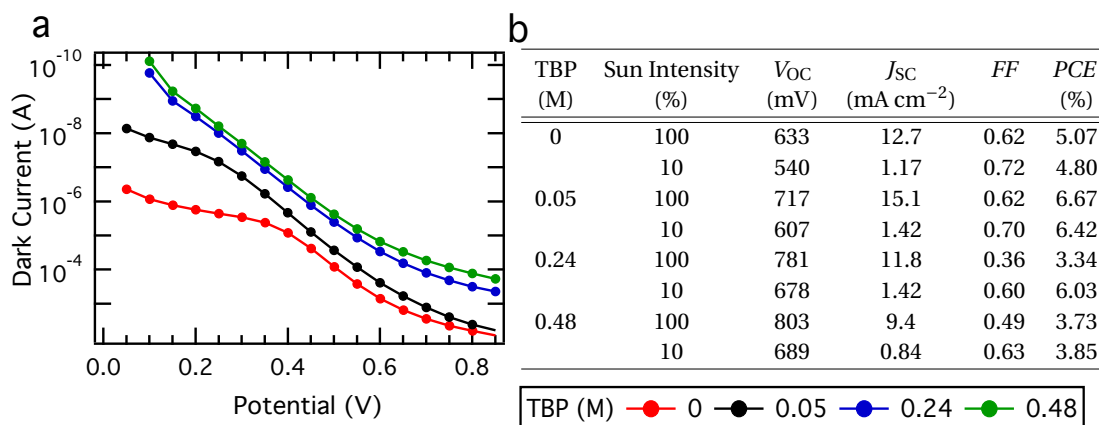
This investigation demonstrated the multiple effects of lithium ions on the device working mechanisms and performance of solid-state perovskite solar cells. These effects are already known from the study of ssDSSCs and liquid DSSCs thus confirming the validity of this characterization technique. Increasing the concentration of  $\text{Li}^+$  ions shifts the conduction band to lower forward bias. It further influences the shape of the DOS, and increases the transport time and the lifetime of the electrons within the  $\text{mTiO}_2$ . Perovskite solid-state devices without any  $\text{Li}^+$  exhibit an additional series resistance at high forward bias related to the transport inside the HTM. The resistance at intermediate frequencies related to the perovskite material displays values within the same range for all cases at 0 V and for system without  $\text{Li}^+$ , this resistance is detectable over the whole potential range.

#### 4.3.3 Influence and Role of 4-*tert*-butylpyridine as Additive

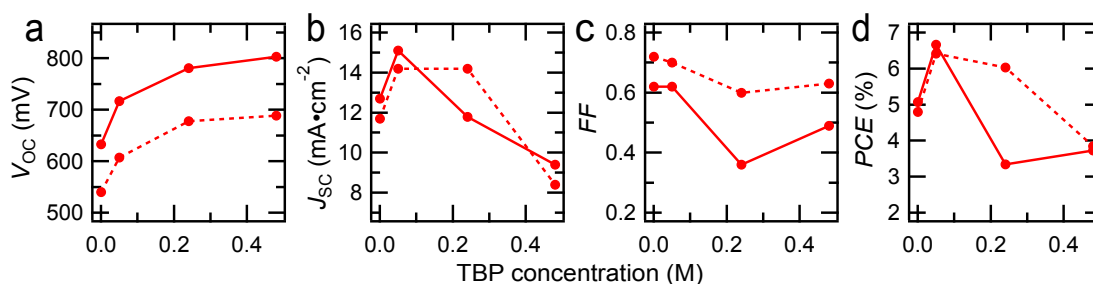
Following the analysis of the effect of concentration variation of the LiTFSI additive in the HTM solution on the device mechanisms of perovskite-based solid-state cells, a similar study examining the effect of the other common additive – TBP – was carried out. As before, the complete devices were characterized using IS conducted in the dark. Using the model described in detail above the IS plots were interpreted and fitted accordingly.

The role of TBP in DSSCs has been investigated [38, 161–164] to some extent and has been determined to contribute to a conduction band shift of the  $\text{mTiO}_2$ . It has also been found to play a role as a recombination blocking layer, as it attaches to the  $\text{TiO}_2$  surface, preventing electrons recombining with the redox couple or solid HTM. The dark current characteristics and photovoltaic performance parameters extracted from  $J$ - $V$  measurements under 10 and 100% sunlight intensity of perovskite devices with different TBP concentrations are presented in Figure 4.18.

Figure 4.19 presents a graphical representation of the evolution of the photovoltaic performance parameters (adapted from Figure 4.18 (b)). As the concentration of TBP is increased



**Figure 4.18.** (a) Dark current measurement of devices with different TBP concentrations: 0 (red), 0.05 (black), 0.24 (blue) and 0.48 M (green). (b) Photovoltaic performance parameters extracted from  $J-V$  measurements of devices with varying TBP concentration used in the HTM. All devices were masked to achieve an illuminated area of  $0.285 \text{ cm}^2$ .



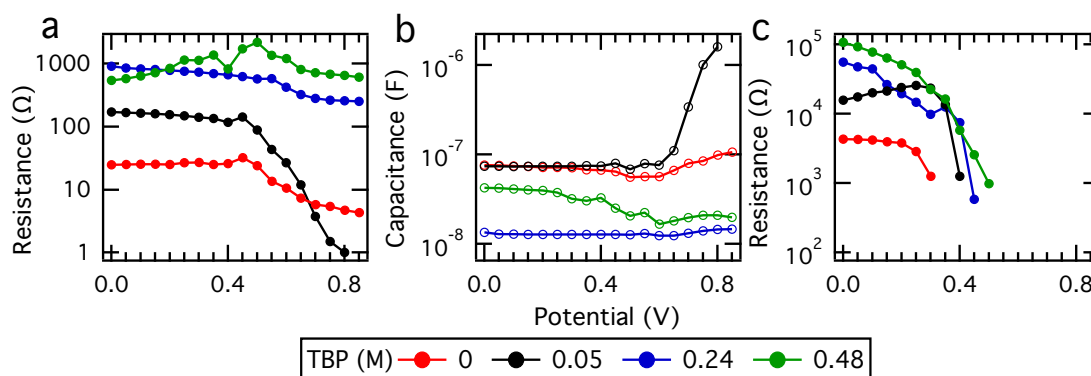
**Figure 4.19.** Graphical representation of the trends in the photovoltaic performance parameters as a function of TBP concentration measured at 100% (solid trace) and 10% (dashed trace) sun intensity. The  $J_{SC}$  determined at 10% sun intensity have been normalised to 100% sun intensity.

a clear, continuous increase of the  $V_{OC}$  is observed. The addition of the TBP shows first an increase in  $J_{SC}$  to a maximum of  $15.1 \text{ mA cm}^{-2}$  and upon further addition the  $J_{SC}$  is observed to decrease again. The latter decrease surely relies on the fact that the driving force for injection of electrons into the  $\text{mTiO}_2$  is reduced with the increasing conduction band position.

The  $FF$  is greatly reduced for the two samples with higher TBP content (0.24 and 0.48 M) especially for the measurements under 1 sun illumination while the ones with no TBP or the standard concentration of 0.05 M show similar values.

Starting with the analysis of the high frequency features, the magnitude of the resistance corresponding to the BC/HTM interface was found to remain largely independent of the applied potential at low forward bias and decrease at higher forward bias values (Figure 4.20 (a)). As the concentration of TBP used is increased, the overall magnitude of the resistance increases. Pyridine compounds are known to adsorb onto gold electrodes [165] and therefore could function as a blocking layer for the charge-transfer at the interface between the HTM and gold.





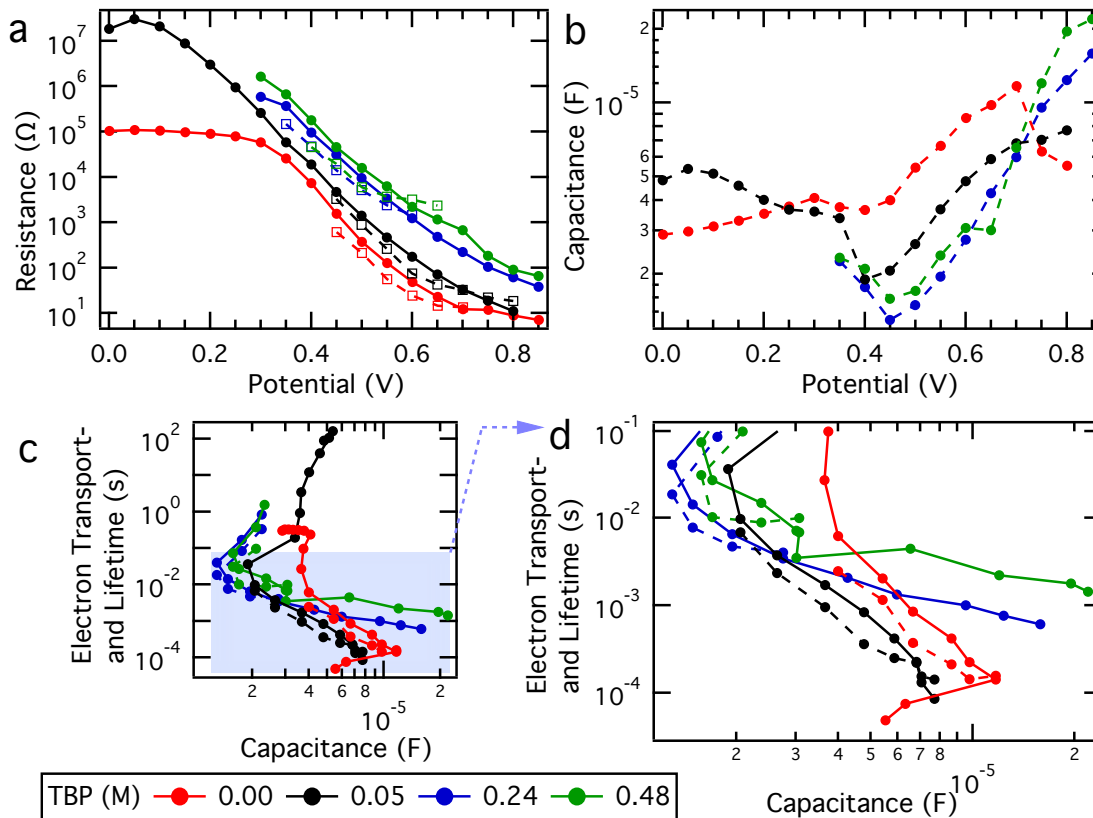
**Figure 4.20.** (a) High frequency resistance, (b) corresponding capacitance and (c) intermediate frequency resistance attributed to the perovskite material extracted by IS measurements in the dark for devices with 0 (red), 0.05 (black), 0.24 (blue) and 0.48 M (green) of TBP used in the HTM solution.

This would result in the observed increase in the magnitude of the high frequency resistance feature as the concentration of TBP is increased in the device fabrication.

Additionally previous studies [40, 41] have shown that the inclusion of  $\text{Li}^+$  ions to the HTM solution act as a *p*-type dopant of the spiro-MeOTAD. However due to the high binding strength of the  $\text{Li}^+$  ions, a certain proportion is certain to bind to the TBP molecules, resulting in an overall lower doping level of the HTM. Consequently the transport resistance of the HTM  $R_{\text{HTM}}$  will increase as the concentration of TBP increases as there is a lower proportion of  $\text{Li}^+$  ions available to *p*-dope the HTM. As such this suggests that the high frequency feature may initially be dominated by the BC/HTM interface for 0 M TBP, and as the TBP concentration is increased the contribution from the transport resistance of the HTM or the increased blocking of the adsorbed TBP becomes more significant (see Figure 4.20 (a)).

The associated capacitance for this resistance, presented in Figure 4.20 (b) was found to remain independent of the applied potential up to approximately 600 mV, after which it is observed to increase in a similar fashion as the associated resistance decreases. In the case of devices with TBP concentrations exceeding 0.24 M, this increase is preceded by a small decrease in magnitude.

The resistance extracted from the additional RC feature at intermediate frequency attributed to the perovskite material (Figure 4.20 (c)) was found to be considerably lower for devices with no TBP content. For devices containing any quantity of TBP, the resistance of this intermediate frequency feature was an order of magnitude larger than in the case of devices containing no TBP. The observed increase in the resistance of the perovskite component, suggests that this feature is influenced by the presence and concentration of TBP. This could be due to an indirect effect of the TBP binding with the  $\text{Li}^+$  ions decreasing the concentration of ‘free’  $\text{Li}^+$  ions, thus leading to an increase in the transport resistance of the perovskite and the HTM (as previously stipulated).



**Figure 4.21.** (a) Transport (dashed circles), recombination (solid circles) resistance and (b) corresponding chemical capacitance extracted from IS measurements. (c)–(d) Calculated electron lifetimes,  $\tau_n$  (solid) and transport lifetimes,  $\tau_{trans}$  (dotted) as a function of the chemical capacitance of the  $mTiO_2$ . Measurements conducted in the dark for devices with 0 (red), 0.05 (black), 0.24 (blue) and 0.48 M (green) of TBP used in the HTM solution.

The dark current measurements (Figure 4.18 (a)) show a clear difference for the different devices. As the TBP content increases the resultant formation of a blocking layer hinders the charge-transfer at the BL as well as at the  $mTiO_2$  interfaces and consequently the current decreases for devices with higher TBP content. This is reflected in the observed change of the charge-transfer/recombination resistance of the  $mTiO_2$  (Figure 4.21 (a)). The transport resistance of the electrons inside the  $mTiO_2$  shows a shift to higher forward potentials according to the increased concentration of the pyridine additive.

As the concentration of TBP increases,  $C_\mu$  is observed to shift to higher forward bias (Figure 4.21 (b)). This demonstrates an upward shift in the conduction band of the  $mTiO_2$  as has been observed for DSSCs. This is also reflected in the mentioned shift in transport resistance. The shift in the conduction band as a result of increasing TBP concentration is further apparent in the increasing  $V_{OC}$  of the devices as seen in Figure 4.18 (b).

The electron lifetime and transport times are calculated and when represented against chemical capacitance as shown, allow a comparison at similar Fermi level, see Figure 4.21 (c)–(d).

As in the case when the  $\text{Li}^+$  content was changed, in the region of low forward bias the lifetime undergoes a large change at similar capacitances. At higher forward bias the increasing lifetime with increasing TBP concentration is expected, as TBP is known to block the recombination of electrons. The case where no TBP is added does not fall into this trend in that it exhibits a higher electron lifetime than the device with 0.05 M TBP. This may be a result of the contradictory effect due to the high amount of 'free'  $\text{Li}^+$  ions that improve the conductivity and thus the lifetime.

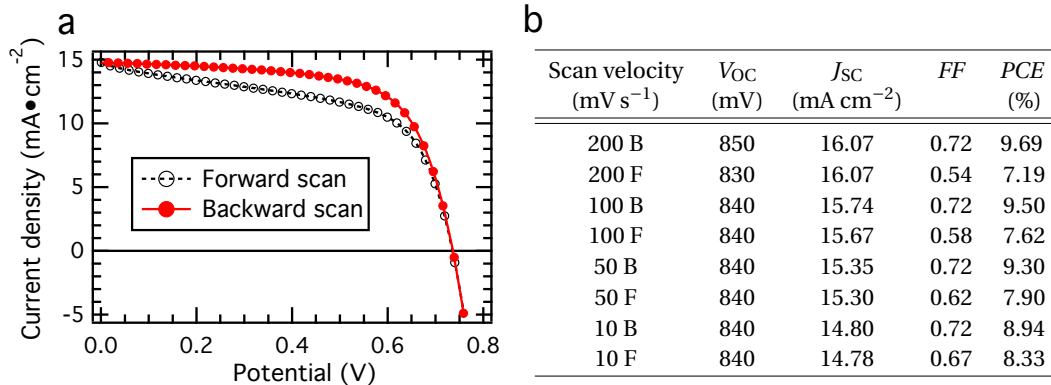
It was found that the TBP added to the HTM solution acts as a recombination blocking agent, increasing the recombination resistance for the electrons at high TBP content. Additionally, as in the case of conventional DSSCs, the TBP leads to a shift in the conduction band of the  $\text{mTiO}_2$ , which is observed in the chemical capacitance. This directly influences the  $V_{\text{OC}}$  of the devices, leading to an increase in  $V_{\text{OC}}$  as the CB is shifted upwards with increasing TBP concentration. Additionally the poorer  $FF$  of devices as the concentration of TBP is increased results from increasing series resistance due to greater transport resistance of the less  $p$ -doped HTM,  $R_{\text{HTM}}$ . This highlights the additional indirect effects of increasing the TBP concentration. Its high binding strength results in a decreased concentration of 'free'  $\text{Li}^+$  ions, which greatly influences the device mechanism and thus photovoltaic performance. Additionally the higher series resistance is also a result of the increased adsorption of TBP at the gold back contact, hindering the charge-transfer at the HTM/BC interface.

#### 4.4 Standard Devices Under Illumination

The previous investigations outlined in this chapter were conducted under dark conditions. The impedance measurements revealed that most of the basic concepts from the related liquid and solid-state DSSC devices remain valid. However there exist differences between these and the perovskite solid-state based system, such as the additional RC feature at intermediate frequencies and e.g. the behavior of  $J_{\text{SC}}$  and  $V_{\text{OC}}$  with increasing HTM overlayer observed in previous sections.

When the current-voltage characteristics of these perovskite-based solid-state solar cells are measured under illumination a strong hysteresis in the  $J$ - $V$  curves becomes apparent (Figure 4.22 (a)) and is observed to manifest predominantly in the forward scan (from low to high forward bias). This phenomenon is not detectable in the dark current measurements. Figure 4.22 (b) displays the  $PCE$  values of a perovskite-based solid-state solar cell determined using different scan velocities. The  $PCE$  determined from the forward scan from low to high forward bias is strongly dependent on the scan velocity employed in the data acquisition procedure while the backward scan from high to low forward bias shows nearly no dependence on scan velocity. This indicates the existence of some slow charge carriers involved in the current and voltage generation resulting in the observed hysteresis in the  $J$ - $V$  characteristics.

Similar slow reaction times are observed in the transient photocurrent and photovoltage dynamics of the perovskite devices shown in Figure 4.23. The rise and decay of the pho-



**Figure 4.22.** (a)  $J$ - $V$  curves of a standard perovskite solid-state device measured in the forward (black) and backward (red) scan direction at a scan velocity of  $100 \text{ mV s}^{-1}$ . (b)  $PCE$  values for a device scanned with different velocities. Here from  $0 \text{ V}$  to  $V_{OC}$  and back, F= forward scan, B= backward scan. The results presented in (a) and (b) correspond to different devices.

tocurrent and the photovoltage were fitted according to the least squares method using a double exponential fit, from which the associated time constants presented in Table 4.3 were determined.<sup>4</sup> The time constants extracted from the fitting procedure correspond to the fast and slow rise/decay components.

After the red light LED pulse the current dynamics reveal an initial steep rise of the current (where  $\tau_1$  is the associated time constant determined for this rise) which is observed to decay rapidly. Following this initial fast decay the photocurrent undergoes a slow rise (slow rise time constant  $\tau_2$ ). After the red light pulse is stopped the fast initial decay (fast decay time constant  $\tau_1$ ) of the photocurrent is followed by a slow decay (slow decay times constant  $\tau_2$ ). Similar observations can be made for the photovoltage rise and decay after the light pulse. The time constants determined for the slow component of the photocurrent yielded values of about 16 ms and 15 ms for the rise and decay respectively (see  $\tau_2$  extracted from the fitting in Table 4.3). Similarly the time constants associated with the photovoltage rise and decay were found to be 33 ms and 25 ms respectively.

This slow time constant phenomenon manifests itself in the IS measurements under illumination as a response in the very low frequency regime (between 10 and 0.05 Hz in the Nyquist plot displayed in Figure 4.24). There exist several possible origins for this slow process, which clearly has an influence on the  $PCE$  of these types of devices. It is clear that this feature is pre-

<sup>4</sup> The photovoltage and photocurrent transient decays presented in Figure 4.23 were fitted using the least squares method to the following double exponential decay, Equation 4.1.

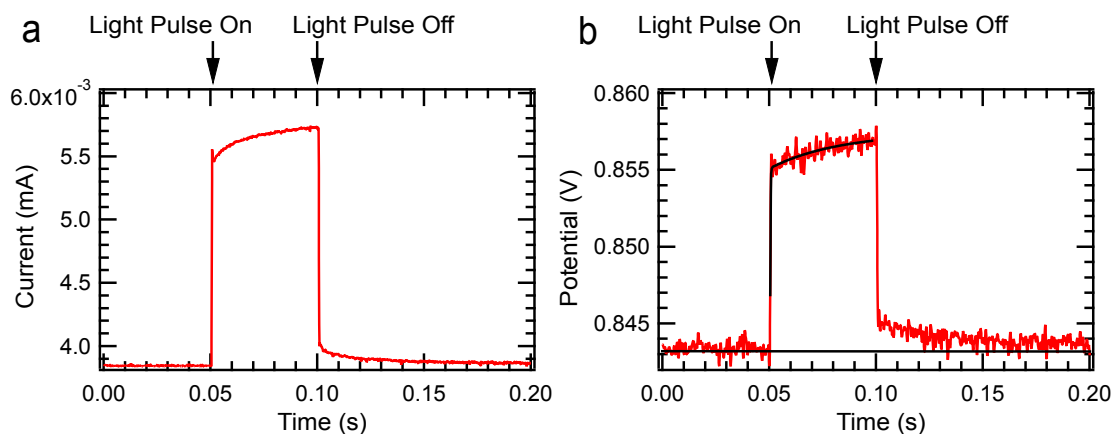
$$y_0 + A_1 \exp\left\{\frac{-(x-x_0)}{\tau_1}\right\} + A_2 \exp\left\{\frac{-(x-x_0)}{\tau_2}\right\} \quad (4.1)$$

where  $y_0$  is the offset,  $A_1$  and  $A_2$  are the first and second amplitude,  $\tau_1$  and  $\tau_2$  are the time constants for the lifetimes of the fast and slow rise/decay processes respectively.  $x_0$  is a constant corresponding to the time the red light pulse was switched on and off. The extracted time constants are summarized in Table 4.3.

#### 4.4. Standard Devices Under Illumination

**Table 4.3.** Lifetime time constants for the fast and slow rise/decay processes extracted from photocurrent and photovoltage transient decay measurements.

Time Constants (s)	Photocurrent		Photovoltage	
	Rise	Decay	Rise	Decay
$\tau_1$	0.000 118(3)	0.000 122(2)	0.000 16(2)	0.000 25(1)
$\tau_2$	0.0163(6)	0.0153(5)	0.033(7)	0.025(3)

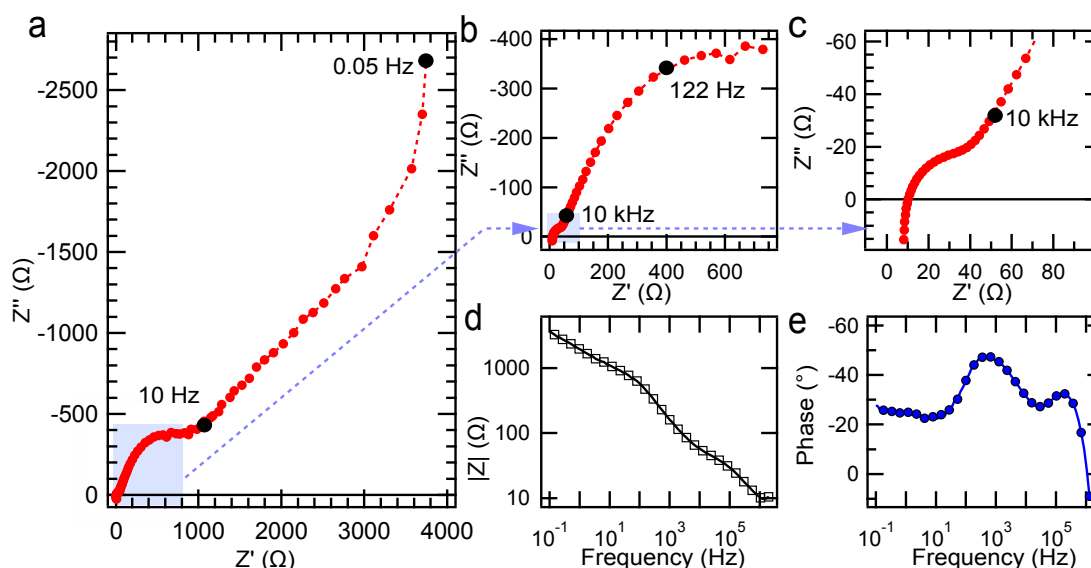


**Figure 4.23.** (a) Transient current dynamics at  $J_{SC}$  and (b) transient photovoltage dynamics at  $V_{OC}$ .

dominantly a light induced effect, as it does not appear to the same extent for measurements conducted under dark conditions. Origins of this phenomenon are possibly ion intercalation, ionic charge-transport and/or a ferroelectric effect.

The intercalation of  $\text{Li}^+$  ions into the  $\text{TiO}_2$  electrode has been reported to increase the photovoltaic performance of DSSCs [166–168]. When  $\text{Li}^+$  are present in the electrolyte or the hole-transport material lithium is photointercalated into the  $\text{TiO}_2$  under illumination and applied forward bias. The inclusion of lithium into anatase  $\text{TiO}_2$  leads to the phase transition from tetragonal  $\text{TiO}_2$  to orthorhombic  $\text{Li}_{1/2}\text{TiO}_2$  [169] and increases the conductivity of the  $\text{TiO}_2$  photoanode [170].

To further examine the observed slow process, a perovskite device without HTM – hence without any lithium ions present – was fabricated and measured under illumination to verify if such a slow phenomenon is still observable. The slow time constant feature remained visible in the IS response even in the absence of the HTM, hence excluding a photointercalation phenomenon as a possible origin and indicating its relationship to the perovskite material. As described in Section 4.2, an additional resistive element was observed at low forward bias for IS measurements conducted in the dark and attributed to a charge-transport through the perovskite material. This feature was observed to vanish when the IS measurement was conducted under illumination. This demonstrates that the ability of this perovskite interfacial layer to transport electronic charges is strongly increased under illumination. Consequently



**Figure 4.24.** (a) Nyquist plot of a device measured under illumination at 0 V. Plots (b)–(c) show the high frequency range from MHz down to about 10 Hz. Corresponding Bode plots displaying (d) magnitude and (e) phase as a function of the frequency.

the electronic conductivity of the perovskite layer between the  $\text{mTiO}_2$  and the HTM will be high under illumination.

In addition to the electronic conductivity of this perovskite material it is most likely also an ionic conductor where some charge carriers may be transported by the diffusion of ions. The ionic conduction within the perovskite material is probably resulting from the migration of halide ions, in this case iodide ions or the associated vacancies. This ionic conduction by diffusion in the perovskite material is assumed to occur on a considerably slower timescale than its electronic conduction and hence is believed to be associated with a comparatively slow time constant, thus manifesting in the very low frequency region as a Warburg type diffusion. Furthermore it is likely that the ionic conduction only manifests when the electronic conductivity is limited (i.e. at low electron density at around 0 V applied bias) and/or when the ions within the material become mobile (i.e. under light or increased temperature). If these assumptions are valid the origin of the unique IS response of perovskite-based solar cells can be separated into two chief contributions. Firstly its electronic conduction of charges which manifests at intermediate frequencies and secondly its ionic conduction which appears at very low frequencies. Both these processes are clearly strongly dependent on the light intensity, drastically increasing in magnitude when exposed to light. Hence under illumination the conduction of electronic charges is enhanced and the related charge-transport resistance (visible under dark conditions) is greatly reduced. Similarly assuming that under illumination the mobility of ions and hence their diffusion within the perovskite material is increased, this explains the appearance of the slow time constant process at very low frequencies in the IS response.

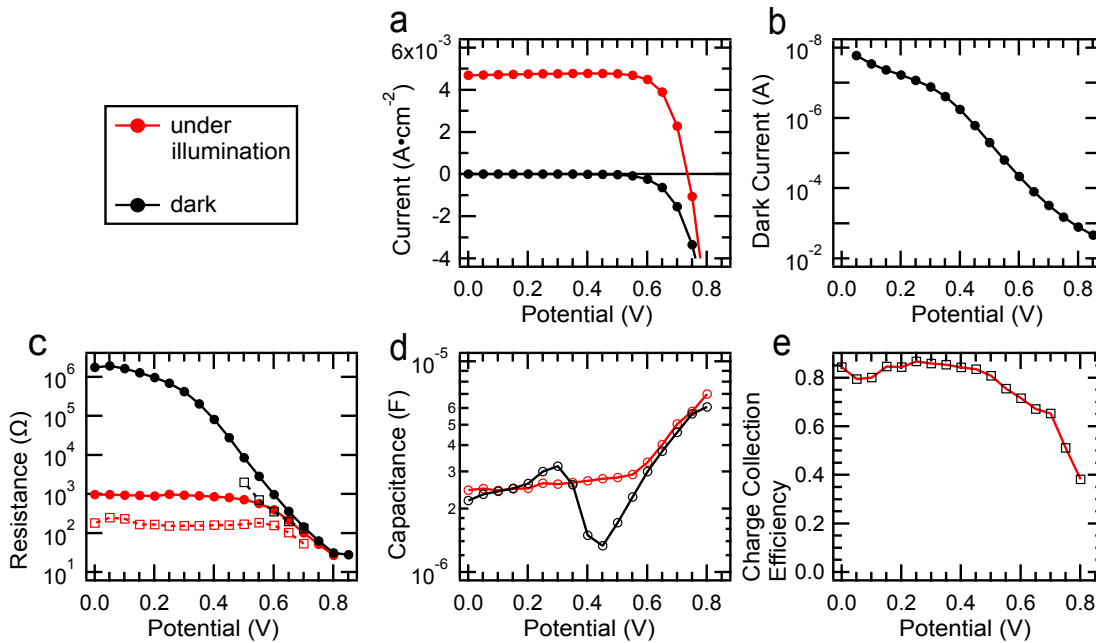
From these observations it appears that this perovskite materials is a mixed conductor with separate ionic and electrical conductivities. While I believe that the observed slow component in the IS response is a result of the ionic conduction of the perovskite material, other possible contributions such as the previously mentioned ferroelectric effect [171] can not be excluded. Frost *et al.* demonstrate that organic-inorganic hybrid perovskite materials such as  $\text{CH}_3\text{NH}_3\text{PbI}_3$  show instantaneous electrical polarization [172]. This is a result of the orientational disorder of the polar  $\text{CH}_3\text{NH}_3^+$  cation within the perovskite cage which can lead to the formation of ferroelectric domains within the material. This photoferroic property may account for the observed hysteresis in the  $J$ - $V$  curves, which manifests predominantly in one scan direction (from low to high forward bias). The orientation of the ferroelectric domains will be influenced by the applied potential and the scan direction, hence giving rise to the hysteresis. The origin of this hysteresis has also been attributed to the slow filling of traps resulting due to defects within the perovskite absorber material [173] but this seems unlikely as this does not fully account for the differences observed here when devices are measured at different scan speeds.

Apart from the slow component visible in the Nyquist plot the following elements can be observed under illumination for perovskite-based solar cells. As in the case for the measurements conducted in the dark, a high frequency RC-arc for the BC/HTM interface and the feature associated with the chemical capacitance and the recombination resistance of the  $\text{mTiO}_2$  are detectable. At lower light intensities (less than 50%) a transmission line for the transport inside the  $\text{TiO}_2$  is also visible.

To further clarify the role of illumination on this system, the  $J$ - $V$  characteristics and the IS fitting results determined in the dark and under illumination are presented in Figure 4.25 (a)–(b) and (c)–(d) respectively. Here the light intensity used is only 40% using an LED array. At high forward bias the behavior of the increasing chemical capacitance is observed to be similar when measured in the dark or under illumination. Alternatively the recombination resistance as well as the transport resistance for the electrons are greatly reduced when under illumination. The charge collection efficiency  $\eta_{coll}$  which can be calculated according to;

$$\eta_{coll} = \left( 1 + \frac{\tau_{trans}}{\tau_n} \right)^{-1} \quad (4.2)$$

and is hence greatly dependent on the recombination and transport resistances, shows about 80 to 85% (see Figure 4.25 (e)). As already observed in the relationship between the transport and recombination resistance in the dark, see Figure 4.25 (c), the charge collection efficiency is a critical parameter to achieve high photocurrents in such devices. In the case of a typical liquid DSSC, the charge collection efficiency is generally over 95%, even at full sunlight intensity. In comparison,  $\eta_{coll}$  determined for perovskite-based devices using Equation 4.2 is already considerably lower (80 to 85%) at only 40% light intensity. Further increasing the light intensity to 100% leads to further reduction in  $\eta_{coll}$  to below 80%. Hence the application of this fitting procedure enables the identification of a key parameter, the charge collection efficiency, that can be utilized to further optimize these type of devices. From this investigation it is



**Figure 4.25.** (a)  $J-V$  characteristic in the dark (black) and under illumination at 40% sunlight intensity by LED (red). (b) Dark current displayed on logarithmic scale. Extracted impedance result of (c) the recombination resistance (solid circles), the transport resistance (open squares) and (d) the chemical capacitance. (e) Charge collection efficiency calculated from  $R_{ct}$  and  $R_{trans}$  determined from IS measurement conducted under 40% light intensity.

clear that the  $J_{SC}$  can be further improved in these perovskite-based devices by e.g. reducing the recombination while maintaining a similar transport resistance. This would lead to an increased  $J_{SC}$  and  $V_{OC}$  and finally to an overall increased device efficiency.

## 4.5 Additional Discussion

The IS response associated with the perovskite material, manifesting at intermediate frequencies needs to be addressed in further detail. Injection of charge carriers from and to the perovskite with the  $TiO_2$  is clearly demonstrated by the change of the capacitance associated with the recombination arc generating the current (Figure 4.5) and in the publications of Abrusci *et al.* [156]. When no  $mTiO_2$  is present in the device structure no real increase in the capacitance is visible (with the simplification mentioned for the fitting procedure from Figure 4.4 (a)–(b)) showing that the capacitance can be used as a clear indicator for the active part of the  $mTiO_2$  in the charge-transfer processes. The origin of the RC element at intermediate frequencies at low forward bias in the dark is, as already mentioned above, related to the electronic charge-transport within the perovskite. This feature is strongly dependent on the material and structural properties. The role of the nature and morphology of the perovskite material on its IS response will be examined in further detail in the Chapter 5. In the investigations of the effect of the spiro-MeOTAD overlayer thickness or the variation of the content of



the TBP and LiTFSI additives this element appeared relatively unaffected with the exception of the low TBP concentration case. This is attributed to the indirect effect of TBP binding with  $\text{Li}^+$  ions decreasing the concentration of 'free'  $\text{Li}^+$  ions, thus leading to an increase in the transport resistance of the perovskite and the HTM. It is assumed that there is a relatively conformal film of the perovskite on top of the BL and on the  $\text{mTiO}_2$ , hence charges have to be channeled *via* this perovskite film. As such it acts like an intermediate layer between the  $\text{mTiO}_2$  and the HTM. This is further validated by the disappearance of this feature when the devices are under illumination and the perovskite is very conductive.

## 4.6 Conclusions

In this chapter solid-state mesoscopic solar cells using lead-iodide based perovskite deposited onto submicrometer thick mesoporous  $\text{TiO}_2$  in combination with spiro-MeOTAD as a HTM are investigated using IS. Through comparison with the well-known liquid and solid-state DSSC systems, these devices are analyzed and interpreted, systematically establishing an equivalent circuit model that can be applied to the IS analysis of this type of devices. This is the first complete model reported for these type of devices. This model is then employed to explore the effect of the concentration variation of the common HTM solution additives, TBP and LiTFSI on the device parameter. Additionally the influence of the overlayer thickness of the HTM on top of the  $\text{mTiO}_2$  was investigated. From these experiments the working mechanisms of these perovskite devices are explored and the presented model used for the IS interpretation is validated. The complex nature of this system is exposed and the interplay of various components, i.e. additive ratios, is highlighted. The experimental results show the multiple roles and effects of the  $\text{Li}^+$  ion and TBP concentrations in the HTM on the internal electrical parameters, and consequently on the overall device performance.

The model presented further identifies the separate features corresponding to the electronic and ionic conductivities of the lead-iodide based perovskite material. These features are unique to this system and are believed to greatly depend on the morphology and nature of the perovskite material as these define its transport and electrical properties.

### 4.6.1 Perspectives

This study describes the systematic development of an equivalent model to analyze perovskite-sensitized solar cells. As such this investigation shows that IS is a useful tool for characterizing this type of system and the developed IS model can be applied to examine the perovskite material in working device configurations to identify the limiting processes reducing the overall efficiency of the solar cells. It exposes the complex nature of this system and the interplay between the various components at the interfaces within the device.

Furthermore it was demonstrated to be a valuable tool in the research of factors that influence the device performance (such as the influence of additives) exposing their role and contribu-

## **Chapter 4. Impedance Spectroscopic Analysis of Perovskite Solid-State Solar Cells**

---

tion to the device operating mechanisms. The following Chapter 5 uses the model established in this chapter to examine the role of the perovskite nature, composition and morphology on the device photovoltaic performance.

# 5 Morphological Studies of $\text{CH}_3\text{NH}_3\text{PbI}_3$ Perovskite

Section 5.4 is based on the publication Dualeh *et al.* *Advanced Functional Materials*, 2014.

## 5.1 Introduction

The solution processability of the organic-inorganic perovskite material  $\text{CH}_3\text{NH}_3\text{PbI}_3$  is one of its major advantages. The simplest method of deposition requires only a simple heating step to convert the deposited precursor solution (consisting of the organic and inorganic components in an appropriate solvent) to the crystalline perovskite form. In this deposition method the molar ratio of the precursors is critical and its influence on the power conversion efficiency has been reported [174]. The morphology, stoichiometry and crystallinity of the material greatly influences the overall photovoltaic device performance and as such the deposition technique of the material is of crucial importance, as demonstrated by Burschka *et al.* [175] and Bi *et al.* [176]. In just over two years the reported efficiencies for the solid-state  $\text{CH}_3\text{NH}_3\text{PbI}_3$  hybrid perovskite-based solar cells using spiro-MeOTAD have increased from 9% [49] to over 15% [150] mainly through changes and improvements in the deposition methods and treatments. Hence all the treatments and conditions the material is exposed to as part of and/or following the conversion to the final perovskite have a non-negligible impact on the quality and nature of the perovskite layer. Recent reports in 2013 have demonstrated *PCEs* of 15% from a planar heterojunction perovskite solar cell [177] which is attributed to the formation of extremely uniform flat films of the mixed halide perovskite  $\text{CH}_3\text{NH}_3\text{PbI}_{3-x}\text{Cl}_x$  by vapor deposition. This indicates that the perovskite absorbers can result in highly efficient solar cells in the simplest planar device configuration, but is heavily dependent on the nature of the perovskite film formed.

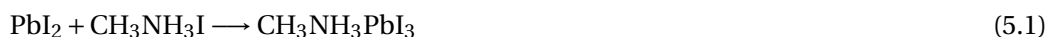
## 5.2 Perovskite Formation: Morphology, Structure and Composition

The nature and morphology of the perovskite film deposited on the mesoporous scaffold is critical for the photovoltaic performance of the solar cell devices. Unfortunately this property

is heavily dependent on the processing conditions of the material and consequently difficult to control. In this chapter the morphological structure of the perovskite film is examined using scanning electron microscopy (SEM), using X-ray diffraction (XRD) and UV-vis absorption spectroscopy to expose the nature and composition of the material. Impedance spectroscopy (IS) measurements are used to interpret and understand the role of these properties of the perovskite material on the working device mechanisms and photovoltaic performance of perovskite-sensitized solid-state solar cells. While many different procedures and recipes have been reported the work presented here focused on the simplest deposition technique where the perovskite is processed by spin-coating from a precursor solution containing all of its components and subsequently annealed to remove excess solvent and drive the crystal growth of the perovskite. This chapter will examine the role of various individual components used in different perovskite precursor solution recipes in addition to examining specific parameters influencing the formation mechanism.

### 5.3 Solvent Effects

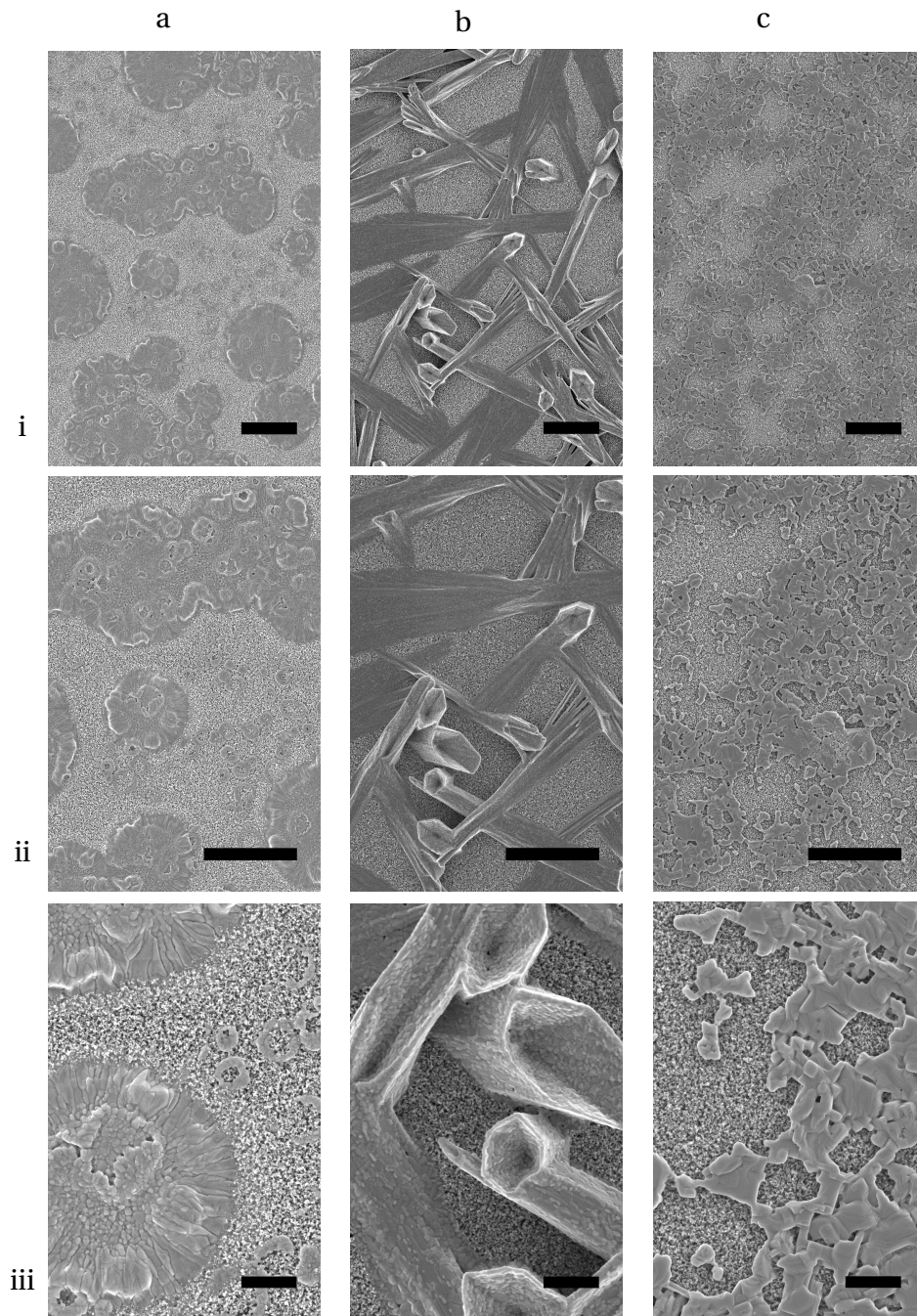
As previously discussed one of the major advantages of this type of perovskite material is the ease with which it can be processed from solution. The simplest deposition techniques involve spin-coating a solution containing the precursor materials – the inorganic PbX<sub>2</sub> (where X = I, Br or Cl) and organic CH<sub>3</sub>NH<sub>3</sub>I species – from a common solvent, i.e.  $\gamma$ -butyrolactone (GBL) or *N,N*-dimethylformamide (DMF). This leads to the formation of a film of deposited material on the substrate which is typically heated at approximately 100°C to remove the solvent and drive the crystallization of the material. Figure 5.1 shows SEM images of mTiO<sub>2</sub> films onto which such precursor solutions were deposited and heat treated. As can be observed, depending on the choice of solvent and precursor mixture used in the deposition process, there are large variations in the resultant film morphology. The perovskite crystallization is dependent on multiple factors including the volatility of the solvent, the degree of wetting of the substrate and the solubility of the precursor materials. Figure 5.1 illustrates the differences in crystal morphology of the perovskite material when deposited from (a) GBL or (b) DMF using PbI<sub>2</sub> and CH<sub>3</sub>NH<sub>3</sub>I (1 to 1 molar ratio) as precursors. In both these cases after deposition by spin-coating the as-deposited films are annealed at 100°C for 10 minutes during which they are observed to undergo a rapid color change from yellow<sup>1</sup> to dark brown, indicating the complete conversion to the perovskite material (Equation 5.1).



In the case of GBL, the perovskite forms circular islands and rings of material varying in size, displaying internal structuring of the islands from the centre outwards. In contrast when DMF is used instead of GBL, the perovskite crystals adopt hexagonal-based needle like shapes.

---

<sup>1</sup> The perovskite precursor mixture in solution used here, containing PbX<sub>2</sub> (where X=I or Cl) and CH<sub>3</sub>NH<sub>3</sub>I in GBL or DMF appears clear yellow in color. In contrast the color of CH<sub>3</sub>NH<sub>3</sub>PbI<sub>3</sub> perovskite crystal material is dark brown.

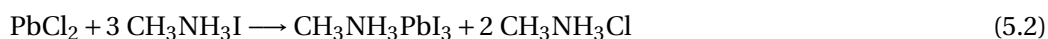


**Figure 5.1.** SEM images of mTiO<sub>2</sub> films with perovskite material formed from (a) PbI<sub>2</sub> : CH<sub>3</sub>NH<sub>3</sub>I in GBL, (b) PbI<sub>2</sub> : CH<sub>3</sub>NH<sub>3</sub>I in DMF and (c) PbCl<sub>2</sub> : 3 CH<sub>3</sub>NH<sub>3</sub>I in DMF. Black scale bars correspond to (i)–(ii) 5 μm and (iii) 1 μm.

Considering the case where the inorganic precursor PbI<sub>2</sub> is replaced by PbCl<sub>2</sub> as reported by Lee *et al.* [50] and Ball *et al.* [51], results in a further different film morphology as visible in Figure 5.1 (c). The resultant film morphology of the PbCl<sub>2</sub> based solution consists of smaller

crystal structures, which form an interconnected network across the mTiO<sub>2</sub> substrate.

To ensure a 1:3 ratio of Pb to I, a 1 to 3 molar ratio of PbCl<sub>2</sub> to CH<sub>3</sub>NH<sub>3</sub>I is used, which results in the formation of 2 molar equivalents of CH<sub>3</sub>NH<sub>3</sub>Cl as according to Equation 5.2. Furthermore due to the poor solubility of PbCl<sub>2</sub> in GBL, DMF is used as a common solvent for the perovskite precursors.



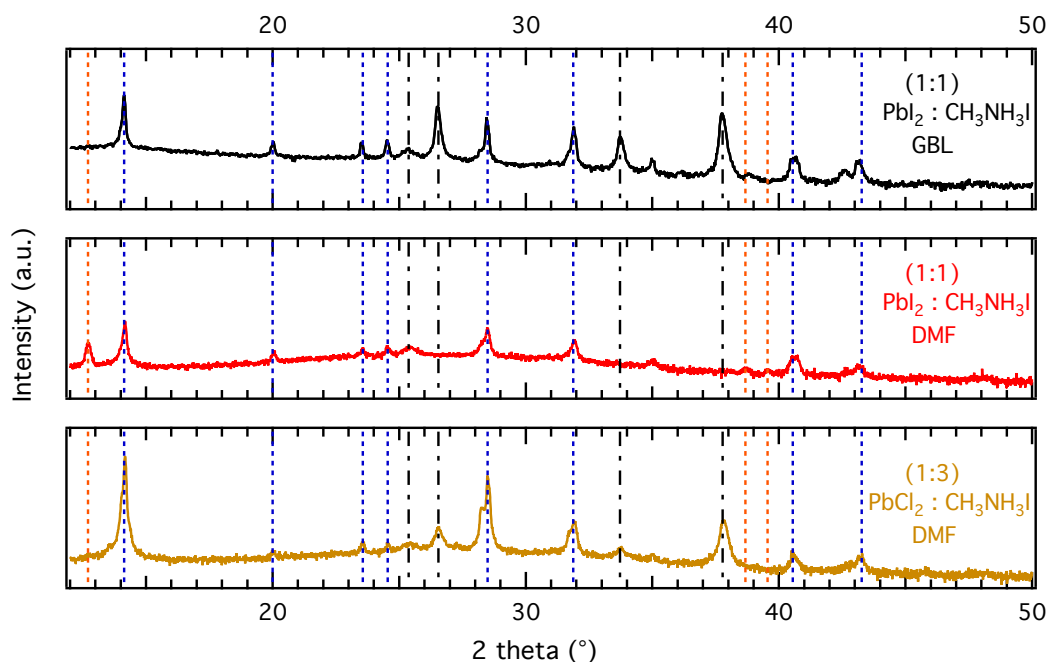
The replacement of PbI<sub>2</sub> by PbCl<sub>2</sub> leads to a noteworthy difference in the perovskite deposition procedure. When PbCl<sub>2</sub> is employed the as-deposited spin-coated film requires a significantly longer annealing time (at 100°C) to form the perovskite material. As mentioned above, the perovskite is formed after less than 10 minutes when PbI<sub>2</sub> is used as a precursor observed in an almost immediate color change to dark brown. Replacing PbI<sub>2</sub> by PbCl<sub>2</sub> increases the conversion time to 45 minutes, apparent in the very slow color change of the perovskite film from yellow, through orange/red, to dark brown. This indicates that when PbI<sub>2</sub> is used the tendency to form the hybrid perovskite crystal is greater than in the case of PbCl<sub>2</sub>. The simple mixing of PbI<sub>2</sub> and CH<sub>3</sub>NH<sub>3</sub>I will lead to the formation of the perovskite in a solid-state reaction. Hence during the solution processing approach examined here, the short annealing time reflects the facilitated perovskite crystallization by driving the evaporation of the organic solvent which is visible in the rapid color change to dark brown. On the other hand the long annealing time required when the precursor solution mixture uses PbCl<sub>2</sub> suggests that in addition to the removal of solvent there is an energetic requirement necessary to drive the crystallization and subsequent formation of the perovskite.

For all three different precursor solution mixtures described there appear to exist large areas where the structure of the mTiO<sub>2</sub> can be distinguished. It is important to note that these 'exposed mTiO<sub>2</sub>' areas may still be covered by a thin layer of perovskite material, allowing the structure of the mTiO<sub>2</sub> underneath to be discerned. While there are large variations in the crystal morphology of the perovskite film formed, depending on the solvent and precursors used, these measurements indicate that the nature of the material is the same regardless.

XRD measurements (Figure 5.2<sup>2</sup>) illustrate the similarity of the nature of the perovskite formed. In the case when PbI<sub>2</sub> is used, changing the solvent from GBL to DMF leads to no change in the position of the XRD peaks observed. However when GBL is used the peaks are narrower, suggesting that the individual crystallites formed are bigger than when DMF is used as a solvent. This appears contradictory to the relative sizes of the structures displayed in the SEM images in Figure 5.1, which suggest that the hexagonal-needle shapes formed from DMF are larger than the perovskite islands formed from GBL. However it is possible that these shapes actually consist of individual smaller crystallites whose size contributes to the width of the XRD peaks. If this is the case, the XRD measurement suggests that these individual crystallites

---

<sup>2</sup> The perovskite sample prepared from 1:1 molar ratio of PbI<sub>2</sub> : CH<sub>3</sub>NH<sub>3</sub>I in DMF was deposited on mTiO<sub>2</sub> directly on a glass substrate and thus lacks the FTO peaks.



**Figure 5.2.** XRD diffractograms of mTiO<sub>2</sub> films with perovskite material formed from PbI<sub>2</sub> : CH<sub>3</sub>NH<sub>3</sub>I in GBL (black), PbI<sub>2</sub> : CH<sub>3</sub>NH<sub>3</sub>I in DMF (red) and PbCl<sub>2</sub> : 3 CH<sub>3</sub>NH<sub>3</sub>I in DMF (yellow). The vertical lines indicate the peaks associated with PbI<sub>2</sub> (orange), CH<sub>3</sub>NH<sub>3</sub>PbI<sub>3</sub> perovskite (blue) and the FTO/mTiO<sub>2</sub> substrate (dot/dash black).

are bigger when GBL is used in relative to when DMF is used. Additionally the appearance of the peak at 12.7° (dashed orange line) indicates the presence of pure PbI<sub>2</sub> when DMF is used as a solvent.

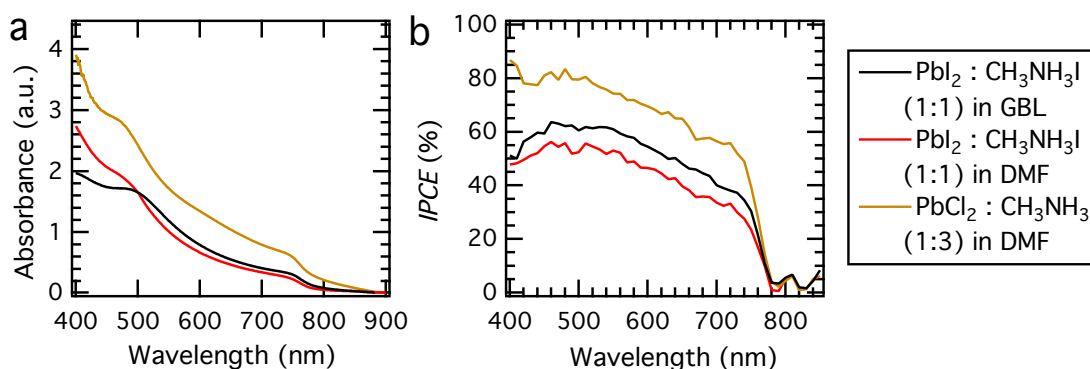
For the perovskite formed from PbCl<sub>2</sub>, the position of the CH<sub>3</sub>NH<sub>3</sub>PbI<sub>3</sub> perovskite peaks are the same, confirming that the chemical nature of the material is identical regardless of the solvent or precursor used. However the higher relative intensities of the peaks at 14.17, 28.49 and 43.27° corresponding to the (110), (220) and (330) reflections respectively, imply that this perovskite is more orientated. The preferential orientation of the perovskite when PbCl<sub>2</sub> is used as the inorganic precursor component has been previously observed in XRD diffractograms of perovskite deposited on glass substrates [178]. It has been stipulated that this preferential orientation of the perovskite crystal may be beneficial for efficient and fast charge-transport through the material.

As shown the perovskite crystal growth and the resulting film morphology is strongly dependent on the choice of solvent used in the precursor solution as well as the nature of the precursor species. Moreover these parameters influence the amount of perovskite that is formed on the substrate – the material loading – which is reflected in the absorbance of the film (Figure 5.3) and consequently on the current density of the corresponding photovoltaic

## Chapter 5. Morphological Studies of CH<sub>3</sub>NH<sub>3</sub>PbI<sub>3</sub> Perovskite

**Table 5.1.** Photovoltaic performance parameters extracted from  $J$ - $V$  measurements under standard AM1.5G illumination ( $100 \text{ mW cm}^{-2}$ ) of devices using different solvents. All devices were masked to achieve an illuminated area of  $0.285 \text{ cm}^2$ . Integrated current density determined from the IPCE spectra.

Precursors	Solvent	Integrated Current Density ( $\text{mA cm}^{-2}$ )	$V_{\text{OC}}$ (mV)	$J_{\text{SC}}$ ( $\text{mA cm}^{-2}$ )	$FF$	$PCE$ (%)
PbI <sub>2</sub> : CH <sub>3</sub> NH <sub>3</sub> I	GBL	13.28	813	14.37	0.63	7.33
PbI <sub>2</sub> : CH <sub>3</sub> NH <sub>3</sub> I	DMF	11.10	792	10.50	0.75	6.33
PbCl <sub>2</sub> : 3 CH <sub>3</sub> NH <sub>3</sub> I	DMF	17.49	957	17.41	0.68	11.20



**Figure 5.3.** (a) UV-vis absorption spectra of mTiO<sub>2</sub> films with perovskite material formed from PbI<sub>2</sub> : CH<sub>3</sub>NH<sub>3</sub>I in GBL (black), PbI<sub>2</sub> : CH<sub>3</sub>NH<sub>3</sub>I in DMF (red) and PbCl<sub>2</sub> : 3 CH<sub>3</sub>NH<sub>3</sub>I in DMF (yellow). (b) IPCE spectra of devices fabricated under the same conditions.

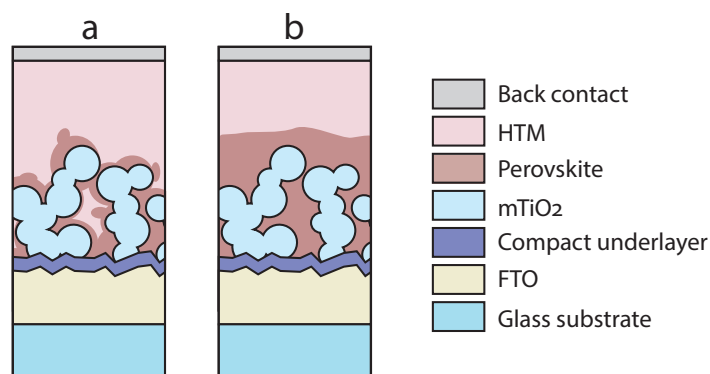
devices. The photovoltaic performance parameters extracted from  $J$ - $V$  measurements are shown in Table 5.1. The solvent effect on the light harvesting ability of the perovskite film are small, with the film deposited from GBL displaying slightly higher absorbance, culminating in a increase in the  $J_{\text{SC}}$ .

On the other hand significant enhancement in the absorbance of the film across the entire spectrum is observed when the inorganic precursor is changed from PbI<sub>2</sub> to PbCl<sub>2</sub> (Figure 5.3) which is reflected in the increase in current density from 10–14  $\text{mA cm}^{-2}$  to  $> 17 \text{ mA cm}^{-2}$  (Table 5.1).

### 5.3.1 Perovskite Infiltration and Transport Mechanisms

The perovskite film morphology influences the device working mechanisms as the structure of the film defines the device configuration. As described in the Chapter 1, in addition to its role as light harvesting material the perovskite material can also transport charges. In the case when there are large ‘exposed’ mTiO<sub>2</sub> areas (as observed when PbI<sub>2</sub> is used), this allows easy infiltration of the HTM (spiro-MeOTAD) deep into the pores of the mTiO<sub>2</sub> scaffold, Figure 5.4 (a). As a result the effective area of the charge separation interface between the





**Figure 5.4.** Schematic of device configuration when (a) areas of exposed  $m\text{TiO}_2$  allows infiltration of the HTM into the pores and (b) when the perovskite forms a dense capping layer on top of the  $m\text{TiO}_2$ .

perovskite and spiro-MeOTAD is larger. Consequently following its primary role as efficient light absorber, the secondary role of the perovskite is predominantly in the charge separation where electrons and holes are transported in the  $m\text{TiO}_2$  and HTM respectively. When the amount of perovskite material deposited is greater and there is a more uniform capping layer of material covering the  $m\text{TiO}_2$  film (as in the case when  $\text{PbCl}_2$  is used), the infiltration of HTM into the pores is hindered and it forms only a separation layer between the perovskite capping layer and the back contact, Figure 5.4 (b). Consequently in this device configuration it is conceivable that charge-transport within the perovskite plays a more important role within the devices in addition to charge separation.

In Chapter 4 perovskite-based solid-state solar cells are analyzed by IS, from which a working equivalent circuit model is developed and validated to interpret the frequency response of these devices. The IS response associated with the perovskite material was found to manifest at intermediate frequencies at low forward bias when measured in the dark. This feature was observed to disappear when the devices were measured under illumination and the conductivity of the perovskite material is greatly enhanced. The perovskite material used to fabricate the samples in these investigations was deposited by spin-coating a 1 to 1 molar ratio solution of  $\text{PbI}_2$  and  $\text{CH}_3\text{NH}_3\text{I}$  in GBL. As outlined above the extent of perovskite infiltration into the  $m\text{TiO}_2$  scaffold is greatly dependent on the deposition technique and the precursor solution recipe. The use of  $\text{PbCl}_2$  instead of  $\text{PbI}_2$  as a precursor material has considerable impact on the perovskite film morphology, amount of material deposited on the  $m\text{TiO}_2$  and on the photovoltaic performance of solid-state devices as is evident from the measurements conducted.

In this section the IS response of perovskite solid-state devices are examined to determine the role of the chosen precursor used on the internal electrical processes of the device working mechanisms. The previously studied system using a 1 to 1 molar ratio solution of  $\text{PbI}_2$  and  $\text{CH}_3\text{NH}_3\text{I}$  in GBL is compared to the case when a precursor solution of 1 to 3 molar ratio solution of  $\text{PbCl}_2$  and  $\text{CH}_3\text{NH}_3\text{I}$  in DMF is used. These two systems represent the optimized

conditions for a one-step deposition method by spin-coating a precursor solution using  $\text{CH}_3\text{NH}_3\text{I}$  for  $\text{PbI}_2$  or  $\text{PbCl}_2$  respectively.

In the region of low forward bias, the dark current characteristics presented in Figure 5.5 (a)<sup>3</sup> show a lower current for the samples prepared using the  $\text{PbCl}_2$  precursor suggesting better blocking properties at the blocking layer (BL)/HTM interface for this system. Recalling the differences in film morphology and material deposited, when  $\text{PbCl}_2$  is used as a precursor instead of  $\text{PbI}_2$  the amount of perovskite material deposited is greater (as seen in the higher light absorption of the film) and a more uniform capping layer on top of the  $\text{mTiO}_2$  is created. As suggested the perovskite material is expected to have a higher fraction of pore-filling, greatly reducing (even eliminating) the interface between the HTM and the BL. Consequently this is reflected in the lower measured dark current relative to the case when  $\text{PbI}_2$  is used, where a higher degree of pore infiltration by the HTM is expected due to the absence of a conformal and dense capping layer of perovskite material.

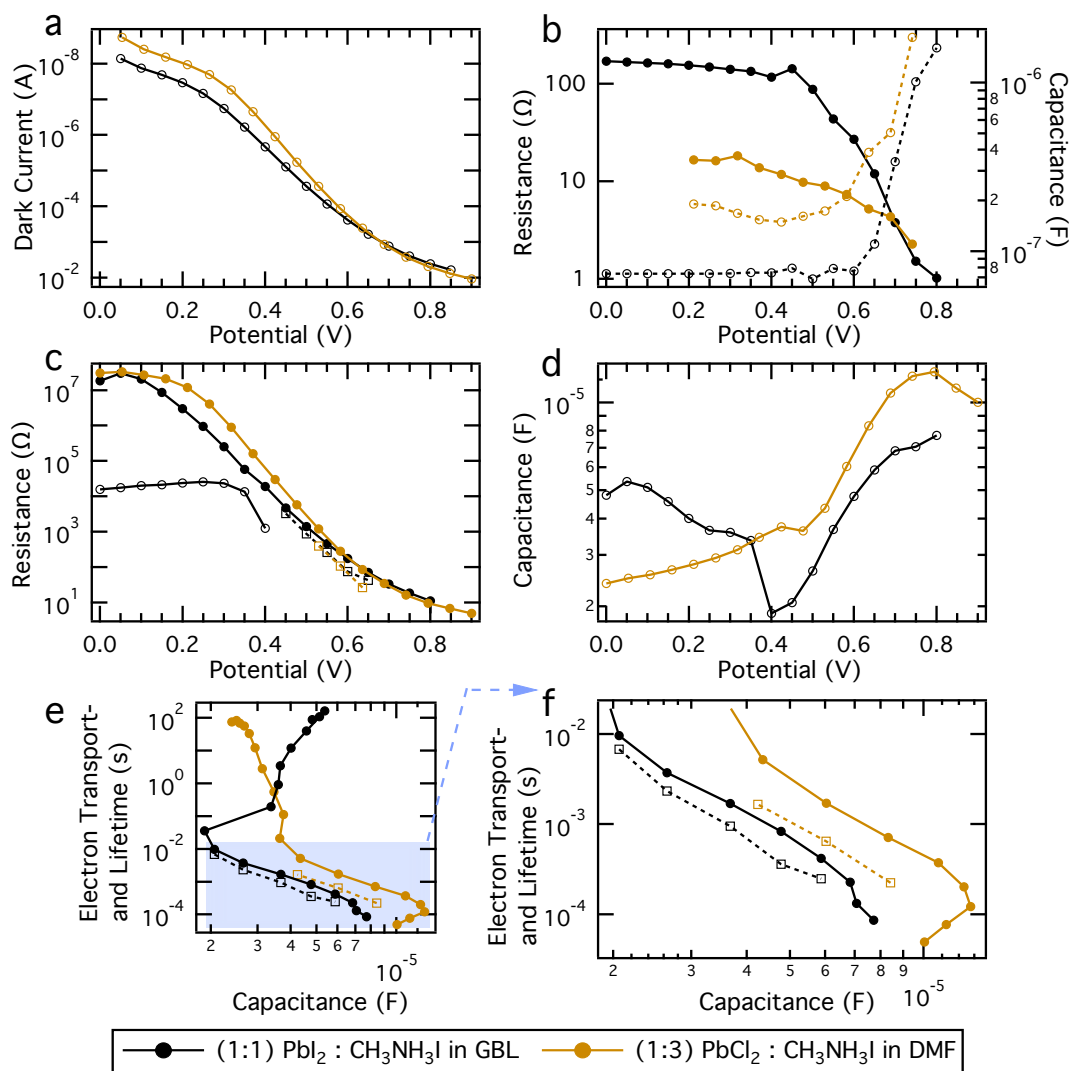
Similar reasoning can be applied to the more rapid increase in dark current at high forward bias for the  $\text{PbCl}_2$  system. Considering the schematics of perovskite infiltration in Figure 5.4 the formation of a more dense perovskite film, limiting and/or preventing HTM infiltration, will result in a smaller contribution from the HTM to the overall series resistance. This is reflected in a faster increase in the current with increasing forward bias and a higher *FF* (0.63 and 0.68 respectively, Table 5.1) determined from the photovoltaic performance. In such a device configuration the perovskite is assumed to play a more prominent role in the charge-transport process, which in light of the high diffusion coefficients it is believed to have, further supports these observations as it too will contribute to a lower series resistance and improved *FF*.

As observed in Chapter 4, when  $\text{PbI}_2$  is used as a precursor the IS response shows a feature at low forward bias in the intermediate frequencies region which has been attributed to the IS response of the perovskite material. For the system using a solution of 1 to 3 molar ratio mixture of  $\text{PbCl}_2$  and  $\text{CH}_3\text{NH}_3\text{I}$  in DMF in the perovskite deposition this feature is no longer observed. This suggests that in this latter case the electronic conductivity of the perovskite material is enhanced, resulting in a decrease in the associated resistance observed for such devices (cf. Chapter 4). Taking into account this exception the IS response is interpreted following a similar procedure as presented in the previous chapter. The charge-transfer processes at the back contact (BC)/HTM interface and within the HTM material manifest in the high frequency region. The recombination characteristics at the BL/HTM interface at low forward bias and at higher forward bias – when the  $\text{mTiO}_2$  is conductive – the transport and recombination responses at the  $\text{mTiO}_2$ /HTM interface take place in the low frequency domain.

The parameters extracted from the IS measurements conducted on these type of devices in the

---

<sup>3</sup> The measurement data for the system consisting of 1 to 1 molar ratio solution of  $\text{PbI}_2$  and  $\text{CH}_3\text{NH}_3\text{I}$  in GBL is adapted from Section 4.3.3 Chapter 4.



**Figure 5.5.** (a) Dark current measurement of devices made with different perovskite precursor solutions plotted in log scale against the potential. (b) High frequency resistance and associated capacitance, (c) recombination (solid circles), transport (dashed squares) and perovskite associated (open circles) resistance and (d) chemical capacitance extracted from IS measurements conducted in the dark. (e)–(f) Calculated electron lifetimes,  $\tau_n$  as a function of the chemical capacitance of the mTiO<sub>2</sub>.

dark are presented in Figure 5.5 (b)–(f) with respect to applied forward bias. The magnitude of the resistance manifesting at high frequency related to the BC/HTM response was found to be lower for the sample prepared with PbCl<sub>2</sub> (Figure 5.5 (b)). This is in good agreement with the previous observations, reasoning that the higher perovskite infiltration and material loading reduces the amount of HTM infiltration into the pores as well as the HTM overlayer, resulting in a diminished contribution to the HTM IS response. This lower resistance gives rise to the higher *FF* achieved for this system when PbCl<sub>2</sub> is used. Furthermore regardless

of the precursor used in the perovskite deposition, the samples show similar values for the associated capacitance of this interface across the entire potential range.

The intermediate frequency response assigned directly to the perovskite material is only observed for the case when  $\text{PbI}_2$  is used as a precursor as outlined above (see black trace with open circles in Figure 5.5 (c)). This proves the origin of this feature as the perovskite material and further indicates that it is greatly dependent on the nature of deposition of the material. The XRD measurements presented in Figure 5.2 indicate that there is no detectable difference in the chemical composition of the resultant perovskite formed using either  $\text{PbI}_2$  or  $\text{PbCl}_2$ . This is further validated by the similar UV-vis absorption spectra measured displayed in Figure 5.3 (a). The deposition method using  $\text{PbCl}_2$  has been reported to lead to a more oriented growth of the perovskite crystal leading to improved charge-transport within the perovskite layer [178]. This is in good agreement with the observation of the disappearance of the perovskite IS response at intermediate frequencies here, reflecting the increased conductivity of the perovskite film following its formation using the  $\text{PbCl}_2$  precursor.

The recombination resistance of the  $\text{mTiO}_2$  depicted in Figure 5.5 (c) reflects the same trends observed in the dark current measurements. The associated chemical capacitance shown in Figure 5.5 (d) displays distinct differences for the two samples. In the low forward bias regime, the capacitance is dominated by the BL/HTM interface and generally is relatively independent of the applied forward bias. In the case of the system using  $\text{PbCl}_2$ , this capacitance is observed to increase slightly with increasing forward bias in this region. This behavior partially hides the characteristic drop in capacitance at a forward bias of approximately 400 mV typically seen for such solid-state devices and clearly observed for the  $\text{PbI}_2$  case. This drop in capacitance at the BL/HTM interface is only very weakly visible for the  $\text{PbCl}_2$  system, providing further evidence for the hindered HTM infiltration and thus reduced interfacial contact between the BL and the HTM. At an applied forward bias  $> 400$  mV the  $\text{mTiO}_2$  becomes conductive and its chemical capacitance increases exponentially. This behavior is similar for the devices using  $\text{PbI}_2$  and  $\text{PbCl}_2$ . At very high forward bias, the chemical capacitance is observed to level off slightly for the case using  $\text{PbI}_2$  and even decrease for  $\text{PbCl}_2$ . This phenomena is explained in further detail in Section 5.4.

The electron lifetime, Figure 5.5 (e)–(f), is calculated from the recombination resistances and represented against the chemical capacitance. At a similar DOS this clearly reveals a longer lifetime for the samples prepared using  $\text{PbCl}_2$  and is reflected in the higher  $V_{\text{OC}}$  of 957 mV relative to 813 mV when  $\text{PbI}_2$  is employed. This is attributed to a decrease in the recombination losses between the  $\text{mTiO}_2$  and the HTM by improved perovskite coverage increasing the spatial separation between the  $\text{mTiO}_2$  and the HTM.

The IS model developed in the previous chapter was successfully applied to the interpretation of perovskite solar cells fabricated following a different precursor solution recipe. The IS analysis presented here clearly reveals differences in the internal electrical processes when different precursor solutions ( $\text{PbI}_2$  versus  $\text{PbCl}_2$ ) are used in the deposition step leading to very

different perovskite film morphology and structure. This measurement technique is hence useful in the characterization of the perovskite material, its properties and film morphology and the resultant effects on the device working mechanisms.

### 5.3.2 Solvent properties

As is evident from the results presented, the perovskite formation from solution is heavily dependent on the chosen solvent and its interactions with the precursor components. Hence the properties of the solvent chosen plays a crucial role in the conversion process and thus on the resultant film morphology. The affinity between the perovskite components and the solvent, the volatility of the latter and the wettability of the mTiO<sub>2</sub> by the solvent all determine the rate of perovskite conversion. The primary factor to consider is the solubility of the perovskite precursor materials in the solvent, which is dependent on the balance of the existing intermolecular forces between the components, and as a result controls the perovskite conversion. Consequently the polarity of the solvent and its volatility are important properties to consider.

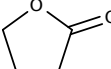
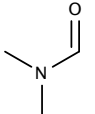
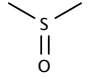
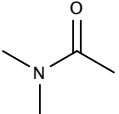
The polarity of a solvent is generally determined by its dielectric constant ( $\epsilon$ ), broadly classifying solvents as polar ( $\epsilon > 15$ ) and non-polar ( $\epsilon < 15$ ). The dielectric constant is a measure of the solvent's ability to reduce the electric field strength surrounding a charged particle when this is immersed in the solvent, hence decreasing the effective internal charge of the added solute. These properties are listed in Table 5.2 for the solvents used.

While GBL and DMF both have high boiling points (204 and 152°C) and dielectric constants (41.8 and 36.7 [179]), the individual intermolecular interactions these solvents have with the perovskite precursors lead to considerable differences in the film morphology formed as observed above (Figure 5.1). In addition the large dipole moments (3.97 and 3.86 Debye [180]) classify GBL and DMF as polar aprotic solvents, indicating their ability to solvate positively charged species *via* their negatively charged dipole. This property has particular importance when precursor components are changed, thus leading to changes in the solvation strength.

The formation of the different perovskite polymorphic phases observed is solvent-controlled, dependent on the solubility and hence polarity of the solvent. Recent reports [181] suggest that the use less polar solvents such as ethanol leads to supersaturation and precipitation of the nucleation seeds. The low solubility of the CH<sub>3</sub>NH<sub>3</sub>PbI<sub>3</sub> in this solvent locks the crystallites in their specific structures which grow further as more material is deposited. However in the case of higher polarity solvents such as DMF or GBL, the solvent can redissolve the perovskite CH<sub>3</sub>NH<sub>3</sub>PbI<sub>3</sub> formed, leading to the formation of different perovskite polymorphic structures. This accounts for the difference observed between DMF and GBL here, where the higher polar GBL can dissolve more CH<sub>3</sub>NH<sub>3</sub>PbI<sub>3</sub> in the precursor solution confirming solubility-controlled nucleation as the origin for the different crystal morphology.

It is also important to consider the solvent-surface interaction between the mTiO<sub>2</sub> substrate

**Table 5.2.** Solvent molecular structures and properties.

Solvent		Structure	bp <sup>a</sup> (°C)	D <sup>b</sup> (g ml <sup>-1</sup> )	μ <sup>c</sup> (Debye)	ε <sup>d</sup>
γ-butyrolactone	GBL		204	1.130	3.97	41.78
N,N-dimethylformamide	DMF		152	0.945	3.86	36.7
Dimethylsulfoxide	DMSO		189	1.096	3.9	46.7
N,N-dimethylacetamide	DMAc		166	0.937	3.72	37.8

<sup>a</sup> Boiling point (bp) under a pressure of 1 bar

<sup>b</sup> Density (*D*) in g ml<sup>-1</sup> at 20°C

<sup>c</sup> Dipole moment (*μ*) measured at 20°C

<sup>d</sup> Dielectric constant (*ε*)

and the solvent. A strong interaction can hinder the crystal growth of the perovskite and preferential adsorption can direct the growth, defining the structure of the film morphology formed.

The interplay of the entirety of these properties in tandem with the material characteristics of the precursor materials, defines the nature and strength of the intermolecular interactions between the species and hence governs the conversion reaction. This is clearly evident in the vastly different perovskite crystal film morphologies resulting from the use of different solvents.

Solvents with similar properties marking them as possible candidates for the deposition of the perovskite precursors are dimethylsulfoxide (DMSO) and *N,N*-dimethylacetamide (DMAc) which are more polar than GBL and DMF respectively.

## 5.4 Perovskite Annealing Temperature

In this section the CH<sub>3</sub>NH<sub>3</sub>PbI<sub>3</sub> perovskite used as light absorber is deposited onto to the mTiO<sub>2</sub> by spin-coating from a 1:3 molar ratio solution of PbCl<sub>2</sub> and CH<sub>3</sub>NH<sub>3</sub>I in DMF following the procedure reported by Lee *et al.* [50]. In the standard case these films are subsequently annealed at 100°C for 45 minutes leading to the formation of the lead-iodide based perovskite material. Here the effect and importance of the annealing temperature during the final

## 5.4. Perovskite Annealing Temperature

**Table 5.3.** Conversion temperature and associated time taken.

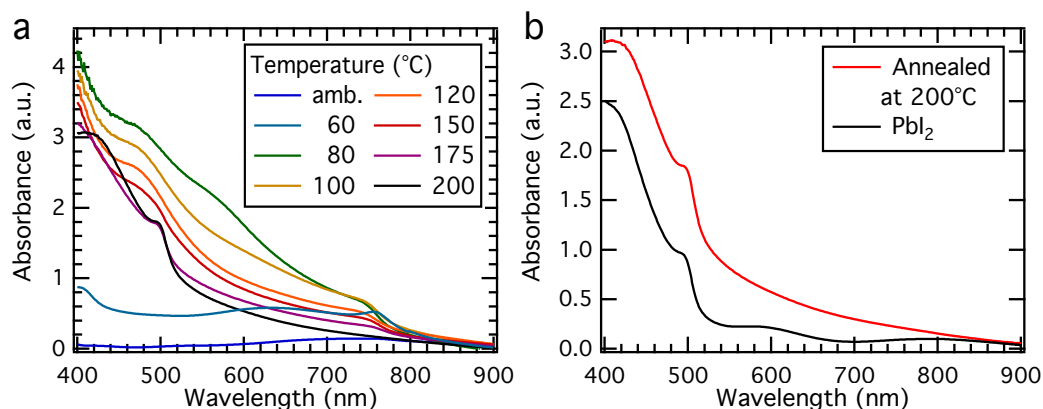
Temperature (°C)	Time Taken (hours)
ambient <sup>a</sup>	20
60	20
80	3
100	0.75
120	0.25
150	0.25
175	0.17
200	0.17

<sup>a</sup> ambient temperature consisted of room temperature at approximately 20°C

conversion step is investigated, relating it to the perovskite film morphology and its influence on the device working mechanisms [182]. These perovskite films formed are analyzed using UV-vis absorption spectroscopy, SEM and XRD measurements. This exposes the role of the annealing temperature of the perovskite on its film composition and morphology. The variation of the annealing temperature during the perovskite conversion step was correlated with the photovoltaic performance of solid-state solar cells using spiro-MeOTAD as HTM and further examined by IS to gain better understanding of the internal electrical parameters under working conditions.

For most of the techniques where the perovskite material is deposited from solution, a subsequent heat treatment of the film is required. This has the dual purpose of removing any excess solvent remaining in the film as well as facilitating the formation of the perovskite crystal structure. Contrary to the case when  $\text{PbI}_2$  is used as a precursor as reported by Kim *et al.* [49] which requires only 10 minutes of heating at 100°C to complete the conversion to the final perovskite form, when  $\text{PbCl}_2$  is used the conversion is complete only after annealing the material for 45 minutes like reported by Lee *et al.* [50].

In the work presented here the annealing temperature of the perovskite film after deposition by spin-coating was varied. The conversion to the final perovskite was regarded as complete once the film showed a stable absorption profile resulting in a uniform dark brown color. For low temperatures this conversion took considerably longer, 3 hours at 80°C relative to 45 minutes at 100°C. At 60°C, even when left for more than 20 hours the conversion was not complete as indicated by poorer film coloration. In the case of high annealing temperatures (> 150°C) the conversion was observed to occur almost instantaneously and in the case for temperatures above 200°C to quickly convert to yellow. This yellow color is attributed to the formation of  $\text{PbI}_2$  as elucidated in further detail in the subsequent sections. The amount of time used for the annealing of the perovskite films at different temperatures is presented in Table 5.3.



**Figure 5.6.** (a) UV-vis absorption spectra for  $\text{mTiO}_2$  films with perovskite annealed at different temperatures. (b) UV-vis absorption spectra for  $\text{mTiO}_2$  films with pure  $\text{PbI}_2$  (black) and perovskite annealed at  $200^\circ\text{C}$  (red). The sample annealed at  $200^\circ\text{C}$  has higher absorption between 500 and 800 nm due to the contribution from the perovskite in this region.

#### 5.4.1 Optical Characterization

The ultraviolet-visible absorption spectra of the perovskite material deposited on  $\text{mTiO}_2$  and annealed at different temperatures are presented in Figure 5.6 (a).

The samples annealed at 80 to  $150^\circ\text{C}$  show the typical absorption spectrum of the perovskite  $\text{CH}_3\text{NH}_3\text{PbI}_3$  as reported [48, 50, 131, 183]. Increasing the annealing temperature of the perovskite from 60 to  $100^\circ\text{C}$  shows an increase in the absorbance across the entire spectral range, indicating that the extent of conversion is lower at such low annealing temperatures. This is further highlighted by the extremely low absorbance of samples that were simply dried at ambient room temperatures without further heat treatment. This latter case demonstrates that removal of the solvent from the film is insufficient to form the perovskite from these precursors and that energy is required to drive this conversion. This is confirmed by the lack of the features associated with the absorbance of  $\text{PbI}_2$  corresponding to a peak at 500 nm or perovskite absorption onset at 770 nm, which indicates that these dried precursor films contain only  $\text{PbCl}_2$  and  $\text{CH}_3\text{NH}_3\text{I}$ .

The samples annealed at  $80^\circ\text{C}$  show an additional absorption shoulder at 590 nm. The origin of this feature remains unclear. However it could be related to the broad absorption observed for the samples dried at  $60^\circ\text{C}$  between 570 and 640 nm. Taking this exception into account the samples annealed at  $100^\circ\text{C}$  showed the highest absorbance. Further increasing the annealing temperature leads not only to a decrease in absorbance but also the additional appearance of  $\text{PbI}_2$  absorption feature at 500 nm. A spectrum of pure  $\text{PbI}_2$  deposited on  $\text{mTiO}_2$  is shown in Figure 5.6 (b). For samples heated at  $200^\circ\text{C}$  the perovskite characteristics are almost no longer discernible and the spectra resembles that of pure  $\text{PbI}_2$  with slightly higher light absorption between 600 and 800 nm. This confirms that the yellow color of these films is due to the



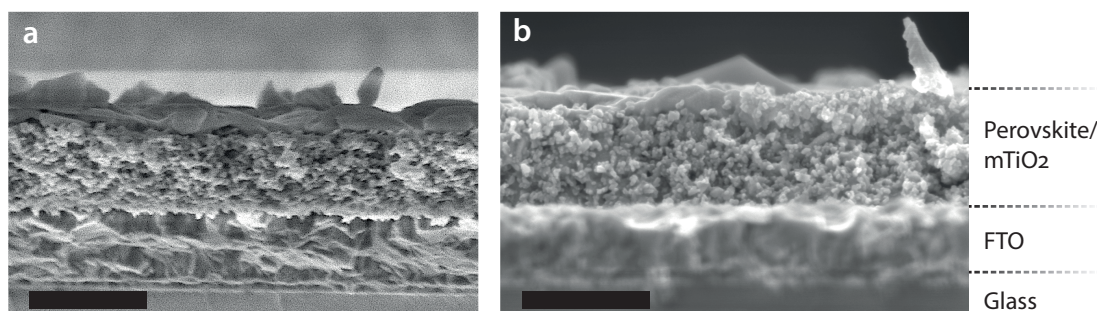
formation of  $\text{PbI}_2$  at these high temperatures. This is in agreement with surface photovoltage spectroscopy measurements made by Supasai *et al.* [184] where the appearance of the  $\text{PbI}_2$  bandgap after heating  $\text{CH}_3\text{NH}_3\text{PbI}_3$  samples above  $140^\circ\text{C}$  was observed. The absorption onset of the perovskite remains constant for samples annealed between  $60$  and  $175^\circ\text{C}$ , indicating that the optical bandgap of the perovskite is unaffected by the annealing temperatures. This further confirms that the nature of the perovskite formed is unchanged by the annealing temperature and is found to be in good agreement with the  $\text{CH}_3\text{NH}_3\text{PbI}_3$  perovskite. For the samples treated at ambient temperatures (where there is no formation of perovskite) or at very high temperatures (where the formation of  $\text{PbI}_2$  is dominant), the bandgap absorption onset is not visible.

### 5.4.2 Scanning Electron Microscopy: Film Morphology

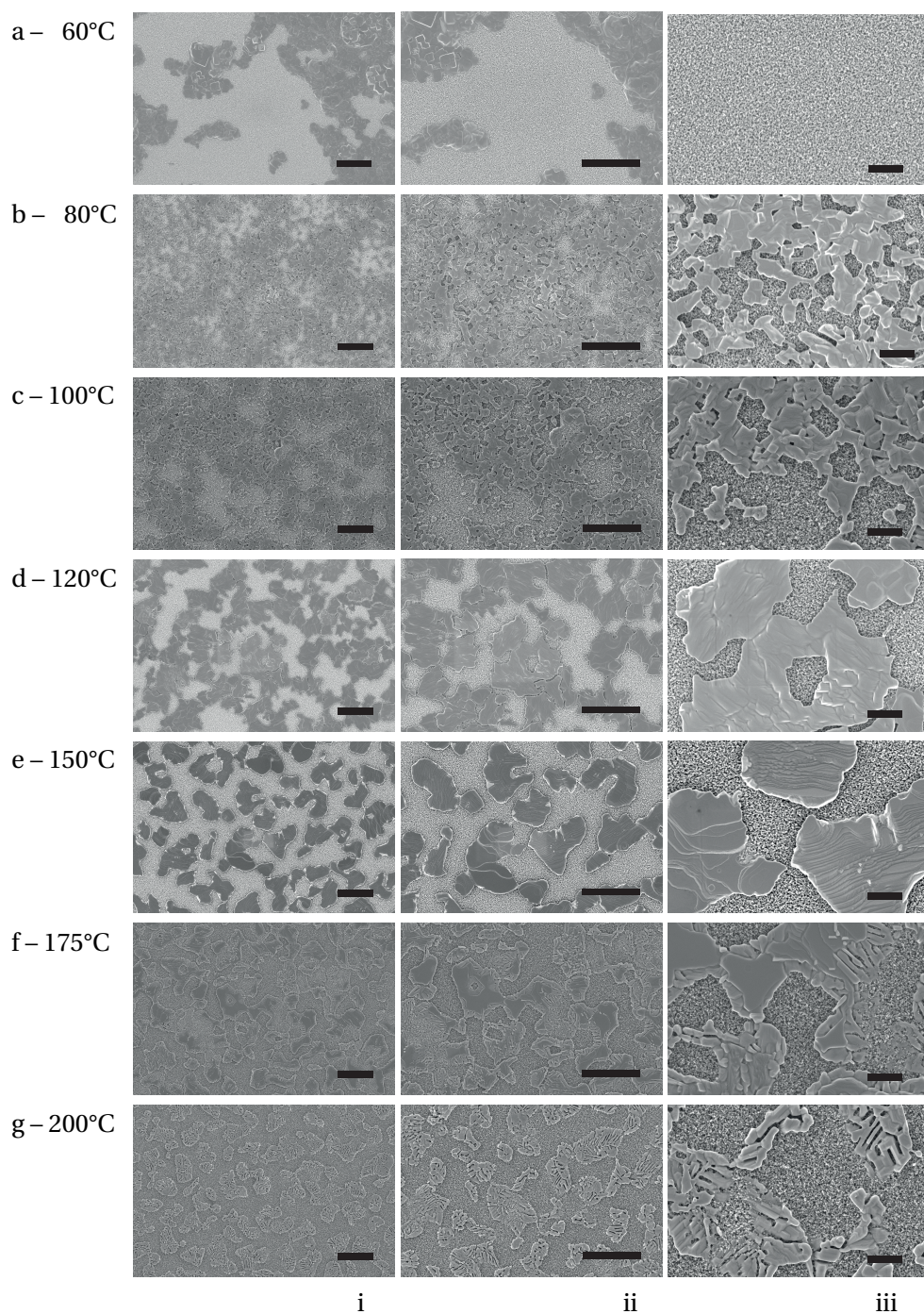
The influence of the annealing temperature on the morphology and structure of the perovskite layer formed on the  $\text{mTiO}_2$  were examined by scanning electron microscopy. For samples annealed at  $60^\circ\text{C}$  no homogeneous film was formed, rather large islands of precursor material ( $\text{PbCl}_2$  and  $\text{CH}_3\text{NH}_3\text{I}$ ) are seen (Figure 5.8 (a)). This is validated as the islands lack the clear crystalline structure typically observed for such perovskite materials and the large areas of exposed  $\text{TiO}_2$  visible in Figure 5.8 (a)-iii.

The use of annealing temperatures of  $80^\circ\text{C}$  results in a drastic change in the appearance of the film formed. The typical structure of the perovskite is visible. The coverage of the  $\text{mTiO}_2$  is much higher and the shape of the individual crystallites is much better defined. This is clearly evident in the layer of perovskite material formed on top of the  $\text{mTiO}_2$  as seen in Figure 5.7 (a). The film formed upon annealing at  $100^\circ\text{C}$  is relatively similar in appearance to that formed at  $80^\circ\text{C}$  (Figure 5.8 (b)–(c)) even though the time for the conversion process is longer at  $80^\circ\text{C}$ . Furthermore the gaps between the perovskite crystallites is slightly larger in the case of  $100^\circ\text{C}$ .

Increasing the annealing temperature to  $120^\circ\text{C}$  the morphology of the perovskite adopts a larger individual size for the islands of material (Figure 5.8 (d)). They no longer form a densely interconnected network, but rather larger islands with larger gaps in between, resulting in



**Figure 5.7.** Cross sectional images of samples annealed at (a)  $80^\circ\text{C}$  and (b)  $150^\circ\text{C}$ . The black scale bars correspond to 500 nm.



**Figure 5.8.** SEM images of  $\text{mTiO}_2$  films with deposited perovskite solution heat treated at (a)  $60^\circ\text{C}$ , (b)  $80^\circ\text{C}$ , (c)  $100^\circ\text{C}$ , (d)  $120^\circ\text{C}$ , (e)  $150^\circ\text{C}$ , (f)  $175^\circ\text{C}$  and (g)  $200^\circ\text{C}$ . Black scale bars correspond to (i)–(ii)  $5\ \mu\text{m}$ , (iii)  $1\ \mu\text{m}$ .

seemingly larger uncovered  $\text{mTiO}_2$  areas. Here it is important to note that it is believed that these ‘exposed  $\text{mTiO}_2$ ’ areas are still covered by a thin layer of perovskite material, hence revealing the structure of the  $\text{mTiO}_2$  underneath (see cross sectional image in Figure 5.7 (b)).

As the annealing temperature is further increased the size of perovskite islands is increased and furthermore internal structuring becomes discernable (Figure 5.8 (e)–(g)). This is most extreme at the highest annealing temperature investigated (200°C).

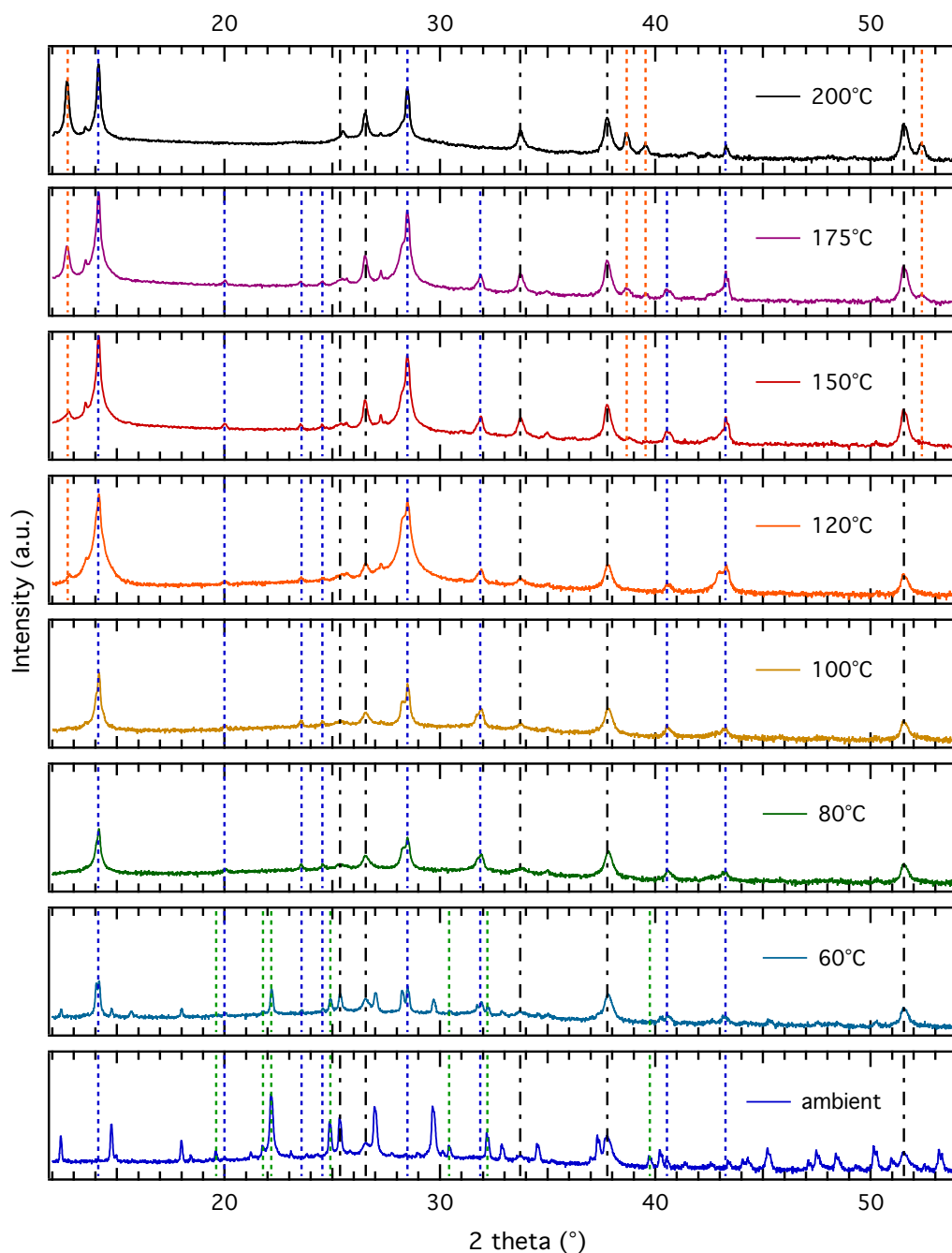
It can be assumed that the rate of perovskite crystallization is similarly enhanced as the annealing temperature is increased. High temperatures resulted in the rapid growth of large crystalline islands from a few nucleation sites and the associated large gaps in between. Lower temperatures on the other hand allowed the formation and subsequent crystal growth from a large number of nucleation sites, leading to the formation of smaller islands.

### 5.4.3 X-ray Diffraction: Perovskite Conversion and Composition

X-ray diffraction measurements were conducted to investigate the nature of the material formed following the annealing process. As expected, low annealing temperatures result in incomplete conversion to the perovskite (Figure 5.9). The XRD diffractograms for samples dried at ambient temperature for > 20 hours show a large number of peaks that are mainly attributed to the precursor materials. The presence of  $\text{PbCl}_2$  peaks (indicated by dashed green vertical lines in Figures 5.9 and in 5.10) indicate that simply drying the films to remove the excess solvent is insufficient to convert the precursor solution to the desired perovskite material. In addition to the  $\text{PbCl}_2$  peaks there are several peaks that remain unidentified. These could be attributed to the possible formation of products such as lead(II) oxychloride [185] arising as a result of the slow drying in the presence of water. Heating at 60°C for > 20 hours also still shows strong evidence of the presence of these precursor materials. However, in this case, a set of additional peaks appears (indicated by blue lines), matching those reported for the  $\text{CH}_3\text{NH}_3\text{PbI}_3$  crystallized in the tetragonal perovskite structure [131, 186, 187]. The peaks at 14.17, 28.49 and 43.27° are respectively assigned to the (110), (220) and (330) planes. The presence of these peaks indicates that the conversion, while incomplete, does take place to a small extent at these low annealing temperatures.

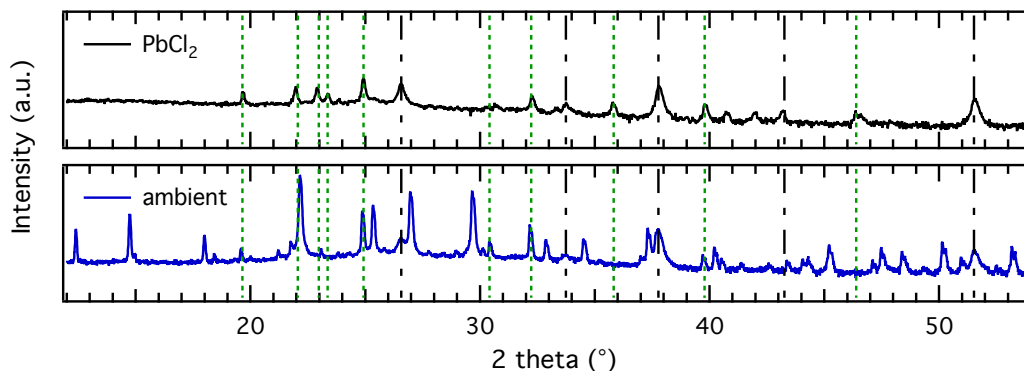
Hence recalling the SEM image for the corresponding sample prepared at 60°C, the islands of material observed can be confirmed to consist largely of dried precursors, with only a small proportion being converted to perovskite material (clearly visible in large areas of exposed  $\text{mTiO}_2$  in Figure 5.8 (a)) Once the annealing temperature is increased to 80°C, the peaks for the precursors are no longer present and only the peaks for the perovskite material remain. As in the case of the SEM images, the XRD diffractograms for the sample annealed at 100°C shows little difference to the 80°C sample. As the annealing temperature is increased to 175°C, the intensity of the perovskite (110), (220) and (330) peaks increases due to an increased conversion rate. From previous work it is known that this perovskite material shows a tendency for preferential orientation with the *a*-axis [50, 144, 178] parallel to the film plane. Hence this implies that the *c*-axis is normal to the film plane.

The observed increase in intensity of the reflections from the row of reciprocal lattice normal to the film plane suggests increased orientation of the perovskite crystalline domains with



**Figure 5.9.** X-ray diffraction patterns of perovskite samples annealed at different temperatures. The perovskite was deposited on mesoporous  $\text{TiO}_2$  coated onto FTO substrates. The vertical lines indicate the peaks associated with  $\text{CH}_3\text{NH}_3\text{PbI}_3$  perovskite (blue),  $\text{PbI}_2$  (orange),  $\text{PbCl}_2$  (green) and the FTO/ $\text{mTiO}_2$  substrate (dot/dash black).

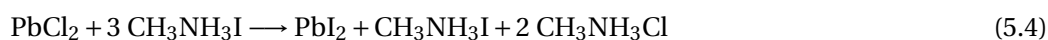
increases in annealing temperature. Similar observations were made for AlN films [188], ZnO



**Figure 5.10.** X-ray diffraction patterns of perovskite samples dried at ambient temperature for 20 hours (blue) and pure  $\text{PbCl}_2$  (black). The perovskite was deposited on mesoporous  $\text{TiO}_2$  coated onto FTO substrates. The vertical lines indicate the peaks associated with  $\text{PbCl}_2$  (green) and the FTO/ $\text{mTiO}_2$  substrate (dot/dash black).

films prepared by sol-gel techniques and then exposed to different heat treatments [189] and FePt thin films with face-centered-tetragonal (001) texture [190]. Another origin of the observed increased intensity of the peak intensity may arise from the phenomenon of microabsorption, where larger crystallite phases preferentially interact with the diffracting beam, thus leading to a distortion of the diffraction intensities. For heat treatments at  $200^\circ\text{C}$  the intensity of the perovskite is decreased and is explained by the decrease in material formed at these high temperatures.

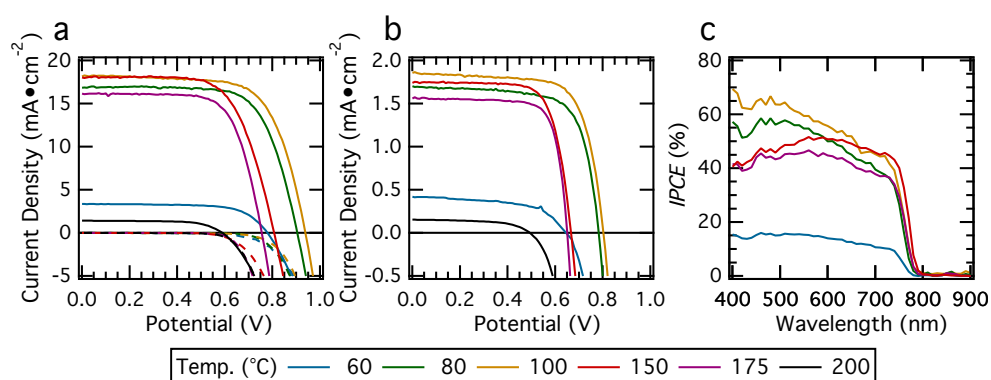
In addition, for annealing temperatures above  $120^\circ\text{C}$  a set of peaks that have been identified as belonging to  $\text{PbI}_2$  appear [175, 191]. Moreover at lower temperatures the conversion to the perovskite dominates the reaction (Reaction 5.3), however at higher annealing temperatures, there is the additional formation of  $\text{PbI}_2$  (Reaction 5.4) [184].



The perovskite crystal material has been reported to be stable up to  $300^\circ\text{C}$ , at which point the organic component decomposes, leaving behind the inorganic  $\text{PbI}_2$  following Reaction 5.5 [147, 171]. However recent studies [184] show that the  $\text{CH}_3\text{NH}_3\text{PbI}_3$  perovskite begins to transform to  $\text{PbI}_2$  at temperatures significantly below  $300^\circ\text{C}$  (at approximately  $140^\circ\text{C}$ ). In this study the perovskite material is not formed and then heated at a higher temperature but formed directly at different annealing temperatures, hence there are additional factors to consider. The excess organic  $\text{CH}_3\text{NH}_3\text{Cl}$  formed in this reaction is believed to sublime, thus leaving only the  $\text{CH}_3\text{NH}_3\text{PbI}_3$  perovskite on the  $\text{mTiO}_2$  film as observed in the XRD measurements. The rate of sublimation of the organic species  $\text{CH}_3\text{NH}_3\text{Cl}$  will increase with

**Table 5.4.** Photovoltaic performance parameters extracted from  $J$ - $V$  measurements under standard AM1.5G illumination ( $100 \text{ mW cm}^{-2}$ ) of devices using different annealing temperatures. All devices were masked to achieve an illuminated area of  $0.285 \text{ cm}^2$ .

Temperature ( $^{\circ}\text{C}$ )	$V_{\text{OC}}$ (mV)	$J_{\text{SC}}$ ( $\text{mA cm}^{-2}$ )	$FF$	$PCE$ (%)
60	779	3.35	0.68	1.78
80	905	16.89	0.70	10.64
100	938	18.37	0.68	11.66
150	807	17.96	0.64	9.66
175	755	15.66	0.70	8.52
200	589	1.38	0.67	0.56



**Figure 5.11.**  $J$ - $V$  characteristics taken under standard AM1.5G illumination at (a)  $100 \text{ mW cm}^{-2}$  (solid) and in the dark (dashed) and at (b)  $10 \text{ mW cm}^{-2}$  for devices made using different annealing temperatures for the perovskite. (c)  $IPCE$  spectra for perovskite solar cell devices measured without light bias. As such the intensity of the response is slightly underestimated in comparison to the  $J_{\text{SC}}$  values determined from the  $J$ - $V$  measurements.

temperature, as will that of the precursor  $\text{CH}_3\text{NH}_3\text{I}$ , thus driving Reaction 5.4 in addition to Reaction 5.3. From these measurements it becomes evident that formation of the perovskite films is composed of multiple processes; solvent vaporization, perovskite crystallization and the sublimation of excess organic  $\text{CH}_3\text{NH}_3\text{Cl}$  need to take place. These processes occur simultaneously and their relative rates determine the composition of the final film and contribute to the different film morphologies observed in the SEM images above.

#### 5.4.4 Photovoltaic Performance

Solid-state solar cells were fabricated using the perovskite as sensitizer and spiro-MeOTAD as hole-transport material. The perovskite material was deposited as described from solution containing a 1:3 molar ratio of  $\text{PbCl}_2$  and  $\text{CH}_3\text{NH}_3\text{I}$  in DMF and annealed at different temperatures followed by the subsequent deposition of the HTM by spin-coating. The current-voltage ( $J$ - $V$ ) characteristics measured under standard AM1.5G illumination ( $100 \text{ mW cm}^{-2}$ ) of these devices are presented in Figure 5.11, the corresponding photovoltaic parameters of which are

summarized in Table 5.4.

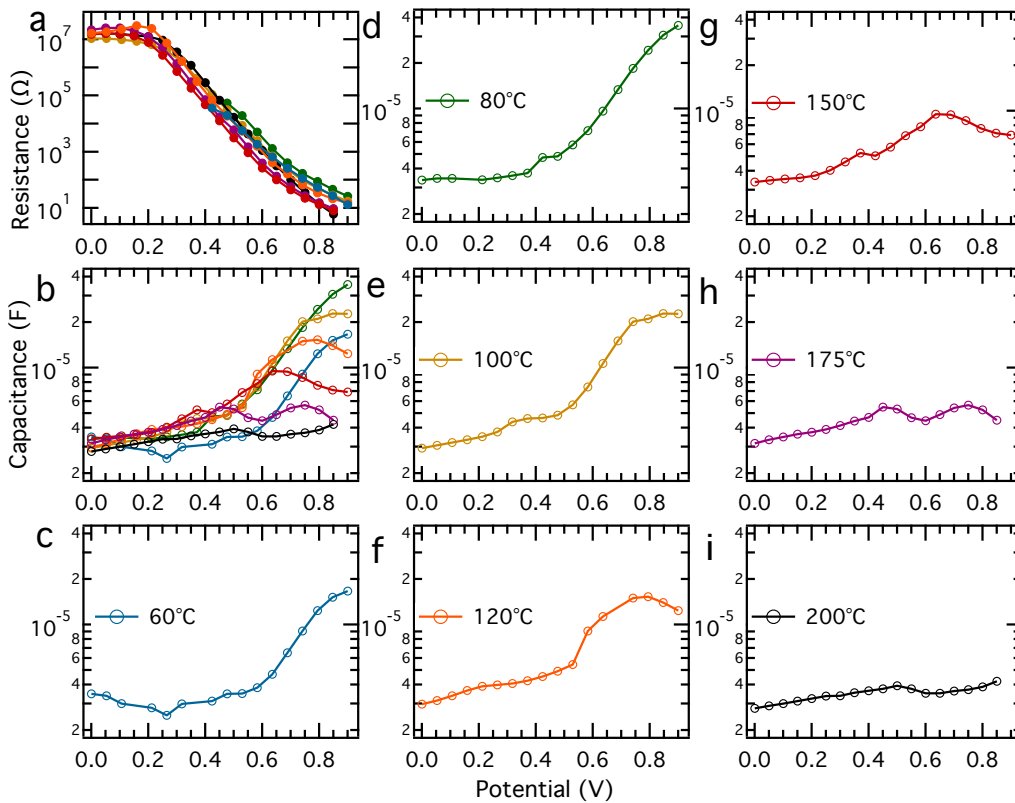
A clear correlation is observed between the annealing temperature of the perovskite and the photovoltaic performance of the devices. Samples that were annealed at 100°C gave the highest power conversion efficiency at 11.66% as a result of the high  $V_{OC}$  and  $J_{SC}$ , 938 mV and 18.37 mA cm<sup>-2</sup> respectively. At low annealing temperatures (60°C) both of these parameters are decreased as a consequence of incomplete conversion to the perovskite material, leading to lower light harvesting as there is insufficient perovskite pigment present. The devices annealed at 80°C displayed high  $PCE$ , and generally their parameters were only slightly lower than the maximum values observed at 100°C. This is in agreement with the previous measurements that showed a large degree of similarity between samples prepared at 80 and 100°C.

As the annealing temperature is increased further above 100°C, the  $V_{OC}$  is observed to decrease significantly, leading to a fall in  $PCE$ . The  $J_{SC}$  remains high up to an annealing temperature of 150°C (17.96 mA cm<sup>-2</sup>) before it too decreases. This trend can be explained by the formation of PbI<sub>2</sub> at these high temperatures instead of perovskite as seen in the UV-vis and the XRD measurements. As a consequence the light harvesting abilities of the material is reduced, resulting in the decrease in  $J_{SC}$  and  $V_{OC}$ . The trend in the  $J_{SC}$  is reflected in the UV-vis absorption and the  $IPCE$  spectra measured for the samples and presented in Figure 5.11. The  $IPCE$  spectral shape is similar for samples annealed at 60 to 100°C, and in good agreement to that reported for the CH<sub>3</sub>NH<sub>3</sub>PbI<sub>3</sub> perovskite [175]. The intensity of the  $IPCE$  response reflects the amount of perovskite formed and hence is a measure of the extent of perovskite conversion, lowest for devices annealed at 60°C and highest for 100°C. Higher annealing temperatures not only lead to a decrease in the  $IPCE$  intensity but also to a change in the spectral shape, displaying a decrease in the region between 400 and 650 nm. This is attributed to the competitive light absorption from the additional formation of PbI<sub>2</sub>.

### 5.4.5 Impedance Spectroscopy: Deviation from Chemical Capacitive Behavior

In order to determine the origin for the decrease in the  $V_{OC}$  of the devices as the temperature for the perovskite annealing is increased above 100°C, impedance spectroscopy measurements were conducted on the completed devices in the dark and under illumination.

The impedance response under dark conditions is examined and the data fitted using the model developed in the previous chapter (cf. Chapter 4). The high frequency feature corresponding to the charge-transfer resistance between the back contact and the HTM, as well as any charge-transport resistance within the HTM (if insufficiently doped) was found to remain more or less unchanged regardless of the annealing temperature used. This work focused on the intermediate to low frequency region in which the transport and recombination of charges manifests. Figure 5.12 shows the recombination resistance  $R_{ct}$  and associated chemical capacitance  $C_{\mu}$  determined from the impedance measurements conducted on devices in the dark. As can be seen the behavior of the recombination resistance remains relatively similar for all devices, no matter the annealing temperature used. This however is not the case for the



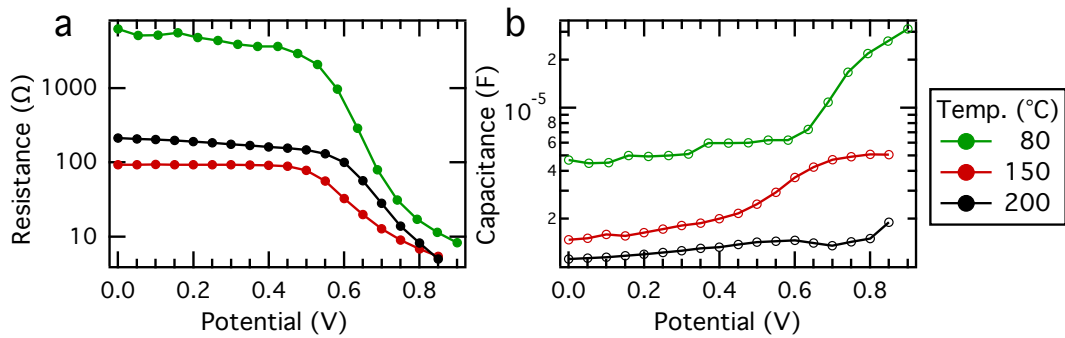
**Figure 5.12.** (a) Recombination resistance and (b)–(i) associated chemical capacitance determined from impedance spectroscopy measurements conducted on devices in the dark.

chemical capacitance.

In the case where the perovskite was heated at 80°C the chemical capacitance shows the typical behavior expected of such devices. At low forward bias, where the  $\text{mTiO}_2$  is insulating and the charges flow through the compact  $\text{TiO}_2$  underlayer, the associated capacitance at this interface is low. As the applied bias increases and the  $\text{mTiO}_2$  becomes conductive (usually at an applied bias > 400 mV), the chemical capacitance increases exponentially. This exponential behavior of the chemical capacitance is characteristic for such nanostructured materials and has been extensively reported [53, 58, 60, 78].

In the region of low forward bias, where the current flows over the blocking underlayer, the behavior of the chemical capacitance is similar for all devices, exhibiting a small increase in capacitance with increasing forward bias. As in the other measurements, the samples prepared at 100°C and 80°C behave relatively similar, with the exception that at very high forward bias, the chemical capacitance for the device annealed at 100°C does not continue to increase, but instead shows a levelling off. Increasing the temperature further shows that the chemical capacitance deviates from its exponential increase at progressively lower forward bias. While for samples heated at 175°C the chemical capacitance still shows some initial increase before





**Figure 5.13.** (a) Recombination resistance and (b) associated capacitance extracted from impedance spectroscopy measurements conducted under 100% sun light intensity.

remaining constant, annealing the perovskite at 200°C resulted in the chemical capacitance displaying no considerable increase at all.

In the case of bulk heterojunctions devices, the capacitance has been observed to behave similarly, here the decrease of the capacitance at high forward applied bias was attributed to the formation of an injection limitation [192, 193]. These types of devices display Schottky diode behavior at the metal-semiconductor contact. For Schottky diodes, the barrier height of this junction can limit the injection of the minority carrier under moderate to large forward bias thus determining the minority carrier concentration in the bulk semiconductor material [194]. Due to this injection limitation the charge collection is reduced and leads to the formation of a peak in the capacitance instead of increasing indefinitely with increasing forward bias. Furthermore this might evolve into a strong negative capacitive component [194].

In the systems under consideration here injection of electrons from and to the  $m\text{TiO}_2$  is dependent on the energy level alignment between the conduction bands of the  $m\text{TiO}_2$  and the perovskite material. The conduction band energy for the perovskite material has been reported to be only slightly higher than that of  $m\text{TiO}_2$  ( $-3.93$  eV and  $-4.00$  eV below vacuum level for the perovskite and  $\text{TiO}_2$  respectively (cf. Figure 4.2 Chapter 4) [49]). Hence any upward shift of the CB of  $\text{TiO}_2$  or downward shift of the CB of the perovskite would result in an injection barrier and thus prevent charge build up in the  $m\text{TiO}_2$ .

When high forward bias is applied in the dark, the CB in the  $m\text{TiO}_2$  is unpinned. The upward shift of the CB of the  $m\text{TiO}_2$  at high forward bias will lead to a misalignment of the energy levels. While the recombination resistance showed the expected decrease in magnitude (see Figure 5.13 (a)) with increasing annealing temperature, the behavior of the chemical capacitance under illumination was observed to be similar to the situation in the dark (Figure 5.13 (b)). However the magnitude of the capacitance decreases with increasing annealing temperature. The effect of the increasing content of  $\text{PbI}_2$ , acting as a sink for charges, is magnified under illumination. The presence of  $\text{PbI}_2$  reduces the concentration of photogenerated charges, thus reducing the charge density within the film.

A misalignment of the bands could possibly arise due to the increasing proportion of  $\text{PbI}_2$  that forms with increasing annealing temperature. It is possible that the  $\text{PbI}_2$  acts as a sink for charges injected from the perovskite, preventing the buildup within the  $\text{mTiO}_2$  and accounting for the energy level misalignment. This is clearly shown in the case for samples annealed at  $200^\circ\text{C}$  which contain a high proportion of  $\text{PbI}_2$ . The capacitance does not show any significant increase indicating that there is no injection from and into the  $\text{mTiO}_2$  and thus no buildup of charges in the  $\text{mTiO}_2$ . The peak in the chemical capacitance, before the observed decrease at high forward bias occurs at lower applied potential as the annealing temperature of the perovskite is increased. This indicates that the misalignment of the energy levels and the formation of a barrier at the  $\text{mTiO}_2$  occur at lower applied forward bias.

As can be seen from Figure 5.14 the electron lifetime, calculated from the extracted IS parameters, decreases as the annealing temperature is increased from  $80$  to  $200^\circ\text{C}$ . This clearly reflects the evolution of the open-circuit potential extracted from the  $J$ - $V$  characteristics for devices made using increasing annealing temperatures. These displayed an initial increase in  $V_{\text{OC}}$  as the annealing temperature increased up to  $100^\circ\text{C}$  corresponding to incomplete conversion to the perovskite material at low temperatures. This was subsequently followed by a decrease in  $V_{\text{OC}}$  as the annealing temperature is further increased. The electron lifetime of the devices was observed to be longest for devices annealed at  $80$  and  $100^\circ\text{C}$ , steadily decreasing as temperatures increase to  $200^\circ\text{C}$ . Similarly devices treated at  $60^\circ\text{C}$  also showed a lower electron lifetime, arising from the incomplete conversion of the precursors to the perovskite material.

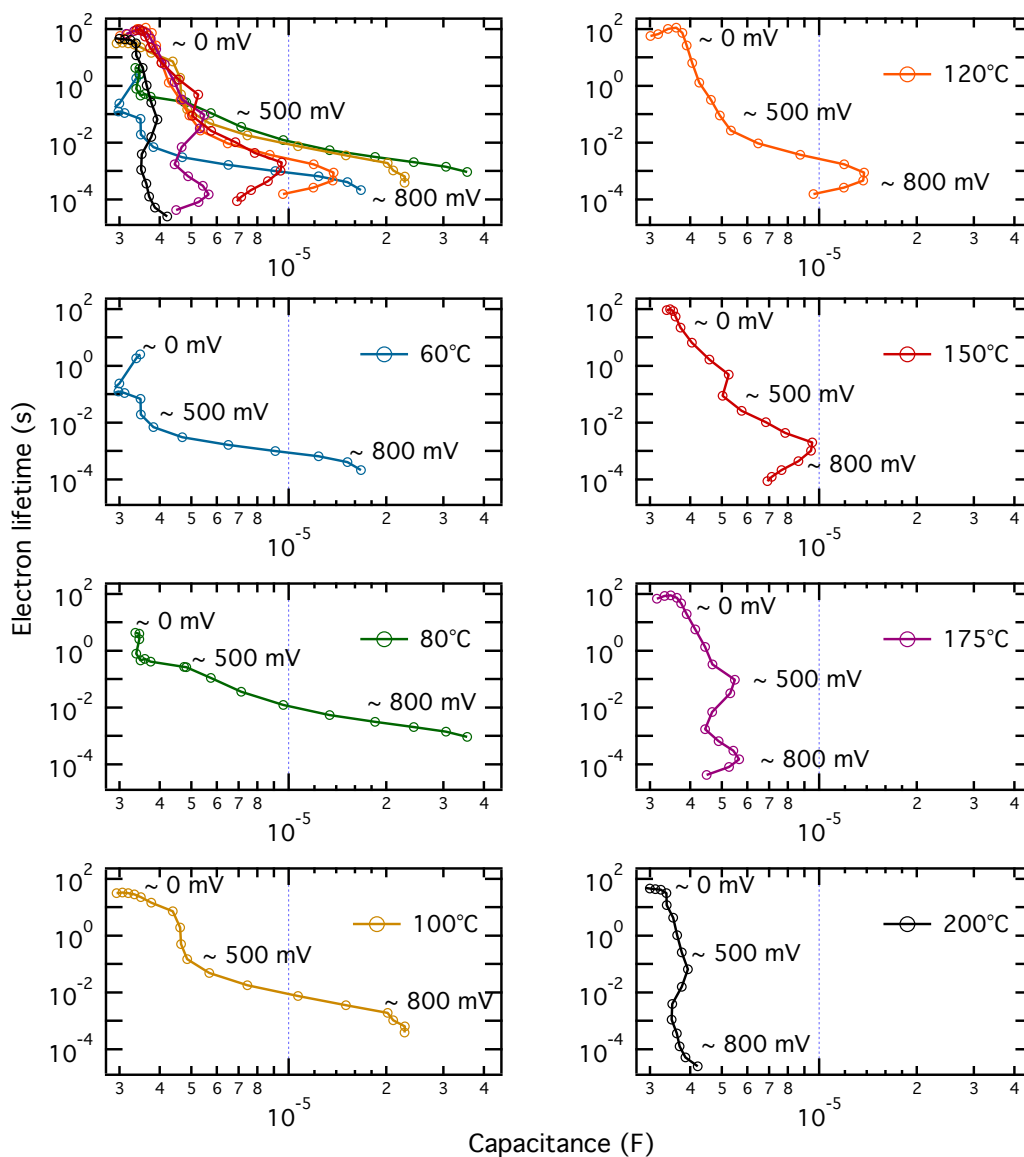
From the observations made from the IS measurements it is possible to deduce that the heat treatment of the perovskite precursors at too high temperatures changes the energy levels within the formed perovskite material in such a way as to hinder the electron injection from and into the  $\text{mTiO}_2$  at high forward bias. It remains unclear whether this is due to the change in morphology of the formed perovskite film or due to the increasing proportion of  $\text{PbI}_2$  formed.

### 5.5 $\text{PbI}_2$ Compositional Effects

When the  $\text{CH}_3\text{NH}_3\text{PbI}_3$  perovskite is formed or treated at temperatures  $> 140^\circ\text{C}$ ,  $\text{PbI}_2$  starts to form as shown in the previous Section 5.4 which is detrimental to the photovoltaic performance of the perovskite solar cells. In order to further explore the observations made, the effect of the  $\text{PbI}_2$  content on the perovskite film morphology, its properties and on the resultant device performance was investigated.

Typically the precursor solution is prepared using a 1 to 1 molar ratio of  $\text{PbI}_2$  and  $\text{CH}_3\text{NH}_3\text{I}$  dissolved in GBL at 30–40 wt% (which corresponds to a concentration of 0.8–1.2 M  $\text{PbI}_2$ ).  $\text{CH}_3\text{NH}_3\text{I}$  helps to solubilize  $\text{PbI}_2$  in the solution. Solutions of varying molar ratio of the precursor components were prepared by mixing different proportions of 1 M solutions of

## 5.5. PbI<sub>2</sub> Compositional Effects



**Figure 5.14.** Electron lifetime calculated as described from the impedance spectroscopic measurements.

PbI<sub>2</sub> and CH<sub>3</sub>NH<sub>3</sub>I in DMF<sup>4</sup>. DMF was chosen due to the poor solubility of PbI<sub>2</sub> in GBL. The proportion of PbI<sub>2</sub> in the sample solutions was increased from an equimolar solution of 1:1 ratio of PbI<sub>2</sub> and CH<sub>3</sub>NH<sub>3</sub>I to a 1:0 ratio consisting of pure 0.5 M solution of PbI<sub>2</sub> by decreasing the aliquots of CH<sub>3</sub>NH<sub>3</sub>I added to the mixture.

<sup>4</sup> The total volume of the solutions was kept constant by completing with DMF solvent to ensure that the PbI<sub>2</sub> concentration was constant at 0.5 M for all mixtures.

**Table 5.5.** Photovoltaic performance parameters extracted from  $J$ - $V$  measurements under standard AM1.5G illumination ( $100 \text{ mW cm}^{-2}$ ) of devices prepared using different PbI<sub>2</sub> content. All devices were masked to achieve an illuminated area of  $0.285 \text{ cm}^2$ .

PbI <sub>2</sub> : CH <sub>3</sub> NH <sub>3</sub> I	$V_{OC}$ (mV)	$J_{SC}$ (mA cm <sup>-2</sup> )	$FF$	$PCE$ (%)
1:1	788	9.92	0.76	6.04
1:0.8	759	9.68	0.74	5.55
1:0.5	747	7.39	0.63	3.50
1:0.2	749	2.99	0.58	1.31
1:0	585	0.53	0.66	0.21

### 5.5.1 Scanning Electron Microscopy: Film Morphology

As is illustrated in Figure 5.15 when deposited from a 1 to 1 molar ratio solution of PbI<sub>2</sub> to CH<sub>3</sub>NH<sub>3</sub>I in DMF, the perovskite film formed after annealing is cone-like in structure as previously shown in Section 5.3. The structure appears to be partially hollow, hexagonal in shape and 1–2  $\mu\text{m}$  in diameter. As the proportion of PbI<sub>2</sub> is increased to 1:0.8 the perovskite crystal structure becomes less defined, slightly smaller and more needle like in appearance.

Further increasing the content of PbI<sub>2</sub> leads to an observed interconnection of the needle-like structure, a reduction in the size of the needles and finally forming a relatively flat film of material on top of the mTiO<sub>2</sub>. Additionally as the proportion of PbI<sub>2</sub> is increased the internal structuring of the perovskite crystals becomes more apparent which is similar to the changes observed in the perovskite film morphology when it is annealed at higher temperatures (Figure 5.8). Hence this can be correlated with the increasing PbI<sub>2</sub> content within the perovskite film.

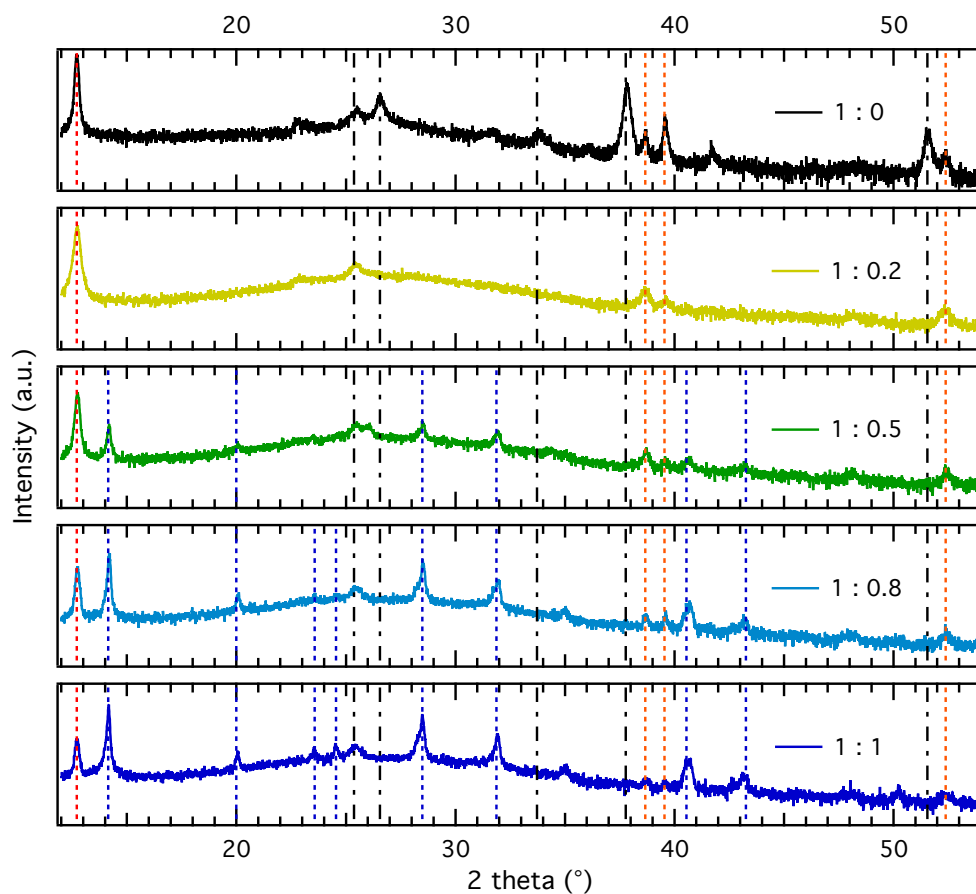
### 5.5.2 X-ray Diffraction: Perovskite Composition

The XRD measurements, presented in Figure 5.16, allow the changes in the composition of the perovskite film formed to be monitored. As the proportion of PbI<sub>2</sub> in the precursor solution increases the peaks corresponding to the CH<sub>3</sub>NH<sub>3</sub>PbI<sub>3</sub> (indicated by dashed blue lines) decrease and completely disappear at a molar ratio of 1 to 0.2 of PbI<sub>2</sub> to CH<sub>3</sub>NH<sub>3</sub>I. Interestingly the presence of pure PbI<sub>2</sub> is confirmed by the associated XRD peaks at 12.7 and 39.5° (dashed orange lines) even in the sample with 1 to 1 molar ratio. These peaks become more intense and narrow as the PbI<sub>2</sub> fraction of the precursor solution increases.

### 5.5.3 Optical and Photovoltaic Characterization

The trends observed in the XRD measurements (Figure 5.16) account for the changes visible in the UV-vis absorption measurements displayed in Figure 5.17 (a). These indicate a decrease in the absorption of the mTiO<sub>2</sub>/perovskite across the entire visible spectrum as the proportion of PbI<sub>2</sub> increases. Furthermore for samples with a molar ratio of 1:0.5 to 1:0 the PbI<sub>2</sub> absorption

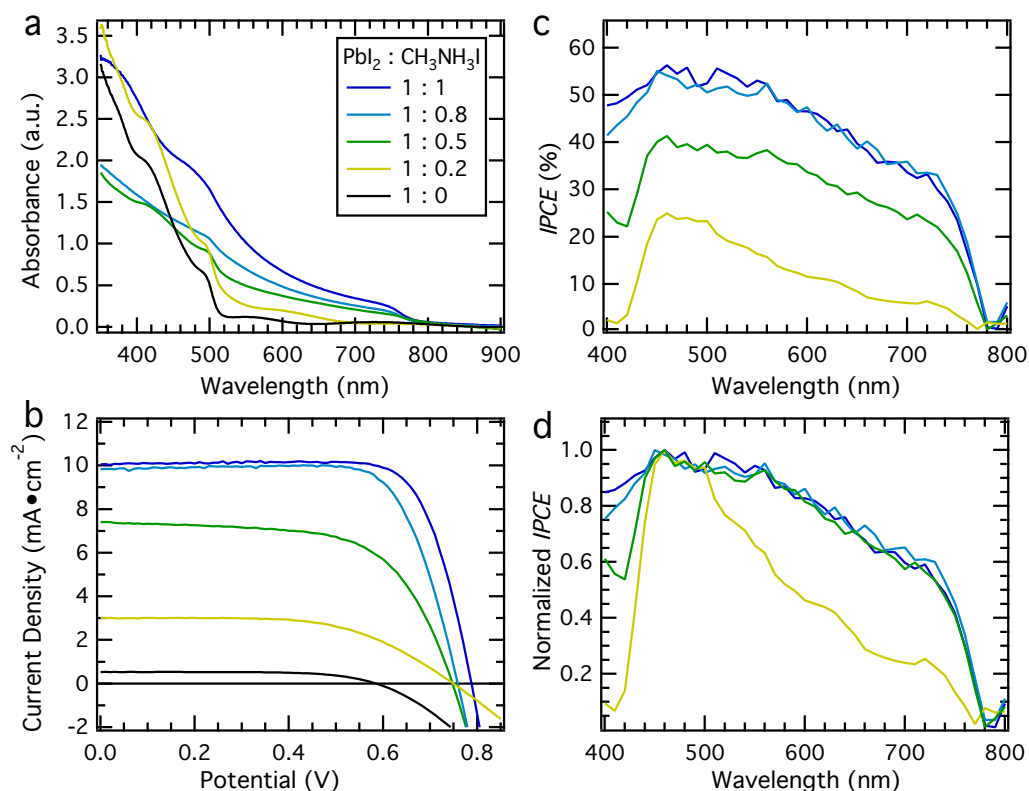




**Figure 5.16.** XRD diffractograms of  $\text{mTiO}_2$  films with deposited perovskite solution containing different  $\text{PbI}_2$  content. The vertical lines indicate the peaks associated with  $\text{PbI}_2$  (dashed orange), perovskite (dashed blue) and  $\text{mTiO}_2$  (black dot/dash).

feature at 500 nm is apparent. The decrease in absorption with increasing  $\text{PbI}_2$  content is reflected in the decrease in the *IPCE* of the solar cells (Figure 5.17 (b) and (d)) which is further represented by the decrease in  $J_{\text{SC}}$  (Figure 5.17 (a) and Table 5.5).

When the shape of the *IPCE* spectrum is considered, the response for samples with molar ratios of 1:1 to 1:0.5 is similar as clearly illustrated in the normalized *IPCE* spectrum shown in Figure 5.17 (d). Devices prepared using a high  $\text{PbI}_2$  proportion of 1:0.2 relative to the  $\text{CH}_3\text{NH}_3\text{I}$  display a lower response between 500 and 800 nm, which is attributed to the higher  $\text{PbI}_2$  composition of the film, has no absorbance in this wavelength range (as seen in Figure 5.17 (a)). It was not possible to accurately measure the *IPCE* spectra for devices prepared with pure  $\text{PbI}_2$  (corresponding to a molar ratio of 1:0) due to the extremely low signal intensity detected arising from the low currents generated. Incidentally from the similar shape of the UV-vis absorption spectra and the XRD measurements, it is evident that the perovskite films prepared with a



**Figure 5.17.** (a) UV-vis absorption spectra, (b) photovoltaic performance, (c) IPCE spectra and (d) normalized IPCE spectra of  $\text{mTiO}_2$  films with deposited perovskite solution containing different  $\text{PbI}_2$  content.

molar ratio of 1:0.2 are almost indistinguishable from the pure  $\text{PbI}_2$  films. Therefore these films consist of largely pure  $\text{PbI}_2$  and the slight differences (higher  $J_{\text{SC}}$ ,  $V_{\text{OC}}$  and absorbance) can be attributed to the contribution of the small proportion of  $\text{CH}_3\text{NH}_3\text{PbI}_3$  perovskite formed.

The photovoltaic performance, presented in Figure 5.17 and summarized in Table 5.5, of the solar cells show clear dependency on the proportion of  $\text{PbI}_2$  present in the perovskite precursor solution<sup>5</sup>. In particular the  $J_{\text{SC}}$  decreases significantly due to the lower light harvesting abilities of the film as with proportion of  $\text{Pb}_2$  increases. Additionally a decrease in the  $V_{\text{OC}}$  and a tendency to lower  $FF$  is observed. The behavior of the photovoltaic parameters as a function of the  $\text{PbI}_2$  content are similar to those observed in Section 5.4 when the annealing temperature is increased to above  $140^\circ\text{C}$  leading to the formation of  $\text{PbI}_2$ .

<sup>5</sup> The PCEs presented here are low due to the necessary change in solvent from GBL (for which the highest efficiencies are reported) to DMF and the lower weight percent in solution resulting from the poor solubility of  $\text{PbI}_2$ . These changes were made to accurately prepare precursor solutions with varying molar ratios by mixing different aliquots of predissolved 1 M solutions of  $\text{PbI}_2$  and  $\text{CH}_3\text{NH}_3\text{I}$  in DMF. Consequently the 1:1 mixture contained only 0.5 M  $\text{PbI}_2$ , which is considerably less than the standard concentrations used for high efficiency solar cells.

### 5.5.4 Impedance Spectroscopy: Confirmation of Chemical Capacitive Behavior

While apparent that the contribution of  $\text{PbI}_2$  is detrimental to the photovoltaic performance of perovskite solar cells, impedance spectroscopy was used to further investigate its effect on the internal electrical processes and device mechanisms.

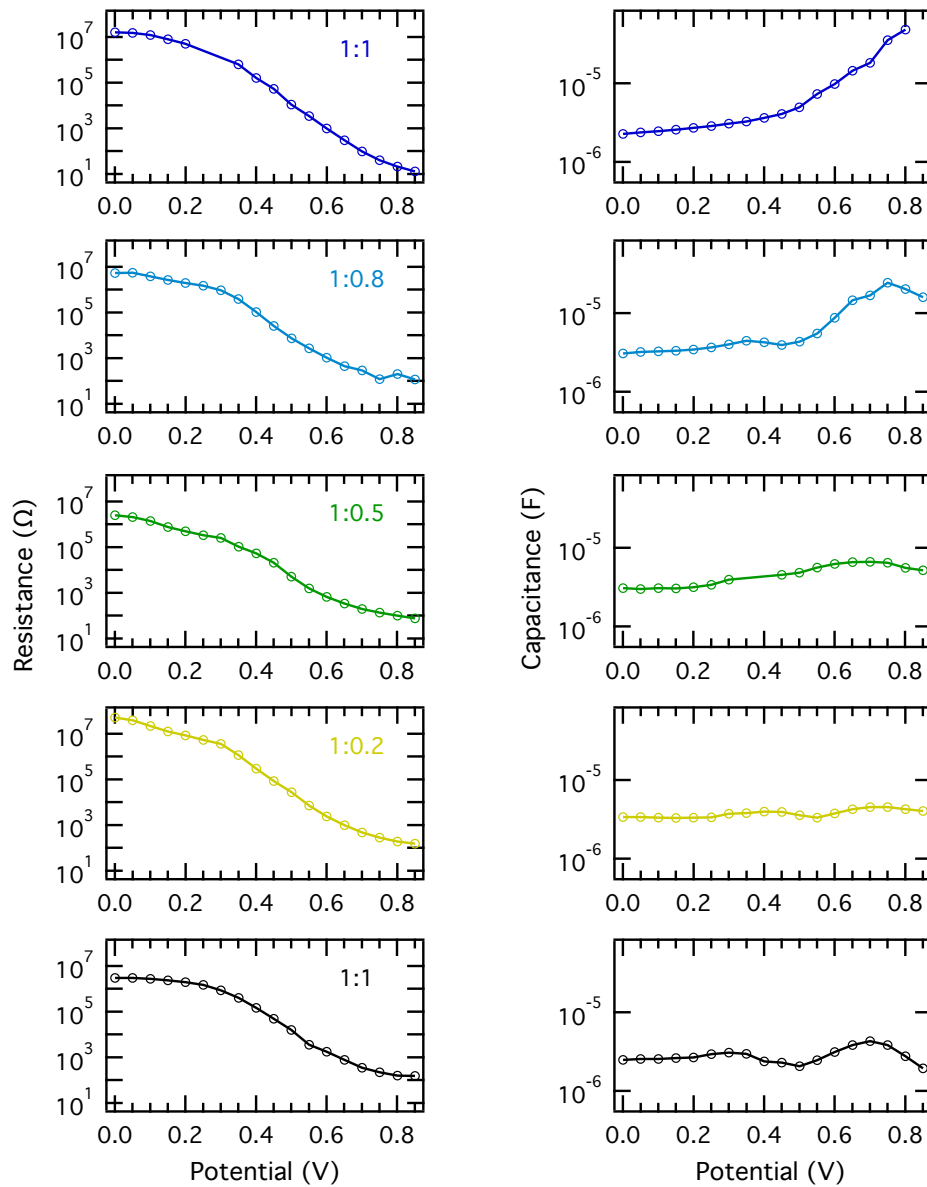
In Figure 5.12 of Section 5.4 the behavior of the chemical capacitance of the perovskite solar cells was shown to be strongly influenced by the annealing temperature used in the formation process of the perovskite. At high annealing temperatures the chemical capacitance deviated from its characteristic exponential increase, levelling off and even decreasing at high forward bias.

The recombination resistance and the associated capacitance determined from the IS measurement of perovskite devices with varying  $\text{PbI}_2$  content is presented in Figure 5.18. The behavior and magnitude of the recombination resistance is similar regardless of the  $\text{PbI}_2$  content within the perovskite film. This was also the case for perovskite devices prepared using different annealing temperatures presented in Section 5.4. However the response of the capacitance at high forward bias was different with relation to the increasing  $\text{PbI}_2$  content. Devices prepared using a 1:1 molar ratio of  $\text{PbI}_2$  and  $\text{CH}_3\text{NH}_3\text{I}$  showed the characteristic exponential increase at high forward bias. As the proportion of  $\text{PbI}_2$  increases the chemical capacitance deviates from this typical exponential reaching a plateau and even decreasing. The deviation from the typical response of the capacitance was found to be similar to the behavior observed when the annealing temperature is increased. As the proportion of  $\text{PbI}_2$  becomes greater the increase in the capacitance is significantly reduced, as observed for devices with 1:0.5 molar ratio. In the case of devices containing a high proportion of  $\text{PbI}_2$ , prepared from a 1:0.2 molar ratio, and pure  $\text{PbI}_2$ , no significant increase is observed. This is similar to the case described above for annealing temperatures of  $200^\circ\text{C}$ , which was shown to largely form pure  $\text{PbI}_2$ .

One of the suggested explanations for this behavior was that formation of an energy level misalignment where the  $\text{PbI}_2$  acts as a sink for charges injected from the perovskite, as a result preventing the buildup of charges within the  $\text{mTiO}_2$ . This is in good agreement with the results presented here and further confirms those previously showing the effects of changing the annealing temperature of the perovskite material. For such devices, where the material is predominantly  $\text{PbI}_2$ , the chemical capacitance exhibits no significant increase as a function of the applied potential, indicating that there is no buildup of charges inside the  $\text{mTiO}_2$  and consequently no injection of charges into and from the  $\text{mTiO}_2$ . The presence of  $\text{PbI}_2$  is hence clearly detrimental to the photovoltaic performance of the perovskite solar cells, not only due to the decreased light harvesting abilities, but additionally due to the  $\text{PbI}_2$  acting as a sink for charges. The latter resulting in a decrease of the electron lifetime of charges which is generally reflected in a decrease in the  $V_{\text{OC}}$  of the devices.

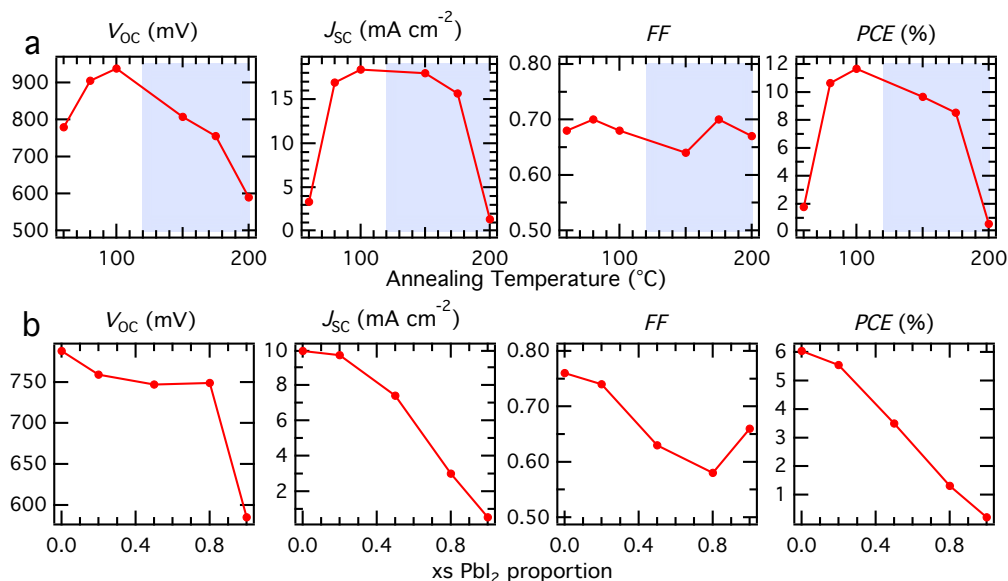
Moreover it is interesting to note that for the devices with high  $\text{PbI}_2$  content there is a discernible drop in the chemical capacitance at 400–450 mV. This feature has been attributed





**Figure 5.18.** Recombination resistance and chemical capacitance determined from IS measurements conducted in the dark for perovskite solar cells with different  $\text{PbI}_2$  content.

to the contribution of the capacitance at the interface between the blocking underlayer and the HTM (cf. Chapter 4). The presence of high quantities of  $\text{PbI}_2$  may disrupt the formation of a continuous perovskite film, allowing the direct contact between the underlayer and the HTM, thus decreasing the transport of charges *via* the perovskite film. This is supported by the appearance of the deposited material on the  $\text{mTiO}_2$  as seen in the SEM images in Figure 5.15.



**Figure 5.19.** Change in photovoltaic parameters extracted from  $J$ - $V$  measurements as a function of (a) the annealing temperature of the perovskite and (b) as a function of the excess  $\text{PbI}_2$  content. Tinted area in (a) corresponds to temperature range where additionally  $\text{PbI}_2$  is formed.

## 5.6 $\text{PbI}_2$ Content

The photovoltaic parameters extracted from the  $J$ - $V$  measurements presented in Figure 5.17 and in Section 5.4 Figure 5.11 are presented as a function of the associated (a) annealing temperature<sup>6</sup> and (b)  $\text{PbI}_2$  content<sup>7</sup> in Figure 5.19. From the XRD measurements conducted on perovskite films annealed at different temperatures, it was shown that  $\text{PbI}_2$  is additionally formed at temperatures above  $120^\circ\text{C}$ , indicated by the shaded region in Figure 5.19 (a). The trends in the photovoltaic parameters in this region are almost identical to those as a function of increasing  $\text{PbI}_2$  content, displaying a decrease in  $V_{\text{OC}}$ ,  $J_{\text{SC}}$  and  $PCE$ . Major factors contributing to these trends are the decrease in electron lifetime, leading to the falling  $V_{\text{OC}}$  and the lower light harvesting abilities, reflected in the decrease in  $J_{\text{SC}}$ , as the content of  $\text{PbI}_2$  in the active layer of the perovskite devices increases. The investigation of the effect of the annealing temperature was based on the one step deposition of a 1 to 3 molar ratio solution of  $\text{PbCl}_2$  and  $\text{CH}_3\text{NH}_3\text{I}$  in DMF while the second investigation employed solutions of varying ratios of  $\text{PbI}_2$  and  $\text{CH}_3\text{NH}_3\text{I}$  in DMF. Consideration of only the photovoltaic parameters as either a function of annealing temperature (when  $T > 120^\circ\text{C}$ , see tinted area of Figure 5.19 (a)) or of increasing  $\text{PbI}_2$  content while disregarding the absolute magnitude of the individual parameters, shows great similarity in the observed trends. This demonstrates that irrespective of the deposition technique or the precursors used, the effect of increasing  $\text{PbI}_2$  within the

<sup>6</sup> Adapted from Section 5.4.

<sup>7</sup> The excess (xs.)  $\text{PbI}_2$  proportion is determined from the molar ratio of  $\text{PbI}_2$  and  $\text{CH}_3\text{NH}_3\text{I}$  in solution. As such the 1:1 solution corresponds to an xs.  $\text{PbI}_2$  proportion of 0 and the 1:0 solution mixture corresponds to an xs.  $\text{PbI}_2$  proportion of 1.

matrix of the active layer is the same.

## 5.7 Conclusions

The film morphology and composition are shown to be crucial for the photovoltaic device performance of solid-state perovskite solar cells. In this chapter the effect of various parameters such as the chosen solvent and the annealing temperature on the perovskite film formation are investigated. Furthermore the nature of the inorganic precursor,  $\text{PbI}_2$  versus  $\text{PbCl}_2$ , and its role in the conversion process from the as-deposited solution to the perovskite crystal is examined.

### 5.7.1 Solvent Effects

In Section 5.3 the film structure and morphology of the perovskite crystal formed from a 1:1 molar ratio solution of  $\text{PbI}_2$  and  $\text{CH}_3\text{NH}_3\text{I}$  is shown to change from circular islands when GBL is used as a solvent to cone/needle like for DMF. The importance of the choice of solvent is highlighted as the associated solubility, volatility and wettability properties are crucial in the perovskite film formation, determining the film morphology and composition.

Furthermore the difference between the use of  $\text{PbI}_2$  and  $\text{PbCl}_2$  as inorganic precursor was examined. The use of  $\text{PbCl}_2$  in place of  $\text{PbI}_2$  greatly increases the time required to convert the as-deposited material to the perovskite crystal when it is annealed at  $100^\circ\text{C}$  (from less than 10 to 45 minutes). This suggests some major rearrangement of the components and/or the presence of an energy barrier when  $\text{PbCl}_2$  is used. Moreover the film morphology adopts a more dense, interconnected network of crystallites rather than the large cone/needle like structure adopted when  $\text{PbI}_2$  is used, leading to higher *PCEs*.

### 5.7.2 Perovskite Annealing Temperature

In Section 5.4 the role of the annealing temperature used in the conversion process to form the perovskite material from the deposited precursor solution of  $\text{PbCl}_2$  and  $\text{CH}_3\text{NH}_3\text{I}$  in DMF (1:3 molar ratio) was investigated. This parameter was found to have critical impact on the formed perovskite film morphology and thus the power conversion efficiency of the solar cells fabricated. The film morphology was examined by UV-vis spectroscopy, SEM imaging and XRD, which all indicate that a minimum temperature of  $80^\circ\text{C}$  is required to sufficiently form the  $\text{CH}_3\text{NH}_3\text{PbI}_3$  perovskite. Using lower temperatures or simply drying the  $\text{mTiO}_2$  film after the perovskite precursor solution is deposited leads to incomplete conversion. These low temperatures remove the solvent from the solution, leaving the dried precursors on the film, but are insufficient to lead to the perovskite formation, thus indicating that there is an energy requirement (endothermic reaction) to the formation of the perovskite. On the other hand as the perovskite annealing temperature is increased, the film morphology undergoes clear

changes forming distinct islands of materials on the surface of the film that display internal structuring as the temperature is increased further. This is accompanied by an increased amount of  $\text{PbI}_2$  content in the film, as seen in the XRD measurements and in the UV-vis spectra.

These changes in film morphology are correlated with the photovoltaic performance of solid-state solar cells. The highest performance was achieved for devices fabricated using an annealing temperature between 80 and 100°C. This corresponds to samples that showed complete conversion of the precursors to the perovskite, no additional  $\text{PbI}_2$  formation, as well as a film morphology consisting of a type of interconnected network of perovskite crystallites. Furthermore these conditions showed the highest absorbance (a direct result of the extent of perovskite conversion) leading to the highest short-current density.

IS spectroscopy was used to further examine the internal electrical processes within these devices and gain a better understanding of the role of the film morphology and perovskite conversion mechanism on the device performance. A clear trend in the chemical capacitance was observed. Increasing the annealing temperature of the perovskite led to deviation from the typical exponential behavior of the chemical capacitance at high forward bias. This is believed to be due to a misalignment of the energy levels and the formation of a barrier at the  $\text{mTiO}_2$  at high forward bias. This effect becomes more dominant and occurs at lower forward applied bias as the annealing temperature is increased, until the capacitance is observed to not increase at all for the devices with the perovskite annealed at 200°C. This can be correlated with the increasing  $\text{PbI}_2$  content within the perovskite material and the increasing size of the perovskite crystallite islands formed on the  $\text{mTiO}_2$  film. The formation of  $\text{PbI}_2$  at higher annealing temperatures may moreover act as a sink for the charges, thus limiting the injection of charges to and from the  $\text{mTiO}_2$ .

### 5.7.3 $\text{PbI}_2$ Compositional Effects

The role of the  $\text{PbI}_2$  content in the perovskite film was studied in Section 5.5. The increasing content of  $\text{PbI}_2$  was monitored by UV-vis spectroscopy and XRD and a clear influence on the film morphology was observed. Similar trends in the photovoltaic performance and the IS response were observed with respect to the  $\text{PbI}_2$  content as in the case for devices annealed at temperatures above 120°C in Section 5.4.

In this chapter the importance of the perovskite formation mechanism on the film morphology and consequently on the solar cell device performance is highlighted through intensive characterization of the perovskite film formed and of the solar cells fabricated. The choice of solvent and precursor mixture is crucial to achieve high *PCEs*. The detrimental effect of the formation and/or addition of  $\text{PbI}_2$  was investigated and the associated trends observed in the device photovoltaic performance and working mechanisms are believed to be general for the  $\text{CH}_3\text{NH}_3\text{PbI}_3$  perovskite, regardless of the deposition process. Thus to achieve high *PCEs* the formation/conversion procedure of the perovskite material is critical. Several parameters that

influence the morphology and composition of the formed perovskite film have been explored, revealing several strategies that can be adopted to control the formation of the perovskite film and thus the resultant device *PCE*.

### 5.7.4 Perspectives

Future studies should investigate the effects of different solvents in greater depth. Dimethoxyethane and dimethyl sulfoxide are possible candidates that could be considered. The choice of solvent was shown to strongly influence and direct the growth of the perovskite film. Grain boundaries in the perovskite material are believed to act as recombination centres and thus detrimental to the charge collection efficiency of the devices. Examining the relationship between the growth of the perovskite and the formation of grain boundaries between crystal domains in the material would provide valuable knowledge that can be implemented to improve the device performance. Similarly formation of larger perovskite crystallites that can scatter light and hence increase the optical path length within the material can be explored.

The crystal structure of organic-inorganic based hybrid perovskite has been engineered through the implementation of ammonium carboxylic acid as the organic component by Mercier *et al.* [195]. This demonstrates that the assembly of these perovskite materials can be predicted and controlled through the use of templating agents and/or careful selection of the structure and functionality of the organic cationic species. The presence and/or absence of additives to the perovskite precursor solution is likely to also influence the perovskite crystal formation. These strategies offer a multitude of possible avenues of research by which the crystal structure and morphology can be tuned that to this date have not been explored in any considerable depth.

While the simplicity of solution processing of the perovskite material is one of its advantages, the formation of highly uniform films by thin film evaporation techniques have resulted in high *PCEs*. This further confirms that the film morphology is of critical importance for good photovoltaic performance. The use of such materials as light absorbers in solar cells is still a relatively new concept thus not only are the device mechanisms still not completely understood, but the optimum film morphology, thickness and composition parameters have not yet been isolated. New perovskite film morphologies and structures, processing techniques, treatments and recipes are continually being discovered. This, in addition to the optimization of the deposition parameters and device configuration has resulted in the rapid increase in reported *PCEs* approaching 16%.



# 6 Thermal Analysis of Methyl Ammonium Lead-Trihalide Perovskite

## 6.1 Introduction

In the previous chapter (Section 5.4 Chapter 5) the role of the annealing temperature on the formation of the perovskite film from the as-deposited precursor solution was investigated. Significant differences in film morphology, composition and overall device performance were observed as a function of the annealing temperature. These parameters have proven to be critical to the photovoltaic performance of such perovskite solar cells [147, 196, 197].

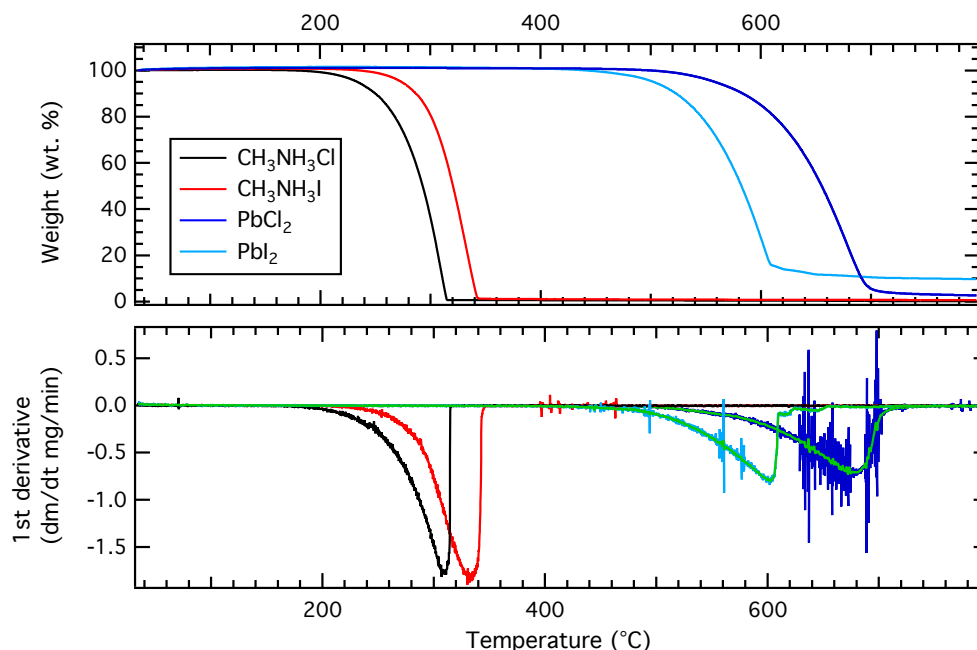
In this chapter the thermal properties of the perovskite material are examined. The individual components and precursors are analyzed in order to correctly identify their contributions to the thermodynamic behavior of the perovskite material formed. Additionally the formation of the perovskite material of the general form  $\text{CH}_3\text{NH}_3\text{PbX}_3$  (where  $\text{X}=\text{I}$  or  $\text{Cl}$ ) from mixed precursor solutions of  $\text{PbX}_2$  and  $\text{CH}_3\text{NH}_3\text{X}$  (where  $\text{X}$  can be  $\text{I}$  or  $\text{Cl}$ ) is considered in order to gain insight into the effect of the formation of the excess organic component.

This study helps to clarify the role of the precursors' composition used in the perovskite solution mixture, highlighting the importance of the molar ratio between the inorganic and organic components.

## 6.2 Thermogravimetric Analysis

Thermogravimetric Analysis (TGA) is a method of thermal analysis that involves the characterization of physical and chemical properties of materials that exhibit mass loss as a function of increasing temperature.

It is used here to determine the behavior of the individual organic and inorganic components that make up the building blocks for the  $\text{CH}_3\text{NH}_3\text{PbI}_3$  perovskite in question. The sublimation behavior of the isolated organic component is examined in depth and correlated with its behavior in the direct thermogravimetric measurement of various perovskite precursor solutions and of the  $\text{CH}_3\text{NH}_3\text{PbI}_3$  perovskite powder.



**Figure 6.1.** TGA heating curves of individual precursor powders expressed as weight % as a function of applied temperature and the corresponding 1st derivatives.

### 6.2.1 Precursor Materials

The quality of the perovskite film is strongly dependent on the conditions of the conversion/-formation step. As this typically involves a heat treatment, a thermal analysis of the individual components is necessary to provide valuable insight into the thermal stability and properties of the precursors and of the final product.

TGA follows the mass loss of the materials when subjected to controlled heating under  $N_2$  atmosphere. The thermal stability of the precursor materials is investigated by heating at a steady rate of  $10^\circ\text{C min}^{-1}$  from 30 to  $800^\circ\text{C}$ . The TGA curves are presented in Figure 6.1 and the relevant extracted parameters are summarized in Table 6.1.

The organic components –  $\text{CH}_3\text{NH}_3\text{I}$  and  $\text{CH}_3\text{NH}_3\text{Cl}$  – undergo 100% weight loss in one step suggesting that these materials undergo sublimation, the onset of which occur at  $234$  and  $185^\circ\text{C}$  respectively (see Table 6.1). This is further validated by the sharpness of the transition step in the differential TGA curves. In contrast the inorganic components,  $\text{PbI}_2$  and  $\text{PbCl}_2$  undergo 90 and 95% weight loss at considerably higher temperatures of  $646$  and  $714^\circ\text{C}$  respectively. The broad weight loss profile, reflected in the broad peaks seen in the 1st derivative TGA curve imply that these inorganic materials undergo thermal decomposition. This is further highlighted by the tail in the weight % after the material has undergone the majority of its weight loss. The fact that the weight loss is not 100% indicates that some residue remain which



**Table 6.1.** Quantitative TGA for the precursor materials used, indicating the temperature of the onset of weight loss, and at which 20% and 100% weight loss has occurred. Samples were heated at  $10^{\circ}\text{C min}^{-1}$  from 30 to  $800^{\circ}\text{C}$  under a  $20\text{ ml min}^{-1}$   $\text{N}_2$  gas flow.

Precursors	Onset weight loss ( $^{\circ}\text{C}$ )	20% weight loss ( $^{\circ}\text{C}$ )	100% weight loss ( $^{\circ}\text{C}$ )
$\text{CH}_3\text{NH}_3\text{Cl}$	185	267	315
$\text{CH}_3\text{NH}_3\text{I}$	234	300	345
$\text{PbCl}_2$	500	612	714
$\text{PbI}_2$	444	546	646

may be some decomposition products and/or impurities present in the material<sup>1</sup>.

The direct phase transition from solid to gas – sublimation – occurs for materials that have an appreciable vapor pressure and thus when provided with sufficient energy will undergo this endothermic change. Ideally this transition involves no compound decomposition. Such thermodynamic processes follow zero-order kinetics resulting in a constant rate of mass loss  $dm/dt$  by sublimation, at a constant temperature. Consequently the mass loss of the material is linear under isothermal conditions. As such TGA can be applied to determine the enthalpy  $\Delta H_{sub}$  and temperature  $T_{sub}$  of sublimation [198]. From the initial TGA heat curves for  $\text{CH}_3\text{NH}_3\text{I}$  and  $\text{CH}_3\text{NH}_3\text{Cl}$  the temperature range for sublimation is found lie between  $200$  and  $350^{\circ}\text{C}$ . The temperature of sublimation  $T_{sub}$  has been defined as the point at which 20% of mass loss has occurred [199].

The enthalpy of sublimation  $\Delta H_{sub}$  can be related to the vapor pressure  $p$  and temperature  $T$  of the solid using the Clausius-Clapeyron relation, where  $R$  is the gas constant ( $8.3145\text{ JK}^{-1}\text{ mol}^{-1}$ ) according to Equation 6.1;

$$\frac{d \ln p}{dt} = \frac{\Delta H_{sub}}{RT^2} \quad (6.1)$$

The vapor pressure of a material can in turn be related to the mass loss due to sublimation using an expression presented by Langmuir [199, 200];

$$p = \frac{1}{A} \left( \frac{2\pi RT}{M_w} \right)^{1/2} m_{sub} \quad (6.2)$$

where  $A$  is the exposed sublimation surface area (here we take the area calculated from the diameter of the crucible containing the samples during the measurements) and  $M_w$  is the molecular mass of the material. The instantaneous rate of mass loss by sublimation  $m_{sub}$  at a temperature  $T$  can be derived from the TGA 1st derivative.

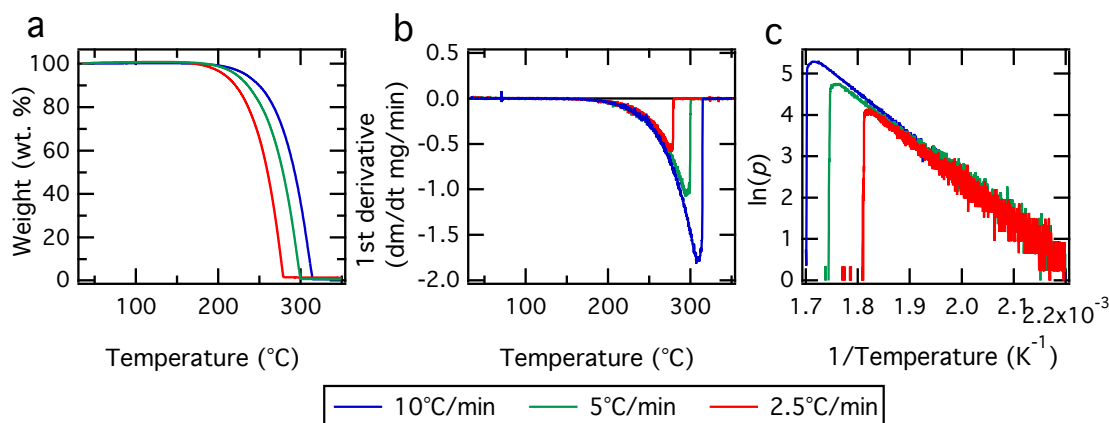
$$m_{sub} = \frac{dm}{dt} = \frac{\Delta mass}{\Delta t} \quad (6.3)$$

<sup>1</sup> The  $\text{PbI}_2$  is purchased from Sigma Aldrich with a 99% purity. It thus contains 1% impurities that may or may not undergo thermal decomposition or evaporation up to  $800^{\circ}\text{C}$  under  $\text{N}_2$  atmosphere.

## Chapter 6. Thermal Analysis of Methyl Ammonium Lead-Trihalide Perovskite

**Table 6.2.** Sublimation enthalpy and temperature of  $\text{CH}_3\text{NH}_3\text{Cl}$  determined from a linear least-squares fitting of the thermogravimetry data obtained at using different heating rates.

Heat rate ( $^{\circ}\text{C min}^{-1}$ )	Slope (K)	$y$ -intercept	Regression coefficient $R^2$	$\Delta H_{sub}$ ( $\text{kJ mol}^{-1}$ )	$T_{sub}$ ( $^{\circ}\text{C}$ )
10	$-10201 \pm 41$	$22.91 \pm 0.07$	0.994934	$84.8 \pm 0.3$	$172 \pm 1$
5	$-9643 \pm 47$	$21.79 \pm 0.09$	0.986347	$80.2 \pm 0.4$	$170 \pm 1$
2.5	$-9575 \pm 54$	$21.6 \pm 0.1$	0.980173	$79.6 \pm 0.4$	$171 \pm 1$



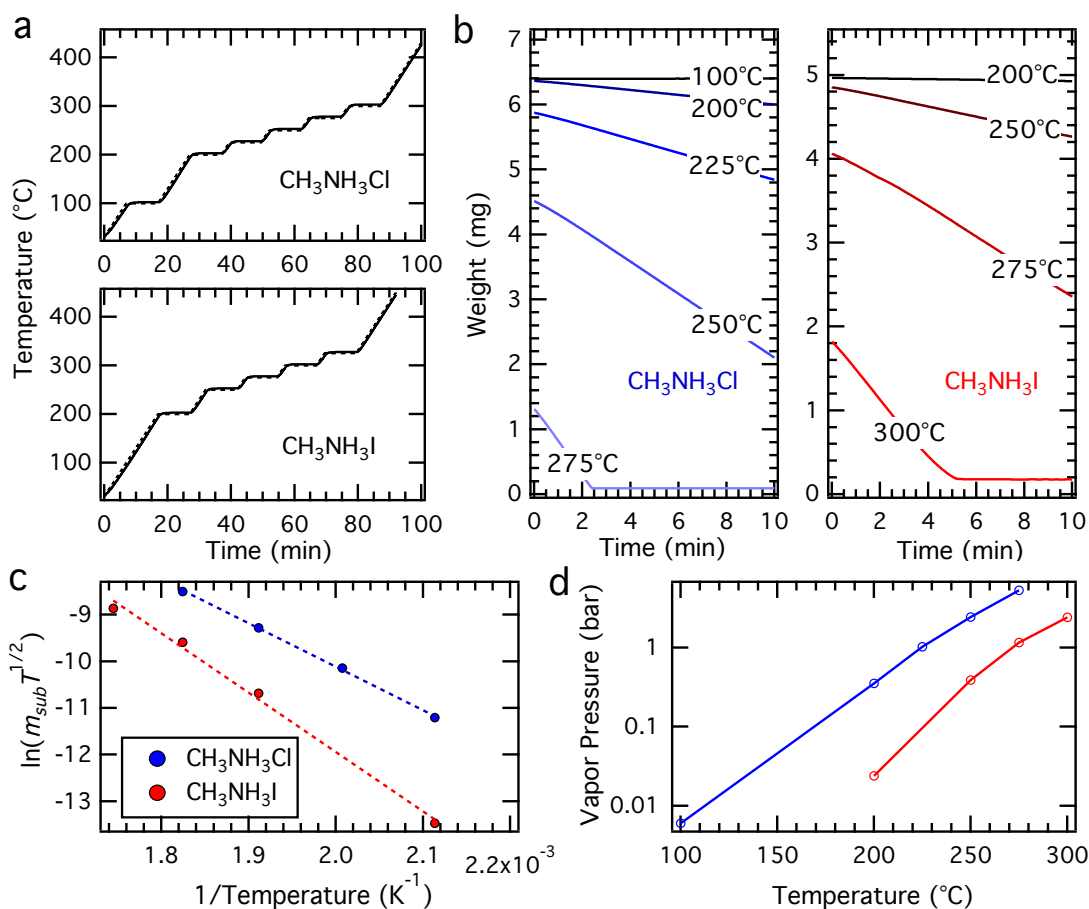
**Figure 6.2.** (a) TGA heating curves of the  $\text{CH}_3\text{NH}_3\text{Cl}$  precursor and (b) corresponding 1st derivatives measured at different heating rates; 10 (blue), 5 (green) and  $2.5^{\circ}\text{C min}^{-1}$  (red). (c) Calculated  $\ln p$  versus  $1/T$ .

Integrating Equation 6.1 yields Equation 6.4 which allows the determination of the enthalpy and temperature of sublimation from the slope and  $y$ -intercept of the linear plot of  $\ln p$  versus  $1/T$ , see Figure 6.2:

$$\ln p = -\frac{\Delta H_{sub}}{RT} + \frac{\Delta H_{sub}}{RT_{sub}} \quad (6.4)$$

The assumption is made that the heat of sublimation is independent of temperature in the temperature range considered here. Additionally the observation of a linear trend of  $\ln p$  versus  $1/T$  confirms that sublimation is the only process leading to mass loss and that there is no additional thermal decomposition taking place.

Here it is important to consider the influence of the heating rate used for the data acquisition. I have performed thermogravimetric measurements of the organic precursor  $\text{CH}_3\text{NH}_3\text{Cl}$  heating at 10, 5 and  $2.5^{\circ}\text{C min}^{-1}$  from 30 to  $450^{\circ}\text{C}$  under a  $20 \text{ ml min}^{-1}$   $\text{N}_2$  gas flow, the results of which are presented in Figure 6.2. The standard reported procedure is most often  $10^{\circ}\text{C min}^{-1}$ , but using different heating rates will lead to differences in the TGA heat curve obtained for the material as clearly visible in Figure 6.2 (a). The onset of mass loss appears to remain more or less the same regardless of the heat rate used. However this is not the case for the temperature at which the material has undergone 100% mass loss.



**Figure 6.3.** (a) Program (dashed) and sample (solid) temperature profiles for determination of the isothermal mass loss rate for  $\text{CH}_3\text{NH}_3\text{Cl}$  and  $\text{CH}_3\text{NH}_3\text{I}$ . (b) Isothermal mass loss of  $\text{CH}_3\text{NH}_3\text{Cl}$  (blue) and  $\text{CH}_3\text{NH}_3\text{I}$  (red) determined from TGA. (c) Calculated  $\ln(m_{\text{sub}} T^{1/2})$  versus  $1/T$  for  $\text{CH}_3\text{NH}_3\text{Cl}$  (blue) and  $\text{CH}_3\text{NH}_3\text{I}$  (red) used to determine the heat and temperature of sublimation. (d) Corresponding vapor pressure for the materials.

The heat and temperature of sublimation was calculated for each heating rate using the approach described above using Figure 6.2 (c), the values of which are summarized in Table 6.2. As the heating rate is decreased the calculated value of the heat of sublimation decreases, indicating that employing too fast heating rates leads to overestimation of this parameter. The temperature of sublimation was found to be relatively independent of the heating rate at approximately 171°C. Hence a more accurate determination of the enthalpy is to consider the isothermal mass loss of the materials [199].

In order to determine the isothermal mass loss of the materials, thermogravimetric measurements are run using temperature profiles with multiple isothermal regions of 10 minutes, see Figure 6.3 (a). Figure 6.3 (b) shows the mass loss as a function of time for the different isothermal regions, the linear mass loss at each temperature confirming that no additional decomposition is occurring. As expected, the slope of the mass loss increases with increasing

## Chapter 6. Thermal Analysis of Methyl Ammonium Lead-Trihalide Perovskite

**Table 6.3.** Sublimation enthalpy and temperature of CH<sub>3</sub>NH<sub>3</sub>Cl and CH<sub>3</sub>NH<sub>3</sub>I determined from a linear least-squares fitting of the thermogravimetry data.

Precursor	Slope (K)	y-intercept	Regression coefficient $R^2$	$\Delta H_{sub}$ (kJ mol <sup>-1</sup> )	$T_{sub}$ (°C)
CH <sub>3</sub> NH <sub>3</sub> Cl	-9339±184	8.6±0.4	0.999227	78±2	195±9
CH <sub>3</sub> NH <sub>3</sub> I	-12722±659	13.5±1.3	0.994670	105±5	247±26

temperature exhibiting the relationship between the temperature and the rate of mass loss. For each isotherm, the slope of the mass loss is determined and can be associated with the rate of mass loss by sublimation  $m_{sub}$  following Equation 6.3 [199].

Substituting Equation 6.2 into Equation 6.4 the following relationship (Equation 6.5) is obtained:

$$\ln(m_{sub}T^{1/2}) = -\frac{\Delta H_{sub}}{RT} + \frac{\Delta H_{sub}}{RT_{sub}} - \frac{1}{2} \ln\left(\frac{2\pi R}{A^2 M_w}\right) \quad (6.5)$$

Consequently  $\Delta H_{sub}$  can be determined from the linear slope of  $\ln(m_{sub}T^{1/2})$  versus  $1/T$  (Figure 6.3 (c)) where the y-intercept yields a value for  $T_{sub}$ . The extracted parameters are presented in Table 6.3.

The values determined for  $\Delta H_{sub}$  were 78 and 105 kJ mol<sup>-1</sup> for CH<sub>3</sub>NH<sub>3</sub>Cl and CH<sub>3</sub>NH<sub>3</sub>I respectively. The lower  $\Delta H_{sub}$  for CH<sub>3</sub>NH<sub>3</sub>Cl illustrates that the Cl containing organic component requires less energy to undergo the direct phase transition from solid to gas. This is further reflected in its lower  $T_{sub}$ , 195°C versus 247°C for CH<sub>3</sub>NH<sub>3</sub>I. As such, CH<sub>3</sub>NH<sub>3</sub>Cl undergoes sublimation more readily than CH<sub>3</sub>NH<sub>3</sub>I and is expected to have a more substantial vapor pressure. Furthermore the value determined for  $\Delta H_{sub}$  by this isothermal method is in good agreement with that determined from the constant heating technique when the slowest heating rate is employed (79.6 ± 0.4 kJ mol<sup>-1</sup>). This suggests that this first method can be used to determine this parameter, but to prevent overestimation a very slow heating rate must be employed. There is a discrepancy between the  $T_{sub}$  values determined by the two methods; 171 ± 2°C and 195 ± 9°C for the constant heating and isothermal methods respectively. Unlike  $\Delta H_{sub}$ , which is overestimated by the constant heating technique,  $T_{sub}$  is more accurately determined by this method from the more precisely resolved y-intercept.

Using the data from the TGA it is straightforward to calculate an approximate vapor pressure for the materials using Equation 6.2 (the results of which are depicted in Figure 6.3 (d)) which clearly demonstrates the higher vapor pressure for CH<sub>3</sub>NH<sub>3</sub>Cl as predicted. However it is important to note that the exposed surface area of the materials from which sublimation occurs was calculated from the area of the crucible within which the samples were placed. This area was assumed to be equal for both materials. Furthermore the masses of material used within the measurement was treated as equivalent for the two samples. In reality the material are powders and hence the effective surface area from which sublimation is significantly

**Table 6.4.** Possible combinations of perovskite precursors and products formed

Solution	Precursor		Molar ratio inorganic : organic	Expected perovskite	Excess
	Inorganic	Organic			
1	PbI <sub>2</sub>	CH <sub>3</sub> NH <sub>3</sub> Cl	1:3	CH <sub>3</sub> NH <sub>3</sub> PbCl <sub>3</sub>	2 CH <sub>3</sub> NH <sub>3</sub> I
2	PbI <sub>2</sub>	CH <sub>3</sub> NH <sub>3</sub> I	1:1	CH <sub>3</sub> NH <sub>3</sub> PbI <sub>3</sub>	-
3	PbCl <sub>2</sub>	CH <sub>3</sub> NH <sub>3</sub> I	1:3	CH <sub>3</sub> NH <sub>3</sub> PbI <sub>3</sub>	2 CH <sub>3</sub> NH <sub>3</sub> Cl
4	PbCl <sub>2</sub>	CH <sub>3</sub> NH <sub>3</sub> Cl	1:1	CH <sub>3</sub> NH <sub>3</sub> PbCl <sub>3</sub>	-

different. As a result of these assumptions, the calculation of the vapor pressure provide approximative and not exact values.

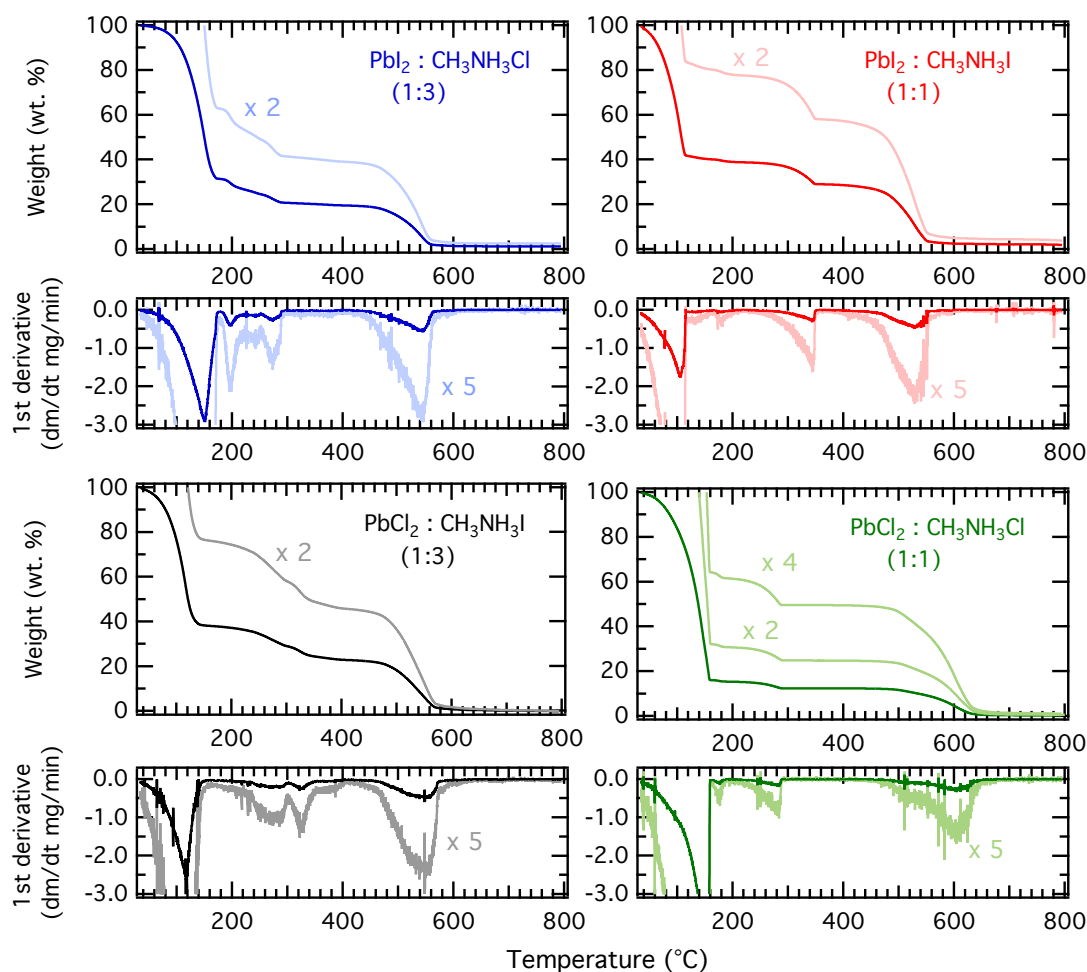
### 6.2.2 Perovskite Mixtures

Investigating the thermal behavior of the individual precursor components has provided the necessary knowledge to analyze the thermogravimetric behavior of the complete system. As previously described the deposition technique applied here is from a solution containing the precursor materials. The possible combinations of the precursors investigated are expected to form a perovskite material of the general formula CH<sub>3</sub>NH<sub>3</sub>PbX<sub>3</sub> (where X=Cl or I) are summarized in Table 6.4. Here we consider the two cases; the formation of the perovskite from 1) a 1:1 molar ratio of precursors based on the same halide (Equation 6.6) or 2) a 1:3 molar ratio mixture where the inorganic and organic components contain different halides (Equation 6.7). The molar ratio in the mixtures was determined to maintain the relationship between the Pb atom and the halide atom in the perovskite material at 1 to 3. As a result, when the identity of the halide material in the inorganic and organic components are different, a 2 molar quotient of organic material is formed as excess. This is based on the assumption that unlike the iodide-bromide mixed-halide perovskite system [145], for iodide-chloride mixtures the mixed-halide perovskites of the form CH<sub>3</sub>NH<sub>3</sub>PbI<sub>2</sub>Cl or CH<sub>3</sub>NH<sub>3</sub>PbICl<sub>2</sub> do not exist [201]. These mixtures are expected to lead to the formation of CH<sub>3</sub>NH<sub>3</sub>PbI<sub>3</sub> when CH<sub>3</sub>NH<sub>3</sub>I is used as a precursor and similarly form CH<sub>3</sub>NH<sub>3</sub>PbCl<sub>3</sub> when CH<sub>3</sub>NH<sub>3</sub>Cl is used (see Table 6.4).



In order to determine the role of the different precursor components on the thermal behavior and properties of the perovskite material formed, the systems using PbX<sub>2</sub> and CH<sub>3</sub>NH<sub>3</sub>X (where X can be Cl or I) as the precursor components are compared. The perovskite solutions, contain 0.7 M of the inorganic component and use DMF or DMSO as solvent. DMSO was used for the perovskite mixtures 1 and 4, expected to form CH<sub>3</sub>NH<sub>3</sub>PbCl<sub>3</sub>, due to the poor solubility of CH<sub>3</sub>NH<sub>3</sub>Cl in DMF.

Thermogravimetric analysis was carried out on the solutions heated at 10°C min<sup>-1</sup> from 30



**Figure 6.4.** TGA heating curves and corresponding 1st derivatives for the perovskite solutions heated at  $10^{\circ}\text{C min}^{-1}$  under a constant gas flow of  $\text{N}_2$  ( $20 \text{ ml min}^{-1}$ ) from 30 to  $800^{\circ}\text{C}$ ; solution 1 – 1:3 molar ratio of  $\text{PbI}_2$  and  $\text{CH}_3\text{NH}_3\text{Cl}$  in DMSO (blue), solution 2 – 1:1 molar ratio of  $\text{PbI}_2$  and  $\text{CH}_3\text{NH}_3\text{I}$  in DMF (red), solution 3 – 1:3 molar ratio of  $\text{PbCl}_2$  and  $\text{CH}_3\text{NH}_3\text{I}$  in DMF (black), solution 4 – 1:1 molar ratio of  $\text{PbCl}_2$  and  $\text{CH}_3\text{NH}_3\text{Cl}$  in DMSO (green).

to  $800^{\circ}\text{C}$  under a constant gas flow of  $\text{N}_2$ . Figure 6.4 shows the heat curve from the TGA measurement for the four solutions. The initial large decrease corresponding to over 60% mass loss observed for all samples arises due to the loss of solvent. Once this is achieved it is believed that the material formed corresponds to the  $\text{CH}_3\text{NH}_3\text{PbX}_3$  perovskite and – in the case of solutions 1 and 3 – any excess organic  $\text{CH}_3\text{NH}_3\text{Y}$ .

The calculated contributions of the various possible components to the overall weight % of the perovskite are presented in Table 6.5, displaying the weight % of the solid perovskite products and in a 35 wt% solution.

Following this initial mass loss from the solvent vaporization, the solutions containing only

## 6.2. Thermogravimetric Analysis

**Table 6.5.** Calculated weight % contributions of expected components to total mass for the different perovskite mixtures

Component (%)	Perovskite Mixture							
	1		2		3		4	
	1 PbI <sub>2</sub> 3 CH <sub>3</sub> NH <sub>3</sub> Cl Solid	Sol.	1 PbI <sub>2</sub> 1 CH <sub>3</sub> NH <sub>3</sub> I Solid	Sol.	1 PbCl <sub>2</sub> 3 CH <sub>3</sub> NH <sub>3</sub> I Solid	Sol.	1 PbCl <sub>2</sub> 1 CH <sub>3</sub> NH <sub>3</sub> Cl Solid	Sol.
Total material <sup>a</sup>	100	35 <sup>b</sup>	-	-	100	35	-	-
CH <sub>3</sub> NH <sub>3</sub> PbI <sub>3</sub>	-	-	100	35	82.11	28.74	-	-
CH <sub>3</sub> NH <sub>3</sub> PbCl <sub>3</sub>	52.09	18.23	-	-	-	-	100	35
PbI <sub>2</sub>	-	-	74.36	26.03	61.06	21.37	-	-
PbCl <sub>2</sub>	41.91	14.67	-	-	-	-	80.46	28.16
CH <sub>3</sub> NH <sub>3</sub> I	47.91 <sup>c</sup>	16.77 <sup>c</sup>	25.64	8.97	21.06	7.37	-	-
CH <sub>3</sub> NH <sub>3</sub> Cl	10.18	3.56	-	-	17.89 <sup>c</sup>	6.26 <sup>c</sup>	19.53	6.84
CH <sub>3</sub> NH <sub>2</sub>	4.68	1.64	5.01	1.75	4.11	1.44	8.99	3.15
HI	-	-	20.63	7.22	16.94	5.93	-	-
HCl	5.50	1.92	-	-	-	-	10.50	3.69

<sup>a</sup> Total material weight % when excess organic material is formed in addition to the perovskite.

<sup>b</sup> For ease of comparison all solutions were calculated based on a total of 35 wt%.

<sup>c</sup> Excess organic component formed.

one type of halide and a 1 to 1 molar ratio of inorganic to organic component (solutions 2 and 4) undergo two further distinct steps of weight loss.

Solution 2, the pure iodide system, containing 35% by weight, displays a 9–10% weight loss between 300 and 350°C and a 26–30% mass loss between 450 and 550°C. The first step, corresponding to 10% mass lost originates due to the liberation of the organic component of the perovskite material formed (CH<sub>3</sub>NH<sub>3</sub>I), which has been suggested to be in the form of the free amine, CH<sub>3</sub>NH<sub>2</sub>, and HI [171]. The total amount of mass lost in this step corresponds to approximately 25% of the perovskite material mass, which is in good agreement with the calculated amount of the organic component, see Table 6.5. Furthermore the temperature range of this mass loss step corresponds to that determined for the CH<sub>3</sub>NH<sub>3</sub>I precursor in Section 6.2.1 Table 6.1. The remaining material can be deduced to be mainly PbI<sub>2</sub> which undergoes thermal decomposition at 500°C as seen previously, Figure 6.1. Any remaining mass is a metallic residue and/or impurity.

The pure chloride mixture (solution 4) when prepared to contain 0.7 M of the inorganic component, PbCl<sub>2</sub>, correlates to weight % of 17.5%. This solution displayed a mass loss of 3–3.5% between 220 and 300°C, which is in agreement with the calculated mass loss of 6.84% from a 35 wt% solution (Table 6.5) corresponding to the loss of the organic CH<sub>3</sub>NH<sub>3</sub>Cl component. The temperature range of this mass loss step is slightly lower than in the case for solution 2, which corresponds well to the shift in the 100% weight loss step observed between the organic precursors, CH<sub>3</sub>NH<sub>3</sub>Cl at 315°C and CH<sub>3</sub>NH<sub>3</sub>I at 345°C (Table 6.1).

## Chapter 6. Thermal Analysis of Methyl Ammonium Lead-Trihalide Perovskite

---

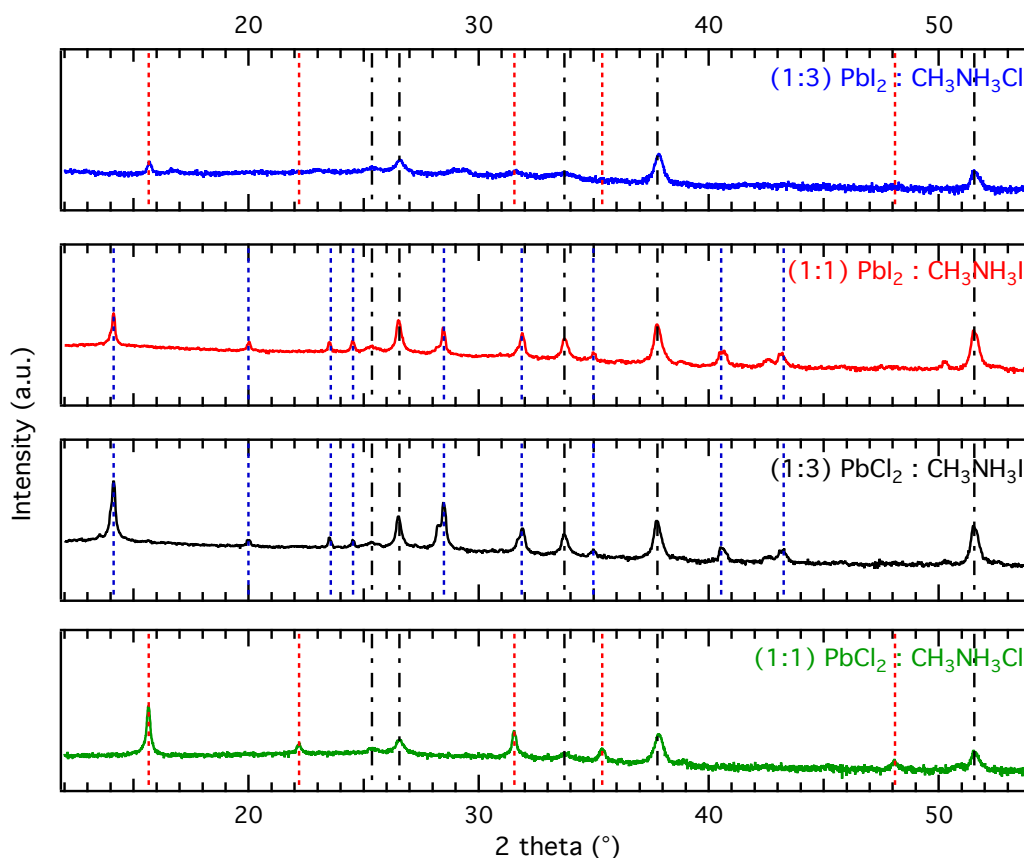
After the liberation of its organic component, solution 4 undergoes a mass loss of 13% between 500 and 650°C, corresponding to the decomposition of the inorganic  $\text{PbCl}_2$  constituent. This mass loss step is shifted by approximately 50–100°C relative to the inorganic decomposition step of the pure iodide system, reflecting the shift observed in the weight loss step of the thermal decomposition of the pure inorganic precursors (cf. Figure 6.1), hence confirming the nature of the inorganic component as  $\text{PbI}_2$  and  $\text{PbCl}_2$  for solutions 2 and 4 respectively. This is further supported by the magnitude of the mass loss step, which is within error of the calculated 28%  $\text{PbCl}_2$  contribution in a 35 wt% solution (Table 6.5).

In the case of the mixed halide systems (solution 1 and 3) the TGA curves become more complicated, in particular regarding the loss of the organic component. The formation of perovskite from the mixed halide precursors results in the additional byproduct of 2 molar equivalents of organic material. Where the pure halide systems undergo a simple, single step for the loss of the organic component, the mixed halide systems show two distinct stages in this weight loss step, which is clearly seen as two minima in the region between 200 and 300°C in the 1st derivative of the TGA curve. As previously mentioned these mixed halide systems lead to the formation of excess organic material which undergoes sublimation as the perovskite material is heated, manifesting as an additional mass loss step in the TGA curve.

Solution 3, a 1 to 3 molar mixture of  $\text{PbCl}_2$  and  $\text{CH}_3\text{NH}_3\text{I}$  at 35 wt% in DME, displays sequential mass losses of approximately 6–7%, 5% and 1–2% between 200 and 400°C. From Table 6.5 it is possible to identify these processes and correlated them with the initial sublimation of the 2 molar equivalents of  $\text{CH}_3\text{NH}_3\text{Cl}$  (6.26% weight loss), followed by the liberation of the organic component of the perovskite in the form of  $\text{HI}$  and  $\text{CH}_3\text{NH}_2$  (5.93 and 1.44% weight loss respectively). This implies that the loss of the organic component of the perovskite follows the initial liberation of  $\text{HI}$  followed subsequently by the  $\text{CH}_3\text{NH}_2$ . Finally the mass loss of 22% between 450 and 550°C matches the decomposition of the inorganic  $\text{PbI}_2$  component.

While similar features are observed for the other mixed halide system (solution 1) the temperature range of the mass loss step corresponding to the inorganic component decomposition is attributed to the decomposition of  $\text{PbI}_2$  and not  $\text{PbCl}_2$ . As a result it is possible to infer that the perovskite formed from this mixture is not the pure  $\text{CH}_3\text{NH}_3\text{PbCl}_3$ , but likely is a mixture of the trichloride perovskite  $\text{CH}_3\text{NH}_3\text{PbCl}_3$ , the triiodide perovskite  $\text{CH}_3\text{NH}_3\text{PbI}_3$  and the  $\text{PbI}_2$  precursor. Additionally the concerned mass loss step corresponds to 20% which is equal to the mass of the  $\text{PbI}_2$  in the solution mixture, consisting of a 29 wt% mixture with 0.7 M of  $\text{PbI}_2$  and 1:3 molar ratio with  $\text{CH}_3\text{NH}_3\text{Cl}$ . The mass loss between 200 and 300°C associated with the loss of the organic component corresponds to 8–9% which coincides with the loss of 3 molar equivalents of  $\text{CH}_3\text{NH}_3\text{Cl}$ . This might suggest that this mixture does not form any type of perovskite and heating the mixture simply dries the precursor components. However the presence of the features in the organic mass loss step imply that the organic component is not lost in a single sublimation step, as would be the case if the materials were simply dried. This indicates that the organic component is somehow incorporated into the material matrix and subsequently stepwise liberated in the form of any excess organic material,  $\text{HCl}$  and  $\text{CH}_3\text{NH}_2$ .





**Figure 6.5.** XRD measurements of perovskite films deposited from mixed precursor solutions; solution 1 – 1:3 molar ratio of  $\text{PbI}_2$  and  $\text{CH}_3\text{NH}_3\text{Cl}$  in DMSO (blue), solution 2 – 1:1 molar ratio of  $\text{PbI}_2$  and  $\text{CH}_3\text{NH}_3\text{I}$  in DMF (red), solution 3 – 1:3 molar ratio of  $\text{PbCl}_2$  and  $\text{CH}_3\text{NH}_3\text{I}$  in DMF (black), solution 4 – 1:1 molar ratio of  $\text{PbCl}_2$  and  $\text{CH}_3\text{NH}_3\text{Cl}$  in DMSO (green). The vertical lines indicate the peaks associated with triiodide perovskite  $\text{CH}_3\text{NH}_3\text{PbI}_3$  (blue), trichloride perovskite  $\text{CH}_3\text{NH}_3\text{PbCl}_3$  (red) and the FTO/ $\text{mTiO}_2$  substrate (dotted black line).

XRD measurements were conducted to confirm the nature of the perovskite formed from the different perovskite precursor solution mixtures and are presented in Figure 6.5. Solutions 2 and 3, corresponding to the 1:1  $\text{PbI}_2$  and  $\text{CH}_3\text{NH}_3\text{I}$  and 1:3  $\text{PbCl}_2$  and  $\text{CH}_3\text{NH}_3\text{I}$  mixtures, are observed to show the peaks associated with the expected triiodide perovskite  $\text{CH}_3\text{NH}_3\text{PbI}_3$ . Solution 4, the pure chloride system (1:1 molar ratio of  $\text{PbCl}_2$  and  $\text{CH}_3\text{NH}_3\text{Cl}$ ) clearly displays the XRD diffraction peaks in good agreement to those reported for the trichloride perovskite  $\text{CH}_3\text{NH}_3\text{PbCl}_3$  [178]. Interestingly in the case of solution 1, the 1:3 mixture of  $\text{PbI}_2$  and  $\text{CH}_3\text{NH}_3\text{Cl}$ , only a small peak at  $15.7^\circ$  is visible. This peak is attributed to the (110) reflection for  $\text{CH}_3\text{NH}_3\text{PbCl}_3$ . Hence from the XRD diffractogram it is apparent that this mixture does lead to the formation of the  $\text{CH}_3\text{NH}_3\text{PbCl}_3$  perovskite, while the TGA measurement suggests the formation of a  $\text{PbI}_2$  component (which is however not detected by XRD). Hence it is possible that some mixed-halide perovskite forms, which is predominantly based on the trichloride

form (as evident from the XRD data), but which undergoes thermal decomposition to  $\text{PbI}_2$  at high temperatures.

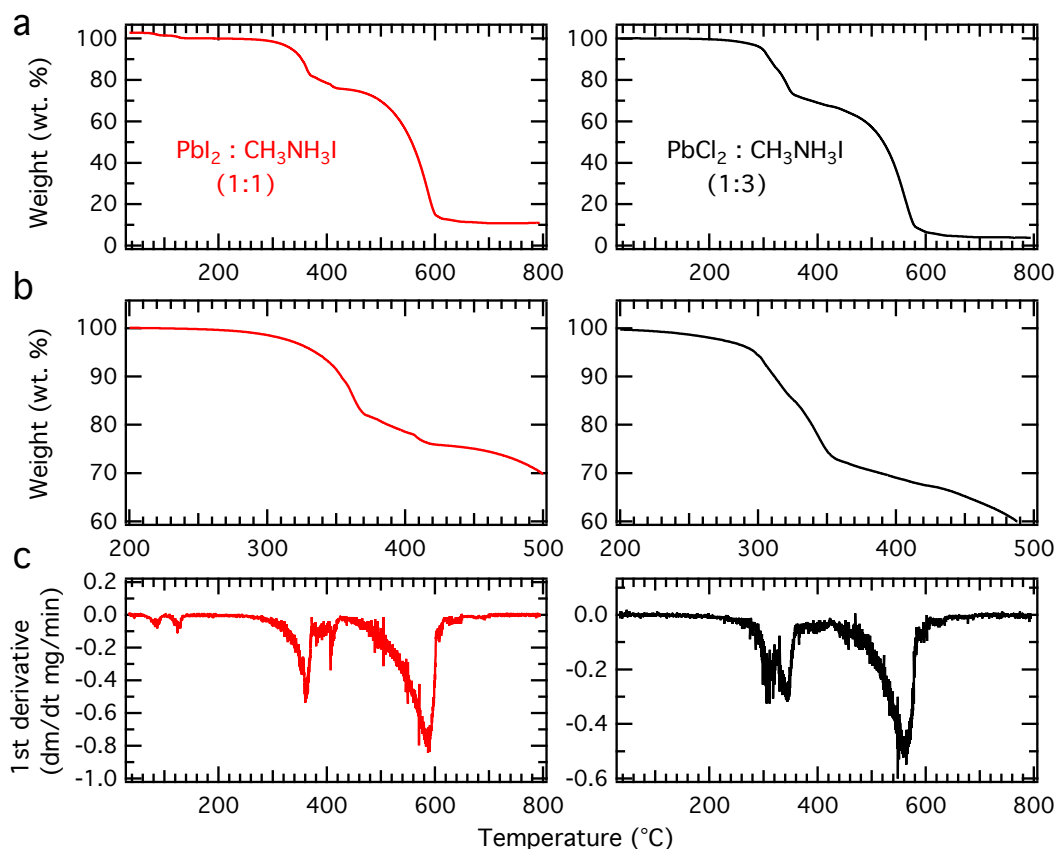
These results clearly portray the liberation of the excess organic material as additional features in the TGA curves of the mixed halide systems (solutions 1 and 3) while the pure halide system display this mass loss in a single step. Furthermore only the pure chloride system (solution 4) leads to the clear formation of the trichloride perovskite  $\text{CH}_3\text{NH}_3\text{PbCl}_3$ , evident in the shift of the inorganic decomposition to higher temperatures. For all other mixtures it is clear that the main inorganic component is  $\text{PbI}_2$  regardless of the initial inorganic precursor used in the perovskite solution. It has been suggested that there may be small non-negligible doping effects from the presence of Cl [178] that may result in the small differences in the onset of the thermal decomposition. This however is outside the scope of this work. Solution 1, the 1:3 mixture of  $\text{PbI}_2$  and  $\text{CH}_3\text{NH}_3\text{Cl}$ , seems to lead to the formation of a mixture of formed perovskite and unreacted precursors.

### 6.2.3 Perovskite Powder

In addition to the TGA analysis of the perovskite material as it forms from solution (either DMF or DMSO), thermal analysis was conducted on perovskite powders. This investigation was carried out only on the perovskite mixtures that lead to the formation of the triiodide perovskite  $\text{CH}_3\text{NH}_3\text{PbI}_3$ , solutions 2 and 3 corresponding to a 1 to 1 molar ratio mixture of  $\text{PbI}_2$  and  $\text{CH}_3\text{NH}_3\text{I}$  and a 1 to 3 molar ratio of  $\text{PbCl}_2$  and  $\text{CH}_3\text{NH}_3\text{I}$  in DMF respectively. The formation of this perovskite was confirmed by the XRD diffractograms presented in Figure 6.5. The perovskite precursor solution was drop cast onto glass substrates and annealed at  $100^\circ\text{C}$  until the as-deposited yellow film changed colour to dark brown. This took approximately 10 minutes for solution 2 (based on  $\text{PbI}_2$ ) and 45 minutes for solution 3 (based on  $\text{PbCl}_2$ ). The perovskite powder was scratched off the substrate and used directly for the thermal analysis.

The direct TGA measurements of the perovskite solution mixtures presented in Section 6.2.2 provided useful information on the thermal behavior of the perovskite products. However it is necessary to compare these results with the perovskite powders to account for any differences that might arise due to the different perovskite formation procedures. The perovskite solution is typically deposited and annealed under dry conditions, hence in the presence of oxygen. However the direct TGA measurements were conducted under an inert atmosphere consisting of a constant  $\text{N}_2$  gas flow. The TGA curves of the  $\text{CH}_3\text{NH}_3\text{PbI}_3$  perovskite formed from the two perovskite mixtures are presented in Figure 6.6.

The first major difference in the direct TGA measurement of the perovskite solution mixtures and the powder is the absence of the 60% mass loss corresponding to the vaporization of the solvent. Two small mass losses take place for the solution-based on the  $\text{PbI}_2$  precursor at  $85^\circ\text{C}$  and  $125^\circ\text{C}$ , clearly visible as two small minima in the 1st derivative, which were previously hidden under the large change in mass arising from the removal of solvent. These are most likely due to the removal of absorbed  $\text{H}_2\text{O}$  from the perovskite material as has been previously



**Figure 6.6.** (a) TGA heating curves, (b) magnification of region for organic mass loss and corresponding (c) 1st derivatives for the perovskite powders heated at  $10^\circ\text{C min}^{-1}$  under a constant gas flow of  $\text{N}_2$  ( $20 \text{ ml min}^{-1}$ ) from 30 to  $800^\circ\text{C}$ ; 1:1 molar ratio of  $\text{PbI}_2$  and  $\text{CH}_3\text{NH}_3\text{I}$  in DMF (red), 1:3 molar ratio of  $\text{PbCl}_2$  and  $\text{CH}_3\text{NH}_3\text{I}$  in DMF (black).

reported [187].

The mass loss step between  $550$  and  $600^\circ\text{C}$  for both solutions is in good agreement with the thermal decomposition of the inorganic  $\text{PbI}_2$  proportion of the perovskite formed. As was the case for the TGA curves of the perovskite solutions, the differences between the samples are mostly in the liberation of the organic material. For the sample prepared from  $\text{PbI}_2$  (solution 2), the material undergoes 20% mass loss followed by approximately 5–6% mass loss. This is in excellent agreement with the calculated (Table 6.5) consecutive loss of the HI species followed by the  $\text{CH}_3\text{NH}_2$  component. In the case of the direct TGA measurement of the corresponding perovskite solution it was not possible to differentiate these two mass losses, appearing as a single mass loss step. The mass loss step corresponding to the  $\text{CH}_3\text{NH}_2$  component is not as clearly defined, resulting in a broader feature in the 1st derivative. This suggests that this species is not as readily lost as the HI and more tightly bound into the perovskite matrix, likely by hydrogen bonding.

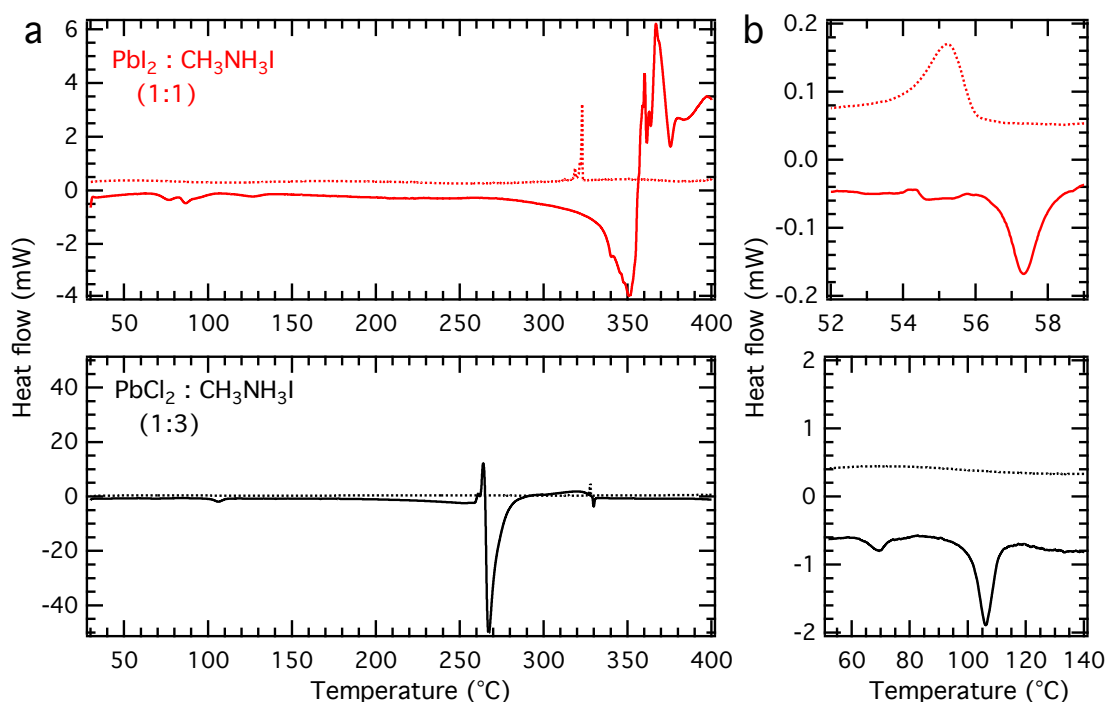
For the perovskite using the  $\text{PbCl}_2$  precursor (solution 3) apart from the absence of the loss of solvent, the TGA curve is very similar to that determined from the direct measurement of the solution mixture. The loss of the organic material occurs in three stages between 250 and 400°C, with mass losses of 16, 12 and 5%, which is in relatively good agreement of the loss of the excess 2 molar equivalents of  $\text{CH}_3\text{NH}_3\text{Cl}$  formed, followed by the loss of HI and  $\text{CH}_3\text{NH}_2$ . This suggests that the excess  $\text{CH}_3\text{NH}_3\text{Cl}$  formed remains incorporated in the perovskite matrix even after heating the sample at 100°C for 45 minutes. This was confirmed by isothermal heating of the material at 125°C for 60 minutes which exhibited only approximately 2% mass loss. Similar to solution 2, the final mass loss of 5% attributed to the loss of the amine constituent is apparent as a slope in the TGA curve between 350 and 400°C rather than an abrupt mass loss step further confirming the theory that this species is more firmly fixed in the perovskite matrix than the HI component.

### 6.3 Differential Scanning Calorimetry

Differential Scanning Calorimetry is a technique often used complementary to TGA. Unlike TGA where characteristics of a material are determined as a function increasing temperature due to the associated mass loss, DSC measures the difference in the heat flow necessary to increase the temperature of the sample and a reference as a function of temperature. Hence while TGA provides information about the materials' decomposition/degradation pathways, oxidation, combustion and thermal stability or loss of volatiles, DSC is more sensitive to any phase transitions taking place, resulting in a difference in the amount of heat flow between the sample and reference, indicating an endothermic or exothermic process.

The DSC thermograms of the  $\text{CH}_3\text{NH}_3\text{PbI}_3$  perovskite powder prepared from solution 2 (1:1 molar ratio mixture of  $\text{PbI}_2$  and  $\text{CH}_3\text{NH}_3\text{I}$ ) and from solution 3 (1:3 molar ratio mixture of  $\text{PbCl}_2$  and  $\text{CH}_3\text{NH}_3\text{I}$ ) as described previously are displayed in Figure 6.7. The heating (solid line) and cooling (dashed line) thermograms were recorded consecutively by heating the sample from 30 to 200°C and cooling down again two times. The same features at low temperature were reproduced during the second heating/cooling cycle. Additional measurements were made to examine the behavior at higher temperatures by conducting a thermogram from 30 and 400°C and cooling down. In this case the second heating/cooling cycle did not reproduce the same thermal features due to the associated sublimation and decomposition of the organic component of the perovskite when it was heated to 400°C in the first cycle.

The heating curve of the perovskite-based on the  $\text{PbI}_2$  precursor shows a large endothermic feature that begins at 300°C and has a peak at 350°C. This process corresponds to the liberation of the organic component of the perovskite. The broadness of this feature indicates that this process is not straightforward and has multiple stages, pointing to the separate loss of the HI and the  $\text{CH}_3\text{NH}_2$  species. Additionally there are endothermic features between 65 and 100°C and at 125°C which are believed to correspond to the loss of absorbed  $\text{H}_2\text{O}$  and/or excess solvent still present in the material. This is further validated by the absence of these



**Figure 6.7.** (a) DSC heating (solid trace) and cooling (dashed trace) curves, (b) magnification of low temperature features, for the perovskite powders heated at  $10^\circ\text{C min}^{-1}$  from 30 to  $400^\circ\text{C}$ ; 1:1 molar ratio of  $\text{PbI}_2$  and  $\text{CH}_3\text{NH}_3\text{I}$  in DMF (red), 1:3 molar ratio of  $\text{PbCl}_2$  and  $\text{CH}_3\text{NH}_3\text{I}$  in DMF (black). The DSC scans have been corrected to account for the baseline drift.

peaks in the second cycle as any absorbed  $\text{H}_2\text{O}$  and/or solvent will have been removed from the material in the first cycle. The tetragonal to cubic phase transition of this perovskite has been reported to occur between  $54\text{--}57^\circ\text{C}$  [187] and similarly observed in DSC measurements. In Figure 6.7 (b) the DSC thermogram for the region of this transition is shown for the two perovskite powders. In the case of the  $\text{PbI}_2$ -based perovskite the thermograms shows peaks at  $57.3^\circ\text{C}$  and  $55.2^\circ\text{C}$  for the heating and cooling cycles respectively and reproduced in the second cycle. These are in very good agreement for the reported tetragonal to cubic phase transition of  $\text{CH}_3\text{NH}_3\text{PbI}_3$  [187]. The asymmetry of the DSC peaks has been suggested to indicate the presence of a transient intermediate phase but remains relatively unclear [187].

Considering the case for the  $\text{PbCl}_2$  precursor-based perovskite powder (from solution 3), the DSC thermogram shows significant differences. In contrast to the  $\text{PbI}_2$  case, no features for the tetragonal to cubic phase transition are distinguishable in the temperature range between  $55$  and  $58^\circ\text{C}$  for the perovskite formed from  $\text{PbCl}_2$  within the limit of the experiment. This insinuates that subtle structural differences exist between the perovskite materials formed depending on the precursor solution used, culminating in the differences in the crystal phase while the general crystal structure and perovskite composition is the same.

However the heating curve shows two peaks at  $68.8$  and  $106.1^\circ\text{C}$ , see Figure 6.7. The lack of these features in subsequent second cycles indicates that they arise most likely from the

removal of excess solvent or absorbed H<sub>2</sub>O from the perovskite powder. The transition at 106°C has been attributed to the melting of the amorphous phase (CH<sub>3</sub>NH<sub>3</sub>)<sub>5</sub>PbCl<sub>4</sub>I<sub>3</sub> resulting from excess CH<sub>3</sub>NH<sub>3</sub>Cl [202]. Its loss at higher temperatures results in the disappearance of this feature in the second heating cycle. This process can be related to the different perovskite film morphologies observed when CH<sub>3</sub>NH<sub>3</sub>Cl is present [203].

The onset of the high temperature endothermic peak in the heating curve begins at approximately 190°C before there is a sudden competitive exothermic process at 250°C, resulting in a positive peak in the DSC thermogram. This suggests that the endothermic process of sublimation of the organic species is in competition with some exothermic process. This exothermic process is believed to be associated with the removal of the excess 2 molar equivalents of CH<sub>3</sub>NH<sub>3</sub>Cl from the perovskite crystal structure as this feature is not present for the PbI<sub>2</sub> precursor-based perovskite powder. This removal may result in an energetically favourable rearrangement of the perovskite crystal lattice. This is followed by an intense endothermic peak at 267.2°C caused by the complete loss of all organic components.

Interestingly the cooling curve from 400°C is almost identical for the two samples, regardless of the inorganic precursor used, displaying a similar sharp peak between 323 and 327°C. As previously stated, following the heating step to 400°C, the organic component of the perovskite has been liberated, leaving behind only the inorganic PbI<sub>2</sub>. This is confirmed by the similar behavior of the cooling curve for the two samples. In both cases, once the organic material has been removed, what remains is PbI<sub>2</sub>, which appears to undergo some phase transition at these elevated temperatures. This is most likely due to the change in the crystalline structure of the PbI<sub>2</sub>, the most common consisting of the *2H*, *4H* and *12R* polytypes. It is known that the *12R* PbI<sub>2</sub> polytype structure is stable at high temperatures (reportedly from approximately 420 K (147°C) to the boiling point of PbI<sub>2</sub>, approximately 675 K (402°C) [204]), whilst the *2H* PbI<sub>2</sub> polytype is stable for crystals formed at room temperature [204–208]. Hence the observed peak in the cooling thermogram of the perovskite is probably due to the reversible transition from the *12R* to *2H* polytype.

## 6.4 Conclusions

In this chapter the thermal behavior of the perovskite material was explored using TGA and DSC measurements. The thermal properties of the individual organic, CH<sub>3</sub>NH<sub>3</sub>I and CH<sub>3</sub>NH<sub>3</sub>Cl, and inorganic components, PbI<sub>2</sub> and PbCl<sub>2</sub>, was used to gain knowledge of possible sublimation and/or decomposition mechanisms. Furthermore the sublimation of the organic component was studied in depth as this process plays a critical role in the formation of the perovskite film during the heat treatment of the deposited perovskite solution. These results were used to correctly interpret the TGA curves of perovskite material formed directly from solution using different mixtures of precursors in solution.

The perovskite material of interest, CH<sub>3</sub>NH<sub>3</sub>PbX<sub>3</sub> (where X = I or Cl) was formed by mixing different molar ratios of the precursors PbX<sub>2</sub> and CH<sub>3</sub>NH<sub>3</sub>X using DMF or DMSO as solvent.

It was found that only the pure chloride system (1:1 molar ratio of  $\text{PbCl}_2$  and  $\text{CH}_3\text{NH}_3\text{Cl}$ ) led to the complete formation of the trichloride perovskite  $\text{CH}_3\text{NH}_3\text{PbCl}_3$ , as confirmed by the shift of the TGA mass loss step corresponding to the decomposition of the inorganic species and by XRD. The sublimation of the excess organic product formed was observed as a separated process in the TGA curves and further confirmed in DSC measurements. The organic component of the perovskite decomposes by the subsequent loss of HI and  $\text{CH}_3\text{NH}_2$  where the latter species is more tightly incorporated into the perovskite matrix. The phase transition from tetragonal to cubic structure was observed only for the  $\text{PbI}_2$  precursor-based perovskite. The structural transition of  $\text{PbI}_2$  from the  $12R$  to the  $2H$  polytype when cooling down from high temperature were observed from the DSC thermograms.

### 6.4.1 Perspectives

In this chapter I examined the thermal properties and deduced the underlying principles driving the formation of the perovskite material from solution-based precursor mixtures. Subtle differences in the conversion process of the material were revealed and it is highly likely that these will influence the photovoltaic performance of the material in solid-state mesoscopic solar cells. The indicated flexibility in the recipe to form desired triiodide perovskite endorses us to fine tune the crystallization procession by mixing proper ratios of organic to inorganic compounds. Furthermore it provides insight into the thermal behavior and stability of the material, a useful parameter that needs to be considered for its application in solar cells.

Further research should be conducted to unravel the difference in crystal structure and phase of the perovskite material depending on the treatments and formation techniques employed. *In situ* variable temperature X-ray diffraction measurements would provide valuable information about the temperature dependence of the crystal structure. In addition to exposing the phase transitions of the material this technique could be used to monitor the formation process of the perovskite in a similar fashion to the TGA experiments presented herein.





## 7 General Conclusions and Summary

The main focus of the studies conducted within the framework of this thesis aimed to achieve a more fundamental understanding of the device mechanisms of solid-state mesoscopic solar cells. The operating processes of these devices are greatly dependent on the individual component properties and the interplay between them, requiring systematic analysis to gain insight into the inherent complexity of the system. As evident from the work presented here, it is necessary to consider the system as a whole unit, where specific factors and parameters effect the photovoltaic performance differently depending on the device configuration and composition.

The key component of dye-sensitized solar cells is the light harvesting unit, thus it is unsurprising that this is the area that has been most extensively developed. It is this feature that encompasses the uniqueness of the DSSC, allowing the color and transparency of the solar cell to be tuned by the implementation of different types of sensitizers. This has a clear relation with the light harvesting ability of the device, however to achieve good photovoltaic performance the interface between the sensitized metal oxide semiconductor and the hole mediator (either liquid electrolyte or solid-state hole-transport material) is critical. In this thesis, particular emphasis is placed upon the examination of this interface and the associated interaction with the solid-state HTM spiro-MeOTAD.

To improve the understanding of the device mechanisms and contribute to the development of highly efficient and stable photovoltaic devices impedance spectroscopy is used extensively. This technique is used to examine the internal electrical processes and the relevant interfaces within the devices under operating conditions. Additionally diverse characterization techniques are used to analyze key optical and structural parameters that are instrumental to the photovoltaic performance of solid-state mesoscopic solar cells.

- **Chapter 2** presents a comprehensive investigation using impedance spectroscopy of the charge-transport and transfer mechanisms in solid-state DSSCs employing spiro-MeOTAD as HTM. In contrast to the multitude of sensitizers that have led to steadily increasing *PCEs*, spiro-MeOTAD is still the main material of choice for solid-state meso-

scopic solar cells since it was first reported as a HTM more than 15 years ago. However the operating processes of this system were still poorly understood, in part because characterization techniques were optimized and targeted for the traditional counterpart using a liquid electrolyte. The differences in the electronic processes occurring in ssDSSCs and their associated timescales require measurement procedures to be reevaluated and adapted.

In this chapter I investigated the electronic processes and interfacial contribution of ssDSSCs type devices using IS. To simplify the complexity of the system, no light harvesting sensitizer was employed. Different device configurations are employed to differentiate between the transport process within the individual components making up the ssDSSC. Consequently the transport properties of spiro-MeOTAD as a HTM were examined and the contribution to the IS response was isolated. From these observations a model was developed to interpret the impedance frequency response. Using the established model the influence of temperature on the IS parameters was exposed. Subsequent analysis using the Arrhenius equation determined the activation energy of hole-hopping transport in undoped spiro-MeOTAD. This value was found to be in good agreement with similar organic amorphous materials in literature validating the proposed procedure and IS equivalent model.

Undoped, pristine spiro-MeOTAD has low conductivity. To achieve high *PCEs* in solar cells the conductivity of the HTM is increased by various doping methods. Here the procedure of chemically *p*-doping spiro-MeOTAD through the addition of a chemical *p*-type Co(III) complex dopant is compared with the commonly employed method of photodoping, taking place under exposure to atmospheric oxygen and light. From IS analysis it was determined that both doping procedures increase the conductivity of the spiro-MeOTAD, observed in a decrease in its transport resistance. The IS analysis revealed subtle differences in the effect of the different doping methods. In addition to decreasing the charge-transport resistance of the HTM, the process of photodoping was observed to improved the ohmic contact between the HTM and back contact.

Using the developed model, the internal electrical processes within ssDSSCs in working conditions can be probed and explored. As has been demonstrated in this chapter this approach provides valuable insight into the device mechanics which can be adopted in the quest to achieve high performance photovoltaic devices. While future work should involve the development on device fabrication methods that eliminate the need for oxygen, it is apparent that the role of oxygen is complex and multifold.

- **Chapter 3** presents the use of different series of organic molecular sensitizers as light harvesting species in ssDSSCs. The individual properties of the dye molecules were evaluated, attributed to their molecular structure and correlated with their photovoltaic performance in ssDSSCs using spiro-MeOTAD. Focus was placed on the interface between the sensitized mTiO<sub>2</sub> surface and the HTM. Optical measurements exposed the beneficial de-aggregating properties of spiro-MeOTAD when employing a highly

---

aggregating near-infrared squaraine sensitizer.

IS and transient photovoltage decay measurements were used to systematically examine the influence of the molecular sensitizers on the recombination and transport processes within the working devices. This method exposed the influence of dye surface coverage and dipole moment on the position of the mTiO<sub>2</sub> conduction band and thus on the  $V_{OC}$ . These observations were confirmed by various other characterization methods. Furthermore the importance of efficient charge separation to achieve good photovoltaic performance and its relation to the molecular structure for a series of ullazine based sensitizers was exposed using photoinduced absorption measurements and IS.

In this chapter I presented thorough studies of ssDSSCs using different molecular sensitizers, demonstrating the importance of systematic analysis of the systems to determine the factors affecting the photovoltaic performance and correlate them to the molecular structure. This highlights the need for the careful and targeted design of sensitizers to fulfill the necessary requirements to achieve high *PCE* and long-term stability. Crucially the nature of the mesoscopic solar cells requires the system in its entirety to be considered, as has been demonstrated here, examining the interfaces and interplay between the elements.

- **Chapter 4** introduces the use of the hybrid organic-inorganic lead-iodide based perovskite material CH<sub>3</sub>NH<sub>3</sub>PbI<sub>3</sub> instead of a molecular dye as light harvesting material in solid-state mesoscopic solar cells using spiro-MeOTAD. Despite the record breaking *PCEs* achieved with this relatively recent approach, the fundamental operating mechanisms of these type of devices remain unclear. In this chapter I investigate the IS response of these type of devices. Unique features associated to the ionic and electronic transport properties of the perovskite material are identified and analyzed, exposing the contribution to the transport processes within the solar cell. Using a similar approach as in **Chapter 2** an equivalent circuit model is developed and consequently tested and validated. The effect of varying common parameters such as the additive concentration in the HTM solution and the HTM overlayer thickness on top of the mTiO<sub>2</sub> on the extracted IS parameters was investigated. The results from these systematic studies were used in our laboratory to optimize the device performance and achieve high *PCEs*.

This study developed a valuable tool that can be used in the characterization of these type of systems, thus improving the understanding of their basic functioning. It was additionally found that the IS response attributed to the perovskite is greatly dependent on the nature and composition of the perovskite film. Hence this method can also be used to probe the perovskite material within devices under working conditions.

- **Chapter 5** follows on from **Chapter 4** where the role of the perovskite morphology on the device photovoltaic performance is investigated. The film morphology and nature was found to be dependent on the deposition procedure and subsequent treatments. In this chapter I examined the influence of specific factors and parameters on the

formation of the perovskite film. The solvent properties are crucial in the deposition step; determining the wetting and infiltration of the  $\text{mTiO}_2$  by the precursor solution and the rate of solvent evaporation and hence perovskite growth.

I present an in-depth investigation of the effect of the annealing temperature used to treat the as-deposited perovskite precursor solution and drive the conversion process. The film morphology of the perovskite formed is determined by the temperature at which it is annealed as revealed by the results obtained by scanning electron microscopy. From optical and X-ray diffraction measurements it was found that the conversion of the perovskite is temperature dependent and that the additional formation of  $\text{PbI}_2$  occurs at high temperatures. This detrimental formation of  $\text{PbI}_2$  results in a misalignment of the energy levels, preventing the injection from and into the  $\text{mTiO}_2$  and thus the consequent buildup of charges. This is revealed by IS measurement as a deviation from the typical exponential increase in the extracted chemical capacitance. The same trends were observed when the proportion of  $\text{PbI}_2$  in the precursor solution was increased.

Future work needs to further investigate the multitude of parameters influencing the formation of the perovskite film and thus contributing to its morphology, composition and crystallinity. To further improve upon the already excellent photovoltaic performances, the nature of the perovskite film can still be further optimized. Particularly in order to achieve better reproducibility of results, the formation process needs to be better understood and controlled.

- **Chapter 6** builds on the concept of the formation of the perovskite material from a precursor solution containing a mixture of the organic and inorganic components presented in **Chapter 5**. The thermal properties of the individual components are investigated, identifying the contributions to the thermal behavior of the perovskite material. The approach presented in this chapter permits the formation mechanism of the perovskite material to be monitored. When mixed halide solutions are employed where the organic and inorganic components contain different halide atoms, an excess of organic material is formed as is revealed by thermogravimetric analysis.

Differential scanning calorimetry measurements reveal phase transitions of the crystal structure that the  $\text{CH}_3\text{NH}_3\text{PbI}_3$  perovskite undergoes at specific temperatures. Small differences are observed for the perovskite material formed from different precursor solutions. It is conceivable that such subtle differences in crystal structure and/or phase affect the transport properties of the material and thus the resultant photovoltaic performance. Hence this study conveys the need to conduct systematic material characterization for the perovskite material to elucidate the origins for variations in device operating processes.

The field of solid-state mesoscopic solar cells using spiro-MeOTAD as HTM has witnessed incredible development in recent years, leading to record breaking efficiencies. While excellent *PCEs* have been achieved, the rapid and continual evolution is an indication that this

---

technology still has room for improvement. With each new discovery, new questions arise concerning the functioning of this system opening new avenues for research.

As is evident from the scope of this thesis, the main area of development is the light harvesting unit of the device. While this unit is the key element of this system, to achieve good photovoltaic performance, the HTM and its interaction with the sensitized metal oxide semiconductor is of crucial importance. The strategies I have presented focus on understanding the interfacial properties within the device, essential to understanding its operating mechanisms. I believe that the IS models and characterization procedures presented herein are valuable tools in gaining knowledge of the internal electrical workings and interfaces within these devices. The complexity of this system supplies it with a richness and seemingly endless potential for further research and development. I hope that our work contributes in the advancement and improvement of high performance solar cells with the aim to generate clean, renewable and low-cost energy to meet the world's future needs.



# 8 Experimental Methods

## 8.1 Materials and Synthesis

All chemicals were purchased from Sigma-Aldrich and used as received. The hole-transport material, 2,2',7,7'-tetrakis(*N,N*-di-*para*-methoxyphenylamine)-9,9'-spirobifluorene (spiro-MeOTAD), was purchased from Merck KGaA and used as received. The CH<sub>3</sub>NH<sub>3</sub>I precursor used in the fabrication of perovskite-based solar cells was synthesized in our laboratory as reported [49]. The molecular sensitizers were synthesized according to reported procedures.

## 8.2 Characterization Methods

### 8.2.1 Optical Spectroscopy

#### UV-vis Absorption

The steady-state UV-vis absorption spectra were recorded using a Varian Cary 5 spectrophotometer in transmission mode. A 10 mm path length quartz cell was used to measure the spectra of dye solutions. The dye solvent was typically used as a blank reference. The absorption spectra of sensitized TiO<sub>2</sub> films was recorded using mTiO<sub>2</sub> films deposited on microscopic glass slides. Blank TiO<sub>2</sub> was used as a reference.

#### Dye Loading

Dye loading was determined using optical measurements. Sensitized TiO<sub>2</sub> were immersed in a known volume of tetrabutylammonium hydroxide (TBAOH) in a respective solvent at a known concentration to desorb the dye molecules. The UV-vis spectrum of the resulting dye solution was measured. The Beer-Lambert law (Equation 8.1) relates the absorbance  $A$  of the solution with its concentration  $c$ ;

$$A = \epsilon \times c \times l \quad (8.1)$$

where  $\epsilon$  – the molar extinction coefficient,  $c$  – concentration of the absorbing species and  $l$  – the optical path length. From this the number of dye molecules can be calculated. With the additional knowledge of the TiO<sub>2</sub> film thickness, area, pore size and porosity, the concentration of dye molecules on the surface of the mTiO<sub>2</sub> – its surface coverage – can be estimated as follows. The TiO<sub>2</sub> particles are treated as uniform spheres that are connected without overlap. The effective surface area is calculated by determining the number of TiO<sub>2</sub> particles that occupy the mTiO<sub>2</sub> layer and – assuming that no area is lost at the points of connection between the individual TiO<sub>2</sub> particles – multiplying by the area of a perfect sphere with a diameter corresponding to the particle size of the TiO<sub>2</sub>. With the knowledge of the number of desorbed dye molecules previously calculated the corresponding surface coverage can be determined.

### Emission Spectroscopy

The emission spectra were recorded on a Horiba Jobin Yvon Fluorolog spectrofluorometer using a 450 W xenon arc lamp, double-grating excitation and emission monochromators. Time-correlated single photon counting experiments were conducted using an emission photomultiplier in front-face mode allowing photon-counting detection. A pulsed laser diode provided the excitation beam at 406 nm using a 515 nm filter to eliminate scatter from the laser. For sensitized TiO<sub>2</sub> films a 460 nm laser was used to prevent the direct excitation of the TiO<sub>2</sub>.

### 8.2.2 X-ray Diffraction

Samples were deposited on glass or FTO substrates (as specified). X-ray powder diagrams were recorded on a X'Pert MPD PRO (Panalytical) operated in BRAGG-BRENTANO geometry, using a RTMS X'Celerator detector, a ceramic tube (Cu anode,  $\lambda = 1.54060 \text{ \AA}$ ) and a secondary graphite (002) monochromator. No further modification was made to mount to the samples and adjustments were made to the automatic divergence slit and the beam mask to account for the dimensions of the sample films. An acquisition time of 7.5 min deg<sup>-1</sup> was employed with a step size of 0.008°.

### 8.2.3 Fourier Transformed Infrared Spectroscopy

Attenuated total reflection FTIR (ATR-FTIR) was used to examine the adsorption mode of the sensitizers on the TiO<sub>2</sub> surface. A FTS 7000 FTIR spectrophotometer (Digilab, USA) employing a diamond anvil ('golden gate') was used to conduct the measurements. The samples were placed in intimate contact with the anvil throughout the duration of the measurement and the spectra were generated from 64 individual scans at a resolution of 2 cm<sup>-1</sup>. The data was processed through the subtraction of the spectra corresponding to TiO<sub>2</sub>, carbon dioxide and surface water molecules. No ATR corrections were made.



### 8.2.4 Photoinduced Absorbance

The photoinduced absorbance spectra of samples were recorded across a wavelength range from 500 to 1600 nm following excitation by a photomodulated 9 Hz square wave generated by a blue LED. The illumination probe source was provided by a halogen lamp. After passing through the sample the beam is refocused through the slits of a double monochromator (Gemini-180, Jobin Yvon Ltd., UK) coupled to a diode (dual color solid-state detector – Si/In-GaAs) for detection. Data acquisition was made by a dual phase lock-in amplifier (SR 830, Stanford Research System, USA) locked at the light modulation frequency, recording the measured signal as the change in transmission as a function of the wavelength ( $\Delta T/T(\lambda)$ ). Samples were prepared using TiO<sub>2</sub> deposited on microscopic glass as substrates.

### 8.2.5 Thermal Analysis

Thermogravimetric analysis (TGA) was performed using a TGA 4000 (Perkin Elmer), heating at steady constant rates as specified (typically between 2.5 and 10°C min<sup>-1</sup>) under a constant 20 ml min<sup>-1</sup> N<sub>2</sub> gas flow. The investigated temperature intervals were between a minimum of 30°C to a maximum of 800°C. Ceramic crucibles and approximately 5–15 mg of sample material were employed for each measurement.

Differential scanning calorimetry (DSC) measurements were conducted using a DSC8000 (Perkin Elmer) calorimeter at a rate of 10°C min<sup>-1</sup> from 30 to 400°C under N<sub>2</sub>. Approximately 2–5 mg of sample powder was used in each experiment using aluminium pans and lids.

The data was recorded and analyzed using Pyris – Instrument Managing Software (Perkin Elmer).

## 8.3 Crystal Structure

The 3D representation of the perovskite crystal structure in Chapter 4 was produced using VESTA Version 3 ©2006 – 2014 Koichi Momma and Fujio Izumi.

## 8.4 Solar Cell Fabrication

### 8.4.1 Solid-State Dye-Sensitized Solar Cells

Fluorine-doped tin-oxide (FTO) glass substrates (TEC 15, Pilkington) were etched using hydrochloric acid and zinc powder to achieve the correct electrode configuration prior to cleaning by ultrasonication in water and ozone treatment. A compact TiO<sub>2</sub> layer (approximately 30–50 nm) by spray pyrolysis was deposited using titanium diisopropoxide bis(acetylacetonate) (TAA) solution in ethanol (EtOH) at a 1:10 volume ratio as a precursor and oxygen as a carrier gas at 450°C. Before and after preparation of mesoporous TiO<sub>2</sub> layers of 2.0–2.2 μm by

Table 8.1. Dye solution specifications

Dye Series	Solvent Composition	Concentration (mM)	Additive (mM)	Sensitization time (minutes)
Squaraine <sup>a</sup>	EtOH	0.05	CDCA 20	60
D- $\pi$ -A <sup>b</sup>	<i>t</i> -BuOH/MeCN <sup>c</sup> 1:1 v/v	0.1	-	60
Ullazine	THF/EtOH <sup>d</sup> 1:4 v/v	0.1	-	60

<sup>a</sup> JD10/YR6<sup>b</sup> C218/C220/JK2/Y123<sup>c</sup> *tert*-butanol/acetonitrile<sup>d</sup> tetrahydrofuran/ethanol

screen-printing, the substrates were treated with 20 mM titanium tetrachloride (TiCl<sub>4</sub>) solution at 70°C for 30 minutes and sintered for 30 minutes at 500°C. The dye solutions used to sensitize the mTiO<sub>2</sub> films were prepared according to the specifications given in Table 8.1. The hole-transport material was prepared by dissolving spiro-MeOTAD in chlorobenzene to give a 0.15 M solution. The cobalt(III) complex, tris(2-(1H-pyrazol-1-yl)-4-*tert*-butylpyridine)-cobalt(III)-tris(bis(trifluoro-methylsulfonyl)-imide) coded FK209<sup>1</sup> was added to the HTM solution as a *p*-type dopant to give 1.5% doping of spiro-MeOTAD. Furthermore 0.12 M 4-*tert*-butylpyridine (TBP) and 0.2 M lithium bis(trifluoromethylsulfonyl)imide (LiTFSI) were added to the HTM solution. Both the cobalt(III) complex FK209 and the LiTFSI salt were predissolved in acetonitrile (MeCN). 40  $\mu$ l of this solution was deposited onto the sensitized TiO<sub>2</sub> films and allowed to infiltrate for 30 seconds prior to spin-coating for 30 seconds at 2000 rpm. Finally 200 nm thick silver counter electrodes were thermally evaporated onto the films completing the cell fabrication. The devices were fabricated and sealed under red light and controlled dry conditions with less than 5% humidity levels. The encapsulation of the devices was achieved using a 25  $\mu$ m thick hot-melting polymer spacer (Surlyn, DuPont) and a microscope coverslip.

#### 8.4.2 Perovskite Based Solid-State Mesoscopic Solar Cells

FTO glass substrates were patterned by laser etching to give the desired electrode configuration. After undergoing thorough cleaning by mechanical scrubbing using Hellmanex, ultra-sonication and finally ozone cleaning, a TiO<sub>2</sub> compact layer was deposited on the substrates by spray pyrolysis at 450°C using the TAA precursor diluted in ethanol (1:20 volume ratio) and oxygen as the carrier gas. The substrates were subsequently immersed in a 0.02 M aqueous solution of TiCl<sub>4</sub> for 30 minutes at 70°C, after which they were rinsed with water and heated at 500°C for 20 minutes. The submicron mesoporous TiO<sub>2</sub> layer was deposited by spin-coating TiO<sub>2</sub> paste (Dyesol 18NR-T) diluted in ethanol at 1:2.5 by weight at 2000 rpm. The

<sup>1</sup> cf. Appendix Figure A.2 for molecular structure.

films were heated step-wise to 500°C at which they were sintered for 15 minutes. While still hot, the substrates were transferred into a dry box. All subsequent deposition steps were carried out under dry conditions. The perovskite precursor solution was prepared and deposited as described in the text. Precursor solutions were prepared at 30 wt% and dissolved by heating at 60°C overnight. In Chapter 4 the HTM solution was prepared by dissolving 0.059 M spiro-MeOTAD in chlorobenzene, to which 1% molar ratio of cobalt(III) dopant FK209, 0.05 M TBP and 0.009 M LiTFSI were added. In Chapter 5 the HTM solution was prepared by dissolving 0.05 M spiro-MeOTAD in chlorobenzene, to which 5% molar ratio of cobalt(III) dopant FK209, 0.2 M TBP and 0.03 M LiTFSI were added. The HTM solution was deposited on the perovskite sensitized films by spin-coating at 4000 rpm for 30 seconds unless specified otherwise. The devices were completed by thermal evaporation of 60 nm of Au counter electrode. Cells were not sealed, but stored in the dark under dry conditions and measured in normal ambient atmosphere.

## 8.5 Solar Cell Characterization

### 8.5.1 Photovoltaic Characterization

The current-voltage characteristics were determined using a digital source meter (Keithley Model 2400) to apply an external potential bias to the solar cells and measuring the generated photocurrent. The emission spectrum from a 450 W xenon lamp (Oriel) was matched to the standard AM1.5G using a Schott K113 Tempax sunlight filter (Prazisions Glas & Optik GmbH). The exact light intensities of the measurements were determined using a calibrated Si diode as reference. The *IPCE* spectra were recorded as a function of the wavelength using a Model SR830 DSP lock-in amplifier (Stanford Research Systems). The excitation beam was provided by a 300 W xenon lamp (ILC technology), focused through a Gemini-180 double monochromator (Jobin Yvon Ltd.) and chopped at approximately 2 Hz.

### 8.5.2 Impedance Spectroscopy

The impedance measurements were performed using a Bio-Logic SP300 potentiostat. A DC potential bias was applied and overlaid by a sinusoidal AC potential perturbation of 15 mV over a frequency range of 7 MHz to 0.1 Hz (for the measurements under illumination the lowest frequency is 0.01 Hz). The applied DC potential bias was changed by approximately 50 mV steps from 850 mV to 0 mV. Measurements were conducted in the dark and under illumination using an LED light source. The resulting impedance spectra were fitted using the ZView software (Scribner Associates Inc.)

### 8.5.3 Transient Photocurrent and Photovoltage Measurements

The transient photovoltage and photocurrent measurement setup is similar to the description by O'Regan *et al.* [82, 209]. White bias light was provided by an array of diodes (Lumiled model LXHL-NWE8 white star). For the small perturbation red light pulsed diodes (LXHL-ND98 redstar, 0.2 s square pulse width, 100 ns rise and fall time) were used, controlled by a fast solid-state switch. The voltage dynamics were recorded *via* a Keithley 2602 sourcemeter. The voltage decay measurements were performed from zero current (at  $V_{OC}$ ). Small perturbation transient photocurrent measurements were performed in a similar way to the open-circuit voltage decay measurements but here holding a fixed potential while measuring the photocurrent transients. The decays were fitted with a double exponential decay.

# A Appendix

## A.1 Molecular Structures

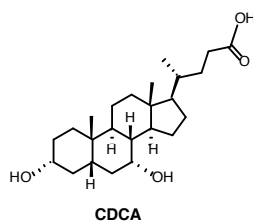


Figure A.1. Molecular structure of chenodeoxycholic acid (CDCA).

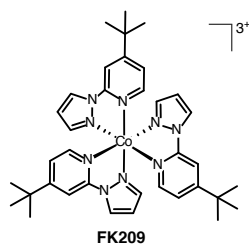


Figure A.2. Molecular structure of cobalt(III) complex FK209. The salt used the TFSI<sup>-</sup> anion.

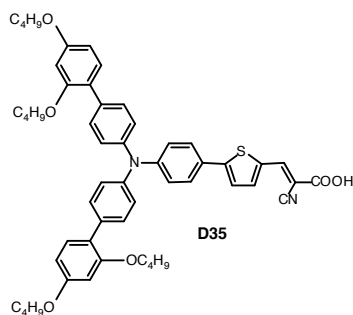


Figure A.3. Molecular structure of D- $\pi$ -A dye D35.

### A.2 Impedance Fitting Procedure for Perovskite Solar Cells

In this work I have identified and analyzed the behavior of the individual components contributing to the IS Nyquist spectra. As outlined the chemical capacitance of the  $\text{mTiO}_2$  is a feature with characteristic behavior. As such it is best to commence fitting data by considering the low frequency recombination arc in isolation. This feature can be fitted by a simple RC element from which the recombination resistance and associated capacitance are easily extracted and their behavior as a function of applied potential can be used as a guideline to identify specific potential regions. As observed in Chapter 4 at low forward bias both the capacitance and the resistance are more or less constant, identifying this region as where the  $\text{mTiO}_2$  is non-conducting and the current is driven *via* the underlayer/HTM interface. This region can thus be fitted using the model shown in Figure 4.4 (a) plus two RC elements in series representing the BC/HTM interface at high frequency and the transport feature associated with the perovskite.

Returning to the capacitance of the recombination arc, the observed sudden drop is followed by a rapid increase as the applied potential moves to higher forward bias. This indicates the region where the  $\text{mTiO}_2$  becomes conducting, and Nyquist plots are typically complicated by the appearance of a  $45^\circ$  line at intermediate frequencies. This typically applies for only a few potentials and the data can be fitted using the transmission line model. Furthermore in this potential region the transport resistance of the perovskite, manifesting at intermediate frequencies, is observed to drastically decrease as the  $\text{mTiO}_2$  becomes conductive and usually even disappears. Upon its disappearance the data can be fitted well using only a transmission line model and an RC element in series for the BC/HTM interface.

Finally at high forward bias, with the disappearance of the  $45^\circ$  line, it is generally possible to identify the three separate RC elements which can be fitted in series. Unfortunately these do not always appear as distinct arcs, rather they tend to merge due to the similarity of their time constants. The intermediate and low frequency arcs representing the perovskite and the recombination features respectively sometimes appear to merge, thus manifesting as a deformed arc, which clearly originates from two individual processes. Here it is important to note that the feature for the perovskite transport is sometimes not apparent at very high forward bias. In the case of devices where the HTM overlayer is very thick or it is insufficiently doped, the high frequency arc may also consist of two individual processes, corresponding to the BC/HTM interface and the charge-transport within the HTM. This usually becomes evident as a deformation at high frequency. To check the validity of the fit using this approach, it is useful to compare the values of recombination resistance and associated capacitance extracted from this complete fit and initial isolated fit. Additionally it is also possible to separately fit the high frequency region related to the BC/HTM interface and (if only moderately doped or with a thick overlayer) the charge-transport of the HTM prior to employing the complete model incorporating all elements. This provides further verification of the accurateness of the conducted data fit. In all cases constant phase elements are used in place of ideal capacitors to fit the data, taking into account the deviation from ideality of such nanostructured devices.

# Nomenclature

## List of Abbreviations

2D	Two-dimensional
3D	Three-dimensional
<i>APCE</i>	Absorbed-to-current conversion efficiency
AC	Alternating current
AM	Air Mass
AM1.5G	Reference solar spectral irradiance according to ASTM G-173-03 standard
ASTM	American Society for Testing and Materials
AU	Astronomical unit of distance
BC	Back contact
BL	Compact TiO <sub>2</sub> blocking layer
bp	Boiling point
C218	A D- $\pi$ -A sensitizer - cf. Figure 3.8, page 66
C220	A D- $\pi$ -A sensitizer - cf. Figure 3.8, page 66
CB	Conduction band
CDCA	Chenodeoxycholic acid - cf. Appendix Figure A.1
CPDT	Cyclopentylidithiophene bridge unit
CPE	Constant phase element
D- $\pi$ -A	Donor- $\pi$ -bridge-Acceptor
D35	A D- $\pi$ -A sensitizer - cf. Appendix Figure A.3
DC	Direct current
DFT	Discrete Fourier Transform
DMF	<i>N,N</i> -dimethylformamide - cf. Table 5.2, page 143
DMSO	Dimethylsulfoxide - cf. Table 5.2, page 143
DOS	Density of trap states
DSC	Differential scanning calorimetry
DSSC	dye-sensitized solar cell
<i>EQE</i>	External quantum efficiency
ETM	Electron-transport material
<i>FF</i>	Fill factor
FK102	A cobalt(III) complex - cf. Figure 1.7, page 13
FK209	A cobalt(III) complex - cf. Appendix Figure A.2

## Appendix A. Appendix

---

FTIR	Fourier transform infrared
FTO	Fluorine-doped tin oxide
GBL	$\gamma$ -butyrolactone - cf. Table 5.2, page 143
HOMO	Highest occupied molecular orbital
HT	Hole-transport
HTM	Hole-transport material
ICT	Intramolecular charge-transfer
<i>IPCE</i>	Incident photon-to-electron conversion efficiency
<i>IQE</i>	Internal quantum efficiency
IR	Infrared
IS	Impedance spectroscopy
JD10	A squaraine sensitizer - cf. Figure 3.1, page 59
JD21	A ullazine sensitizer - cf. Figure 3.15, page 74
JD25	A ullazine sensitizer - cf. Figure 3.15, page 74
JD26	A ullazine sensitizer - cf. Figure 3.15, page 74
JD27	A ullazine sensitizer - cf. Figure 3.15, page 74
JD29	A ullazine sensitizer - cf. Figure 3.15, page 74
JD30	A ullazine sensitizer - cf. Figure 3.15, page 74
JK2	A D- $\pi$ -A sensitizer - cf. Figure 3.8, page 66
<i>LHE</i>	Light harvesting efficiency
LED	Light emitting diode
LiTFSI	Lithium bis(trifluoromethylsulfonyl)amide - cf. Figure 1.7, page 13
LUMO	Lowest unoccupied molecular orbital
MPP	Maximum power point
mTiO <sub>2</sub>	Mesoporous titanium dioxide, TiO <sub>2</sub>
NHE	Normal hydrogen electrode
NIR	Near-infrared
NMR	Nuclear magnetic resonance
<i>PCE</i>	Solar-to-electrical power conversion efficiency
PFF	Pore-filling fraction
PIA	Photoinduced absorption
rpm	Revolutions per minute
S	Sensitizer
SEM	Scanning Electron Microscopy
spiro-MeOTAD	A hole-transporting material - cf. Figure 1.5, page 7
SQ1	A squaraine sensitizer - cf. Figure 3.1, page 59
ssDSSC	Solid-state dye-sensitized solar cell
TBP	4- <i>tert</i> -butylpyridine - cf. Figure 1.7, page 13
TCO	Transparent conducting oxide
TCSPC	Time-correlated single photon counting
TDDFT	Time-dependent density functional theory
TGA	Thermogravimetric analysis



## A.2. Impedance Fitting Procedure for Perovskite Solar Cells

---

THF	Tetrahydrofuran
TLC	Thin layer chromatography
TPA	Triphenylamine
UV	Ultraviolet
VB	Valence band
vis	Visible
XRD	X-ray diffraction
Y123	A D- $\pi$ -A sensitizer - cf. Figure 3.8, page 66
YR6	A squaraine sensitizer - cf. Figure 3.1, page 59

### List of Symbols

$\Delta H_{sub}$	Enthalpy of sublimation - cf. Equation 6.1, page 171
$\epsilon$	Molar extinction coefficient/Dielectric constant
$\eta_{coll}$	Charge collection efficiency
$\eta_{inj}$	Charge injection efficiency
$\Gamma$	Surface dye coverage
$\kappa$	Conductivity
$\lambda$	Wavelength
$\mu$	Charge-carrier mobility/Dipole moment
$\omega$	Angular frequency
$\omega_{ct}$	Characteristic recombination frequency
$\omega_d$	Characteristic carrier diffusion frequency
$\Sigma$	Positional disorder parameter - Bässler model
$\sigma$	Stefan-Boltzmann constant/Energy disorder parameter - Bässler model
$\tau$	Lifetime
$\tau_n$	Electron lifetime
$\tau_{sol}$	Lifetime of the excited state dye species in solution
$\tau_{TiO_2}$	Lifetime of the excited state dye species adsorbed onto TiO <sub>2</sub>
$A$	Surface area/Absorbance/Pre-exponential factor
$c$	Speed of light/Concentration
$C_{BC}$	Capacitance at BC/HTM interface
$C_{BL}$	Capacitance at BL/hole-transport mediator interface
$C_C$	Capacitance at interface between counter-electrode and liquid electrolyte
$C_{HTM}$	Capacitance of the HTM
$C_\mu$	Chemical capacitance
$c_\mu$	Distributed chemical capacitance, measured per unit length per area
$d$	Thickness of mesoporous metal oxide layer
$E$	Electric field
$e$	Elementary charge
$e^-$	Electron
$e_{CB}^-$	TiO <sub>2</sub> CB electrons
$E_A$	Activation Energy
$E_F$	Position of the Fermi level

## Appendix A. Appendix

---

$E_g$	Bandgap energy
$h$	Planck's constant
$h^+$	Electron hole
$I$	Current
$I_0$	Diode reverse saturation current
$I_{photo}$	Photocurrent
$J$	Current density
$J_0$	Photon flux
$J_{MPP}$	Current density at maximum power point
$J_{SC}$	Short-circuit current density
$k$	Rate constant
$k_B$	Boltzmann constant
$k_{rec}$	Recombination rate constant
$k_{trans}$	Charge-transport rate constant
$l$	Optical path length
$m$	Diode ideality factor/Mass
$M_w$	Molecular mass
$m_{sub}$	Mass lost by sublimation - cf. Equation 6.3, page 171
$n$	CPE exponent/Total electron density
$p$	Porosity/Vapor pressure
$P_{in}$	Incident solar power
$P_{max}$	Electrical power
$R$	Electrical resistance
$R$	Gas constant
$R_{BC}$	Charge-transfer resistance at BC/HTM interface
$R_{BL}$	Charge-transfer resistance at BL/hole-transport mediator interface
$R_{ct}$	Macroscopic charge-transfer (recombination) resistance
$r_{ct}$	Distributed recombination resistance, measured per unit length per area
$R_C$	Charge-transfer resistance at interface between counter-electrode and liquid electrolyte
$R_{HTM}$	Charge-transport resistance of the HTM
$R_{trans}$	Macroscopic transport resistance
$r_{trans}$	Distributed transport resistance, measured per unit length per area
$R_{series}$	Series resistance
$R_{shunt}$	Parallel (shunt) resistance
$T$	Temperature/Transmission
$t$	Time
$T_{sub}$	Temperature of sublimation
$V$	Voltage
$V_{app}$	Applied potential
$V_C$	Corrected potential from IR drop calculation
$V_{MPP}$	Voltage at maximum power point

## A.2. Impedance Fitting Procedure for Perovskite Solar Cells

---

$V_{OC}$	Open-circuit potential
$W_d$	Warburg diffusion resistance of redox species
$Z$	Electrical impedance
$Z_d$	Warburg diffusion element



# Bibliography

- [1] Green, M. A.; Emery, K.; Hishikawa, Y.; Warta, W.; Dunlop, E. D. *Progress in Photovoltaics: Research and Applications* **2013**, *22*, 1–9.
- [2] O'Regan, B.; Grätzel, M. *Nature* **1991**, *353*, 737–740.
- [3] Yella, A.; Lee, H. W.; Tsao, H. N.; Yi, C.; Chandiran, A. K.; Nazeeruddin, M. K.; Diau, E. W. G.; Yeh, C. Y.; Zakeeruddin, S. M.; Grätzel, M. *Science* **2011**, *334*, 629–634.
- [4] Kroeze, J. E.; Hirata, N.; Schmidt-Mende, L.; Orizu, C.; Ogier, S. D.; Carr, K.; Grätzel, M.; Durrant, J. R. *Advanced Functional Materials* **2006**, *16*, 1832–1838.
- [5] Juozapavicius, M.; O'Regan, B.; Anderson, A. Y.; Grazulevicius, J. V.; Mimaite, V. *Organic Electronics* **2012**, *13*, 23–30.
- [6] Leijtens, T.; Ding, I. K.; Giovenzana, T.; Bloking, J. T.; McGehee, M. D.; Sellinger, A. *ACS Nano* **2012**, *6*, 1455–1462.
- [7] Unger, E. L.; Morandeira, A.; Persson, M.; Zietz, B.; Ripaud, E.; Leriche, P.; Roncali, J.; Hagfeldt, A.; Boschloo, G. *Physical Chemistry Chemical Physics* **2011**, *13*, 20172–20177.
- [8] Hsu, C.-Y.; Chen, Y.-C.; Lin, R. Y.-Y.; Ho, K.-C.; Lin, J. T. *Physical Chemistry Chemical Physics* **2012**, *14*, 14099–14109.
- [9] Tennakone, K.; Kumara, G. R. R. A.; Kumarasinghe, A. R.; Wijayantha, K. G. U.; Siri-manne, P. M. *Semiconductor Science and Technology* **1999**, *10*, 1689–1693.
- [10] Chung, I.; Lee, B.; He, J.; Chang, R. P. H.; Kanatzidis, M. G. *Nature* **2012**, *485*, 486–489.
- [11] Tsujimoto, K.; Nguyen, D.-C.; Ito, S.; Nishino, H.; Matsuyoshi, H.; Konno, A.; Kumara, G. R. A.; Tennakone, K. *The Journal of Physical Chemistry C* **2012**, *116*, 13465–13471.
- [12] Zhang, W.; Zhu, R.; Li, F.; Wang, Q.; Liu, B. *The Journal of Physical Chemistry C* **2012**, *115*, 7038–7043.
- [13] Zhang, W.; Cheng, Y.; Yin, X.; Liu, B. *Macromolecular Chemistry and Physics* **2011**, *212*, 15–23.
- [14] Bach, U.; Lupo, D.; Comte, P.; Moser, J.-E.; Weissortel, F.; Salbeck, J.; Spreitzer, H.; Grätzel, M. *Nature* **1998**, *395*, 583–585.
- [15] Burschka, J.; Dualeh, A.; Kessler, F.; Baranoff, E.; Cevey-Ha, N.-L.; Yi, C.; Nazeeruddin, M. K.; Grätzel, M. *Journal of the American Chemical Society* **2012**, *133*, 18042–18045.
- [16] Chen, C. Y.; Wang, M. K.; Li, J. Y.; Pootrakulchote, N.; Alibabaei, L.; Ngoc-le, C.; Decoppet, J. D.; Tsai, J. H.; Grätzel, C.; Wu, C. G.; Zakeeruddin, S. M.; Grätzel, M. *ACS Nano*

## Bibliography

---

- 2009, 3, 3103–3109.
- [17] Wang, M.; Grätzel, C.; Moon, S.-J.; Humphry-Baker, R.; Rossier-Iten, N.; Zakeeruddin, S. M.; Grätzel, M. *Advanced Functional Materials* **2009**, 19, 2163–2172.
- [18] Chen, P.; Yum, J.-H.; De Angelis, F.; Mosconi, E.; Fantacci, S.; Moon, S.-J.; Humphry-Baker, R.; Ko, J.; Nazeeruddin, M. K.; Grätzel, M. *Nano Letters* **2009**, 9, 2487–2492.
- [19] Cai, N.; Moon, S.-J.; Cevey-Ha, N.-L.; Moehl, T.; Humphry-Baker, R.; Wang, P.; Zakeeruddin, S. M.; Grätzel, M. *Nano Letters* **2012**, 11, 1452–1456.
- [20] Schmidt-Mende, L.; Bach, U.; Humphry-Baker, R.; Horiuchi, T.; Miura, H.; Ito, S.; Uchida, S.; Grätzel, M. *Advanced Materials* **2005**, 17, 813–815.
- [21] Kwon, Y. S.; Lim, J.; Song, I.; Song, I. Y.; Shin, W. S.; Moon, S.-J.; Park, T. *Journal of Materials Chemistry* **2012**, 22, 8641–8648.
- [22] Rani, S.; Mehra, R. M. *Journal of Renewable and Sustainable Energy* **2009**, 1, 033109.
- [23] Plank, N. O. V.; Howard, I.; Rao, A.; Wilson, M. W. B.; Ducati, C.; Mane, R. S.; Bendall, J. S.; Louca, R. R. M.; Greenham, N. C.; Miura, H.; Friend, R. H.; Snaith, H.; Welland, M. E. *The Journal of Physical Chemistry C* **2009**, 113, 18515–18522.
- [24] Docampo, P.; Snaith, H. *Nanotechnology* **2011**, 22, 225403.
- [25] Tiwana, P.; Docampo, P.; Johnston, M. B.; Herz, L.; Snaith, H. *Energy & Environmental Sciences* **2012**, 5, 9566–9573.
- [26] Tétreault, N.; Horvath, E.; Moehl, T.; Brillet, J.; Smajda, R.; Bungener, S.; Cai, N.; Wang, P.; Zakeeruddin, S. M.; Forro, L.; Magrez, A.; Grätzel, M. *ACS Nano* **2010**, 4, 7644–7650.
- [27] Bendall, J. S.; Etgar, L.; Tan, S. C.; Cai, N.; Wang, P.; Zakeeruddin, S. M. *Energy & Environmental Sciences* **2011**, 4, 2903–2908.
- [28] Marchioro, A.; Dualeh, A.; Punzi, A.; Grätzel, M.; Moser, J.-E. *The Journal of Physical Chemistry C* **2013**, 116, 26721–26727.
- [29] O'Regan, B.; Durrant, J. R.; Sommeling, P. M.; Bakker, N. J. *The Journal of Physical Chemistry C* **2007**, 111, 14001–14010.
- [30] Brennan, T. P.; Bakke, J. R.; Ding, I. K.; Hardin, B. E.; Nguyen, W. H.; Mondal, R.; Bailie, C. D.; Margulis, G. Y.; Hoke, E. T.; Sellinger, A.; McGehee, M. D.; Bent, S. F. *Faraday Discussions* **2012**, 14, 12130–12140.
- [31] O'Regan, B.; Xiaoe, L.; Ghaddar, T. *Energy & Environmental Sciences* **2012**, 5, 7203–7215.
- [32] Docampo, P.; Hey, A.; Guldin, S.; Gunning, R.; Steiner, U.; Snaith, H. *Advanced Functional Materials* **2012**, 22, 5010–5019.
- [33] Ding, I. K.; Tétreault, N.; Brillet, J.; Hardin, B. E.; Smith, E. H.; Rosenthal, S. J.; Sauvage, F.; Grätzel, M.; McGehee, M. D. *Advanced Functional Materials* **2009**, 19, 2431–2436.
- [34] Schmidt-Mende, L.; Grätzel, M. *Thin Solid Films* **2006**, 500, 296–301.
- [35] Melas-Kyriazi, J.; Ding, I. K.; Marchioro, A.; Punzi, A.; Hardin, B. E.; Burkhard, G. F.; Tétreault, N.; Grätzel, M.; Moser, J.-E.; McGehee, M. D. *Advanced Energy Materials* **2011**, 1, 407–414.
- [36] Snaith, H.; Humphry-Baker, R.; Chen, P.; Cesar, I.; Zakeeruddin, S. M.; Grätzel, M. *Nanotechnology* **2008**, 19, 12.

- [37] Boschloo, G.; Häggman, L.; Hagfeldt, A. *The Journal of Physical Chemistry B* **2006**, *110*, 13144–13150.
- [38] Katoh, R.; Kasuya, M.; Kodate, S.; Furube, A.; Fuke, N.; Koide, N. *The Journal of Physical Chemistry C* **2011**, *113*, 20738–20744.
- [39] Chang, Y.-C.; Wu, H.-P.; Reddy, N. M.; Lee, H.-W.; Lu, H.-P.; Yeh, C.-Y.; Diau, E. W.-G. *Faraday Discussions* **2013**, *15*, 4651–4655.
- [40] Abate, A.; Leijtens, T.; Pathak, S.; Teuscher, J.; Avolio, R.; Errico, M. E.; Kirkpatrick, J.; Ball, J. M.; Docampo, P.; McPherson, I.; Snaith, H. *Physical Chemistry Chemical Physics* **2013**, *15*, 2572–2579.
- [41] Snaith, H.; Grätzel, M. *Applied Physics Letters* **2006**, *89*, 262114–3.
- [42] Cappel, U. B.; Daeneke, T.; Bach, U. *Nano Letters* **2013**, *12*, 4925–4931.
- [43] Schölin, R.; Karlsson, M. H.; Eriksson, S. K.; Siegbahn, H.; Johansson, E. M. J.; Rensmo, H. *Journal of the American Chemical Society* **2012**, *116*, 26300–26305.
- [44] Kim, J.-J.; Choi, H.; Paek, S.; Kim, C.; Lim, K.; Ju, M.-J.; Kang, H. S.; Kang, M.-S.; Ko, J. *Inorganic Chemistry* **2011**, *50*, 11340–11347.
- [45] Dualeh, A.; De Angelis, F.; Fantacci, S.; Moehl, T.; Yi, C.; Kessler, F.; Baranoff, E.; Nazeeruddin, M. K.; Grätzel, M. *The Journal of Physical Chemistry C* **2012**, *116*, 1572–1578.
- [46] Hagfeldt, A.; Boschloo, G.; Sun, L.; Kloo, L.; Pettersson, H. *Chemical Reviews* **2010**, *110*, 6595–6663.
- [47] Feldt, S. M.; Gibson, E. A.; Gabrielsson, E.; Sun, L.; Boschloo, G.; Hagfeldt, A. *Journal of the American Chemical Society* **2010**, *132*, 16714–16724.
- [48] Im, J.-H.; Lee, C.-R.; Lee, J.-W.; Park, S.-W.; Park, N.-G. *Nanoscale* **2011**, *3*, 4088–4093.
- [49] Kim, H.-S.; Lee, C.-R.; Im, J.-H.; Lee, K.-B.; Moehl, T.; Marchioro, A.; Moon, S.-J.; Humphry-Baker, R.; Yum, J.-H.; Moser, J.-E.; Grätzel, M.; Park, N.-G. *Scientific Reports* **2012**, *2*, 591.
- [50] Lee, M. M.; Teuscher, J.; Miyasaka, T.; Murakami, T. N.; Snaith, H. *Science* **2012**, *338*, 643–647.
- [51] Ball, J. M.; Lee, M. M.; Hey, A.; Snaith, H. *Energy & Environmental Sciences* **2013**, *6*, 1739–1743.
- [52] Snaith, H.; Moule, A. J.; Klein, C.; Meerholz, K.; Friend, R. H.; Grätzel, M. *Nano Letters* **2007**, *7*, 3372–3376.
- [53] Bisquert, J. *Physical Chemistry Chemical Physics* **2003**, *5*, 5360–5364.
- [54] Dualeh, A.; Moehl, T.; Nazeeruddin, M. K.; Grätzel, M. *ACS Nano* **2013**, *7*, 2292–2301.
- [55] Minna, T.; Janne, H.; Lauri, P.; Peter, L. *International Journal of Photoenergy* **2009**, *2009*, 786429.
- [56] Wang, Q.; Moser, J.-E.; Grätzel, M. *The Journal of Physical Chemistry B* **2005**, *109*, 14945–14953.
- [57] Toivola, M.; Peltokorpi, L.; Halme, J.; Lund, P. *Solar Energy Materials and Solar Cells* **2007**, *91*, 1733–1742.
- [58] Wang, Q.; Ito, S.; Grätzel, M.; Fabregat-Santiago, F.; Mora-Seró, I.; Bisquert, J.; Bessho, T.;

## Bibliography

---

- Imai, H. *The Journal of Physical Chemistry B* **2006**, *110*, 25210–25221.
- [59] Góes, M. S.; Joanni, E.; Muñiz, E. C.; Savu, R.; Habeck, T. R.; Bueno, P. R.; Fabregat-Santiago, F. *The Journal of Physical Chemistry C* **2012**, *116*, 12415–12421.
- [60] Bisquert, J.; Fabregat-Santiago, F.; Mora-Seró, I.; García-Belmonte, G.; Giménez, S. *The Journal of Physical Chemistry C* **2009**, *113*, 17278–17290.
- [61] Fabregat-Santiago, F.; García-Belmonte, G.; Bisquert, J.; Zaban, A.; Salvador, P. *The Journal of Physical Chemistry B* **2002**, *106*, 334–339.
- [62] Bisquert, J.; García-Belmonte, G.; Fabregat-Santiago, F.; Compte, A. *Electrochemistry Communications* **1999**, *1*, 429–435.
- [63] Fabregat-Santiago, F.; Bisquert, J.; Cevey-Ha, N.-L.; Chen, P.; Wang, M.; Zakeeruddin, S. M.; Grätzel, M. *Journal of the American Chemical Society* **2008**, *131*, 558–562.
- [64] Fabregat-Santiago, F.; Bisquert, J.; Palomares, E.; Haque, S. A.; Durrant, J. R. *Journal of Applied Physics* **2006**, *100*, 034510.
- [65] Abate, A.; Hollman, D. J.; Teuscher, J.; Pathak, S.; Avolio, R.; D’Errico, G.; Vitiello, G.; Fantacci, S.; Snaith, H. *Journal of the American Chemical Society* **2013**, *135*, 13538–13548.
- [66] Burschka, J.; Kessler, F.; Nazeeruddin, M. K.; Grätzel, M. *Chemistry of Materials* **2013**, *25*, 2986–2990.
- [67] Boix, P. P.; Lee, Y. H.; Fabregat-Santiago, F.; Im, S. H.; Mora-Seró, I.; Bisquert, J.; Seok, S. I. *ACS Nano* **2012**, *6*, 873–880.
- [68] Boix, P. P.; Larramona, G.; Jacob, A.; Delatouche, B.; Mora-Seró, I.; Bisquert, J. *The Journal of Physical Chemistry C* **2012**, *116*, 1579–1587.
- [69] Borsenberger, P. M.; Pautmeier, L.; Bässler, H. *The Journal of Chemical Physics* **1991**, *94*, 5447–5454.
- [70] Bach, U.; De Cloedt, K.; Spreitzer, H.; Grätzel, M. *Advanced Materials* **2000**, *12*, 1060–1063.
- [71] Poplavskyy, D.; Nelson, J. *Journal of Applied Physics* **2003**, *93*, 341–346.
- [72] Li, L.; Meller, G.; Kosina, H. *Microelectronics Journal* **2007**, *38*, 47–51.
- [73] Rana, O.; Srivastava, R.; Grover, R.; Zulfequar, M.; Husain, M.; Kamalasanan, M. N. *Synthetic metals* **2011**, *161*, 828–832.
- [74] van de Lagemaat, J.; Frank, A. J. *The Journal of Physical Chemistry B* **2000**, *104*, 4292–4294.
- [75] Fabregat-Santiago, F.; Bisquert, J.; García-Belmonte, G.; Boschloo, G.; Hagfeldt, A. *Solar Energy Materials and Solar Cells* **2005**, *87*, 117–131.
- [76] O’Regan, B.; Durrant, J. R. *The Journal of Physical Chemistry B* **2006**, *110*, 8544–8547.
- [77] Cao, Y.; Bai, Y.; Yu, Q.; Cheng, Y.; Liu, S.; Shi, D.; Gao, F.; Wang, P. *Journal of the American Chemical Society* **2009**, *131*, 6290–6297.
- [78] Bisquert, J.; Cahen, D.; Hodes, G.; Rühle, S.; Zaban, A. *The Journal of Physical Chemistry B* **2004**, *108*, 8106–8118.
- [79] Fabregat-Santiago, F.; García-Belmonte, G.; Mora-Seró, I.; Bisquert, J. *Physical Chemistry Chemical Physics* **2011**, *13*, 9083–9118.



- [80] Bisquert, J.; Grätzel, M.; Wang, Q.; Fabregat-Santiago, F. *The Journal of Physical Chemistry B* **2006**, *110*, 11284–11290.
- [81] Bach, U. Solid-state dye-sensitized mesoporous TiO<sub>2</sub> solar cells. Ph.D. thesis, *École Polytechnique Fédérale de Lausanne*, 2000.
- [82] O'Regan, B.; Lenzmann, F. *The Journal of Physical Chemistry B* **2004**, *108*, 4342–4350.
- [83] O'Regan, B.; Lenzmann, F.; Muis, R.; Wienke, J. *Chemistry of Materials* **2002**, *14*, 5023–5029.
- [84] O'Regan, B.; Schwartz, D. T. *Chemistry of Materials* **1998**, *10*, 1501–1509.
- [85] Geiger, T.; Kuster, S.; Yum, J.-H.; Moon, S.-J.; Nazeeruddin, M. K.; Grätzel, M.; Nüesch, F. *Advanced Functional Materials* **2009**, *19*, 2720–2727.
- [86] Shi, Y.; Hill, R. B. M.; Yum, J.-H.; Dualeh, A.; Barlow, S.; Grätzel, M.; Marder, S. R.; Nazeeruddin, M. K. *Angewandte Chemie* **2011**, *123*, 6749–6751.
- [87] Yum, J.-H.; Walter, P.; Huber, S.; Rentsch, D.; Geiger, T.; Nüesch, F.; De Angelis, F.; Grätzel, M.; Nazeeruddin, M. K. *Journal of the American Chemical Society* **2007**, *129*, 10320–10321.
- [88] Dualeh, A.; Delcamp, J. H.; Nazeeruddin, M. K.; Grätzel, M. *Applied Physics Letters* **2012**, *100*, 173512.
- [89] Li, J.-Y.; Chen, C.-Y.; Lee, C.-P.; Chen, S.-C.; Lin, T.-H.; Tsai, H.-H.; Ho, K.-C.; Wu, C.-G. *Organic Letters* **2010**, *12*, 5454–5457.
- [90] Wenger, B.; Grätzel, M.; Moser, J.-E. *Journal of the American Chemical Society* **2005**, *127*, 12150–12151.
- [91] Kuang, D.; Walter, P.; Nüesch, F.; Kim, S.; Ko, J.; Comte, P.; Zakeeruddin, S. M.; Nazeeruddin, M. K.; Grätzel, M. *Langmuir* **2007**, *23*, 10906–10909.
- [92] Cid, J. J.; Yum, J.-H.; Jang, S. R.; Nazeeruddin, M. K.; Ferrero, E. M.; Palomares, E.; Ko, J.; Grätzel, M.; Torres, T. *Angewandte Chemie International Edition* **2007**, *46*, 8358–8362.
- [93] Hagberg, D. P.; Jiang, X.; Gabrielsson, E. *Journal of Materials Chemistry* **2009**, *19*, 7232–7238.
- [94] Jiang, X.; Karlsson, K. M.; Gabrielsson, E.; Johansson, E. M. J.; Quintana, M.; Karlsson, M.; Sun, L.; Boschloo, G.; Hagfeldt, A. *Advanced Functional Materials* **2011**, *21*, 2944–2952.
- [95] O'Regan, B.; Scully, S.; Mayer, A. C.; Palomares, E.; Durrant, J. R. *The Journal of Physical Chemistry B* **2005**, *109*, 4616–4623.
- [96] Sommeling, P. M.; O'Regan, B.; Haswell, R. R.; Smit, H. J. P.; Bakker, N. J.; Smits, J. J. T.; Kroon, J. M.; van Roosmalen, J. A. M. *The Journal of Physical Chemistry B* **2006**, *110*, 19191–19197.
- [97] Tsao, H. N.; Yi, C.; Moehl, T.; Yum, J.-H.; Zakeeruddin, S. M.; Nazeeruddin, M. K.; Grätzel, M. *ChemSusChem* **2011**, *4*, 591–594.
- [98] Wolfbauer, G.; Bond, A. M.; Deacon, G. B.; MacFarlane, D. R.; Spiccia, L. *Journal of the American Chemical Society* **2000**, *122*, 130–142.
- [99] Fantacci, S.; Lobello, M. G.; De Angelis, F. *CHIMIA International Journal for Chemistry* **2013**, *67*, 121–128.

## Bibliography

---

- [100] Cameron, P. J.; Peter, L. M. *The Journal of Physical Chemistry B* **2005**, *109*, 7392–7398.
- [101] Becke, A. D. *Journal of Chemical Physics* **1993**, *98*, 1372.
- [102] Pastore, M.; Mosconi, E.; De Angelis, F.; Grätzel, M. *The Journal of Physical Chemistry C* **2010**, *114*, 7205–7212.
- [103] Bach, U.; Grätzel, M. *Advanced Materials* **2000**, *12*, 447–451.
- [104] Rühle, S.; Greenshtein, M.; Chen, S. G.; Merson, A.; Pizem, H.; Sukenik, C. S.; Cahen, D.; Zaban, A. *The Journal of Physical Chemistry B* **2005**, *109*, 18907–18913.
- [105] Kruger, J.; Plass, R.; Cevey-Ha, N.-L.; Piccirelli, M.; Grätzel, M.; Bach, U. *Applied Physics Letters* **2001**, *79*, 2085–2087.
- [106] Persson, P.; Bergström, R.; Lunell, S. *The Journal of Physical Chemistry B* **2000**, *104*, 10348–10351.
- [107] De Angelis, F.; Tilocca, A.; Selloni, A. *Journal of the American Chemical Society* **2004**, *126*, 15024–15025.
- [108] Dualeh, A.; Humphry-Baker, R.; Delcamp, J. H.; Nazeeruddin, M. K.; Grätzel, M. *Advanced Energy Materials* **2013**, *3*, 496–504.
- [109] Balli, H.; Zeller, M. *Helvetica Chimica Acta* **1983**, *66*, 2135–2139.
- [110] Delcamp, J. H.; Yella, A.; Holcombe, T. W.; Nazeeruddin, M. K.; Grätzel, M. *Angewandte Chemie International Edition* **2012**, *52*, 376–380.
- [111] Inoue, M.; Bruce, T. C. *Journal of the American Chemical Society* **1982**, *104*, 1644–1653.
- [112] Wang, P.; Zakeeruddin, S. M.; Comte, P.; Charvet, R.; Humphry-Baker, R.; Grätzel, M. *The Journal of Physical Chemistry B* **2003**, *107*, 14336–14341.
- [113] Tian, H.; Yang, X.; Chen, R.; Zhang, R.; Hagfeldt, A.; Sun, L. *The Journal of Physical Chemistry C* **2012**, *112*, 11023–11033.
- [114] Boschloo, G.; Hagfeldt, A. *Inorganica Chimica Acta* **2008**, *361*, 729–734.
- [115] Boschloo, G.; Hagfeldt, A. *Chemical Physics Letters* **2003**, *370*, 381–386.
- [116] Haque, S. A.; Tachibana, Y.; Willis, R. L.; Moser, J.-E.; Grätzel, M.; Klug, D. R.; Durrant, J. R. *The Journal of Physical Chemistry B* **2000**, *104*, 538–547.
- [117] Tachibana, Y.; Haque, S. A.; Mercer, I. P.; Durrant, J. R.; Klug, D. R. *The Journal of Physical Chemistry B* **2000**, *104*, 1198–1205.
- [118] Tachibana, Y.; Haque, S. A.; Mercer, I. P.; Moser, J.-E.; Klug, D. R.; Durrant, J. R. *The Journal of Physical Chemistry B* **2001**, *105*, 7424–7431.
- [119] Brown, P.; Kamat, P. V. *Journal of the American Chemical Society* **2008**, *130*, 8890–8891.
- [120] Kamat, P. V. *The Journal of Physical Chemistry C* **2008**, *112*, 18737–18753.
- [121] Kongkanand, A.; Tvrdy, K.; Takechi, K.; Kuno, M.; Kamat, P. V. *Journal of the American Chemical Society* **2008**, *130*, 4007–4015.
- [122] Vogel, R.; Hoyer, P.; Weller, H. *The Journal of Physical Chemistry* **1994**, *98*, 3183–3188.
- [123] Chondroudis, K.; Mitzi, D. B. *Chemistry of Materials* **1999**, *11*, 3028–3030.
- [124] Kagan, C. R.; Mitzi, D. B.; Dimitrakopoulos, C. D. *Science* **1999**, *286*, 945–947.
- [125] Flocken, J.; Guenther, R.; Hardy, J.; Boyer, L. *Physical Review B* **1985**, *31*, 7252–7260.

- [126] Cheng, Z.; Lin, J. *CrystEngComm* **2010**, *12*, 2646–2662.
- [127] Covaliu, C. I.; Chioaru, L. C.; Craciun, L.; Oprea, O.; Jitaru, I. *Optoelectronics and Advanced Materials - Rapid Communications* **2011**, *5*, 1097–1102.
- [128] Mousdis, G. A.; Papavassiliou, G. C.; Raptopoulou, C. P.; Terzis, A. *Journal of Materials Chemistry* **2000**, *10*, 515–518.
- [129] Mitzi, D. B.; Feild, C. A.; Harrison, W. T. A.; Guloy, A. M. *Nature* **1994**, *369*, 467–469.
- [130] Park, N.-G. *The Journal of Physical Chemistry Letters* **2013**, *4*, 2423–2429.
- [131] Etgar, L.; Gao, P.; Xue, Z.; Peng, Q.; Chandiran, A. K.; Liu, B.; Nazeeruddin, M. K.; Grätzel, M. *Journal of the American Chemical Society* **2013**, *134*, 17396–17399.
- [132] Kamaya, N.; Homma, K.; Yamakawa, Y.; Hirayama, M.; Kanno, R.; Yonemura, M.; Kamiyama, T.; Kato, Y.; Hama, S.; Kawamoto, K.; Mitsui, A. *Nature Materials* **2011**, *10*, 682–686.
- [133] Donnelly, N. J.; Randall, C. A. *Applied Physics Letters* **2010**, *96*, 052906.
- [134] Glower, D. D.; Heckman, R. C. *The Journal of Chemical Physics* **1964**, *41*, 877–879.
- [135] Inaguma, Y.; Liquan, C.; Itoh, M.; Nakamura, T.; Uchida, T.; Ikuta, H.; Wakihara, M. *Solid State Communications* **1993**, *86*, 689–693.
- [136] Misusaki, J.; Arai, K.; Fueki, K. *Solid State Ionics* **1983**, *11*, 203–211.
- [137] Boyett, R. *Solid State Ionics* **1995**, *81*, 61–68.
- [138] Chadwick, A.; Strange, J.; Ranieri, G.; Terenzi, M. *Solid State Ionics* **1983**, *9*, 555–558.
- [139] Mitzi, D. B. *Journal of Materials Chemistry* **2004**, *14*, 2355–2365.
- [140] Billing, D. G.; Lemmerer, A. *CrystEngComm* **2007**, *9*, 236–244.
- [141] Mitzi, D. B.; Chondroudis, K.; Kagan, C. R. *Inorganic Chemistry* **1999**, *38*, 6246–6256.
- [142] Fluegel, B.; Zhang, Y.; Mascarenhas, A.; Huang, X.; Li, J. *Physical Review B* **2004**, *70*, 205308.
- [143] Chang, Y. H.; Park, C. H.; Matsuishi, K. *Journal of the Korean Physical Society* **2004**, *44*, 889–893.
- [144] Poglitsch, A.; Weber, D. *Journal of Chemical Physics* **1987**, *87*, 6373–6378.
- [145] Noh, J. H.; Im, S. H.; Heo, J. H.; Mandal, T. N.; Seok, S. I. *Nano Letters* **2013**, *13*, 1764–1769.
- [146] Bi, D.; Yang, L.; Boschloo, G.; Hagfeldt, A.; Johansson, E. M. J. *The Journal of Physical Chemistry Letters* **2013**, *4*, 1532–1536.
- [147] Heo, J. H.; Im, S. H.; Noh, J. H.; Mandal, T. N.; Lim, C.-S.; Chang, J. A.; Lee, Y. H.; Kim, H.-j.; Sarkar, A.; Nazeeruddin, M. K.; Grätzel, M.; Seok, S. I. *Nature Photonics* **2013**, *7*, 486–491.
- [148] Edri, E.; Kirmayer, S.; Cahen, D.; Hodes, G. *The Journal of Physical Chemistry Letters* **2013**, *4*, 897–902.
- [149] Liu, D.; Kelly, T. L. *Nature Photonics* **2014**, *8*, 133–138.
- [150] Wang, J. T.-W.; Ball, J. M.; Barea, E. M.; Abate, A.; Alexander-Webber, J. A.; Huang, J.; Saliba, M.; Mora-Sero, I.; Bisquert, J.; Snaith, H.; Nicholas, R. J. *Nano Letters* **2014**, *14*, 724–730.
- [151] Kim, H.-S.; Mora-Sero, I.; Gonzalez-Pedro, V.; Fabregat-Santiago, F.; Juarez-Perez, E. J.;

## Bibliography

---

- Park, N.-G.; Bisquert, J. *Nature Communications* **2013**, *4*, 2242.
- [152] Dualeh, A.; Moehl, T.; Tétreault, N.; Teuscher, J.; Gao, P.; Nazeeruddin, M. K.; Grätzel, M. *ACS Nano* **2014**, *8*, 362–373.
- [153] Bisquert, J. *Physical Chemistry Chemical Physics* **2011**, *13*, 4679–4685.
- [154] Mora-Seró, I.; Bisquert, J.; Fabregat-Santiago, F.; García-Belmonte, G.; Zoppi, G.; Durose, K.; Proskuryakov, Y.; Oja, I.; Belaidi, A.; Dittrich, T.; Tena-Zaera, R.; Katty, A.; Lévy-Clément, C.; Barrioz, V.; Irvine, S. J. C. *Nano Letters* **2006**, *6*, 640–650.
- [155] Eisenbarth, T.; Caballero, R.; Nichterwitz, M.; Kaufmann, C. A.; Schock, H.-W.; Unold, T. *Journal of Applied Physics* **2011**, *110*, 094506.
- [156] Abrusci, A.; Stranks, S. D.; Docampo, P.; Yip, H.-L.; Jen, A.-K. Y.; Snaith, H. *Nano Letters* **2013**, *13*, 3124–3128.
- [157] Ding, I. K.; Melas-Kyriazi, J.; Cevey-Ha, N.-L.; Chittibabu, K. G.; Zakeeruddin, S. M.; Grätzel, M.; McGehee, M. D. *Organic Electronics* **2010**, *11*, 1217–1222.
- [158] Kim, H.-S.; Lee, C.-R.; Jang, I.-H.; Kang, W.; Park, N.-G. *Bulletin of the Korean Chemical Society* **2012**, *33*, 670–674.
- [159] Bisquert, J. *Physical Chemistry Chemical Physics* **2000**, *2*, 4185–4192.
- [160] Kambe, S.; Nakade, S.; Kitamura, T.; Wada, Y.; Yanagida, S. *The Journal of Physical Chemistry B* **2002**, *106*, 2967–2972.
- [161] Koops, S. E.; O'Regan, B.; Barnes, P. R. F.; Durrant, J. R. *Journal of the American Chemical Society* **2009**, *131*, 4808–4818.
- [162] Howie, W. H.; Harris, J. E.; Jennings, J. R.; Peter, L. M. *Solar Energy Materials and Solar Cells* **2007**, *91*, 424–426.
- [163] Dürr, M.; Rosselli, S.; Yasuda, A.; Nelles, G. *The Journal of Physical Chemistry B* **2006**, *110*, 21899–21902.
- [164] Zhao, Y.; Chen, W.; Zhai, J.; Sheng, X.; He, Q.; Wei, T.; Bai, F.; Jiang, L.; Zhu, D. *Chemical Physics Letters* **2007**, *445*, 259–264.
- [165] Jurkiewicz-Herbich, M.; Slojkowska, R.; Zawada, K.; Bukowska, J. *Electrochimica Acta* **2002**, *47*, 2429–2434.
- [166] Kopidakis, N.; Benkstein, K. D.; van de Lagemaat, J.; Frank, A. J. *Journal of Physical Chemistry B* **2003**, *107*, 11307–11315.
- [167] Harima, Y.; Kawabuchi, K.; Kajihara, S.; Ishii, A.; Ooyama, Y.; Takeda, K. *Applied Physics Letters* **2007**, *90*, 103517.
- [168] Subramanian, A.; Bow, J.-S.; Wang, H.-W. *Thin Solid Films* **2012**, *520*, 7011–7017.
- [169] Cava, R. J.; Murphy, D. W.; Zahurak, S.; Santoro, A.; Roth, R. S. *Journal of Solid State Chemistry* **1984**, *53*, 64–75.
- [170] Nakade, S.; Kambe, S.; Kitamura, T.; Wada, Y.; Yanagida, S. *The Journal of Physical Chemistry B* **2001**, *105*, 9150–9152.
- [171] Stoumpos, C. C.; Malliakas, C. D.; Kanatzidis, M. G. *Inorganic Chemistry* **2013**, *52*, 9019–9038.
- [172] Frost, J. M.; Butler, K. T.; Brivio, F.; Hendon, C. H.; van Schilfgaarde, M.; Walsh, A.

- Materials Science* **2014**, *arXiv:1402.4980*, [cond-mat.mtrl-sci].
- [173] Snaith, H.; Abate, A.; Ball, J. M.; Eperon, G. E.; Leijtens, T.; Noel, N. K.; Stranks, S. D.; Wang, J. T.-W.; Wojciechowski, K.; Zhang, W. *The Journal of Physical Chemistry Letters* **2014**, *n/a*, n/a.
- [174] Wang, Q.; Dong, Q.; Xiao, Z.; Yuan, Y.; Huang, J. *Energy & Environmental Sciences* **2014**, *n/a*, n/a.
- [175] Burschka, J.; Pellet, N.; Moon, S.-J.; Humphry-Baker, R.; Gao, P.; Nazeeruddin, M. K.; Grätzel, M. *Nature* **2013**, *499*, 316–319.
- [176] Bi, D.; Häggman, L.; Boschloo, G.; Yang, L.; Johansson, E. M. J.; Nazeeruddin, M. K.; Grätzel, M.; Hagfeldt, A. *RSC Advances* **2013**, *3*, 18762–18766.
- [177] Liu, M.; Johnston, M. B.; Snaith, H. *Nature* **2013**, *501*, 395–398.
- [178] Colella, S.; Mosconi, E.; Fedeli, P.; Listorti, A.; Gazza, F.; Orlandi, F.; Ferro, P.; Besagni, T.; Rizzo, A.; Calestani, G.; Gigli, G.; De Angelis, F.; Mosca, R. *Chemistry of Materials* **2013**, *25*, 4613–4618.
- [179] Côté, J.-E.; Brouillette, D.; Desnoyers, J. E.; Rouleau, J.-E.; St-Arnaud, J.-M.; Perron, G. *Journal of Solution Chemistry* **1996**, *25*, 1163–1173.
- [180] Perelygin, I. S.; Itkulov, I. G. *Journal of Structural Chemistry* **1996**, *37*, 928–932.
- [181] Chen, Z.; Li, H.; Tang, Y.; Huang, X.; Ho, D.; Lee, C.-S. *Materials Research Express* **2014**, *1*, 015034.
- [182] Dualeh, A.; Tétreault, N.; Moehl, T.; Gao, P.; Nazeeruddin, M. K.; Grätzel, M. *Advanced Functional Materials* **2014**, *n/a*, n/a–n/a.
- [183] Zhao, Y.; Zhu, K. *The Journal of Physical Chemistry Letters* **2013**, *4*, 2880–2884.
- [184] Supasai, T.; Rujisamphan, N.; Ullrich, K.; Chemseddine, A.; Dittrich, T. *Applied Physics Letters* **2013**, *103*, 183906.
- [185] Edwards, R.; Gillard, R. D.; Williams, P. A.; Pollard, A. M. *Mineralogical Magazine* **1992**, *56*, 53–65.
- [186] Kojima, A.; Teshima, K.; Shirai, Y.; Miyasaka, T. *Journal of the American Chemical Society* **2009**, *131*, 6050–6051.
- [187] Baikie, T.; Fang, Y.; Kadro, J. M.; Schreyer, M.; Wei, F.; Mhaisalkar, S. G.; Graetzel, M.; White, T. J. *Journal of Materials Chemistry A* **2013**, *1*, 5628–5641.
- [188] Ishihara, M.; Li, S. J.; Yumoto, H.; Akashi, K.; Ide, Y. *Thin Solid Films* **1998**, *316*, 152–157.
- [189] Ohyama, M.; Kozuka, H.; Yoko, T. *Thin Solid Films* **1997**, *306*, 78–85.
- [190] Xu, Y.; Chen, J. S.; Wang, J. P. *Applied Physics Letters* **2002**, *80*, 3325–3327.
- [191] Beckmann, P. A. *Crystal Research and Technology* **2010**, *45*, 455–460.
- [192] Bisquert, J.; Garcìa-Belmonte, G.; Munar, A.; Sessolo, M.; Soriano, A.; Bolink, H. J. *Chemical Physics Letters* **2008**, *465*, 57–62.
- [193] Garcìa-Belmonte, G.; Munar, A.; Barea, E. M.; Bisquert, J.; Ugarte, I.; Pacios, R. *Organic Electronics* **2008**, *9*, 847–851.
- [194] Green, M. A.; Shewchun, J. *Solid-State Electronics* **1973**, *16*, 1141–1150.
- [195] Mercier, N. *CrystEngComm* **2005**, *7*, 429–432.

## Bibliography

---

- [196] Eperon, G. E.; Burlakov, V. M.; Docampo, P.; Goriely, A.; Snaith, H. *Advanced Functional Materials* **2014**, *24*, 151–157.
- [197] Wu, Y.; Yang, X.; Chen, H.; Zhang, K.; Qin, C.; Liu, J.; Peng, W.; Islam, A.; Bi, E.; Ye, F.; Yin, M.; Zhang, P.; Han, L. *Applied Physics Express* **2014**, *7*, 052301.
- [198] Vieyra-Eusebio, M. T.; Rojas, A. *Journal of Chemical & Engineering Data* **2011**, *56*, 5008–5018.
- [199] Fahlman, B. D.; Barron, A. R. *Advanced Materials for Optics and Electronics* **2000**, *10*, 223–232.
- [200] Langmuir, I. *Physical Review* **1913**, *2*, 329–342.
- [201] Yamada, K.; Nakada, K.; Takeuchi, Y.; Nawa, K.; Yamane, Y. *Bulletin of the Chemical Society of Japan* **2011**, *84*, 926–932.
- [202] Erk, P. *Speaker at HOPV14*. 2014.
- [203] Zhao, Y.; Zhu, K. *Journal of Physical Chemistry C* **2014**, *118*, 9412–9418.
- [204] Jain, A.; Trigunayat, G. C. *Acta Crystallographica* **1996**, *52*, 590–595.
- [205] Chaudhary, S. K. *Crystal Structure Theory and Applications* **2012**, *1*, 21–24.
- [206] Palosz, B.; Steurer, W.; Schulz, H. *Journal of Physics: Condensed Matter* **1999**, *2*, 5285–5295.
- [207] Chaudhary, S. K. *Acta Crystallographica* **1993**, *49*, 454–458.
- [208] Trigunayat, G. C. *Solid State Ionics* **1991**, *48*, 3–70.
- [209] O'Regan, B.; Bakker, K.; Kroeze, J.; Smit, H.; Sommeling, P. M.; Durrant, J. R. *The Journal of Physical Chemistry B* **2006**, *110*, 17155–17160.

# Acknowledgements

It is impossible to express how endlessly grateful I am for all the support, help and advice that I received from many friends, family and colleagues during the course of my doctoral studies. To all of you my deepest thanks.

First of all I would like to thank my supervisor Prof. Michael Grätzel for giving me the opportunity to work on my doctoral thesis at EPFL. Thank you for your support, scientific expertise and for opening the doors to such an interesting field of research and giving me the chance to explore the many different and complex facets of solid-state mesoscopic solar cells. Many thanks also go to my thesis co-advisor Dr. Mohammad K. Nazeeruddin for your assistance, advice and giving me the freedom to find and follow my research interests.

Four years is a long time to spend in one place. I want to thank all the members of LPI for the unique work environment that has made my stay here so unforgettable. Many thanks go to all of you.

Thomas, you introduced me to the world of impedance spectroscopy and were always patient when I came to check and discuss my results with you. For that I am endlessly grateful. Thank you for your constant support, both scientific and personal, encouragement and sharing your wealth of knowledge. Robin, thank you for the thousands of explanations and discussions. Your scientific support and knowledge were invaluable and I feel that I always left your office with a list of things that I wanted to look up, research and learn about. Thank you both for taking the time and effort to proof-read my thesis.

Ines you first introduced me to LPI and the solid-state lab. Thank you for making me feel welcome and pointing me in the right direction! Special thanks also to: Magda for your inexhaustible enthusiasm and support; Julian for making the solid-state lab such a pleasant place to work in; Phil for your motivation, support and for correcting my french abstract and Aravind for all the ALD layers that you made for me. For all the endless hours spent working on the FP7 'ORION' project reports and presentations I want to thank you both; Arianna for your open, friendly support and company at photonics meetings; Nic for the many SEM images and the helpful scientific discussions; Takeru, Jérémie, Nic, Joël and Norman for the friendly atmosphere in the office; Manuel for your humor and amazing technical devices; Aravind, Aswani and Nok for all your scientific help and creating a great atmosphere

## Acknowledgements

---

in the laboratory; Jared, Chenyi, Peng Gao and Florian K. for the synthesis of all the organic sensitizers, organic perovskite precursors and cobalt dopants; Pascal for your tips on screen-printing and providing various metal-oxide pastes; Soo-Jin and Lê for teaching me how to assemble ssDSSCs; Paul L. for laser etching substrates; Carole and Zakeer for your assistance and everyone from the solid-state group for your scientific discussions, help and advice.

Many thanks also go to the many international collaborators including Filippo de Angelis, Simona Fantacci, Ramon Tena-Zaera and all the FP7 project collaborators for the invaluable technical and scientific discussions and contributions!

I am very grateful for all the administrative help and assistance provided by Ursula Gonthier, Nelly Gourdou, Antonella Ragnelli, Carmen Biagini and Heidi Francelet from LPI and Pierrette Paulou-Vaucher and Cathy Buchs from the Doctoral Program in Photonics. Thanks also go to the Marie and Jacky from the chemical magasin and to the teams of the electronic and mechanical workshop for their technical support.

Finally I want to express my heartfelt thanks to my parents. Thank you so much for your inexhaustible encouragement, endless personal and moral support without which I would never have made it this far. Issa and Edna, we may not always agree, but you were always there for me when I needed it (even if this means you two ganging up against me!). Thank you for everything.

Thank you to everyone!

*Lausanne, 2014*

A. D.



## Amalie DUALEH

---

*Date/Place of Birth:* 13 January 1988 / Köln, Germany  
*Nationality:* Germany / Somaliland  
*E-mail:* amalie.dualeh@gmail.com

### Education

---

**Ph.D. in Photonics** 2014  
École Polytechnique Fédérale de Lausanne, Switzerland 2010 – 2014  
*Thesis title:* Analysis of Key Electronic, Optical and Structural Parameters in Mesoscopic Solid-state Solar Cells  
*Thesis supervisors:* Prof. Michael Grätzel & Dr. Md. Khaja Nazeeruddin

- Assembled solid-state mesoscopic solar cells. Evaluation and optimization of device performance by extensive characterization techniques
- Participated in EU FP7 collaborative project; preparation and presentation of research results, progress and technical reports to project partners as work package leader
- Teaching Assistant: Exercise seminars (general and basic quantum chemistry), Laboratory sessions (general chemistry)

**MSci. Joint Honours within Natural Sciences in Physics and Chemistry** 2010  
First Class Honours Degree  
Durham University, United Kingdom 2006 – 2010  
4<sup>th</sup> year research project in Physics Photonics department: Electro-optic Polymers  
3<sup>rd</sup> year dissertation in Chemistry: Photochemistry of HCl and H<sub>2</sub>O molecules on a crystalline ice surface

**International Baccalaureate (IB)** 2006  
43/45; 7 in Physics, Chemistry and Mathematics higher level  
La Chataigneraie, International School of Geneva, Switzerland 1999 – 2006

### Experience

---

**Internship** with Lutheran World Federation (LWF) community services sector in Kakuma refugee camp (**Kakuma, Kenya**) 2009

- Involved in food distribution and event organization to increase awareness about human rights, sexual based violence, child protection and peace education.
- Responsible for capturing and arbitrating cases that were presented in the field, documentation and participation in case conferences.

**Internship** at a non-profit charity and teaching hospital, the Edna Adan Maternity Hospital (**Hargeisa, Somaliland**) 2009

- Assisted the midwives in medical and maternity wards, aided in the reanimation and immunization of newborn babies.
- Conducted laboratory analysis of blood and urine samples, screening for HIV/Aids, Hepatitis B/C and Syphilis and performed minor tasks e.g. wound dressings.

**Student Assistant:** Medical centre under general physician, Dr Jörg Runge (**Hamburg, Germany**) and Department of Medical Laboratory Sciences and Technology, Karolinska Institutet in the field of Pharmacological research (**Stockholm, Sweden**) 2005

## Technical and Professional Skills

---

- **Experimental characterization techniques:** Current-Voltage Photovoltaic characterization, Incident Photon-to-Current Efficiency measurements, Transient Photovoltage and Photocurrent Decay measurements, Electrochemical Impedance spectroscopy, Ultraviolet-Visible spectroscopy, Photoinduced Absorption spectroscopy, Fourier Transform Infrared spectroscopy, Thermal Gravimetric Analysis, Differential Scanning Calorimetry
- **IT skills:** LaTeX, Wavemetrics IgorPro, Maple, Mathematica, Python
- **Languages:** Fluent in English, German and French and beginner in Spanish and Somali

## Publications/Presentations

---

- **Dualeh, A.**, Gao, P., Nazeeruddin, M. K., & Grätzel, M. (2014) Thermal Decomposition of Methylammonium Lead-trihalide Perovskite Photovoltaic Light Harvesters. *Submitted Manuscript*.
- **Dualeh, A.**, Tétreault, N., Moehl, T., Gao, P., Nazeeruddin, M. K., & Grätzel, M. (2014) Effect of Annealing Temperature on Film Morphology for Organic-Inorganic Hybrid Perovskite Solid-State Solar Cells. *Advanced Functional Materials*, n/a. doi: 10.1002/adfm.201304022
- **Dualeh, A.**, Moehl, T., Tétreault, N., Teuscher, J., Gao, P., Nazeeruddin, M. K., & Grätzel, M. (2013). Impedance Spectroscopic Analysis of Lead-Iodide Perovskite-Sensitized Solid-State Solar Cells. *ACS Nano*, 8(1), 362–373. doi: 10.1021/nn404323g
- **Dualeh, A.**, Moehl, T., Nazeeruddin, M. K., & Grätzel, M. (2013). Temperature Dependence of Transport Properties of Spiro-MeOTAD as a Hole Transport Material in Solid-State Dye-Sensitized Solar Cells. *ACS Nano*, 7(3), 2292–2301. doi: 10.1021/nn4005473
- Marchioro, A., **Dualeh, A.**, Punzi, A., Grätzel, M., & Moser, J.-E. (2013). Effect of Posttreatment of Titania Mesoscopic Films by  $\text{TiCl}_4$  in Solid-State Dye-Sensitized Solar Cells: A Time-Resolved Spectroscopy Study. *Journal of Physical Chemistry C*, 116(51), 26721–26727. doi: 10.1021/jp309799u
- **Dualeh, A.**, Humphry-Baker, R., Delcamp, J. H., Nazeeruddin, M. K., & Grätzel, M. (2013). Solid-State Dye-Sensitized Solar Cells Using a Novel Class of Ullazine Dyes as Sensitizers. *Advanced Energy Materials*, 3(4), 496–504. doi:10.1002/aenm.201200701
- **Dualeh, A.**, Delcamp, J. H., Nazeeruddin, M. K., & Grätzel, M. (2012). Near-infrared sensitization of solid-state dye-sensitized solar cells with a squaraine dye. *Applied Physics Letters*, 100(17), 173512. doi:10.1063/1.4707374
- **Dualeh, A.**, De Angelis, F., Fantacci, S., Moehl, T., Yi, C., Kessler, F., et al. (2012). Influence of Donor Groups of Organic D- $\pi$ -A Dyes on Open-Circuit Voltage in Solid-State Dye-Sensitized Solar Cells. *Journal of Physical Chemistry C*, 116(1), 1572–1578. doi: 10.1021/jp209691e
- Burschka, J., **Dualeh, A.**, Kessler, F., Baranoff, E., Cevey-Ha, N.-L., Yi, C., et al. (2012). Tris(2-(1H-pyrazol-1-yl)pyridine)cobalt(III) as p-Type Dopant for Organic Semiconductors and Its Application in Highly Efficient Solid-State Dye-Sensitized Solar Cells. *Journal of the American Chemical Society*, 133(45), 18042–18045. doi: 10.1021/ja207367t
- Shi, Y., Hill, R. B. M., Yum, J.-H., **Dualeh, A.**, Barlow, S., Grätzel, M., et al. (2011). A High-Efficiency Panchromatic Squaraine Sensitizer for Dye-Sensitized Solar Cells. *Angewandte Chemie*, 123(29), 6749–6751. doi:10.1002/ange.201101362
- Project meeting presentation (oral): Seventh Framework Programme, European commission, FP7 project: ORION, Final Project Meeting, San Sebastian, Spain, September 2013. *Representative Work Package leader*.
- Poster presentation: 4th International Conference on Hybrid and Organic Photovoltaics, Uppsala, Sweden. **Dualeh, A.**, Moehl, T., Nazeeruddin, M. K. & Grätzel, M. *Temperature Dependence of*

*Transport-Properties of Spiro-MeOTAD as a Hole Transport Material in Solid-State Dye-Sensitized Solar Cells*, May 2012.

- Poster presentation: E-MRS 2011 Fall Meeting, Warsaw University, Poland. **Dualeh, A.**, De Angelis, F., Fantacci, S., Moehl, T., Yi, C., Kessler, F., Baranoff, E., Nazeeruddin, M. K. & Grätzel, M. *Influence of Donor Groups of Organic D- $\pi$ -A Dyes on Open-Circuit Voltage in Solid-State Dye-Sensitized Solar Cells*, September 2011.
- Poster presentation: 2011 Fall Meeting of the Swiss Chemical Society, EPFL, Switzerland. Shi, Y., Hill, R. B. M., Yum, J.-H., **Dualeh, A.**, Barlow, S., Grätzel, M., Marder, S. R. & Nazeeruddin, M. K. *A High-Efficiency Panchromatic Squaraine Sensitizer for Dye-Sensitized Solar Cells*, September 2011.